Advanced Digital Signal Processing Techniques for Electricity Distribution Grid Monitoring and Diagnostics

by

Md. Shamim Reza

UNSW
AUSTRALIA

A thesis submitted in fulfilment of the requirements for the degree of

Doctor of Philosophy

School of Electrical Engineering and Telecommunications
The University of New South Wales
Sydney, NSW, Australia

October 2014

PLEASE TYPE

THE UNIVERSITY OF NEW SOUTH WALES
Thesis/Dissertation Sheet

Surname or Family name: **Reza**

First name: **Md. Shamim** Other name/s:

Abbreviation for degree as given in the University calendar: **PhD**

School: **Electrical Engineering and Telecommunications** Faculty: **Engineering**

Title: **Advanced Digital Signal Processing Techniques for Electricity Distribution Grid Monitoring and Diagnostics**

Abstract 350 words maximum: (PLEASE TYPE)

The continuous monitoring of the power grid voltage parameters, namely amplitude, frequency and phase is essential for the implementation of key power system functions such as control and protection, load shedding and restoration, assessment of power quality and impact of distributed generation to mention just few.

Such monitoring requires modern digital signal processing (DSP) techniques which should be computationally efficient, accurate, fast and robust against any grid disturbances irrespective of their nature and type. Efficient low bandwidth DSP techniques for voltage monitoring will contribute to an economical realization of the smart grid vision for smart meters, phasor measurement units, and power quality analyser.

The thesis contributes to the previously mentioned topic. First, it offers a comprehensive overview of the grid voltage parameters estimation techniques reported thus far in the technical literature. These techniques are the discrete Fourier Transform (DFT), Kalman filter (KF), least-squares (LS) and phase-locked loop (PLL). There are however limitations associated with these techniques. For instance, the DFT one requires periodic waveforms being sampled. While the KF and the LS offer better performance under grid disturbances, they are computationally demanding techniques for real-time implementation. The PLL is a simple technique to implement in real-time but requires a trade-off between good dynamic performance and estimation accuracy under distorted grid conditions.

The thesis attempts to overcome the above mentioned limitations and proposes and documents the mathematical basis, simulation and experimental implementation of a number of DSP techniques for single-phase grid voltage fundamental frequency and/or amplitude estimation.

First, the grid voltage fundamental frequency is tracked by four proposed techniques which are based on a Teager energy operator, a Newton-type algorithm and a differentiation filter, a voltage modulation, and a demodulation and a differentiation filter. In addition, the thesis reports five techniques to estimate both fundamental voltage amplitude and frequency based on a modified demodulation, the DFT and a second-order generalized integrator (DFT-SOGI), a SOGI and a differentiation filter (SOGI-DF), a cascaded delayed signal cancellation (CDSC), and a linear KF.

The performance of the above nine techniques has been evaluated through simulation and experimentally. A comparison with selected competing techniques reported in the technical literature is also included for a number of cases. These cases cover at all times harmonics being present in the grid voltage under steady-state and in combination with frequency sweep, frequency step, voltage sag and voltage flicker.

The results presented in the thesis confirm that the proposed techniques provide improved performance with respect to the existing techniques for the cases studied as mentioned above. All the proposed techniques can reject the negative effects caused by harmonics and can also meet the accuracy and dynamics as specified by the standard requirements. The techniques based on the voltage modulation, demodulation and differentiation filter, modified demodulation, DFT-SOGI, and SOGI-DF provide improved stability, since they do not include an interdependent loop for the feedback of the estimated fundamental frequency. On the other hand, the techniques relying on the Teager energy operator, Newton-type algorithm and differentiation filter, modified demodulation, SOGI-DF, and CDSC are relatively computationally efficient for being implemented in real-time digital signal processors.

The thesis concludes with a benchmark comparison of all the proposed techniques in terms of a number of key criteria such as accuracy, dynamic performance, stability, simplicity and computational efficiency. The comparison provides a proven way for choosing a suitable technique for single-phase grid voltage fundamental amplitude and/or frequency estimation. Finally, research directions for conducting future research are discussed.

Declaration relating to disposition of project thesis/dissertation

I hereby grant to the University of New South Wales or its agents the right to archive and to make available my thesis or dissertation in whole or in part in the University libraries in all forms of media, now or here after known, subject to the provisions of the Copyright Act 1968. I retain all property rights, such as patent rights. I also retain the right to use in future works (such as articles or books) all or part of this thesis or dissertation.

I also authorise University Microfilms to use the 350 word abstract of my thesis in Dissertation Abstracts International (this is applicable to doctoral theses only).

Md. Shamim Reza ..... Signature

২৩/১০/১৪ ..... Witness

03/10/2014 ..... Date

The University recognises that there may be exceptional circumstances requiring restrictions on copying or conditions on use. Requests for restriction for a period of up to 2 years must be made in writing. Requests for a longer period of restriction may be considered in exceptional circumstances and require the approval of the Dean of Graduate Research.

FOR OFFICE USE ONLY Date of completion of requirements for Award:

THIS SHEET IS TO BE GLUED TO THE INSIDE FRONT COVER OF THE THESIS

ORIGINALITY STATEMENT

'I hereby declare that this submission is my own work and to the best of my knowledge it contains no materials previously published or written by another person, or substantial proportions of material which have been accepted for the award of any other degree or diploma at UNSW or any other educational institution, except where due acknowledgement is made in the thesis. Any contribution made to the research by others, with whom I have worked at UNSW or elsewhere, is explicitly acknowledged in the thesis. I also declare that the intellectual content of this thesis is the product of my own work, except to the extent that assistance from others in the project's design and conception or in style, presentation and linguistic expression is acknowledged.'

Signed Md. Shamim Reza

Date 03/10/2014

COPYRIGHT STATEMENT

'I hereby grant the University of New South Wales or its agents the right to archive and to make available my thesis or dissertation in whole or part in the University libraries in all forms of media, now or here after known, subject to the provisions of the Copyright Act 1968. I retain all proprietary rights, such as patent rights. I also retain the right to use in future works (such as articles or books) all or part of this thesis or dissertation.
I also authorise University Microfilms to use the 350 word abstract of my thesis in Dissertation Abstract International (this is applicable to doctoral theses only).
I have either used no substantial portions of copyright material in my thesis or I have obtained permission to use copyright material; where permission has not been granted I have applied/will apply for a partial restriction of the digital copy of my thesis or dissertation.'

Signed Md. Shamim Reza

Date 03/10/2014

AUTHENTICITY STATEMENT

'I certify that the Library deposit digital copy is a direct equivalent of the final officially approved version of my thesis. No emendation of content has occurred and if there are any minor variations in formatting, they are the result of the conversion to digital format.'

Signed Md. Shamim Reza

Date 03/10/2014

Abstract

The continuous monitoring of the power grid voltage parameters, namely amplitude, frequency and phase is essential for the implementation of key power system functions such as control and protection, load shedding and restoration, assessment of power quality and impact of distributed generation to mention just few.

Such monitoring requires modern digital signal processing (DSP) techniques which should be computationally efficient, accurate, fast and robust against any grid disturbances irrespective of their nature and type. Efficient low bandwidth DSP techniques for voltage monitoring will contribute to an economical realization of the smart grid vision for smart meters, phasor measurement units, and power quality analyser.

The thesis contributes to the previously mentioned topic. First, it offers a comprehensive overview of the grid voltage parameters estimation techniques reported thus far in the technical literature. These techniques are the discrete Fourier Transform (DFT), Kalman filter (KF), least-squares (LS) and phase-locked loop (PLL). There are however limitations associated with these techniques. For instance, the DFT one requires periodic waveforms being sampled. While the KF and the LS offer better performance under grid disturbances, they are computationally demanding techniques for real-time implementation. The PLL is a simple technique to implement in real-time but requires a trade-off between good dynamic performance and estimation accuracy under distorted grid conditions.

The thesis attempts to overcome the above mentioned limitations and proposes and documents the mathematical basis, simulation and experimental implementation of a number of DSP techniques for single-phase grid voltage fundamental frequency and/or amplitude estimation.

First, the grid voltage fundamental frequency is tracked by four proposed techniques which are based on a Teager energy operator, a Newton-type algorithm and a differentiation filter, a voltage modulation, and a demodulation and a differentiation filter. In addition, the thesis reports five techniques to estimate both fundamental voltage amplitude and frequency based on a modified demodulation, the DFT and a second-order generalized integrator (DFT-SOGI), a SOGI and a differentiation filter (SOGI-DF), a cascaded delayed signal cancellation (CDSC), and a linear KF.

The performance of the above nine techniques has been evaluated through simulation and experimentally. A comparison with selected competing techniques reported in the technical literature is also included for a number of cases. These cases cover at all times harmonics being present in the grid voltage under steady-state and in combination with frequency sweep, frequency step, voltage sag and voltage flicker.

The results presented in the thesis confirm that the proposed techniques provide improved performance with respect to the existing techniques for the cases studied as mentioned above. All the proposed techniques can reject the negative effects caused by harmonics and can also meet the accuracy and dynamics as specified by the standard requirements. The techniques based on the voltage modulation, demodulation and differentiation filter, modified demodulation, DFT-SOGI, and SOGI-DF provide improved stability, since they do not include an interdependent loop for the feedback of the estimated fundamental frequency. On the other hand, the techniques relying on the Teager energy operator, Newton-type algorithm and differentiation filter, modified demodulation, SOGI-DF, and CDSC are relatively computationally efficient for being implemented in real-time digital signal processors.

The thesis concludes with a benchmark comparison of all the proposed techniques in terms of a number of key criteria such as accuracy, dynamic performance, stability, simplicity and computational efficiency. The comparison provides a proven way for choosing a suitable technique for single-phase grid voltage fundamental amplitude and/or frequency estimation. Finally, research directions for conducting future research are discussed.

Acknowledgements

I would like to acknowledge the financial support provided for my PhD studies through the Tuition Fee Scholarship (TFS) at the University of New South Wales (UNSW) and the Australian Postgraduate Award Industry (APAI) supported by the Australian Research Council.

The research project was carried out under the supervision of Prof. Vassilios G. Agelidis and Dr. Mihai Ciobotaru, both from Australian Energy Research Institute (AERI) and School of Electrical Engineering and Telecommunications, UNSW, Sydney, NSW-2052, Australia.

I would like to express my deepest and sincere gratitude to my supervisors for their continuous support, guidance, motivation and inspiration throughout my PhD studies. Their timely and continuous input in my research work was a great source towards the successful completion of this work. I am grateful to my supervisor Prof. Vassilios G. Agelidis for giving me rare and precious opportunity to begin my PhD studies.

I would also like to thank Dr. Baburaj Karanayil for his valuable assistance in the laboratory. I am also thankful to all my fellow PhD students at AERI who assisted me many times and gave me support in different ways.

I would also like to thank all my colleagues in the Department of Electrical and Electronic Engineering (EEE) of Bangladesh University of Engineering and Technology (BUET) for giving me the encouragement to start my PhD studies.

Lastly, I am forever grateful to my wife for her understanding, encouragement and endless patience. I would also like to express my deepest gratitude to my parents and parents-in-law for their endless love and affection.

Table of Contents

List of Figures

List of Tables

List of Abbreviations

AC	Alternating current
ACD	Anticonjugate decomposition
ACDSC	Anticonjugate decomposition and cascaded delayed signal cancellation
ADALINE	Adaptive linear combiner
AMI	Advanced metering infrastructure
ANF	Adaptive notch filter
AVF	Adaptive vectorial filter
BPF	Band-pass filter
CDSC	Cascaded delayed signal cancellation
DC	Direct current
DF	Differentiation filter
DFT	Discrete Fourier Transform
DG	Distributed generation
DSC	Delayed signal cancellation
DSP	Digital signal processing
DS1103	dSPACE1103
DSPOC	Decomposition of single-phase system into orthogonal components
ECKF	Extended complex Kalman filter
EKF	Extended Kalman filter
EnKF	Ensemble Kalman filter
EPLL	Enhanced phase-locked loop
FFT	Fast Fourier Transform
FIR	Finite-impulse-response
FLL	Frequency-locked loop
IEC	International Electrotechnical Commission
IEEE	Institute of Electrical and Electronics Engineers
IET	Institution of Engineering and Technology
IFL	Instantaneous voltage flicker level
IIR	Infinite-impulse-response
IRDFT	Inverse recursive discrete Fourier Transform

KF	Kalman filter
LKF	Linear Kalman filter
LPF	Low-pass filter
LPM	Linear prediction model
LS	Least-squares
MAF	Moving average filter
MF	Modulating function
MG	Microgrid
NLKF	Nonlinear Kalman filter
NN	Neural network
NTA	Newton-type algorithm
OC	Orthogonal components
PC	Personal computer
PCC	Point of common coupling
PI	Proportional and integral
PLL	Phase-locked loop
PM	Prony's method
PMU	Phasor measurement unit
PQ	Power quality
QSG	Quadrature signal generator
QPLL	Quadrature phase-locked loop
RDFT	Recursive discrete Fourier Transform
ROCOF	Rate of change of frequency
RMS	Root mean square
SM	Smart Meter
SOGI	Second-order generalized integrator
SVD	Singular value decomposition
TEO	Teager energy operator
THD	Total harmonic distortion
ZCD	Zero crossing detection
3CS	Three consecutive samples

Nomenclatures

a_{f_0}	Voltage amplitude at frequency f_0
a_f	Voltage amplitude at frequency f
$a_{f+\Delta_f}$	Voltage amplitude at frequency $f+\Delta_f$
$a_{f-\Delta_f}$	Voltage amplitude at frequency $f-\Delta_f$
$\hat{a}_{f_0}$	Estimated value of a_{f_0}
$\hat{a}_f$	Estimated value of a_f
$\hat{a}_{f+\Delta f}$	Estimated value of $a_{f+\Delta f}$
$\hat{a}_{f-\Delta f}$	Estimated value of $a_{f-\Delta f}$
A_1	Fundamental voltage amplitude
$\hat{A}_1$	Estimated value of A_1
A_h	h^{th} harmonic voltage amplitude
$\hat{A}_h$	Estimated value of A_h
A_M	M^{th} harmonic voltage amplitude
A_i	Voltage amplitude of $i\omega$ angular frequency component
$\hat{A}_i$	Estimated value of A_i
A_{fund}	Fundamental voltage amplitude without IFL
$\hat{A}_{fund}$	Estimated value of A_{fund}
ΔA_1	Fundamental voltage amplitude correction factor in NTA
A_F	Amplitude of IFL
$A_{i'}$	Amplitude of the i'^{th} modal component in the grid voltage
$\hat{A}_{i'}$	Estimated value of $A_{i'}$
b	Coefficient of the polynomial in PM
b_1	Difference between N_w and L_1
b_2	Difference between N_{MAF} and L_2

c	Addition of recent voltage sample with the voltage sample delayed by two
$c^{(1)}$	First-order time derivative of c
c_i	Element of the vector C_{PM}
C	Filtered form of c using a FIR filter based on modulating function
C_2	In-quadrature (cosine) output component of oscillator tuned at angular frequency $2\omega_0+\Delta\omega$
C_{PM}	Amplitude and phase angle estimation vector in PM
$\mathrm{CDSC}_{p_1,p_2,p_3,\ldots}$	DSC_{p_1}, DSC_{p_2}, DSC_{p_3} and so on are cascaded in series
$\mathrm{CDSC}_{2,4,8,16,32}$	DSC_2, DSC_4, DSC_8, DSC_{16} and DSC_{32} are cascaded in series
$\mathrm{CDSC}_{4,8,16,32}$	DSC_4, DSC_8, DSC_{16} and DSC_{32} are cascaded in series
d	Two times of previous sample of voltage
$d^{(1)}$	First-order time derivative of d
d_1	Process noise
d_2	Measurement noise
det	Determinant
D	Filtered form of d using a FIR filer based on modulating function
D_{1C}	High frequency oscillations generated by the grid voltage DC offset, fundamental and harmonics after demodulation by $\cos(\omega_0 nT_s)$
D_{1S}	High frequency oscillations generated by the grid voltage DC offset, fundamental and harmonic after demodulation by $\sin(\omega_0 nT_s)$
D_C	High frequency oscillations generated by the grid voltage DC offset and harmonics after demodulation by $\cos(\omega_0 nT_s)$
D_S	High frequency oscillations generated by the grid voltage DC offset and harmonics after demodulation by $\sin(\omega_0 nT_s)$
DSC_{p_1}	Subscript p_1 means that inputs of DSC_{p_1} are delayed by time T/p_1
DSC_{p_2}	Subscript p_2 means that inputs of DSC_{p_2} are delayed by time T/p_2
DSC_{p_3}	Subscript p_3 means that inputs of DSC_{p_3} are delayed by time T/p_3
DSC_2	Subscript 2 means that inputs of DSC_2 are delayed by time $T/2$

DSC_4	Subscript 4 means that inputs of DSC_4 are delayed by time $T/4$
DSC_8	Subscript 8 means that inputs of DSC_8 are delayed by time $T/8$
DSC_{16}	Subscript 16 means that inputs of DSC_{16} are delayed by time $T/16$
DSC_{32}	Subscript 32 means that inputs of DSC_{32} are delayed by time $T/32$
e_v	Error voltage
e_f	Frequency error variable
E	Error vector
f	Fundamental frequency
$\hat{f}$	Estimated value of f
f_0	Nominal fundamental frequency
Δf	Fundamental frequency deviation
$\Delta\hat{f}$	Estimated value of Δf
f_i	Frequency of $i^{'\text{th}}$ modal component in grid voltage
$\hat{f}_i$	Estimated value of f_i
f_s	Sampling frequency
f_{cut}	Cut-off frequency of LPF
f_c	Centre frequency of BPF
f_F	Frequency of IFL
F	Gain of MAF
g_1	Nonlinear process function
g_2	Nonlinear measurement function
h	Order of harmonics (h=2,3,…,M)
H_{PM}	Vandermonde matrix in PM
H_k	Transfer function of BPF at centre frequency kf based on RDFT and IRDFT
H_1	Transfer function of BPF at centre frequency f based on RDFT and IRDFT
i	Order of harmonics including fundamental one (i=1,2,3,…,M)
i'	Order of modal component in voltage of PM (i'=1,2,3,…,M_{PM})
I	Identity matrix

$I_{2\times2}$	2×2 identity matrix
$I_{3\times3}$	3×3 identity matrix
Im	Imaginary
j	Complex operator
J_{NTA}	Jacobian matrix of the NTA
J_{LKF}	State transition or Jacobian matrix of the LKF
J_{EKF}	State transition or Jacobian matrix of the EKF
J_{LS}	Jacobian matrix of the LS
k	Frequency index of the DFT
k_p	Gain of a proportional controller
k_i	Gain of an integral controller
K_{LKF}	Kalman gain of the LKF
K_{EKF}	Kalman gain of the EKF
L_1	floor(N_w) = Closest integer of N_w toward negative infinite
L_2	floor(N_{MAF}) = Closest integer of N_{MAF} toward negative infinite
L_3	floor(N_w/p_1) = Closest integer of N_w/p_1 toward negative infinite
L_{LKF}	Measurement matrix of the LKF
L_{EKF}	Measurement matrix of the EKF
L_{PM}	Order of the polynomial in PM
m	Number of nominal fundamental voltage cycles
M	Maximum order of harmonics
M_{PM}	Number of modal components in voltage of PM
n	Sampling index of the voltage waveform
N_w	Number of samples in a window of time duration T_w
N_{MAF}	Number of simples in a window of MAF
p	Error covariance
P_n	Error covariance matrix
P_{n+1}^-	Predicted error covariance matrix

P_0	Initial error covariance matrix
q	Process noise covariance
q_1	A fixed value of q
qv	In-quadrature component of v
qv_1	In-quadrature component of v_1
$qv_1^{'}$	Estimated value of qv_1
qv_{in}	In-quadrature voltage input to DSC
qv_{out}	In-quadrature voltage output from DSC
qv_h	In-quadrature component of v_h
$qv_h^{'}$	Estimated value of qv_h
qv_i	In-quadrature component of v_i
$qv_i^{'}$	Estimated value of qv_i
Q_n	Process noise covariance matrix
Q	Constant process noise covariance matrix
r	$\cos(2\pi fT_s)$
r_n	$\cos\{2\pi f(n)T_s\}$
R_n	Measurement noise covariance
R	Constant measurement noise covariance
R_1	A fixed value of R
Re	Real
s	Laplace operator
S	Maximum derivative order of modulating function
S_2	In-phase (sine) output component of oscillator tuned at angular frequency $2\omega_0+\Delta\omega$
t	Time in continuous domain
T	Fundamental time period
T_s	Sampling period
T_c	Characteristics time of modulating function
T_{LPF}	Settling time of LPF

T_{RDFT}	Dynamics time delay provided by BPF based on RDFT and IRDFT
T_w	Size of window in time
T_1	Transfer function of BPF used for offset rejection
T_2	Transfer function of IIR DF
T_3	Transfer function of FIR DF based on modulating function
T_4	Transfer function of SOGI
T_5	In-phase transfer function of QSG-SOGI
T_6	In-quadrature transfer function of QSG-SOGI
U_{AD}	Input vector of ADALINE
v	Grid voltage
v'	Estimated value of v
$v^{(1)}$	First-order time derivative of v
$v^{(\ell)}$	ℓ^{th} order time derivative of v
v_0	DC offset
$\hat{v}_0$	Estimated value of v_0
v_1	Fundamental voltage component
v_1'	Estimated in-phase component of v_1
v_h	h^{th} harmonic voltage component
v_h'	Estimated in-phase component of v_h
v_H	Total harmonic voltage component
v_H'	Estimated value of v_H
v_{1C}	Grid voltage demodulated by $\cos(\omega_0 n T_s)$
v_{1S}	Grid voltage demodulated by $\sin(\omega_0 n T_s)$
v_{1CF}	Low-pass filtered of v_{1C}
v_{1SF}	Low-pass filtered of v_{1S}
v_{1C}'	$v_{1C} - S_2$
v_{1SF}'	$v_{1S} - C_2$

v'_{1CF}	Low-pass filtered of v'_{1C}
v'_{1SF}	Low-pass filtered of v'_{1S}
v_1^u	Amplitude normalized of v_1 (u indicates unity)
v_{in}	In-phase voltage input to DSC
v_{out}	In-phase voltage output from DSC
v_i	Voltage component of $i\omega$ angular frequency component
v'_i	Estimated in-phase component of v_i
v_F	IFL
v'_F	Estimated value of v_F
v_{LS}	LS input voltage vector
v_{PM}	PM input voltage vector for amplitude and phase angle estimation
v_d	d component of Park Transform
v_q	q component of Park Transform
v^s	Subtraction between two consecutive samples of v
V_k	DFT of v
v^m	Modulated voltage
W_{AD}	Weight vector of ADALINE
W_{Han}	Hanning window
x	State vector for fundamental and/or harmonics analysis
$\bar{x}$	Predicted value of x
x_{11}	State for in-phase fundamental voltage component
$\bar{x}_{11}$	Predicted value of x_{11}
x_{12}	State for in-quadrature fundamental voltage component
$\bar{x}_{12}$	Predicted value of x_{12}
x_{i1}	State for in-phase voltage waveform of $i\omega$ angular frequency component
$\bar{x}_{i1}$	Predicted value of x_{i1}
x_{i2}	State for in-quadrature voltage waveform of $i\omega$ angular frequency component

x_{i2}^{-}	Predicted value of x_{i2}
x_{M+1}	State for fundamental angular frequency
x_{h1}	State for in-phase voltage waveform of h^{th} harmonic component
x_{h1}^{-}	Predicted value of x_{h1}^{-}
x_{h2}	State for in-quadrature voltage waveform of h^{th} harmonic component
x_{h2}^{-}	Predicted value of x_{h2}^{-}
x_F	State vector for IFL analysis
x_F^{-}	Predicted value of x_F
x_{F1}	State for in-phase component of IFL
x_{F1}^{-}	Predicted value of x_{F1}
x_{F2}	State for in-quadrature component of IFL
x_{F2}^{-}	Predicted value of x_{F2}
x_{F3}	State for frequency of IFL
x_{F3}^{-}	Predicted value of x_{F3}
x_{F4}	State for fundamental voltage amplitude without IFL
x_{F4}^{-}	Predicted value of x_{F4}
x_{LS}	LS estimation vector
X_n	Estimation vector in NTA
ΔX_n	Estimation correction vector in NTA
y	Multiplication between Hanning window and exponential term of the DFT
z	z-Transform operator
z^{-1}	One sample delay
z^{-N_w}	N_w samples delay
$z^{-N_{MAF}}$	N_{MAF} samples delay
z^{-L_1}	L_1 samples delay
z^{-L_2}	L_2 samples delay
z_i	Root of the polynomial in PM
α_{AD}	Reduction factor of the ADALINE

β	Ratio of a fixed value of process and measurement noise covariance (q_1/R_1)
Γ_n	Index function of voltage modulation and 3CS technique
δ	Dirac delta function
γ	Gain of FLL
Δ_f	Frequency resolution of the DFT
ω	Fundamental angular frequency
$\hat{\omega}$	Estimated value of ω
ω_0	Nominal fundamental angular frequency
$\Delta\omega$	Fundamental angular frequency deviation
$\Delta\hat{\omega}$	Estimated value of $\Delta\omega$
$\dot{\omega}$	Dynamics of ω
ω_{cut}	Cut-off angular frequency of LPF
ω_r	Tuning angular frequency of SOGI
$\omega_{\angle T_5}$	Fundamental angular frequency error caused by $\angle T_5\{j\omega(n)\}$
$\Delta\omega_{N_w/2}$	Fundamental angular frequency deviation over a window size of $N_w/2$ samples
ϕ_1	Instantaneous phase angle of the fundamental voltage component
$\hat{\phi}_1$	Estimated value of ϕ_1
ϕ_i	Instantaneous phase angle of the $i\omega$ angular frequency component
$\hat{\phi}_i$	Estimated value of ϕ_i
ψ_1	Initial phase angle (θ_1) plus instantaneous phase angle $\{\Delta\omega(n)nT_s\}$ corresponding to fundamental angular frequency deviation $(\Delta\omega)$
$\hat{\psi}_1$	Estimated value of ψ_1
$\psi_1^{(1)}$	First-order time derivative of ψ_1
$\psi_1^{'}$	Low-pass filtered value of ψ_1
ψ_i	Initial phase angle (θ_i) plus instantaneous phase angle $\{i\Delta\omega(n)nT_s\}$ corresponding to angular frequency deviation $i\Delta\omega$ of $i\omega$ angular frequency component
$\Delta\psi_1$	Phase angle correction factor of fundamental voltage component in NTA

θ_1	Initial phase angle of the fundamental voltage component
θ_h	Initial phase angle of the h^{th} harmonic voltage component
θ_M	Initial phase angle of the M^{th} harmonic voltage component
θ_i	Initial phase angle of the $i\omega$ angular frequency component
$\hat{\theta}_i$	Estimated value of θ_i
$\theta_{i'}$	Initial phase angle of the i'^{th} modal component in grid voltage
$\hat{\theta}_{i'}$	Estimated value of $\theta_{i'}$
θ_{er}	Estimated phase angle error introduced by ω_r/ω
θ_F	Initial phase angle of IFL
φ	Modulating function
φ_S	Modulating function with maximum derivative order S
$\varphi_S^{(\ell)}$	ℓ^{th} order time derivative of φ_S
$\varphi_S^{(1)}$	First-order time derivative of φ_S
ρ	Forgetting factor in voltage modulation and 3CS technique
λ_{LS}	Forgetting factor in SOGI-LS technique
$\sigma_{i'}$	Damping coefficient of the i'^{th} modal component in grid voltage
$\hat{\sigma}_{i'}$	Estimated value of $\sigma_{i'}$
η_{NTA}	Estimation function of NTA
σ	SOGI's gain
ξ	Damping factor of QSG-SOGI
θ_{0-LS}	Initial value of estimation vector in SOGI-LS technique
!	Factorial
□	Transpose operation
#	Complex conjugate operation
◊	Complex conjugate transpose operation
$\lvert\cdots\rvert$	Absolute value
$\lVert\cdots\rVert$	Euclidean norm
$\angle$	Angle

$0_{2\times1}$	2×1 zeros vector
*	Ranking of technique in benchmark comparison

Chapter 1
Introduction

This chapter starts by presenting the background and motivation of the thesis in Section 1.1. The objectives of the PhD research project are then presented in Section 1.2. The methodology and tools used for the research are described in Section 1.3. The contributions and the list of publications obtained from the thesis are given in Sections 1.4 and 1.5, respectively. Finally, Section 1.6 contains the outline of the thesis.

1.1 Background and Motivation

The information and communication technology will be integrated with the traditional grid in the development of future electricity network, the so called 'smart grid' [1-5]. The smart grid is intended to take benefits of all available modern technologies in transforming the traditional grid to one that functions more intelligently to monitor and control grid activities. Functionally, the smart grid is an automated electric power system, where both power and information flows will be bidirectional and the actions of all the users connected to it can be intelligently integrated for enhancing energy utilization, stability, safety and reliability, and reducing wasted resources [1-5]. The bidirectional communication network between the smart grid and metering devices allows collection and distribution of information to consumers, service providers, distribution network companies and utility companies [5-11]. The configurations of the smart grid can be customized for real-time response by using bidirectional information flows. One possible solution to deploy the bidirectional communication in the smart grid is to use advanced metering infrastructure (AMI) [11-13].

An efficient smart grid relies on accurate and secure real-time data collection and transmission service provided by a wide area monitoring systems [14-16]. The monitoring systems are typically built in a centralized manner. In such a system, the measuring units, namely smart meters (SMs) [17-23] and phasor measurement units (PMUs) [24-32] are essential parts to provide real-time information about the grid. These devices function as sensors and are placed throughout the grid, and transfer the measured data to the control

centre by communication network [5-11]. The control centre analyses the measured data and sends corresponding control decisions to maintain the normal operation of the grid.

1.1.1 Smart Meters (SMs)

The SMs are an integral part of the AMI in data collection and communications, and are used as the information gateways in the smart grid vision realization [17-23]. The SMs allow consumers to participate in the functioning of the electricity markets and help distribution networks to play an active role in the running of the smart grid [33].

The SMs are electronic measurement devices and can provide time-based pricing and energy consumption data of a whole house [17, 23]. This information helps to decrease the meter operation costs through remote data exchange and can be used for accurate and timely billing. The SMs can be used to decrease energy usage and energy costs through better information and increasing energy awareness [17, 23]. The SMs also allow electricity consumers to track their own energy usage on the Internet and/or with third-party computer programs [33]. The SMs can also be used for non-intrusive load monitoring which can decompose the energy consumption data into individual load level [18, 20, 34-37]. This information benefits the consumers to make sound energy saving decisions and also allow them to participate in demand response program [38-40].

The grid monitoring is one of the features of the SMs [21, 22, 41-45]. This feature of the SMs enables to share their cost with other applications such as power quality (PQ) analysis. The utilities need to get advance warnings of the PQ problems, such as harmonics, voltage fluctuations and so on, but special PQ analysers are too expensive to be used in large numbers in the distribution grid [22, 41-44]. In this case, the function of the SMs can be extended for PQ monitoring in order to avoid using of a large number of expensive PQ analysers, thus reducing the cost of the distribution grid monitoring [41, 42]. The PQ monitoring demands sparing some of the processing power and memory at the software implementation level since the SMs will be installed once over their lifespan [22, 41, 42]. In this case, low bandwidth sensors can be used in the SMs to reduce hardware costs and spare microprocessors' memory [22, 41, 42]. Consequently, computationally efficient phasor estimation techniques, which will need simple hardware implementations, are required for monitoring of the distribution grid by using the SMs.

1.1.2 Phasor Measurement Units (PMUs)

Phasors can play an important role in the operation, control and protection of the grid [24-32]. The PMUs can provide the estimation of voltage/current phasors, frequency and rate of change of frequency (ROCOF) from the waveforms appearing at their input terminals. The IEEE standard C.37.118.1 is described for synchronised phasor (synchrophasor) measurement instruments deployed for grid monitoring [32]. The objectives of this standard are to define and quantify the performance of the PMUs used in the substations. A set of performance requirements is presented in the IEEE standard C.37.118.1 for evaluating the measurements and compliance with the standard under both steady-state and dynamic conditions in order to make sure that the PMUs will provide similar results when faced with the same group of test waveforms. In addition, time tag (time instant of estimated synchrophasor), synchronization requirements and other essential associations are described to facilitate communication and reliable data application [32]. Synchronization of estimated phasors is achieved by same time sampling of voltage/current waveform using timing signals from the Global Positioning System Satellite (GPS).

Two classes of PMUs, namely P class and M class, have been defined in the IEEE standard C.37.118.1 [32]. The P class is designed for applications necessitating fast reporting speed such as the grid protection and 'P' stands for protection. On the other hand, the M class PMU is scheduled for applications that can be severely affected by the distortions present in the waveforms and do not require fast response. 'M' is used for analytic measurements that often demand greater accuracy but do not need fast response.

As the grid continues to expand and the transmission lines are pushed to their operating limits, the dynamic operation of the grid has become more of a concern [46]. The grid voltage/current phasors offer a way of observing the dynamic phenomena in order to provide a better operation, control and protection of the grid [24-32]. As a result, the synchrophasor measurements using the PMUs are becoming an important element of wide area monitoring systems. The synchrophasor estimated by the PMUs offer several potential benefits including: precise estimation of the grid state can be obtained at frequent intervals, allowing dynamic phenomena to be monitored from a central location and proper control actions can be taken; acceptable quality of the power supplied to the consumers can be ensured; security assessment i.e. the vulnerability of the grid against any incident can be analysed; advanced control using remote feedback becomes possible thereby improving

controller performance; and advanced protection can be implemented with options for improving overall system response to catastrophic events [24-31, 47]. Therefore, improved wide area monitoring systems based on phasor measurements using PMUs with remedial action capabilities allow the operators to utilize the grid in a more efficient way.

1.1.3 Distributed Generation (DG) Systems

Distributed generation (DG) is one of the important ingredients of the emerging smart grid paradigm [48-51]. The integration of DG with the smart grid at levels from consumer premises to centralised plants supports the advance of global energy sustainability [48-51]. The penetration of the DG based on renewable energy sources, such as solar and wind systems, into the grid is ever increasing due to the problems of the global warming and the exhaustion of the fossil fuels [48, 50, 52-54]. The solar and wind energy based DG helps to reduce the use of the traditional environment-hostile power plants and also lowers the greenhouse gas emission [54].

The DG systems are connected to the grid using power converters [49, 51, 53]. The control system of the grid-connected power converters requires proper synchronization to get the current in-phase with the grid voltage at the point of common coupling (PCC). The grid voltage phase angle is usually used for this purpose. On the other side, a large penetration of the DG into the grid may cause fluctuation of the voltage amplitude and frequency, thus may affect the stability and safety conditions of the grid [55, 56]. The grid voltage amplitude and frequency can be considerably affected when the power supplied by the DG is significant in comparison with the rated power of the grid at the PCC [57]. For this reason, many international grid codes are introduced to regulate the characteristics of the DG [58-60]. The grid codes specify the ranges of the voltage amplitude and frequency within which the DG should remain connected with the grid while ensuring stable operation. The DG has to be disconnected from the grid when the grid voltage amplitude and frequency at the PCC exceed their specified ranges. The IEC standard 61727 defines that a photovoltaic system has to be disconnected from the grid when the grid frequency exceeds ±1 Hz of the rated frequency [61]. Therefore, the grid voltage fundamental parameters have to be monitored at the PCC of the DG system in order to achieve a reliable, safe and efficient operation of the grid.

1.1.4 Microgrids (MGs)

Microgrid (MG) is one of the basic elements of future smart grid [62, 63]. It is a small scale version of the centralized electricity system and can be defined as an independent low or medium-voltage distribution electricity network containing various DGs, energy storages, and controllable loads [64-70]. Similar to the bulk power grid, MG generates, distributes, and controls the flow of electricity to the consumers, but it is done locally. It allows integrating renewable resources on the community level and also for consumers' participation in the electricity enterprise [69-71]. If MG is properly coordinated and managed, it can increase the efficiency of the power systems by: supporting large scale penetration of DGs; facilitating the integration of renewable resources; reducing system losses and greenhouse gas emissions; increasing the reliability of the power supply to the consumers; improving power quality; and providing better voltage stability [66-73].

In general, MG can operate as a grid-connected or an islanding mode [70, 74]. In the grid-connected mode, a controller is required to operate in a current control mode, where it controls the flow of power between the power grid and MG. In this mode, the power grid can support the system frequency and bus voltages by covering the power mismatch immediately. On the other hand, the controller operates in a voltage control mode during the islanding condition. In this case, the system frequency and bus voltage may fluctuate with a certain amount of uncertainties because the droop controllers adjust them to cover up instant power mismatch, thus requiring a fast and flexible reaction of under voltage and/or under frequency relays [73, 75, 76]. The frequency control is also important during transition between the grid-connected and islanding modes, where high deviations of frequency can be observed [77, 78]. The IEEE standard 1547 describes that the frequency of a MG cannot differ from the grid frequency more than 0.1% during the reconnection with the grid [77, 78]. Therefore, the monitoring of the voltage parameters is essential for a safe, reliable and efficient operation of MG.

1.1.5 Power Quality (PQ) Analysis

A wide diffusion of nonlinear loads and poorly controlled DG systems connected with the grid create disturbances which are responsible for the deterioration of PQ, involving both the supply and the loading quality [79-81]. The PQ disturbances impose extra losses due to harmonics, decrease the efficiency of power usage, lead to the misoperation of

protection equipment, cause the overheating and isolation collapse of transformers, cables and motors, origin excessive neutral currents in three-phase four-wire systems, lead to low power factor, communication interferences, reduction of torque in certain rotating machines, decreasing the useful life of electrical devices and so on [82-84]. There is also power sensitive equipment, particularly computers, microprocessor-controlled and automated manufacturing devices which are highly vulnerable to PQ disturbances.

The PQ disturbances can be classified into two main groups, such as 'continuous' and 'discrete', and are defined in the IEC standard 61000-4-30 [85]. The continuous type disturbances are observed in each cycle and typically include unbalance, flicker, harmonics and interharmonics [86-88]. On the other hand, the discrete type disturbances appear as isolated and independent events which include voltage sag, voltage swell, oscillatory and impulsive transients, and are identified based on a defined threshold and characterized by a set of parameters, such as root mean square (RMS) or peak magnitude and duration [89-91].

The PQ disturbances may lead to massive financial losses, if they are not mitigated. Thus, the PQ analysis is of increasing concern in the deregulated power market because of a direct economic impact on utilities and industrial consumers. For this reason, there is a growing need to develop PQ monitoring techniques that can detect the disturbances, occurrence time, identify the location and classify the potential sources of disturbances for understanding the underlying cause and to prevent future occurrence [80, 81]. The PQ disturbances are traditionally monitored based on phasor measurement and is the first step to improve the quality of the power supply.

1.2 Objectives of the Thesis

The continuous monitoring of the grid voltage parameters is essential for the implementation of key power system functions such as control and protection, load shedding and restoration, impact of DG and assessment of PQ. The grid voltage parameters are usually estimated by using digital signal processing (DSP) techniques, which should be computationally efficient, accurate, fast and robust against grid disturbances. The main objectives of the thesis are presented in the following.

- To propose robust and stable DSP techniques for real-time single-phase grid voltage monitoring under non-periodic, distorted and adverse grid conditions.

- To provide accurate estimation of fundamental voltage amplitude and frequency of the single-phase grid voltage and also to reject the negative effects caused by the grid disturbances.
- To assess the PQ issues such as DC offset, harmonics amplitude and instantaneous voltage flicker level (IFL) present in the single-phase grid voltage in the presence of other grid disturbances.
- To meet the standard requirements in terms of robustness, accuracy and dynamic performance of the proposed DSP techniques under a wide range of variations of the grid voltage parameters.
- To implement the proposed DSP techniques on a low cost digital signal processor for an economical realization of the smart grid vision for SMs, PMUs and PQ analyser.

1.3 Methodology and Tools Used

The performance of the DSP techniques reported in the thesis is verified using both simulation and experimental results.

MATLAB/Simulink software is used to develop the DSP techniques for simulation in a personal computer (PC) environment. The single-phase grid voltage waveforms under different operating conditions are emulated in MATLAB/Simulink for evaluating the simulation performance of the techniques.

The experimental setup for real-time performance assessment of the DSP techniques is shown in Fig. 1.1. The experimental setup consists of a hardware part and a software part. The hardware part contains a programmable AC power supply, a voltage sensor, a dSPACE1103 (DS1103) control board and a PC. The programmable AC power supply is used to generate the real-time single-phase grid voltage (v_{LN}, where the subscript LN indicates line-to-neutral) under different conditions such as DC offset, harmonics,

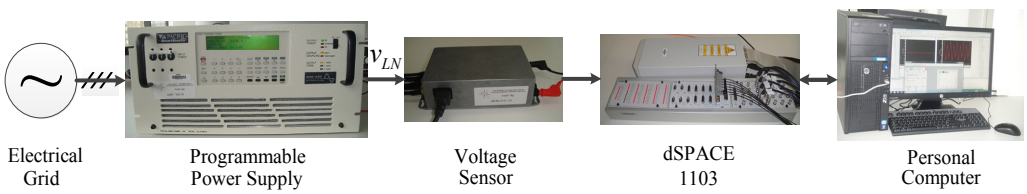

Fig. 1.1 Laboratory setup for real-time experiment.

frequency step, frequency sweep, voltage sag, voltage flicker, notches and spikes. The voltage sensor measures the generated grid voltage and sends it to the 16 bit analogue-to-digital converter of the DS1103 control board. On the other hand, the software part consists of MATLAB/Simulink, DS1103 Real-Time Interface and Control Desk Interface. The MATLAB/Simulink models of the developed DSP techniques are compiled and uploaded to the DS1103 control board using automatic code generation. The Control Desk Interface running on the PC is used to set the parameters in real-time and also to monitor the estimated values.

1.4 Main Contributions of the Thesis

The grid voltage frequency is a universal parameter across the interconnected power system and contains information about the system operation and dynamics. It is a fundamental parameter for frequency relaying applications such as generator protection, load shedding and restoration. On other hand, both fundamental voltage amplitude and frequency are important parameters for monitoring the impact of DG, PQ assessment, power system control and protection. For these reasons, a number of DSP techniques are proposed and documented in the thesis to estimate the single-phase grid voltage fundamental amplitude and/or frequency. Among these techniques, four are reported to estimate the fundamental frequency and are based on:

- A recursive discrete Fourier Transform and a Teager energy operator (RDFT-TEO)
- A Newton-type algorithm and a differentiation filter (NTA-DF)
- Voltage modulation and three consecutive samples (3CS)
- A demodulation and a DF

In addition, five techniques are described to estimate both fundamental voltage amplitude and frequency, and are relying on:

- A modified demodulation
- The discrete Fourier Transform and a second-order generalised integrator (DFT-SOGI)
- A SOGI and a DF (SOGI-DF)

- An anticonjugate decomposition and a cascaded delayed signal cancellation (ACDSC)
- A linear Kalman filter (KF) with a frequency locked loop (LKF-FLL)

The RDFT-TEO technique is faster, shows enhanced accuracy and improves computational efficiency when compared with the RDFT based decomposition of a single-phase system into orthogonal components (RDFT-OC) technique.

The NTA-DF technique avoids real-time matrix inversion operation, reduces matrix dimensions and computational burden, improves accuracy and provides better dynamic speed in comparison with the NTA and a least-squares (NTA-LS) technique.

The voltage modulation and 3CS technique does not require setting a threshold value of the middle sample of 3CS for removing the ill-condition and is less affected by the voltage disturbances when compared with a conventional technique based on the 3CS and a finite-impulse-response (FIR) filter.

The demodulation and DF technique provides better accuracy while keeping same computational effort as compared with the demodulation and a conventional DF technique.

The modified modulation technique demonstrates superior performance as compared to the conventional demodulation one.

The DFT-SOGI technique is less sensitive to the presence of harmonics and also avoids the interdependent loop between the orthogonal voltage system and the frequency estimation at the expense of a higher computational burden when compared with the SOGI based FLL (SOGI-FLL) and phase-locked loop (SOGI-PLL) techniques.

The SOGI-DF technique does not create interdependent loop between the orthogonal voltage system and the frequency estimation, and shows better performance under harmonics as compared to the SOGI and LS (SOGI-LS) technique.

The ACDSC technique offers improved estimation under distorted conditions while providing similar dynamic response in comparison with the SOGI-FLL technique.

The LKF-FLL technique is linear, avoids the derivatives of the nonlinear functions, does not contain nonlinear terms and is computationally less complex when compared with the nonlinear Kalman filter (NLKF). The LKF-FLL technique also provides improved estimation under harmonics as compared to an extended complex Kalman filter (ECKF) technique. The LKF-FLL technique can also be extended for accurate estimation of the grid voltage harmonics including fundamental parameters.

1.5 List of Publications

The contributions of the research works have been published/accepted/submitted in peer reviewed international conferences and journals. The list of these papers is as follows.

1.5.1 Journal Papers

Published or Accepted for Publication (In Press)

[J1] M. S. Reza, M. Ciobotaru, and V. G. Agelidis, "Accurate estimation of single-phase grid voltage parameters under distorted conditions," *IEEE Transactions on Power Delivery*, vol. 29, no. 3, pp. 1138-1146, June, 2014.

[J2] M. S. Reza, M. Ciobotaru, and V. G. Agelidis, "Differentiation filter-based technique for robust estimation of single-phase grid voltage frequency under distorted conditions," *IET Generation, Transmission & Distribution*, vol. 8, issue 5, pp. 907-915, 2014.

[J3] M. S. Reza, M. Ciobotaru, and V. G. Agelidis, "Robust technique for accurate estimation of single-phase grid voltage fundamental frequency and amplitude," *IET Generation, Transmission & Distribution*, 2014 (accepted for publication, in press).

[J4] M. S. Reza, M. Ciobotaru, and V. G. Agelidis, "A robust frequency estimation technique based on three consecutive samples for single-phase systems," *IEEE Journal of Emerging and Selected Topics in Power Electronics*, 2014 (accepted for publication, in press).

[J5] M. S. Reza, M. Ciobotaru, and V. G. Agelidis, "Power system frequency estimation using a Newton-type technique for smart meters," *IEEE Transactions on Instrumentation and Measurement*, 2014 (accepted for publication, in press).

[J6] M. S. Reza, M. Ciobotaru, and V. G. Agelidis, "A modified demodulation technique for single-phase grid voltage fundamental parameters estimation," *IEEE Transactions on Industrial Electronics*, 2014 (accepted for publication, in press).

Currently Under Review

[J7] M. S. Reza, M. Ciobotaru, and V. G. Agelidis, "A frequency adaptive linear Kalman filter for accurate estimation of single-phase grid voltage fundamental amplitude and frequency," *IET Science, Measurement & Technology* (under review).

[J8] M. S. Reza, M. Ciobotaru, and V. G. Agelidis, "Single-phase grid voltage frequency estimation using Teager energy operator based technique," *IEEE Journal of Emerging and Selected Topics in Power Electronics* (Revision 1 under review).

[J9] M. S. Reza, M. Ciobotaru, and V. G. Agelidis, "Grid synchronization technique without using trigonometric functions for accurate estimation of fundamental voltage parameters," *IET Generation, Transmission & Distribution* ((Revision 1 under review).

1.5.2 Conference Papers

[C1] M. S. Reza, M. Ciobotaru, and V. G. Agelidis, "Power quality analysis using piecewise adaptive Prony's method," *in Proceedings of IEEE International Conference on Industrial Technology* (*ICIT*), 2012, pp. 926-931.

[C2] M. S. Reza, M. Ciobotaru, and V. G. Agelidis, "Grid voltage offset and harmonics rejection using second order generalized integrator and Kalman filter technique," *in Proceedings of 7th IEEE International Power Electronics and Motion Control Conference* (*IPEMC*), 2012, pp. 104-111.

[C3] M. S. Reza, M. Ciobotaru, and V. G. Agelidis, "Instantaneous power quality analysis using frequency adaptive Kalman filter technique," *in Proceedings of 7th IEEE International Power Electronics and Motion Control Conference* (*IPEMC*), 2012, pp. 81-87.

[C4] M. S. Reza, M. Ciobotaru, and V. G. Agelidis, "Accurate estimation of grid voltage parameters using singular value decomposition technique," *in Proceedings of 3rd IEEE International Symposium on Power Electronics for Distributed Generation Systems* (*PEDG*), 2012, pp. 794-800.

[C5] M. S. Reza, M. Ciobotaru, and V. G. Agelidis, "Frequency adaptive instantaneous power quality analysis using frequency locked loop based Kalman filter technique," *in Proceedings of 3rd IEEE International Symposium on Power Electronics for Distributed Generation Systems* (*PEDG*), 2012, pp. 767-774.

[C6] M. S. Reza, M. Ciobotaru, and V. G. Agelidis, "Tracking of time-varying grid voltage using DFT based second order generalized integrator technique," *in Proceedings of IEEE International Conference on Power System Technology* (*POWERCON*), 2012, pp. 1-6.

[C7] M. S. Reza, M. Ciobotaru, and V. G. Agelidis, "Frequency adaptive linear Kalman filter for fast and accurate grid voltage parameters estimation," *in Proceedings of IEEE International Conference on Power System Technology* (*POWERCON*), 2012, pp. 1-6.

[C8] M. S. Reza, M. Ciobotaru, and V. G. Agelidis, "Robust estimation of real-time single-phase grid voltage frequency under distorted grid conditions," *in Proceedings of IEEE ECCE Asia Downunder*, 2013, pp. 948-954.

[C9] M. S. Reza, M. Ciobotaru, and V. G. Agelidis, "Real-time estimation of single-phase grid voltage frequency using a modulating function based technique," *in Proceedings of IEEE ECCE Asia Downunder*, 2013, pp. 664-669.

[C10] M. S. Reza, M. Ciobotaru, and V. G. Agelidis, "Estimation of single-phase grid voltage fundamental parameters using fixed frequency tuned second-order generalized integrator based technique," *in Proceedings of 4th IEEE International Symposium on Power Electronics for Distributed Generation Systems* (*PEDG*), 2013, pp. 1-8.

[C11] M. S. Reza, M. Ciobotaru, and V. G. Agelidis, "A recursive DFT based technique for accurate estimation of grid voltage frequency," *in Proceedings of 39th Annual Conference of the IEEE Industrial Electronics Society* (*IECON*), 2013, pp. 6418-6423.

[C12] M. S. Reza, M. Ciobotaru, and V. G. Agelidis, "A demodulation based technique for accurate estimation of real-time single-phase grid voltage

fundamental parameters," *in Proceedings of 39th Annual Conference of the IEEE Industrial Electronics Society* (*IECON*), 2013, pp. 6400-6405.

[C13] M. S. Reza, M. Ciobotaru, and V. G. Agelidis, "A frequency adaptive technique for accurate estimation of single-phase grid voltage fundamental parameters," *in Proceedings of 39th Annual Conference of the IEEE Industrial Electronics Society* (*IECON*), 2013, pp. 6406-6411.

The relation between the chapters of the thesis and the papers published/accepted/submitted above is as follows.

Chapter Number	Publications
Chapter 3	[J8], [C11]
Chapter 4	[J5]
Chapter 5	[J2], [J4], [J6], [C8], [C9], [C12]
Chapter 6	[J1], [J3], [J9], [C6], [C10], [C13]
Chapter 7	[J7], [C3], [C7]

1.6 Thesis Outline

The rest of the thesis is organized as follows:

Chapter 2 provides a comprehensive overview of the commonly used single-phase grid voltage monitoring techniques reported in the technical literature. The pros and cons of the techniques are also documented in this chapter.

Chapter 3 proposes the RDFT-TEO technique to estimate the single-phase grid voltage fundamental frequency. The performance of the technique is evaluated using both simulation and experimental results.

Chapter 4 lays a mathematical basis of the NTA-DF technique for single-phase grid voltage fundamental frequency estimation. The response of the technique is also documented in this chapter using simulation and experimental results.

Chapter 5 reports three techniques relying on the modulation and/or demodulation to estimate the single-phase grid voltage fundamental amplitude and/or frequency. These techniques are based on the voltage modulation and 3CS, demodulation and DF, and

modified demodulation. Selected simulation and/or experimental results are presented after the description of each technique.

Chapter 6 presents three techniques based on a quadrature signal generator (QSG) to obtain the single-phase grid voltage fundamental amplitude and frequency. These techniques are the DFT-SOGI, SOGI-DF and ACDSC. Simulation and/or experimental results are reported to verify the performance of these techniques.

Chapter 7 describes the LKF-FLL technique for single-phase grid voltage fundamental amplitude and frequency estimation. The technique is also extended for harmonics estimation. The performance of the technique is validated using selected simulation results.

Finally, Chapter 8 summarizes the works, presents a benchmark comparison among the proposed techniques and suggests directions for future research.

Chapter 2
Overview of Voltage Monitoring Techniques

This chapter presents a comprehensive overview of the commonly used digital signal processing techniques reported in the technical literature for single-phase grid voltage monitoring. The pros and cons of each technique are also documented after the description of the technique.

2.1 Literature Review

A critical review of the main existing digital signal processing (DSP) techniques used for single-phase grid voltage parameters estimation is presented in this section. The grid voltage parameters, namely amplitude, frequency and phase angle can be estimated by using many DSP techniques, such as discrete Fourier Transform (DFT) [28, 29, 31, 82, 92-102], adaptive linear combiner (ADALINE) [103-111], Newton-type algorithm (NTA) [112-122], least-squares (LS) [82, 123-132], Kalman filter (KF) [133-147], Prony's method (PM) [87, 108, 109, 148-163], neural network (NN) [164-169], singular value decomposition (SVD) [87, 156], phase-locked loop (PLL) [170-192], frequency-locked loop (FLL) [179, 184, 193-202], demodulation [181, 203-213], Teager energy operator (TEO) [214-221], zero crossing detection (ZCD) [213, 222-234], three consecutive samples (3CS) [78, 127, 141, 164, 235-240], root mean square (RMS) [241-243], adaptive notch filter (ANF) [244, 245], decomposition of single-phase systems into orthogonal components (DSPOC) [24, 29, 31, 82] and voltage modulation [246-248]. Among these techniques, the DFT, ADALINE, NTA, LS, KF, PM, NN and SVD are mainly used for grid voltage fundamental and harmonics parameters estimation. On the other hand, the PLL, FLL, demodulation, TEO, ZCD, 3CS, RMS, ANF, DSPOC and voltage modulation techniques are typically used for fundamental voltage parameters estimation.

The following subsections document a critical review of the DFT, ADALINE, NTA, LS, KF, PM, PLL, FLL, demodulation, TEO, ZCD and 3CS techniques presented in discrete time domain and used for single-phase grid voltage parameters estimation.

2.1.1 Discrete Fourier Transform (DFT)

The DFT allows a given periodic signal to be transformed from time domain to frequency domain in the field of DSP [92]. It is the most straight forward mathematical procedure and commonly used for determining the frequency contents of a time domain sequence. As the function of the DFT becomes more widely understood, the applications of it continue to flourish in many areas including power systems, acoustics, imaging/video, audio, instrumentation and communications systems [92].

The DFT of a single-phase grid voltage, $v(n)$, at the n sampling instant can be expressed by [93-95]

$$V_k(n) = \sum_{l=n-N_w+1}^{n} v(l) e^{-j\frac{2\pi kl}{N_w}} \tag{2.1}$$

where k=0,1,2,…,N_w-1 is the DFT frequency index, $N_w=mf_s/f_0$ is the number of voltage samples present in a window, m is the number of nominal fundamental voltage cycles present in the window, f_s is the sampling frequency, f_0 is the nominal fundamental frequency, j is the complex operator and the single-phase grid voltage can be expressed by

$$v(n) = v_0(n) + \sum_{i=1,2,...}^{M} A_i(n)\sin\left\{i\omega(n)nT_s + \theta_i(n)\right\} \tag{2.2}$$

where v_0 is the DC offset, M is the maximum order of harmonics, $\omega=2\pi f$ is the actual fundamental angular frequency, $f=f_0+\Delta f$ is the actual fundamental frequency, Δf is the fundamental frequency deviation, $T_s=1/f_s$ is the sampling period, and A_i and θ_i are the amplitude and initial phase angle of the $i\omega$ (i=1,2,…,M) angular frequency component, respectively.

The frequency resolution of the DFT, as given by (2.1), is $\Delta_f = f_0/m$ and improves when the window size is increased. The DFT can provide accurate estimation of the DC offset, fundamental and harmonics parameters when the value of m=1 and $\omega=\omega_0$, where $\omega_0=2\pi f_0$ is the nominal fundamental angular frequency [94, 95]. Interharmonics can also be estimated with a value of m greater than 1. However, a large size window increases the

computational burden and also slower the dynamic response. In this case, a recursive DFT (RDFT) can be used to reduce the computational effort and is expressed by [93-95]

$$V_k(n) = V_k(n-1) + \left\{ v(n) - v(n-N_w) \right\} e^{-j\frac{2\pi kn}{N_w}} \tag{2.3}$$

The amplitude and initial phase angle of the $i\omega$ (when $\omega=\omega_0$) angular frequency component of the grid voltage can be estimated by (2.4) and (2.5), respectively.

$$\hat{A}_i(n) = \frac{1}{N_w} \left| V_k(n) \right|_{i=k/m=1,2,3,\ldots,M} \tag{2.4}$$

$$\hat{\theta}_i(n) = \tan^{-1} \left[\frac{\mathrm{Im}\left\{ V_k(n) \right\}}{\mathrm{Re}\left\{ V_k(n) \right\}} \right]_{i=k/m=1,2,3,\ldots,M} \tag{2.5}$$

where $|\cdot\cdot|$ denotes absolute value, Im represents imaginary and Re means real. The DC offset of the grid voltage can also be obtained by

$$\hat{v}_0(n) = \frac{1}{N_w} \left| V_0(n) \right| \tag{2.6}$$

The DFT assumes that the grid voltage waveform is periodic and repetitive outside the window and hence may lead to inaccurate results due to a spectral leakage and picket fence effect during time-varying cases [96-99]. However, the spectral leakage can be reduced by using a desirable sidelobe window based DFT [97]. On the other hand, the spectral leakage information can also be used to obtain the time-varying fundamental frequency [98, 99]. However, large size moving windows are required for three DFT operations to avoid the interference caused by lower order harmonics at a cost of increasing computational effort and slower dynamic response [98, 99]. An iterative approach based on the DFT can also be used for frequency estimation at the expense of a high computational burden [100, 101]. On the other side, the frequency estimation using a fixed window RDFT based technique requires high-order finite-impulse-response (FIR) low-pass filter (LPF) to reject the negative effects caused by harmonics [29, 31, 82]. The negative effects of harmonics and the output phase error of the RDFT can also be removed by synchronizing the window size with the actual period of the grid voltage based on a variable sampling frequency [94]. However, the actual period of the grid voltage is updated after a time interval equal to the window size of the RDFT and the variable sampling frequency approach may not be suitable when a single micro-controller is used, since the parameters of other digital

algorithms implemented on the same micro-controller has to be adjusted for the new sampling frequency [94]. The RDFT may also suffer from an accumulation error when implemented on a digital signal processor, however, can be removed by careful coding [28, 102] or several other algorithms as reported in [95] at the cost of additional complexity and computational burden. Chapter 3 presents a relatively simple and computationally efficient technique based on the RDFT and TEO (RDFT-TEO) to estimate the single-phase grid voltage fundamental frequency under distorted conditions.

In summary, the pros and cons of the DFT technique are given in the following.

Pros:
- Relatively simple
- Commonly used for spectral analysis
- Can estimate DC offset, harmonics and interharmonics

Cons:
- Requires period voltage waveform
- Suffers from leakage and picket fence effects due to unsynchronized window
- Computationally demanding for improved frequency resolution
- Interharmonics may introduce error if not modelled

2.1.2 Adaptive Linear Combiner (ADALINE)

The ADALINE technique is developed based on a linear adaptive NN [103]. It is a frequency domain technique and estimates the Fourier coefficients of the grid voltage waveform [103-105]. It is also a relatively computationally efficient technique for estimating the single-phase grid voltage fundamental and harmonics amplitudes and phase angles with known fundamental frequency [103-105]. The technique has an input sequence, an output sequence, a desired response-signal sequence and a set of adjustable parameters called weight vector [103-105]. The weight vector generates Fourier coefficients of the input signal using a weight adjustment algorithm based on a difference error equation. The input vector, $U_{AD}(n)$, of the ADALINE at the n sampling instant of the grid voltage can be defined as

$$U_{AD}(n) = \left[\sin(\omega n T_s) \quad \cos(\omega n T_s) \quad \cdots \quad \sin(M\omega n T_s) \quad \cos(M\omega n T_s) \quad 1\right]^{\square} \qquad (2.7)$$

where the value of ω is assumed as constant and known, and $\square$ denotes transpose operation. The weight vector, $W_{AD}(n)$, of the ADALINE can be defined as

$$W_{AD}(n)=\left[A_1(n)\sin\{\theta_1(n)\}\quad A_1(n)\cos\{\theta_1(n)\}\quad\cdots\right.$$

$$\left.A_M(n)\sin\{\theta_M(n)\}\quad A_M(n)\cos\{\theta_M(n)\}\quad v_0(n)\right]^{\square}$$

$$=\left[w_1(n)\quad w_2(n)\quad\cdots\quad w_{2M-1}(n)\quad w_{2M}(n)\quad w_{2M+1}(n)\right]^{\square}\qquad(2.8)$$

where $w_{2i-1}(n)=A_i(n)\sin\{\theta_i(n)\}$, $w_{2i}(n)=A_i(n)\cos\{\theta_i(n)\}$ and i=1,2,…,M. The grid voltage estimated by the ADALINE can be expressed by [103-105, 110]

$$v'(n)=W_{AD}^{\square}(n)U_{AD}(n)\qquad(2.9)$$

The estimated error signal can also be expressed by

$$e_v(n)=v(n)-v'(n)\qquad(2.10)$$

where the input signal-phase grid voltage is given by (2.2). The weight vector of the ADALINE can be updated by [103-105, 110]

$$W_{AD}(n+1)=W_{AD}(n)+\frac{\alpha_{AD}e_v(n)U_{AD}(n)}{U_{AD}^{\square}(n)U_{AD}(n)}\qquad(2.11)$$

where α_{AD} is a learning parameter called reduction factor and its practical value lies is the range 0.01-1.0 [106]. A low value of α_{AD} increases the estimation accuracy at the cost of a slower convergence of weights. The optimum result of the ADALINE can be obtained for a value of α_{AD}=0.2 [106]. The computational effort of (2.11) can also be reduced by

$$W_{AD}(n+1)=W_{AD}(n)+\frac{\alpha_{AD}e_v(n)U_{AD}(n)}{1+M}\qquad(2.12)$$

where

$$U_{AD}^{\square}(n)U_{AD}(n)=1+\sum_{i=1}^{M}\left\{\sin^2(\omega nT_s)+\cos^2(\omega nT_s)\right\}=1+\sum_{i=1}^{M}1=1+M$$

The amplitudes and initial phase angles of the grid voltage fundamental and harmonics can be estimated by (2.13) and (2.14), respectively.

$$\hat{A}_i(n)=\sqrt{w_{2i-1}^2(n)+w_{2i}^2(n)}\qquad(2.13)$$

$$\hat{\theta}_i(n)=\tan^{-1}\left\{\frac{w_{2i-1}(n)}{w_{2i}(n)}\right\}\qquad(2.14)$$

The DC offset can also be obtained by

$$\hat{v}_0(n) = w_{2M+1}(n) \tag{2.15}$$

The ADALINE technique can provide accurate estimation of the grid voltage fundamental and harmonics amplitudes and phase angles under constant fundamental frequency, but may suffer from inaccuracy during the time-varying frequency condition [103]. In this case, a separate frequency estimation technique based on a PM can be integrated with the ADALINE for frequency adaptive estimation of the grid voltage fundamental and harmonics parameters [107-109]. A PLL can also be combined with the ADALINE to obtain the estimation of the synchronized phasors [110]. On the other hand, the tuning of the reduction factor may require additional algorithms such as a genetic algorithm and a fuzzy logic controller at the cost of high computational burden in real-time implementations [104, 111].

The pros and cons of the ADALINE technique can be summarized as followings.

Pros:
- Estimates Fourier coefficients
- Can estimate DC offset and harmonics

Cons:
- Complex tuning of the reduction factor
- Cannot provide synchronous estimation
- Requires separate frequency tracking technique for frequency adaptive estimation

2.1.3 Newton-Type Algorithm (NTA)

The NTA is a nonlinear technique and is derived using Newton's iterative method, which is very commonly used in load-flow analysis [112]. The grid voltage phasors and frequency estimation using the NTA is considered as an unconstrained optimization problem [112-122]. In this technique, a number of voltage samples represent same number of highly nonlinear equations to be solved for estimating the voltage parameters. The NTA has a good convergence property and the duration of convergence is no longer than the size of the window [112, 116, 117].

The estimation function of the NTA at the n sampling instant of the grid voltage can be expressed by

$$\eta_{NTA}\left(X_n\right) = v_0\left(n\right) + \sum_{i=1,2,\ldots}^{M} A_i\left(n\right)\sin\left\{i\omega\left(n\right)nT_s + \theta_i\left(n\right)\right\} \tag{2.16}$$

where X_n is the estimation vector and can be expressed by

$$X_n = \left[v_0\left(n\right) \quad \omega\left(n\right) \quad A_1\left(n\right) \quad \cdots \quad A_M\left(n\right) \quad \theta_1\left(n\right) \quad \cdots \quad \theta_M\left(n\right)\right]^{\square} \tag{2.17}$$

The estimation error of the NTA can be expressed as

$$e_v\left(n\right) = \eta_{NTA}\left(X_n\right) - v\left(n\right) \tag{2.18}$$

where the input single-phase grid voltage is expressed by (2.2). An error vector can also be defined by

$$E\left(X_n\right) = \left[e_v\left(n\right) \quad e_v\left(n-1\right) \quad \cdots \quad e_v\left(n-2M-1\right)\right]^{\square} \tag{2.19}$$

The estimation vector is updated by [112, 116-118]

$$X_{n+1} = X_n + \left(J_{NTA}^{\square} J_{NTA}\right)^{-1} J_{NTA}^{\square} E\left(X_n\right) \tag{2.20}$$

where J_{NTA} is the Jacobian matrix and its elements are the first-order derivatives of the grid voltage with respect to the estimation variables.

The NTA is a computationally demanding technique for real-time implementation due to the requirement of online matrix inversion [116-118]. Another shortcoming of the technique is that the matrix inversion suffers from singularity when the amplitude of any modelled frequency component is zero [119]. The technique may also suffer from stability issue when an abrupt change occurs in the grid voltage waveform [119]. The computational burden of the NTA can be reduced by using it recursively [120-122]. However, a forgetting factor is introduced in the recursive NTA and the performance depends on the tuning of this parameter [120-122]. A pre-filter can be used with the NTA to reject the unwanted frequency components present in the grid voltage, which helps to reduce the computational burden [112, 119]. Other technique, such as LS can also be combined with the NTA (NTA-LS) to reduce the number of estimation variables for fundamental frequency estimation [119]. In order to avoid the matrix inversion operation and also to reduce the matrix dimensions for real-time implementations, a computationally efficient, accurate and faster frequency estimation technique based on the NTA and a differentiation filter (NAT-DF) is presented in Chapter 4.

In summary, the pros and cons of the NTA technique are given in the following.

Pros:
- Frequency adaptive
- Can estimate DC offset and harmonics

Cons:
- Nonlinear
- Subject to instability when abrupt changes occur in voltage
- Matrix singularity occurs when amplitude of any modelled frequency component is zero
- Computationally demanding due to real-time matrix inversion

2.1.4 Least-Squares (LS)

The LS is a widely used technique to estimate the numerical values of unknown parameters that fit a function of a set of data [82, 123]. It minimizes the sum of squares of residual errors. The only requirement of this technique is that there are at least as many equations as the number of unknowns. The technique provides a direct solution for the unknowns when the equations are linear. The LS technique is also used to solve a set of nonlinear equations that have been linearized using a first-order Taylor-series expansion. Solving nonlinear equations using the LS technique is an iterative process [123].

The grid voltage waveform can be expressed by (2.21) to estimate its fundamental and harmonics amplitudes and phase angles by using the LS technique.

$$\begin{aligned} v(n) &= \sum_{i=1,2,\ldots}^{M} A_i(n)\sin\left\{i\omega(n)nT_s + \theta_i(n)\right\} \\ &= \sum_{i=1,2,\ldots}^{M}\left[A_i(n)\cos\left\{\theta_i(n)\right\}\sin\left\{i\omega(n)nT_s\right\} + A_i(n)\sin\left\{\theta_i(n)\right\}\cos\left\{i\omega(n)nT_s\right\}\right] \end{aligned} \tag{2.21}$$

In the LS technique, it is assumed that the fundamental angular frequency is constant and known $\{\omega(n)=\omega\}$, and the following matrix equation is obtained based on a window size of N_w samples of the grid voltage waveform [123-125].

$$J_{LS}x_{LS} = v_{LS} \tag{2.22}$$

where

$$J_{LS} =$$

$$\begin{bmatrix} \sin\{\omega T_s n\} & \cos\{\omega T_s n\} & \cdots & \sin\{\omega T_s n\} & \cos\{\omega T_s n\} \\ \sin\{\omega T_s (n-1)\} & \cos\{\omega T_s (n-1)\} & \cdots & \sin\{\omega T_s (n-1)\} & \cos\{\omega T_s (n-1)\} \\ \vdots & \vdots & \ddots & \vdots & \vdots \\ \sin\{\omega T_s (n-N_w+1)\} & \cos\{\omega T_s (n-N_w+1)\} & & \sin\{\omega T_s (n-N_w+1)\} & \cos\{\omega T_s (n-N_w+1)\} \end{bmatrix}$$

$$x_{LS} =$$

$$\begin{bmatrix} A_1(n)\cos\{\theta_1(n)\} & A_1(n)\sin\{\theta_1(n)\} & \cdots & A_M(n)\cos\{\theta_M(n)\} & A_M(n)\sin\{\theta_M(n)\} \end{bmatrix}^{\square}$$

$$v_{LS} = \begin{bmatrix} v(n) & v(n-1) & \cdots & v(n-N_w+2) & v(n-N_w+1) \end{bmatrix}^{\square}$$

J_{LS} is the Jacobian matrix, x_{LS} is the estimation vector and v_{LS} is the input voltage vector. The minimum number of voltage samples required for solving (2.22) is N_w=2M. However, over determined system with a value of N_w greater than 2M will provide a better estimation when the grid voltage contains noise and there is measurement error [123]. The LS solution of (2.22) can be expressed by [123-125]

$$x_{LS} = \left(J_{LS}^{\square} J_{LS}\right)^{-1} J_{LS}^{\square} v_{LS} \tag{2.23}$$

The amplitude and initial phase angle of the $i\omega$ angular frequency component can be obtained from x_{LS} and are expressed by (2.24) and (2.25), respectively.

$$\hat{A}_i(n) = \sqrt{\left\{x_{LS}(2i-1)\right\}^2 + \left\{x_{LS}(2i)\right\}^2} \tag{2.24}$$

$$\hat{\theta}_i(n) = \tan^{-1}\left\{\frac{x_{LS}(2i)}{x_{LS}(2i-1)}\right\} \tag{2.25}$$

The grid voltage fundamental frequency can also be estimated by using the LS technique [123]. Based on the LS estimation, the following error vector is obtained.

$$E = \left\{I - \left(J_{LS}^{\square} J_{LS}\right)^{-1} J_{LS}^{\square}\right\} v_{LS} \tag{2.26}$$

where I is an identity matrix. E is a function of ω only and one-dimensional search can be used to the estimate ω [123]. The value of ω that minimizes $\|E\|^2$ is taken as the estimated fundamental angular frequency, where $\|\cdots\|$ denotes Euclidean norm [123].

A moving window based LS technique can be used to obtain the instantaneous value of the grid voltage parameters [123]. It can be seen that (2.23) requires matrix inversion and may suffer from matrix singularities [82, 123]. The accuracy of the LS technique also depends on the window size and the number of variables [82, 123]. The dimension of the matrix increases with the increasing order of harmonics. However, the price paid for a large size matrix is of additional computational effort and dynamic delay [82, 123]. A weighted LS technique can also be used to estimate the grid voltage parameters [126, 127]. On the other hand, a recursive LS or a decoupled recursive LS techniques can be used to reduce the computational effort of the LS technique [128-132].

In summary, the pros and cons of the LS technique are given in the following.

Pros:
- Linear
- Frequency adaptive
- Can estimate harmonics

Cons:
- May suffer from matrix singularity
- Requires large size window under distorted conditions
- Large size window introduces long dynamic delay
- High computational burden for frequency estimation with improved resolution

2.1.5 Kalman Filter (KF)

The KF is a recursive model based LS estimator and can be used to estimate the phasor quantities of the grid voltage waveform [133]. The amplitudes and phase angles of the grid voltage fundamental and harmonic components can be efficiently estimated using a linear KF (LKF) when the fundamental frequency is constant and known [134-137]. However, a nonlinear Kalman filter (NLKF) such as an extended KF (EKF) is used for frequency adaptive estimation of the grid voltage fundamental and harmonic parameters [137-143].

There is flexibility for choosing the states of the KF for grid voltage parameters estimation. The in-phase and in-quadrature components of $i\omega$ (i=1,2,…,M) angular frequency component and the fundamental angular frequency can be considered as the states of the EKF and are expressed by (2.27), (2.28) and (2.29), respectively.

$$x_{i1}(n) = A_i(n)\sin\left\{i\omega(n)nT_s + \theta_i(n)\right\} \tag{2.27}$$

$$x_{i2}(n) = A_i(n)\cos\left\{i\omega(n)nT_s + \theta_i(n)\right\} \tag{2.28}$$

$$x_{M+1}(n) = \omega(n) \tag{2.29}$$

The state vector of the EKF can be expressed by

$$x(n) = \begin{bmatrix} x_{11}(n) & x_{12}(n) & x_{21}(n) & x_{22}(n) & \cdots & x_{M1}(n) & x_{M2}(n) & x_{M+1}(n) \end{bmatrix}^{\square} \tag{2.30}$$

The EKF is described by a nonlinear dynamic process and measurement functions, as given by (2.31) and (2.32), respectively [137-143].

$$x(n+1) = g_1\{x(n)\} \tag{2.31}$$

$$v(n) = g_2\{x(n)\} \tag{2.32}$$

where g_1 is the process function, g_2 is the measurement function and the input single-phase grid voltage is expressed by (2.21). The nonlinear process and measurement functions of the EKF are linearized by means of a first-order Taylor series and are expressed by (2.33) and (2.34), respectively.

$$J_{EKF} = \frac{\partial}{\partial x} g_1\{x(n)\}\Big|_{x=x_{i1},x_{i2},x_{M+1} \text{ where } i=1,2,...,M} \tag{2.33}$$

$$L_{EKF} = \frac{\partial}{\partial x} g_2\{x(n)\}\Big|_{x=x_{i1},x_{i2},x_{M+1} \text{ where } i=1,2,...,M} \tag{2.34}$$

The state transition or Jacobian matrix (J_{EKF}) and the measurement matrix (L_{EKF}) of the EKF can be expressed by (2.35) and (2.36), respectively.

$$J_{EKF} = \begin{bmatrix} \cos\{x_{M+1}(n)T_s\} & \sin\{x_{M+1}(n)T_s\} & 0 & \cdots & 0 & 0 \\ -\sin\{x_{M+1}(n)T_s\} & \cos\{x_{M+1}(n)T_s\} & 0 & \cdots & 0 & 0 \\ 0 & 0 & \ddots & \cdots & 0 & 0 \\ \vdots & \vdots & \cdots & \cos\{Mx_{M+1}(n)T_s\} & \sin\{Mx_{M+1}(n)T_s\} & 0 \\ 0 & 0 & \cdots & -\sin\{Mx_{M+1}(n)T_s\} & \cos\{Mx_{M+1}(n)T_s\} & 0 \\ 0 & 0 & \cdots & 0 & 0 & 1 \end{bmatrix} \tag{2.35}$$

$$L_{EKF} = \begin{bmatrix} 1 & 0 & 1 & 0 & \cdots & 1 & \sum_{i=1,2,...}^{M} inT_s x_{i2}(n) \end{bmatrix} \tag{2.36}$$

To estimate the grid voltage parameters, the steps of the EKF are as follows [135-143].

Time update stage:

Project the state ahead: $x^{-}(n+1)=J_{EKF}x(n)$

Project the error covariance ahead: $P_{n+1}^{-}=J_{EKF}P_nJ_{EKF}^{\square}+Q$

Measurements update stage:

Compute the Kalman gain: $K_{EKF}=P_n^{-}L_{EKF}^{\square}\left(L_{EKF}P_n^{-}L_{EKF}^{\square}+R\right)^{-1}$

Update estimate: $x(n)=x^{-}(n)+K_{EKF}\left\{v(n)-L_{EKF}x^{-}(n)\right\}$

Update error covariance: $P_n=\left(I-K_{EKF}L_{EKF}\right)P_n^{-}$

where x^{-} is the predicted state vector, P_n is the error covariance matrix, P_{n+1}^{-} is the predicted error covariance matrix, Q is the process noise covariance matrix and R is the measurement noise covariance.

The amplitude and instantaneous phase angle $\{\phi_i(n)=i\omega(n)nT_s+\theta_i(n)\}$ of the $i\omega$ angular frequency component and the fundamental frequency can be obtained by (2.37), (2.38) and (2.39), respectively.

$$\hat{A}_i(n)=\sqrt{x_{i1}^2(n)+x_{i2}^2(n)} \tag{2.37}$$

$$\hat{\phi}_i(n)=\tan^{-1}\left\{\frac{x_{i1}(n)}{x_{i2}(n)}\right\} \tag{2.38}$$

$$\hat{f}(n)=\frac{x_{M+1}(n)}{2\pi} \tag{2.39}$$

The real-time application of the KF is limited by the difficulties involved in tuning its parameters accurately for desired performance [137, 144-146]. The error covariances (Q and R) are the tuning parameters which balance the dynamic response against noise sensitivity [137, 144-146]. The poor choice of the filter parameters not only affects the performance but also the stability. The EKF may require additional algorithms to tune these parameters [137]. The derivative of the nonlinear functions in the EKF introduces nonlinear terms and increases computational burden [137, 138]. In addition, the measurement matrix, as given by (2.36), depends on the time index, which may increase the estimation error as the time elapses [137, 138]. The EKF may also not be suitable for large and continuous variation of fundamental frequency [138].

An extended complex KF (ECKF) can provide faster frequency estimation and also shows improved noise rejection capability when compared with the EKF [138-143]. However, the ECKF is not suitable for multiple harmonics tracking because numerical instability may arise at the initial state due to the large error caused by the nonlinear terms [138]. A hybrid technique based on the ECKF and LKF can be used to estimate harmonics under time-varying frequency conditions at the cost of a high computational burden [138]. An iterative technique based on an ensemble KF (EnKF) can also be used for harmonics estimation [147].

For grid voltage parameters estimation, the nonlinear model makes the KF inefficient due to the following reasons: is nonlinear; includes derivatives of the nonlinear functions; contains nonlinear terms; requires high computational burden; necessitates complex tuning of the parameters; and presents convergence problems. To overcome the previously mentioned shortcomings of the EKF for grid voltage parameters estimation, a frequency adaptive LKF based on the FLL (LKF-FLL) is presented in Chapter 7.

The pros and cons of the KF technique can be summarized as followings.

Pros:
- Frequency adaptive
- Can reduce noise effect
- Can predict next step estimation
- Can estimate harmonics

Cons:
- Complex to implement
- Complex tuning of the filter parameters
- May suffer from convergence problem
- Computationally demanding

2.1.6 Prony's Method (PM)

The PM was developed for modelling of uniformly spaced sampled data as a linear combination of a finite number of damped exponentials in an experiment on gases and also extended to interpolate at intermediate data points [148]. The PM is now used to estimate unknown frequencies, damping coefficients, amplitudes and phase angles of the modal components present in a given signal in the areas of power systems, biomedical engineering and speech processing [87, 108, 109, 148-158]. The PM can be used for the estimation of DC offset, harmonics and interharmonics present in a given signal [87, 109,

152, 153]. The technique can provide improved frequency resolution and also does not suffer from spectral leakage when compared with the fast Fourier Transform (FFT) [152, 153, 162].

Based on the PM, the single-phase grid voltage can be expressed by

$$v(n)=\sum_{i'=1,2,\cdots}^{M_{PM}}\left[\frac{A_{i'}(n)}{2}e^{-\sigma_{i'}(n)nT_s+j\left\{2\pi f_{i'}(n)nT_s+\theta_{i'}(n)\right\}}+\frac{A_{i'}(n)}{2}e^{-\sigma_{i'}(n)nT_s-j\left\{2\pi f_{i'}(n)nT_s+\theta_{i'}(n)\right\}}\right] \\ =\sum_{i'=1,2,\cdots}^{M_{PM}}\left\{c_{i'}(n)z_{i'}^{n}(n)+c_{i'}^{\#}(n)z_{i'}^{n\#}(n)\right\} \tag{2.40}$$

where $c_{i'}(n)=A_{i'}(n)e^{j\theta_{i'}(n)}/2$, $z_{i'}(n)=e^{\{-\sigma_{i'}(n)+j2\pi f_{i'}(n)\}T_s}$, M_{PM} is the number of modal components present in the grid voltage, $\#$ denotes complex conjugate operation, and $A_{i'}$, $\sigma_{i'}$, $f_{i'}$ and $\theta_{i'}$ are the amplitude, damping coefficient, frequency and initial phase angle, respectively, of the i'^{th} modal component present in the grid voltage. As it can be noticed, (2.40) contains $2M_{PM}$ number of exponential components.

A high-order polynomial, as given by (2.41), is introduced in the PM to obtain the modal frequencies and damping coefficients [87, 108, 109, 148-158].

$$P_{PM}(z)=z^{L_{PM}}+b(1)z^{L_{PM}-1}+\ldots+b(L_{PM}-1)z^{1}+b(L_{PM})=\sum_{i'=1}^{L_{PM}}(z-z_{i'}) \tag{2.41}$$

where $L_{PM}\geq 2M_{PM}$ and $z_{i'}$ is a root of $P_{PM}(z)=0$. The coefficients $\{b(i'),\ i'=1,2,\ldots,L_{PM}\}$ of the above polynomial can be related with the grid voltage samples using a backward or forward linear prediction model (LPM) [148, 153, 156, 158]. The backward LPM can be expressed by

$$\sum_{i'=1}^{L_{PM}}b(i')v(n+i')=-v(n) \tag{2.42}$$

As it can be seen, at least L_{PM} number of equations based on the LPM is required for obtaining the values of $b(i')$. To solve these set of equations, several techniques such as autocorrelation, covariance, LS and SVD can be used [87, 151, 156, 159, 160].

The frequency and damping coefficient of the i'^{th} modal component of (2.40) can be obtained from $z_{i'}$ and are expressed by (2.43) and (2.44), respectively.

$$\hat{f}_{i'}(n) = \frac{\tan^{-1}\left\{\dfrac{\mathrm{Im}\left(z_{i'}\right)}{\mathrm{Re}\left(z_{i'}\right)}\right\}}{2\pi T_s} \tag{2.43}$$

$$\hat{\sigma}_{i'}(n) = \frac{\ln\left(\left|z_{i'}\right|\right)}{T_s} \tag{2.44}$$

In the PM, the following matrix equation has also to be solved to estimate the amplitudes and phase angles of the exponential components of (2.40).

$$H_{PM} C_{PM} = v_{PM} \tag{2.45}$$

where

$$H_{PM} = \begin{bmatrix} 1 & 1 & \cdots & 1 \\ z_1^1 & z_2^1 & \cdots & z_{L_{PM}}^1 \\ \vdots & \vdots & \ddots & \vdots \\ z_1^{N_w-1} & z_2^{N_w-1} & \cdots & z_{L_{PM}}^{N_w-1} \end{bmatrix}$$

$$C_{PM} = \begin{bmatrix} c_1(n) & c_2(n) & \cdots & c_{L_{PM}}(n) \end{bmatrix}^{\square}$$

$$v_{PM} = \begin{bmatrix} v(n) & v(n-1) & \cdots & v(n-N_w+1) \end{bmatrix}^{\square}$$

where H_{PM} is a Vandermonde matrix and is formed by $z_{i'}$, C_{PM} is the amplitude and phase angle estimation vector, and v_{PM} is the input voltage vector for amplitude and phase angle estimation. The LS solution of (2.45) can be expressed by [87, 108, 109, 149-161]

$$C_{PM} = \left(H_{PM}^{\Diamond} H_{PM}\right)^{-1} H_{PM}^{\Diamond} v_{PM} \tag{2.46}$$

where $\Diamond$ denotes complex conjugate transpose operation. The values of $A_{i'}$ and $\theta_{i'}$ of the i'^{th} modal component of (2.40) can be obtained by (2.47) and (2.48), respectively.

$$\hat{A}_{i'}(n) = 2\left|c_{i'}(n)\right| \tag{2.47}$$

$$\hat{\theta}_{i'}(n) = \tan^{-1}\left[\frac{\mathrm{Im}\left\{c_{i'}(n)\right\}}{\mathrm{Re}\left\{c_{i'}(n)\right\}}\right] \tag{2.48}$$

The following values of amplitudes are obtained when $L_{PM} > 2M_{PM}$.

$$\hat{A}_{i'}(n) = 0, \quad \text{for } i' = 2M_{PM}+1,\ 2M_{PM}+2, \ldots, L_{PM} \tag{2.49}$$

A moving window can be used in the PM to obtain the instantaneous values of the frequencies, damping coefficients, amplitudes and phase angles of the modal components present in the grid voltage. However, the performance of the PM is affected by noise. The PM also requires prior knowledge of the number of modal components present in the grid voltage [87, 108, 109, 148-158]. When the number of modal components is not known, a large value of it is assumed and the rooting of a high-order polynomial has to be handled which may increase the computational burden. Moreover, the technique is computationally demanding due to the handling of large size window. However, the number of modal components present in the grid voltage can be reduced by using pre-filtering [163].

In summary, the pros and cons of the PM technique are given in the following.

Pros:
- Frequency adaptive
- Improved frequency resolution
- No spectral leakage
- Can estimate DC offset, harmonics and interhamronics

Cons:
- Requires prior knowledge of the number of model components
- Requires rootling of a high-order polynomial
- Computationally demanding due to handling of large size matrix

2.1.7 Phase-Locked Loop (PLL)

The PLL is a closed-loop system in which an internal oscillator is controlled to synchronize with an external periodical signal by using a feedback loop [170, 171]. The internal oscillator locks its phase with the applied external signal in order to generate phase coherent signal that can be used by control systems in many applications. The PLL is broadly used in the areas of communications, computers and modern electronics. The PLL is also used for synchronization of a grid-connected power converter [172]. The phase angle of the grid voltage obtained by the PLL is used to get the output current of the converter in-phase with the voltage at the point of common coupling (PCC).

The basic structure of the PLL is shown in Fig. 2.1 [170-175], where ϕ_1 is the fundamental instantaneous phase angle, $\hat{\phi}_1$ is the estimated fundamental instantaneous phase angle, $\Delta\hat{\omega}$ is the estimated fundamental angular frequency deviation and $\hat{\omega}$ is the

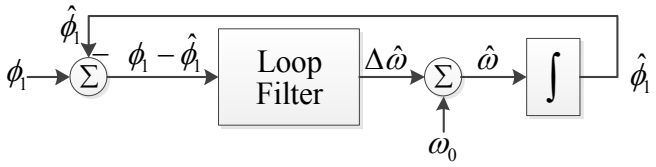

Fig. 2.1 Block diagram of a basic PLL.

estimated fundamental angular frequency. As it can be seen, the PLL is composed of a phase comparator which provides a phase error $(\phi_1 - \hat{\phi}_1)$ to the input of a loop filter. The output of the loop filter is the fundamental angular frequency deviation which is added with the nominal value to get the actual fundamental angular frequency. The nominal fundamental angular frequency is used to increase the initial synchronization process of the PLL. The actual fundamental angular frequency is then integrated to obtain the instantaneous phase angle, as can be noticed in Fig. 2.1.

Several single-phase PLLs are reported in the technical literature, such as Park Transform based PLL [170, 171, 182-185], enhanced PLL (EPLL) [176-179], quadrature PLL (QPLL) [180] and demodulation based PLL [181]. Among these PLLs, the Park Transform based one is commonly used and is shown in Fig. 2.2 [170, 171, 182-185], where v_1' is the estimated in-phase fundamental voltage component, qv_1' is the estimated in-quadrature fundamental voltage component, $\hat{A}_1$ is the estimated fundamental voltage amplitude, and v_d and v_q are the *d* and *q* components of the Park Transform, respectively. As it can be seen, a quadrature signal generator (QSG) generates fundamental voltage orthogonal components and then the Park Transform is used to obtain an approximation of the phase error $(v_q \cong \phi_1 - \hat{\phi}_1)$. A proportional and integral (PI) controller is used as loop filter to get the fundamental angular frequency deviation from the phase error. The estimated fundamental frequency and phase angle are also fed back to the QSG and Park Transform, respectively. The fundamental voltage amplitude of the grid voltage can also be estimated by using the QSG required for the PLL, as can be seen in Fig. 2.2.

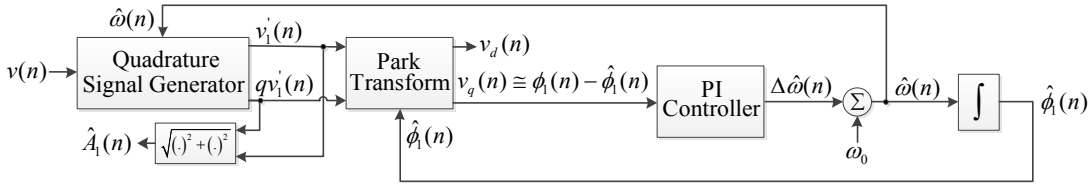

Fig. 2.2 Single-phase PLL based on the Park Transform.

The PLL has a simple structure to estimate the grid voltage fundamental parameters. However, the main challenge of the single-phase PLL is that it requires a virtual orthogonal voltage system [183], unlike the three-phase ones where the orthogonal voltage system is provided by the Clarke Transform [249]. Nevertheless, there are several single-phase QSGs reported in the technical literature, such as based on second-order generalized integrator (SOGI) [196], anticonjugate decomposition and cascaded delayed signal cancellation (ACDSC) [186], filter based techniques [250], transport delay [185, 187], Hilbert Transform [185, 187] and inverse Park Transform [185], which can be used for PLL implementation.

The tuning of the PLL requires a trade-off between a good dynamic performance and estimation accuracy under distorted grid conditions [179, 188-190]. A pre-filter or in-loop filter can also be used to reject the negative effects caused by the grid voltage disturbances at the cost of a slower dynamic response [188, 191]. Another drawback of the PLL is that the phase and frequency are estimated within a single loop which causes large frequency transient during phase jumps under grid faults [192]. The effect of this undesired frequency swing are also reflected back on the phase estimation and hence causes delay in the process of synchronization [192]. Moreover, there are interdependent loops in the PLL, as shown in Fig. 2.2, and hence each of the loops influences the other one at the same time, as a result, the tuning of the controller parameters is more sensitive, thus reducing the stability margins. To avoid the interdependent loop between the orthogonal voltage system and the frequency estimation, the DFT based frequency adaptive QSG-SOGI (DFT-SOGI) technique for single-phase gird voltage fundamental parameters estimation is presented in Chapter 6. Another technique based on QSG-ACDSC is also documented in Chapter 6 to estimate the single-phase grid voltage fundamental parameters.

In summary, the pros and cons of the PLL technique are given in the following.

Pros:
- Relatively simple
- Frequency adaptive

Cons:
- Requires a trade-off between dynamics and estimation accuracy under distorted conditions
- Presents large frequency swing during phase jump
- Contains interdependent loop
- Requires orthogonal voltage waveforms

2.1.8 Frequency-Locked Loop (FLL)

The FLL is reported to estimate the fundamental frequency of the grid voltage waveform and is used for grid synchronization application [193, 194]. Similar to single-phase PLL, the implementation of the FLL requires a single-phase QSG. However, unlike single-phase PLL, the fundamental frequency information required by the QSG is achieved by the FLL consisting of a simple control loop, without using either phase angle or trigonometric functions, [193, 194].

The implementation of the FLL is shown in Fig. 2.3, where γ is the gain of the FLL and $\dot{\omega}$ is the dynamics of the fundamental angular frequency [193, 194]. As it can be noticed, the estimated error voltage and the in-quadrature fundamental voltage component are used as the inputs of the FLL. Similar to PLL, the value of ω_0 is used to increase the initial synchronization process of the FLL. It can also be seen from Fig. 2.3 that the fundamental voltage amplitude and phase angle can be obtained from the orthogonal voltage waveforms generated by the QSG.

Several single-phase QSGs, such as based on SOGI, adaptive vectorial filter (AVF) or ADALINE can be used for FLL implementation [193, 194, 199, 202]. The QSG-SOGI is shown in Fig. 2.4, where ω_r is the tuning angular frequency and σ is the gain of the SOGI [193-196].

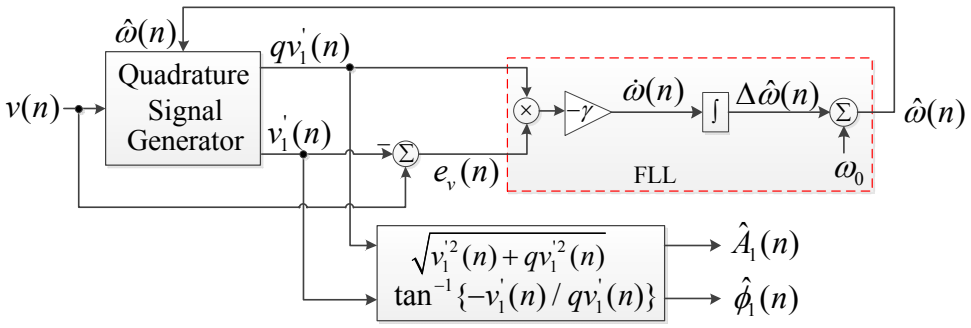

Fig. 2.3 Single-phase FLL.

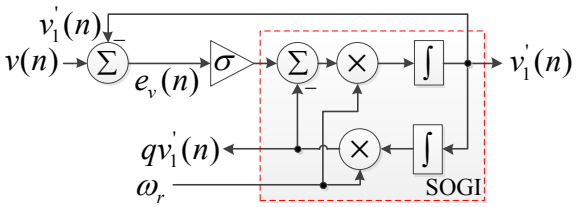

Fig. 2.4 QSG-SOGI.

The simplified frequency dynamics of the QSG-SOGI based FLL (SOGI-FLL) can be expressed by [193, 197, 198]

$$\dot{\omega}(n) = -\frac{\gamma A_1^2(n)}{\sigma\hat{\omega}(n)}\left\{\hat{\omega}(n) - \omega(n)\right\} \tag{2.50}$$

It can be seen from (2.50) that the frequency dynamics of the FLL depends on the gain γ, fundamental voltage amplitude, fundamental angular frequency and SOGI's gain. Therefore, to keep the dynamics of the FLL non-sensitive to the change of the fundamental frequency, amplitude and SOGI's gain, the gain of the FLL can be normalized by $\hat{A}_1^2 / \sigma\hat{\omega}$ and the resultant dynamics can be expressed by

$$\dot{\omega}(n) = -\gamma\left\{\hat{\omega}(n) - \omega(n)\right\} \tag{2.51}$$

The implementation of the SOGI-FLL with the normalised gain of the FLL is shown in Fig. 2.5 [193, 197, 198].

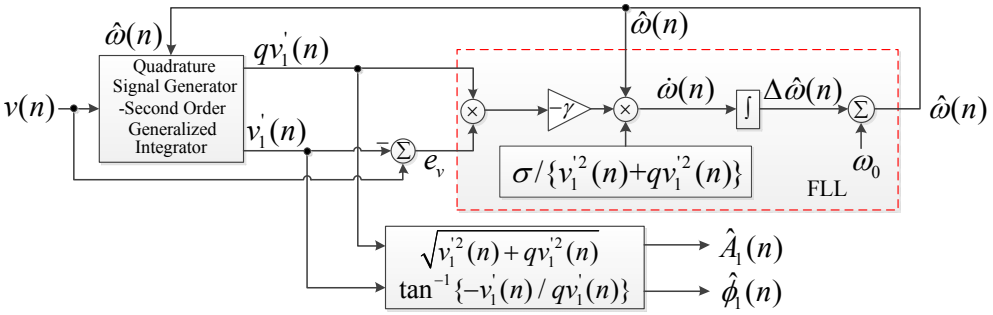

Fig. 2.5 Normalized gain FLL based on the QSG-SOGI.

The FLL is a relatively simple technique to implement on a digital signal processor. However, similar to single-phase PLL, there are interdependent loops between the QSG and FLL influencing one another at the same time and hence the tuning process is sensitive, thus reducing stability margins. Moreover, like single-phase PLL, an optimal tuning of the FLL is required for obtaining a trade-off between good dynamic performance and estimation accuracy [193, 197-200]. Multiple QSG-SOGIs can be combined with the FLL to reject harmonics effects at the cost of additional computational effort [194, 197, 201]. The negative effects caused by the DC offset can also be rejected by using an additional LPF, as reported in [179, 184]. Chapter 6 presents the DFT-SOGI technique for single-phase gird voltage fundamental parameters estimation, where the technique avoids

the interdependent loop between the orthogonal voltage system and the frequency estimation, and also provides improved frequency estimation when compared with the SOGI-FLL technique. A computationally efficient technique consists of the QSG based on a fixed frequency tuned SOGI and a differentiation filter (SOGI-DF) is also reported in Chapter 6 for single-phase grid voltage fundamental amplitude and frequency estimation.

In summary, the pros and cons of the FLL technique are given in the following.

Pros:
- Relatively simple
- Frequency adaptive

Cons:
- Requires a trade-off between dynamics and estimation accuracy under distorted conditions
- Contains interdependent loop
- Requires orthogonal voltage waveforms

2.1.9 Demodulation

The basic principle of the demodulation technique is that a signal from a local oscillator is used to mix with an incoming signal to convert it down to a baseband signal [203]. This technique is well known in the field of communications and is used as a synchronous detection method for extracting the baseband signal from an amplitude modulated signal [203]. It can also be used to estimate the single-phase grid voltage fundamental parameters [181, 203-213].

For estimating the single-phase grid voltage fundamental parameters using the demodulation technique, an undistorted voltage waveform is assumed as given by

$$v(n) = v_1(n) = A_1(n)\sin\{\phi_1(n)\} = A_1(n)\sin\{\omega_0 nT_s + \psi_1(n)\} \tag{2.52}$$

where v_1 is the fundamental voltage component and $\psi_1(n) = \Delta\omega(n)nT_s + \theta_1(n)$ is the initial phase angle (θ_1) plus instantaneous phase angle $\{\Delta\omega(n)nT_s\}$ corresponding to the fundamental angular frequency deviation ($\Delta\omega$). In the demodulation technique, the grid voltage, as given by (2.52), is multiplied by sine and cosine functions, respectively, at nominal grid frequency [181, 203-213]. The demodulated grid voltage can be expressed by (2.53) and (2.54), respectively.

$$v_{1S}(n) = v(n)\sin(\omega_0 nT_s) = \frac{A_1(n)}{2}\cos\{\psi_1(n)\} - \frac{A_1(n)}{2}\cos\{2\omega_0 nT_s + \psi_1(n)\} \tag{2.53}$$

$$v_{1C}(n) = v(n)\cos(\omega_0 nT_s) = \frac{A_1(n)}{2}\sin\{\psi_1(n)\} + \frac{A_1(n)}{2}\sin\{2\omega_0 nT_s + \psi_1(n)\} \tag{2.54}$$

As it can be seen, both v_{1S} and v_{1C} contain oscillations at angular frequencies $\Delta\omega$ and $2\omega_0+\Delta\omega$. The frequency component greater than $\Delta\omega$ in (2.53) and (2.54) can be rejected by using two LPFs, respectively [181, 203-213]. The low-pass filtered demodulated voltages can be approximated by (2.55) and (2.56), respectively.

$$v_{1SF}(n) = \frac{A_1(n)}{2}\cos\{\psi_1(n)\} \tag{2.55}$$

$$v_{1CF}(n) = \frac{A_1(n)}{2}\sin\{\psi_1(n)\} \tag{2.56}$$

v_{1SF} and v_{1CF} can be used to estimate the fundamental voltage amplitude and phase angle, and are obtained by (2.57) and (2.58), respectively.

$$\hat{A}_1(n) = 2\sqrt{v_{1SF}^2(n) + v_{1CF}^2(n)} \tag{2.57}$$

$$\hat{\psi}_1(n) = \tan^{-1}\left\{\frac{v_{1CF}(n)}{v_{1SF}(n)}\right\}_{\text{unwrapped}} \tag{2.58}$$

where subscript ‘unwrapped’ indicates that the estimated sawtooth phase angle is unwrapped. The estimated phase angle can also be differentiated to obtain the fundamental angular frequency deviation and is expressed by

$$\Delta\hat{\omega}(n) = \frac{d}{dt}\hat{\psi}_1(t)\Big|_{t=nT_s} \tag{2.59}$$

where t is time in continuous domain and is discretised by $t=nT_s$.

It can be seen from (2.53) and (2.54) that the oscillations at angular frequency $2\omega_0+\Delta\omega$ have amplitude equal to half of the fundamental voltage amplitude. Therefore, LPFs with high attenuation rate have to be considered to reject these high amplitude oscillations. Thus, high-order LPFs are required which can lead to poor dynamics performance.

The demodulation of harmonics present in the grid voltage introduces oscillations at angular frequencies $h(\omega_0+\Delta\omega)\pm\omega_0$, where h=2,3,…,M. The lowest frequency component introduced by demodulation of harmonics will be around fundamental frequency which is produced by the second harmonic component (h=2). Therefore, the cut-off frequency of the LPFs can be carefully chosen to reject the negative effects caused by the high frequency

oscillations generated by the demodulation of fundamental and harmonic voltage components.

High-order FIR or low-order infinite-impulse-response (IIR) LPFs can be used for rejecting the high frequency oscillations generated by the demodulation [181, 210-212]. However, the high-order FIR filter is computationally demanding for real-time implementation [203, 210, 211]. On the other hand, the IIR LPF is computationally efficient and offers good attenuation at stop-band. A notch filter tuned at second harmonic can also be combined with the IIR LPF to reject the high frequency oscillations generated by the demodulation of the grid voltage fundamental and harmonic components [181]. However, the IIR LPF has slower dynamic response, difficulties for hardware implementation due to stability problem and do not have linear-phase which may be a source of error in phase angle estimation [181, 203, 211-213]. On the other hand, the non-ideal characteristics of the LPFs may also attenuate the amplitude under off-nominal frequency conditions. The frequency estimation using (2.59) can also be affected when the high frequency oscillations are not properly rejected using the LPFs. A separate frequency estimation technique can also be used for frequency adaptive demodulation of the grid voltage at the cost of high computational effort [181, 210]. Chapter 5 presents a FIR DF for estimating the time-varying fundamental frequency from the instantaneous phase angle obtained by the demodulation technique. A modified demodulation technique is also reported in Chapter 5 for estimating the fundamental voltage amplitude and frequency, where an oscillator is integrated with the conventional demodulation technique to reject the negative effects caused by the oscillation at around second harmonic produced by the demodulation of fundamental voltage component.

In summary, the pros and cons of the demodulation technique are given in the following.

Pros:
- Relatively simple
- Frequency adaptive
- Can reject high frequency disturbances

Cons:
- Produces oscillation at around second harmonic with half of the fundamental voltage amplitude
- Provides slower response with IIR LPF
- Computationally demanding when FIR LPF is used
- Fixed frequency demodulation may introduce error during off nominal frequency condition

2.1.10 Teager Energy Operator (TEO)

According to the Newton's law of motion of a mass suspended by a spring, total energy of a pure sinusoidal oscillation (v) is proportional to the square of the product between amplitude and angular frequency, and can be expressed by [214, 215]

$$\text{Total Energy} \propto A_1^2 \omega^2 \tag{2.60}$$

where

$$v(t) = A_1 \sin(\omega t + \theta_1)$$

Teager proves that the energy of the pure sinusoidal oscillation can be obtained by [214-221]

$$A_1^2 \omega^2 = \left(\frac{dv}{dt}\right)^2 - v\frac{d^2v}{dt^2} \tag{2.61}$$

Equation (2.61) is called TEO, which is a nonlinear operator and capable of estimating the instantaneous energy of the pure sinusoidal oscillation. Later, Kaiser proved that the TEO can be obtained from the 3CS of v and can be expressed by [214-221]

$$\text{TEO}\{v(n)\} = A_1^2(n)\left[\sin\{\omega(n)T_s\}\right]^2 = v^2(n) - v(n-1)v(n+1) \tag{2.62}$$

Based on a high sampling frequency (f_s>8f) [214, 215], equation (2.62) can be simplified as given by

$$A_1^2(n)\omega^2(n)T_s^2 \cong v^2(n) - v(n-1)v(n+1) \tag{2.63}$$

where $\sin\{\omega(n)T_s\} \cong \omega(n)T_s$. The above expression can be used to obtain the total energy of v which relies on the 3CS.

It is also reported in the technical literature that the TEO can be used to estimate the fundamental amplitude of the grid voltage with known frequency $\{\omega(n)=\omega\}$ and is obtained by [216-221]

$$\hat{A}_1(n) = \frac{\sqrt{\text{TEO}\{v(n)\}}}{\sin(\omega T_s)} = \frac{\sqrt{v^2(n) - v(n-1)v(n+1)}}{\sin(\omega T_s)} \tag{2.64}$$

The time-varying fundamental amplitude and frequency of the grid voltage can also be obtained using the TEO and are expressed by (2.65) and (2.66), respectively [216, 217].

$$\hat{A}_1(n) = \sqrt{\frac{\text{TEO}\{v(n)\}}{1 - G^2(n)}} \tag{2.65}$$

$$\hat{\omega}(n) = \frac{\cos^{-1}\{G(n)\}}{T_s} \tag{2.66}$$

where

$$G(n) = \frac{1 - \text{TEO}\{v^s(n)\} + \text{TEO}\{v^s(n+1)\}}{\text{TEO}\{v(n)\}}$$

$$v^s(n) = v(n) - v(n-1)$$

The TEO technique is simple to implement and a moving window can be used to obtain the instantaneous value of the grid voltage fundamental amplitude and frequency [216-221]. The grid voltage waveform with a lag/lead phase angle can be obtained using an Inductor-Capacitor, Capacitor-Capacitor, Inductor-Inductor or lag-lead network [220, 221]. However, the technique presents large overshoot/undershoot during voltage transients [221]. The performance of the technique is also affected when the grid voltage disturbances, such as DC offset, harmonics and noise are not properly rejected by filtering. Chapter 3 describes the RDFT-TEO technique for estimating the single-phase grid voltage fundamental frequency, where the technique is relatively simple, computationally efficient and can reject the negative effects caused by the DC offset and harmonics.

In summary, the pros and cons of the TEO technique are given in the following.

Pros:
- Relatively simple
- Frequency adaptive

Cons:
- Cannot provide phase estimation
- Sensitive to voltage dynamics
- Affected by voltage disturbances

2.1.11 Zero Crossing Detection (ZCD)

The ZCD is a relatively simple and most commonly used technique to estimate the grid voltage fundamental frequency [213, 222-226]. The idea of the technique is to measure the time difference between two successive zero crossings of the grid voltage waveform and

the inverse of this time duration is used to estimate the fundamental frequency [213, 222-226]. A sliding window can be used to obtain the instantaneous fundamental frequency.

The ZCD technique can provide accurate results under undistorted grid conditions. However, the frequency estimation is updated after every half fundamental cycle [213, 222-226]. Nevertheless, multiple level crossing strategy can be used to get several estimates of frequency within one fundamental cycle [227]. On the other hand, the grid voltage may contain notches due to the switching of power electronics devices and hence may affect the performance of the technique [94, 226, 228, 229]. The technique may also provide inaccurate results due to the presence of multiple zero crossings introduced by noise [230, 231]. A FIR based pre-filter can be used to reject the voltage notches and noise [232-234]. On the other hand, a curve fitting strategy can also be used to reduce the negative effects caused by noise [213]. The true zero crossing points can also be obtained using other techniques such as NN and wavelet Transform at the cost of increasing complexity and computational burden for real-time implementation on a digital signal processor [226, 228, 229].

In summary, the pros and cons of the ZCD technique are given in the following.

Pros:
- Relatively simple
- Most commonly used for grid frequency estimation

Cons:
- Only provide frequency estimation
- Can be affected by noise and notches

2.1.12 Three Consecutive Samples (3CS)

The grid voltage fundamental frequency estimation technique based on the 3CS relies on a well-known discrete oscillator law as given by [235]

$$v(n) + v(n-2) = 2v(n-1)\cos(2\pi f T_s) \tag{2.67}$$

The above discrete oscillator law is able to generate a sinusoidal signal with a frequency f for a given sampling period T_s and some initial conditions [78, 235]. On the other hand, the frequency of a pure sinusoidal signal can also be obtained using (2.67), when the signal is given and expressed by

$$v(n) = A_1(n)\sin\left\{\omega(n) n T_s + \theta_1(n)\right\} \tag{2.68}$$

The fast estimation of frequency using the 3CS based relation, as given by (2.67), can be obtained for a small sampling period [78]. However, the technique has several shortcomings for estimating the grid voltage fundamental frequency effectively. The first drawback is that the technique is numerically ill-conditioned when the instantaneous value of the middle sample is equal or close to zero i.e. $v(n\text{-}1) \cong 0$ [78, 236, 237]. Another shortcoming of the technique is that the performance is affected due to the presence of grid voltage disturbances, such as DC offset, harmonics or noise [78, 236, 237]. In addition, the technique presents large overshoot/undershoot during voltage transients [78, 236, 237].

The ill-condition of the 3CS based technique can be removed by holding the previously estimated frequency when the instantaneous value of the middle sample is equal or close to zero [78]. However, the methodology of determining the threshold value of $v(n\text{-}1)$ for removing the ill-condition is not reported in [78]. On the other hand, a pre-filtering of voltage waveform is required to increase the robustness of the technique against grid disturbances and a high-order FIR filter can be used for this purpose at the cost of high computational effort [237, 238]. Other techniques, such as KF [141], NN [164], minimum variance [236] and LS [127, 239] can also be combined with the 3CS based one to reduce the negative effects caused by the voltage disturbances. However, the above mentioned techniques have their own limitations. The 3CS based technique can also be integrated with a maximum likelihood method to estimate not only the fundamental frequency but also the fundamental voltage amplitude and DC offset present in the voltage waveform [237, 240]. To remove the shortcomings of the 3CS based technique, Chapter 5 presents a frequency estimation technique based on the 3CS and a voltage modulation strategy.

In summary, the pros and cons of the 3CS based technique are given in the following.

Pros:
- Relatively simple

Cons:
- Only provide frequency estimation
- Sensitive to voltage transients
- Affected by voltage disturbances
- Ill-conditioned when middle sample is equal or close to zero

Chapter 3

Recursive Discrete Fourier Transform Based Technique

This chapter presents a technique based on recursive discrete Fourier Transform and Teager energy operator to estimate the single-phase grid voltage fundamental frequency. The proposed technique is described in Section 3.1. Selected simulation and experimental results are presented in Section 3.2 and 3.3, respectively. Finally, the conclusions of the work are summarized in Section 3.4.

3.1 Power System Frequency Estimation using A Recursive Discrete Fourier Transform and Teager Energy Operator Based Technique

A recursive discrete Fourier Transform (RDFT) and Teager energy operator (TEO) based (RDFT-TEO) technique is documented in this section to estimate the single-phase grid voltage fundamental frequency under distorted grid conditions. The block diagram of the proposed RDFT-TEO technique is shown in Fig. 3.1, where v is the grid voltage, n is the sampling instant, v_1^u is the normalised amplitude fundamental voltage component, superscript u of v_1^u indicates that the estimated fundamental voltage component has unity amplitude, $\hat{f}$ is the estimated fundamental frequency, f_s is the sampling frequency and N_w is the number of voltage samples present in a window of the RDFT. As it can be noticed, the normalised amplitude of the grid voltage fundamental component is obtained using a window based frequency adaptive band-pass filter (BPF) relying on the RDFT and inverse

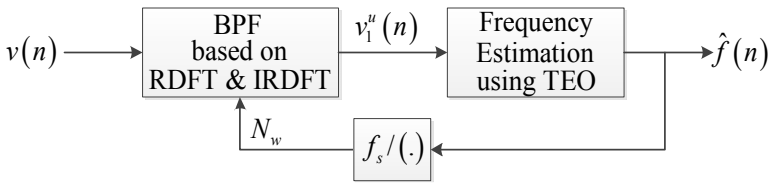

Fig. 3.1 Block diagram of the proposed RDFT-TEO technique for single-phase grid voltage fundamental frequency estimation.

RDFT (IRDFT). The window size of the BPF is equal to the window size of the RDFT. The normalised amplitude of the fundamental voltage component is used to estimate the fundamental frequency using the TEO which relies on three consecutive samples (3CS) of v_1^{μ}. In the RDFT-TEO technique, the value of N_w is used as the number of voltage samples present in one fundamental time period i.e. $N_w=f_s/f$, where f is the fundamental frequency. The estimated fundamental frequency is fed back to obtain the actual value of N_w, as can be noticed in Fig. 3.1. The value of N_w is updated adaptively to synchronize the window size of the BPF with the time-varying grid voltage fundamental time period.

For estimating the fundamental frequency using the RDFT-TEO technique, the generalised expression of a DC offset and harmonically distorted single-phase grid voltage is described by

$$v(n) = v_0(n) + \sum_{i=1,2,\ldots}^{M} v_i(n) \tag{3.1}$$

where v_0 is the DC offset, M is the maximum order of harmonics, v_i is the instantaneous voltage component at the angular frequency $i\omega$ (i=1,2,…,M), and $\omega=2\pi f$ is the fundamental angular frequency. The instantaneous voltage, $v_i(n)$, can be expressed by

$$v_i(n) = A_i(n)\sin\left\{i\omega(n)nT_s + \theta_i(n)\right\}$$

where A_i and θ_i are the amplitude and initial phase angle of the $i\omega$ angular frequency component, respectively, and $T_s=1/f_s$ is the sampling period.

3.1.1 Extraction of Normalised Amplitude Fundamental Voltage Component

A window based frequency adaptive BPF is used to extract the normalised amplitude of the grid voltage fundamental component. The BPF relies on the RDFT and IRDFT [57, 93, 94]. The characteristics of the BPF are presented in this subsection. The discrete Fourier Transform (DFT) of the grid voltage, as given by (3.1), at the n sampling instant can be expressed by [57, 93, 94, 251]

$$V_k(n) = \sum_{l=n-N_w+1}^{n} v(l)\, e^{-j\frac{2\pi kl}{N_w}} \tag{3.2}$$

where k=0,1,2,…,N_w-1 is the DFT frequency index and j is the complex operator. The frequency resolution of the DFT presented by (3.2) is $\Delta f=f$, since the window size is one

fundamental cycle. Similar to (3.2), the DFT of the grid voltage at the (*n*-1) sampling instant can be expressed by

$$V_k(n-1) = \sum_{l=n-N_w}^{n-1} v(l) e^{-j\frac{2\pi kl}{N_w}} \tag{3.3}$$

The following recursive relation can be obtained by subtracting (3.3) from (3.2).

$$V_k(n) = V_k(n-1) + \left\{v(n) - v(n-N_w)\right\} e^{-j\frac{2\pi kn}{N_w}} \tag{3.4}$$

Equation (3.4) is called the RDFT and can be used to estimate the spectral contents present in the grid voltage given by (3.1). On the other hand, the instantaneous time domain voltage for a single frequency *kf* can be obtained by taking the inverse Transform of (3.4) i.e. the IRDFT. Therefore, based on the IRDFT, the instantaneous time domain voltage for the single frequency *kf* can be obtained by [57, 94]

$$v_k(n) = \frac{1}{N_w} V_k(n) e^{j\frac{2\pi kn}{N_w}} \tag{3.5}$$

The RDFT and the IRDFT, as given by (3.4) and (3.5), respectively, can be cascaded in series to implement a digital BPF at the centre frequency *kf*. The discrete transfer function of the BPF at the centre frequency *kf* can be achieved from (3.4) and (3.5). The following expression is obtained from (3.5) after using the value of $V_k(n)$, as given in (3.4).

$$v_k(n) = \frac{1}{N_w} V_k(n-1) e^{j\frac{2\pi kn}{N_w}} + \frac{1}{N_w}\left\{v(n) - v(n-N_w)\right\} \tag{3.6}$$

By replacing *n* with *n*-1, equation (3.5) can also be expressed as

$$v_k(n-1) e^{j\frac{2\pi k}{N_w}} = \frac{1}{N_w} V_k(n-1) e^{j\frac{2\pi kn}{N_w}} \tag{3.7}$$

By combining (3.6) and (3.7), the following relation is obtained.

$$v_k(n) = v_k(n-1) e^{j\frac{2\pi k}{N_w}} + \frac{1}{N_w}\left\{v(n) - v(n-N_w)\right\} \tag{3.8}$$

The following discrete transfer function is obtained after performing the *z*-Transform of (3.8) [93].

$$H_k(z) = \frac{v_k(z)}{v(z)} = \frac{1 - z^{-N_w}}{N_w\left(1 - e^{j2\pi k/N_w} z^{-1}\right)} \tag{3.9}$$

The Bode plot of $H_1(z)$ (for k=1) at the centre frequency equal to nominal fundamental frequency (50 Hz) is shown in Fig. 3.2. As it can be noticed, $H_1(z)$ can reject all the odd and even harmonics including the DC offset. It can also be noticed that $H_1(z)$ provides unity amplitude at the fundamental frequency. Moreover, $H_1(z)$ does not introduce any

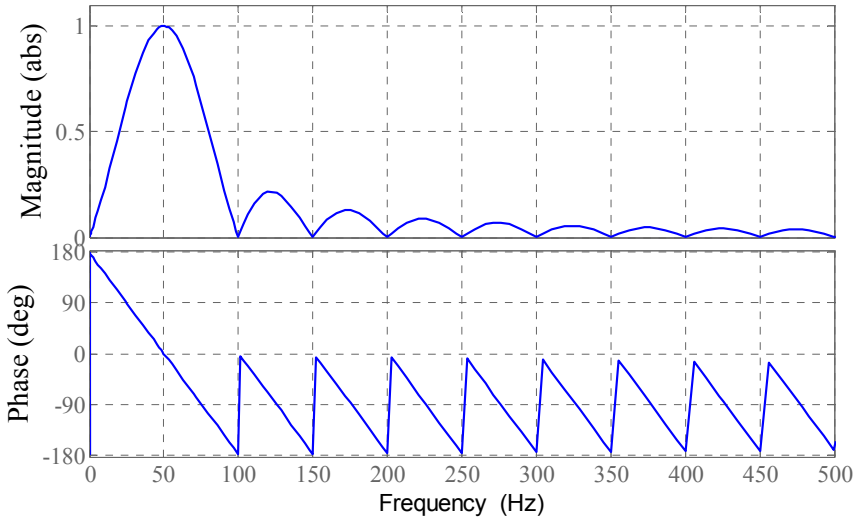

Fig. 3.2 Bode plot of the transfer function $H_1(z)$, as given by (3.9), where k=1, f=50 Hz, f_s=10 kHz and N_w=200.

phase lag/lead at the fundamental frequency. During the variation of frequency, the time-varying harmonics can also be removed adaptively from the grid voltage fundamental component by updating the value of N_w corresponding to the actual fundamental frequency. However, the value of N_w can be integer or non-integer under dynamic conditions. $H_1(z)$ can reject harmonics effectively when the value of N_w is integer. For the non-integer value of N_w i.e. $L_1 \leq N_w < L_1+1$, a rounded function, such as ceil or floor, can be used to obtain an integer value, where L_1 is a positive integer, floor(N_w)=L_1 and ceil(N_w)=L_1+1. However, $H_1(z)$ cannot reject harmonics effectively due to the rounding error produced by the functions floor or ceil. Nevertheless, a linear interpolation can be performed between the samples $v(n\text{-}L_1)$ and $v(n\text{-}L_1\text{-}1)$ to obtain the value of $v(n\text{-}N_w)$ in order to improve the performance of $H_1(z)$. Therefore, the linear interpolation operation can be obtained by [78]

$$z^{-N_w} = (1-b_1)z^{-L_1} + b_1 z^{-L_1-1} \tag{3.10}$$

where $b_1 = N_w - L_1$ and $0 \le b_1 < 1$. The output of the frequency adaptive BPF (based on the transfer function $H_1(z)$) at the n sampling instant can be expressed by

$$v_1(n) = A_1(n)\sin\left\{\omega(n)nT_s + \theta_1(n)\right\} \tag{3.11}$$

where A_1 and θ_1 are the fundamental voltage amplitude and initial phase angle, respectively. The fundamental voltage amplitude can also be estimated from the RDFT, as given by (3.4), and is obtained by

$$\hat{A}_1(n) = \frac{1}{N_w}\sqrt{\left[\mathrm{Re}\left\{V_1(n)\right\}\right]^2 + \left[\mathrm{Im}\left\{V_1(n)\right\}\right]^2} \tag{3.12}$$

where Re and Im denote real and imaginary, respectively. The estimated fundamental voltage amplitude can be used to normalize the fundamental voltage component obtained by (3.11). Therefore, the normalised amplitude of the grid voltage fundamental component can be expressed as

$$v_1^u(n) = \frac{v_1(n)}{\hat{A}_1(n)} = \sin\left\{\omega(n)nT_s + \theta_1(n)\right\} \tag{3.13}$$

The real and imaginary parts of $V_k(n)$, as given by (3.4), can be estimated separately and are given by [95]

$$\begin{aligned}\mathrm{Re}\left\{V_k(n)\right\} &= \mathrm{Re}\left\{V_k(n-1)\right\} + \left\{v(n) - v(n-N_w)\right\}\cos\left(\frac{2\pi kn}{N_w}\right)\\ \mathrm{Im}\left\{V_k(n)\right\} &= \mathrm{Im}\left\{V_k(n-1)\right\} + \left\{v(n) - v(n-N_w)\right\}\sin\left(\frac{2\pi kn}{N_w}\right)\end{aligned} \tag{3.14}$$

The real part of the IRDFT, as given by (3.5), can also be expressed as

$$v_k(n) = \frac{1}{N_w}\left[\mathrm{Re}\left\{V_k(n)\right\}\cos\left(\frac{2\pi kn}{N_w}\right) + \mathrm{Im}\left\{V_k(n)\right\}\sin\left(\frac{2\pi kn}{N_w}\right)\right] \tag{3.15}$$

The implementation of the BPF based on (3.14) and (3.15) (when k=1) for estimating the normalized amplitude grid voltage fundamental component is shown in Fig. 3.3 [57, 93, 94]. As it can be seen, the BPF requires few mathematical operations, two trigonometric functions and N_w+2 transport delays.

In the proposed RFDT-TEO technique, the negative effect caused by the amplitude accumulation error is rejected by normalising the fundamental voltage waveform. On the other hand, the negative effect of the phase accumulation error is neglected based on an

assumption that the phase error is constant within the 3CS of the normalised amplitude of the fundamental voltage waveform. The constant phase error within the 3CS does not have any negative effect in the frequency estimation using the TEO [214, 216, 217, 220].

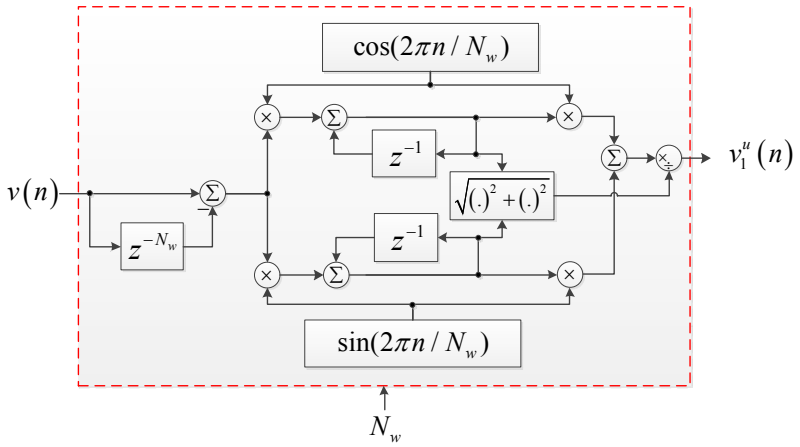

Fig. 3.3 BPF based on the RDFT and IRDFT to extract the amplitude normalised grid voltage fundamental component.

3.1.2 Fundamental Frequency Estimation

The TEO is a nonlinear operator and can be used to estimate the instantaneous energy of a sinusoidal signal [214, 216, 217, 220, 221]. The value of the TEO is equal to the square of the product between amplitude and angular frequency [214, 216, 217, 220, 221]. It is reported in [214] that the TEO can be obtained from the 3CS of a discrete sinusoidal signal. Therefore, based on the constant fundamental voltage parameters within the 3CS of (3.11), the following relation can be obtained to get the value of TEO [214, 216, 217, 220, 221].

$$A_1^2(n)\left[\sin\left\{\omega(n)T_s\right\}\right]^2 = v_1^2(n-1) - v_1(n)v_1(n-2)$$

$$\Rightarrow A_1^2(n)\omega^2(n)T_s^2 \cong v_1^2(n-1) - v_1(n)v_1(n-2) \tag{3.16}$$

where $\sin\{\omega(n)T_s\} \cong \omega(n)T_s$ for a high sampling frequency [214]. It can be seen from the technical literature that the TEO, as given by (3.16), can be used to estimate the fundamental voltage amplitude of the grid voltage, where the fundamental frequency is known or estimated separately [214, 216, 217, 220, 221]. On the other hand, it can be seen from (3.16) that the fundamental frequency can also be estimated using the TEO, where the fundamental voltage amplitude is unity or estimated separately. In this subsection, the TEO

is used to estimate the fundamental frequency of the grid voltage waveform. Based on the normalised amplitude of the fundamental voltage component, as obtained by (3.13), equation (3.16) can be expressed as

$$\sin\left\{\omega(n)T_s\right\} = \sqrt{\left|\left\{v_1^u(n-1)\right\}^2 - v_1^u(n)v_1^u(n-2)\right|} \tag{3.17}$$

In order to avoid the inverse operation of the trigonometric function, $\sin\{\omega(n)T_s\}$ in (3.17) can be approximated by

$$\begin{aligned}\sin\left\{\omega(n)T_s\right\} &= \sin\left\{\omega_0 T_s + \Delta\omega(n)T_s\right\} = \sin(\omega_0 T_s)\cos\left\{\Delta\omega(n)T_s\right\} + \sin\left\{\Delta\omega(n)T_s\right\}\cos(\omega_0 T_s) \\ &\cong \sin(\omega_0 T_s) + \Delta\omega(n)T_s\cos(\omega_0 T_s)\end{aligned} \tag{3.18}$$

where $\omega=\omega_0+\Delta\omega$, $\omega_0=2\pi f_0$ is the nominal fundamental angular frequency, f_0 is the nominal fundamental frequency, $\Delta\omega=2\pi\Delta f$ is the fundamental angular frequency deviation, Δf is the fundamental frequency deviation, $\cos\{\Delta\omega(n)T_s\}\cong 1$ and $\sin\{\Delta\omega(n)T_s\}\cong\Delta\omega(n)T_s$. As it can be seen, both $\sin(\omega_0 T_s)$ and $\cos(\omega_0 T_s)$ are constants and can be estimated offline for real-time implementations. Therefore, the fundamental frequency deviation can be estimated from (3.17) and (3.18) using only 3CS of the normalised amplitude of the fundamental voltage waveform and is expressed by

$$\Delta\hat{f}(n) = \frac{\sqrt{\left|\left\{v_1^u(n-1)\right\}^2 - v_1^u(n)v_1^u(n-2)\right|} - \sin(\omega_0 T_s)}{2\pi T_s\cos(\omega_0 T_s)} \tag{3.19}$$

where $|\cdots|$ indicates absolute value. The actual fundamental frequency can be obtained by

$$\hat{f}(n) = f_0 + \Delta\hat{f}(n) \tag{3.20}$$

The implementation of (3.19) and (3.20) for fundamental frequency estimation is shown in Fig. 3.4. As it can be noticed, the estimation of the fundamental frequency requires few mathematical operations and is also relatively simple to implement. Moreover, only 3CS are required and hence can provide fast estimation of frequency. However, as there is an

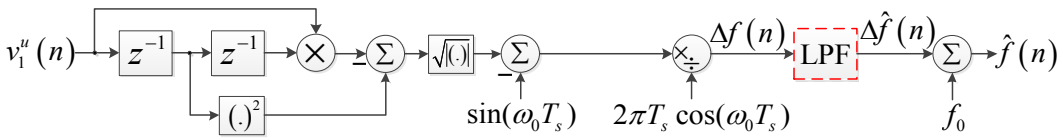

Fig. 3.4 Fundamental frequency estimation using the TEO.

interdependent loop present in Fig. 3.1, the fast tracking of the frequency, when compared to the estimation of the normalised amplitude of the fundamental voltage component, will affect the stability of the technique [252]. Therefore, a first-order infinite-impulse-response (IIR) low-pass filter (LPF) can be cascaded in series with the TEO, as shown in Fig. 3.4, to ensure a smaller bandwidth with respect to the estimation of the fundamental voltage component [252]. The settling time of the first-order LPF can be approximated by [198]

$$T_{LPF} \cong \frac{5}{\omega_{cut}} \tag{3.21}$$

where ω_{cut} is the angular cut-off frequency of the LPF. The following condition has to be satisfied for the purpose of stability of the proposed RDFT-TEO technique.

$$T_{LPF} + 2T_s \geq T_{RDFT} \tag{3.22}$$

where T_{RDFT} is the time delay provided by the BPF during dynamics. Based on the assumption $T_{RDFT} >> 2T_s$ i.e. for a high sampling frequency, equation (3.22) can be approximated by

$$T_{LPF} \geq T_{RDFT}$$

$$\Rightarrow \frac{5}{\omega_{cut}} \geq T_{RDFT}$$

$$\Rightarrow \omega_{cut} \leq \frac{5}{T_{RDFT}} \tag{3.23}$$

The window size of the BPF is used as one fundamental time period. Hence, the value of T_{RDFT} can be approximated by 20 ms for the 50 Hz system. The angular cut-off frequency of the first-order IIR LPF has to satisfy the following condition.

$$\omega_{cut} \leq 250 \text{ rad/s} \tag{3.24}$$

3.2 Simulation Results

The simulation performance of the RDFT-TEO technique for fundamental frequency estimation is documented in this section. A first-order discrete IIR LPF with the cut-off

frequency of equal to 39.8 Hz (ω_{cut}=250 rad/s) is used in the technique. The sampling frequency is chosen as f_s=10 kHz. The estimation of the fundamental frequency steps ±7.5 Hz using the proposed technique is shown in Fig. 3.5, where the grid voltage contains only fundamental component with 1.0 p.u. amplitude. The frequency variation range of 50 Hz ± 7.5 Hz is considered based on the specification of the IEC standard 61000-4-30 [85]. As it can be seen in Fig. 3.5, the settling time of the technique is around 1.5 fundamental cycles.

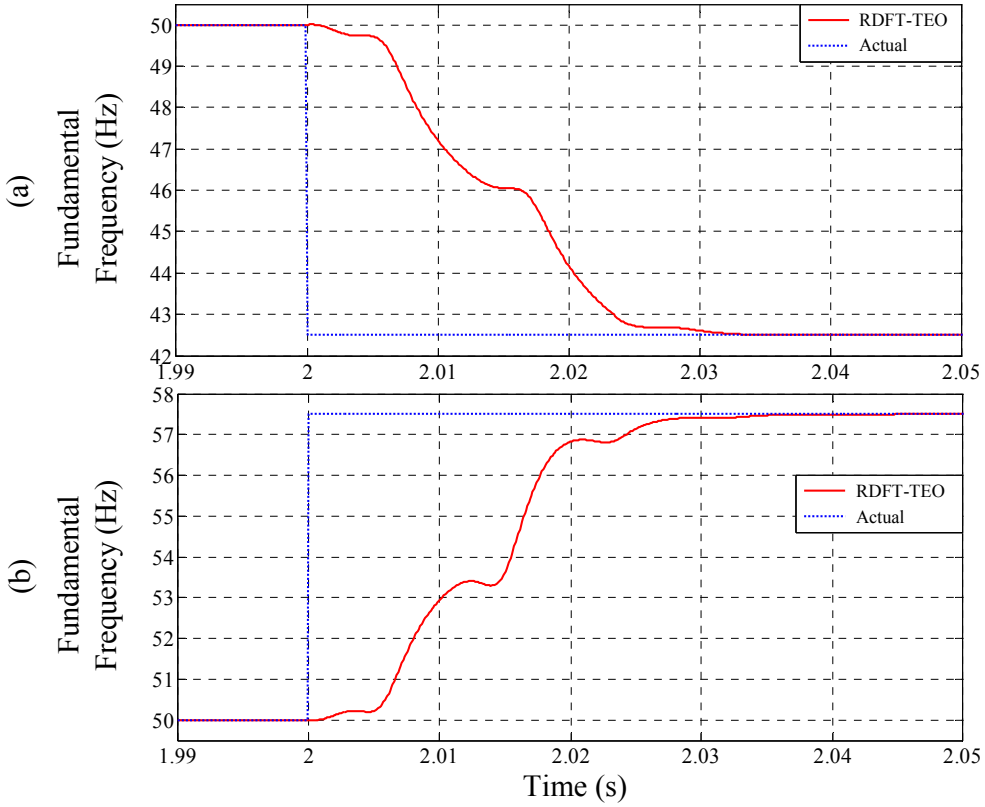

Fig. 3.5 Frequency steps estimation. (a) -7.5 Hz (50 Hz to 42.5 Hz). (a) +7.5 Hz (50 Hz to 57.5 Hz).

For evaluating the steady-state performance of the RDFT-TEO technique, the fundamental component of the grid voltage waveform is distorted by harmonics, as given in Table 3.1, based on the definition for the second level test class in IEC standard 61000-4-13 [119, 253]. The harmonics given in Table 3.1 introduce 14.58% total harmonic distortion (THD). The steady-state error of the estimated fundamental frequency using the RDFT-TEO technique is shown in Fig. 3.6, where the grid voltage contains 1.0 p.u. fundamental amplitude, 14.58% total harmonic distortion (THD), as given in Table 3.1, and the fundamental frequency is varied from 42.5 Hz to 57.5 Hz. As it can be noticed, the proposed technique can provide the estimation of the fundamental frequency range of 50

Hz ± 7.5 Hz with an error less than 0.005 Hz under 14.58% THD. Moreover, the steady-state relative error of the estimated fundamental frequency is less than 0.03%, which is the maximum acceptable value as specified by the IEC standard 61000-4-7 [254], where the relative error can be defined by (3.25) and $|\cdots|$ indicates absolute value.

$$\text{Relative Error (\%)} = \frac{|\text{Actual Value - Estimated Value}|}{\text{Actual Value}} \times 100\% \tag{3.25}$$

Table 3.1 Harmonics as a percentage of fundamental component based on second level test class in IEC standard 61000-4-13

Harmonics					THD
2^{nd}	3^{rd}	4^{th}	5^{th}	7^{th}	14.58%
3.0%	8.0%	1.5%	9.0%	7.5%	

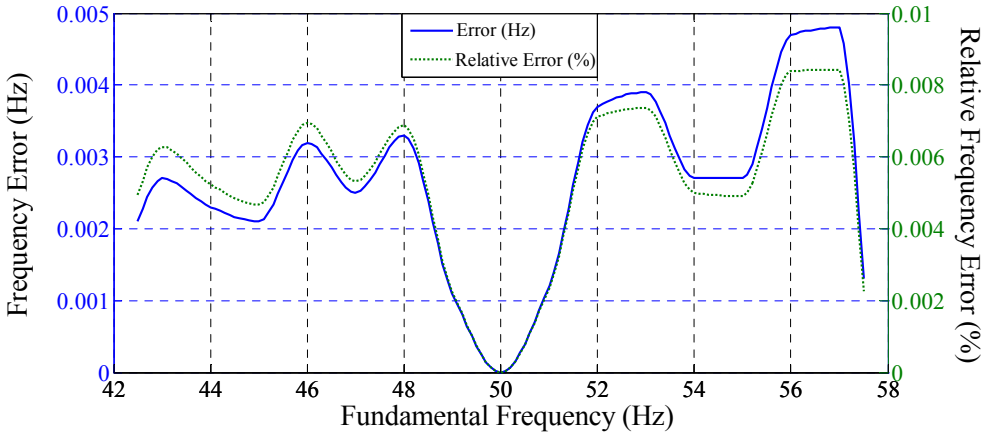

Fig. 3.6 Frequency error in steady-state operation with harmonics, as given in Table 3.1.

3.3 Real-Time Experimental Results

The experimental performance of the RDFT-TEO one is compared with a similar technique based on the RDFT and decomposition of a single-phase system into orthogonal components (RDFT-OC) [82]. The laboratory setup for real-time experiments is presented in Section 1.3 of Chapter 1. The parameters of both techniques are given in Table 3.2.

The following case studies are performed to compare the real-time performance of the RDFT-TEO and RDFT-OC techniques.

Table 3.2 Parameters of the RDFT-TEO and RDFT-OC techniques

RDFT-TEO	RDFT-OC
ω_{cut}=250 rad/s	2 LPFs based on 250 points Hamming window

i. Steady-state with DC offset and harmonics (Case-1)
ii. Frequency step and harmonics (Case-2)
iii. Frequency sweep and harmonics (Case-3)
iv. Voltage sag and harmonics (Case-4)
v. Voltage flicker and harmonics (Case-5)
vi. Phase jump and harmonics (Case-6)

The grid voltage waveforms presented in all the above case studies contain 14.58% THD, as given in Table 3.1.

3.3.1 Case-1: Steady-State with DC Offset and Harmonics

The steady-state performances of the RDFT-TEO and RDFT-OC techniques are compared under DC offset and harmonics. The grid voltage waveform, as shown in Fig. 3.7(a), contains 5% DC offset and 14.58% THD, as given in Table 3.1. The estimation of the nominal fundamental frequency using the RDFT-TEO and RDFT-OC techniques is

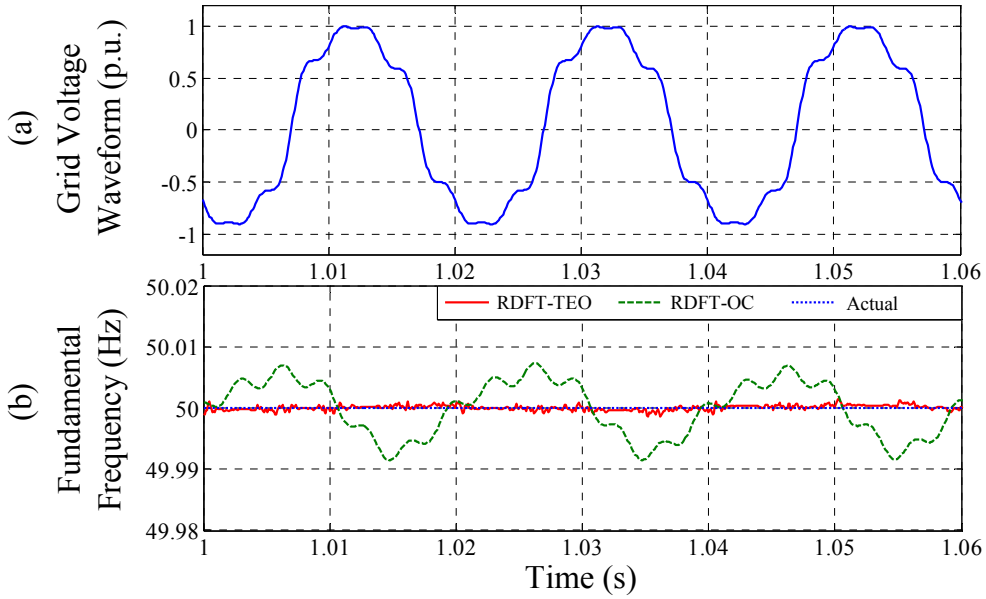

Fig. 3.7 Case-1: Steady-state with DC offset (5%) and harmonics. (a) Grid voltage waveform. (b) Fundamental frequency.

shown in Fig. 3.7(b). As it can be noticed, the RDFT-TEO and RDFT-OC techniques produce 0.003% and 0.017% relative error, respectively, for nominal fundamental frequency estimation under DC offset and harmonics.

3.3.2 Case-2: Frequency Step and Harmonics

The performances of the RDFT-TEO and RDFT-OC techniques are compared under frequency step and harmonics. In this case study, the grid voltage contains -7.5 Hz (50 Hz to 42.5 Hz) frequency step and 14.58% THD, as given in Table 3.1. The fundamental frequency step estimation using the RDFT-TEO and RDFT-OC techniques is depicted in Fig. 3.8. As it can be noticed, the settling time of the proposed RDFT-TEO technique under frequency step is around 1.5 fundamental cycles. It can also be seen that both RDFT-TEO and RDFT-OC techniques can track the frequency step. The steady-state relative error of the estimated fundamental frequency of 42.5 Hz using the RDFT-TEO and RDFT-OC techniques are 0.012% and 0.654%, respectively, under 14.58% THD. The RDFT-TEO technique can provide estimation with a relative error less than 0.03%.

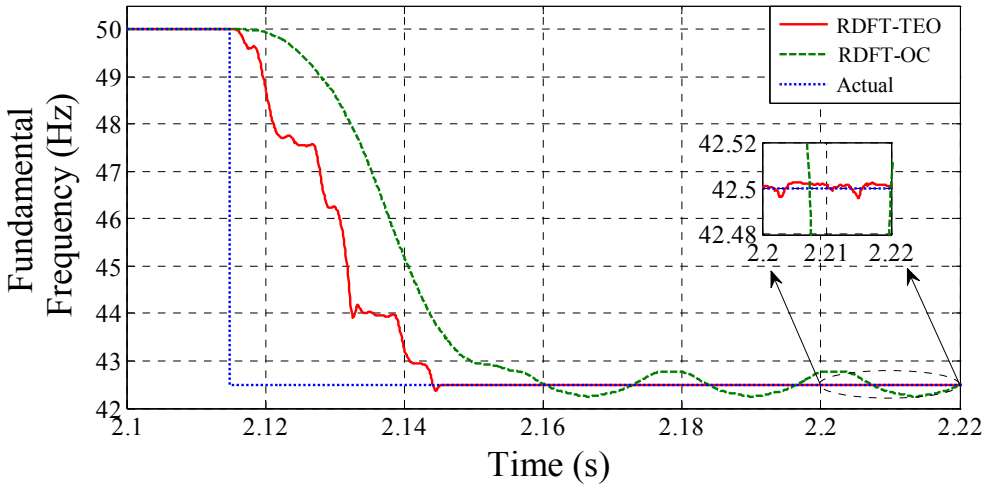

Fig. 3.8 Case-2: Frequency step (-7.5 Hz: 50 Hz to 42.5 Hz) and harmonics.

3.3.3 Case-3: Frequency Sweep and Harmonics

A fundamental frequency sweep of +10 Hz/s up to 57.5 Hz is considered into the grid voltage containing harmonics, as given in Table 3.1. The estimation of the fundamental frequency sweep is shown in Fig. 3.9. As it can be noticed, both RDFT-TEO and RDFT-OC techniques can track the frequency sweep. The steady-state relative error of the

estimated fundamental frequency of 57.5 Hz using the RDFT-TEO and RDFT-OC techniques are 0.005% and 0.051%, respectively, under 14.58% THD.

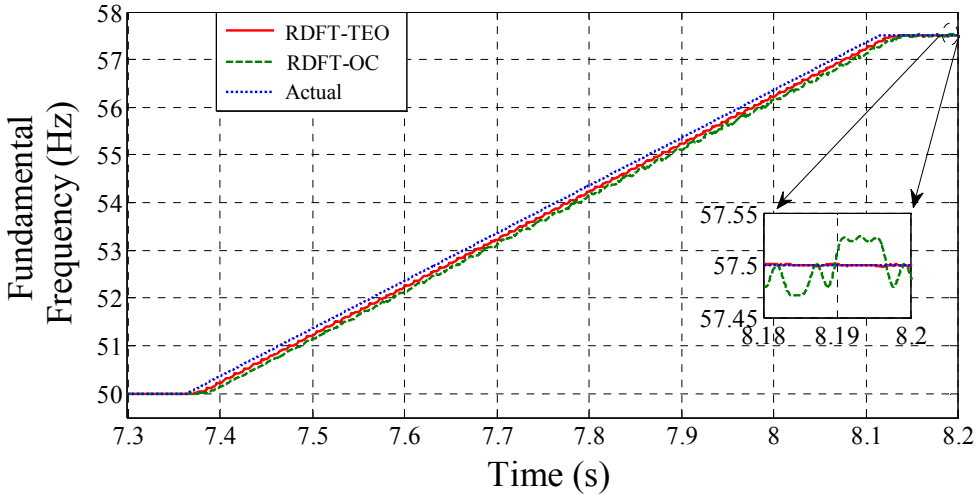

Fig. 3.9 Case-3: Frequency sweep (+10 Hz/s: 50 Hz to 57.5 Hz) and harmonics.

3.3.4 Case-4: Voltage Flicker and Harmonics

The grid voltage waveform, as shown in Fig. 3.10(a), contains voltage flicker and harmonics, as given in Table 3.1. The frequency and amplitude of the triangular voltage flicker are 2.5 Hz and ±5% of fundamental voltage amplitude, respectively. It can be seen from Fig. 3.10(b) that the performance of the RDFT-TEO technique for fundamental

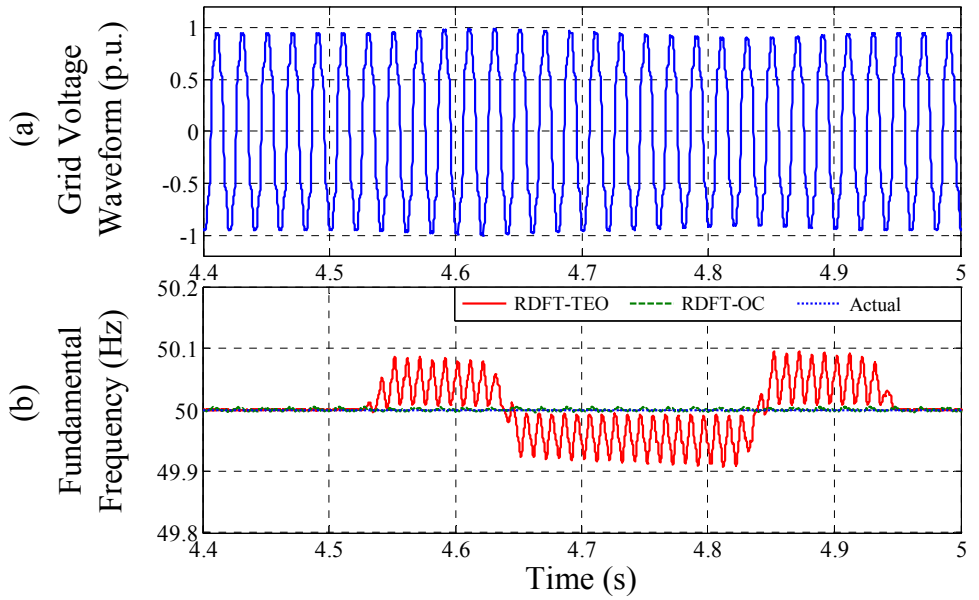

Fig. 3.10 Case-4: Voltage flicker (±5%) and harmonics. (a) Grid voltage waveform. (b) Fundamental frequency.

frequency estimation is more affected by the voltage flicker and harmonics as compared to the RDFT-OC one. During the voltage flicker, the phase error generated by the RDFT is not constant within the 3CS of the amplitude normalised fundamental voltage waveform, thus the RDFT-TEO technique produces ripple in the frequency estimation, as can be seen in Fig. 3.10.

3.3.5 Case-5: Voltage Sag and Harmonics

A grid voltage sag of 30% and 14.58% THD, as given in Table 3.1, is shown in Fig. 3.11(a). The fundamental frequency estimation is shown in Fig. 3.11(b). As it can be observed, the RDFT-TEO technique is more affected by the voltage sag when compared with the RDFT-OC one.

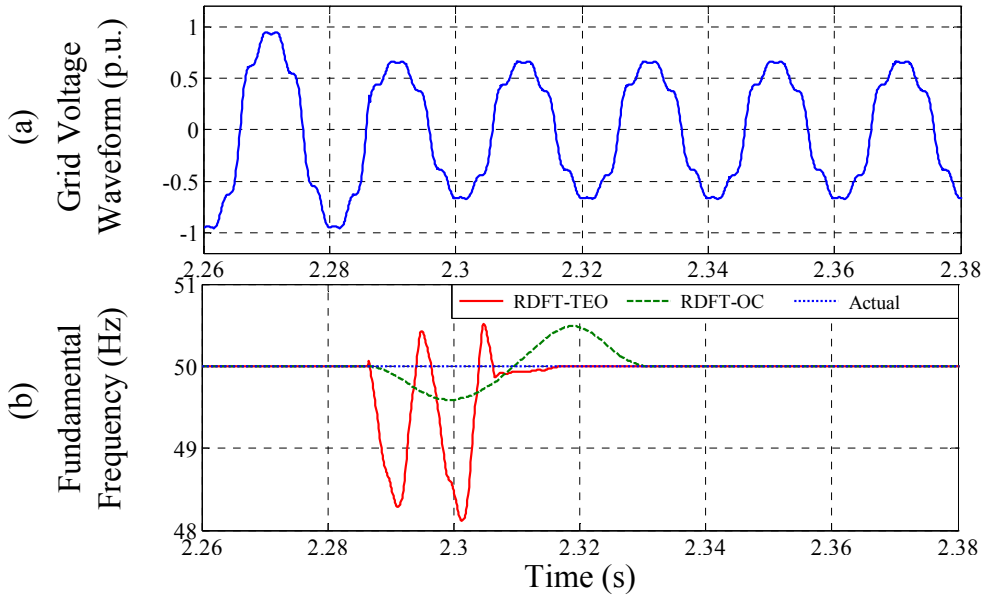

Fig. 3.11 Case-5: Voltage sag (30%) and harmonics. (a) Grid voltage waveform. (b) Fundamental frequency.

3.3.6 Case-6: Phase Jump and Harmonics

The grid voltage waveform, as shown in Fig. 3.12(a), contains a -30° phase jump and harmonics, as given in Table 3.1. For this case, the estimation of the fundamental frequency is shown in Fig. 3.12(b). As it can be observed, the performance of both RDFT-TEO and RDFT-OC techniques is affected by phase jump.

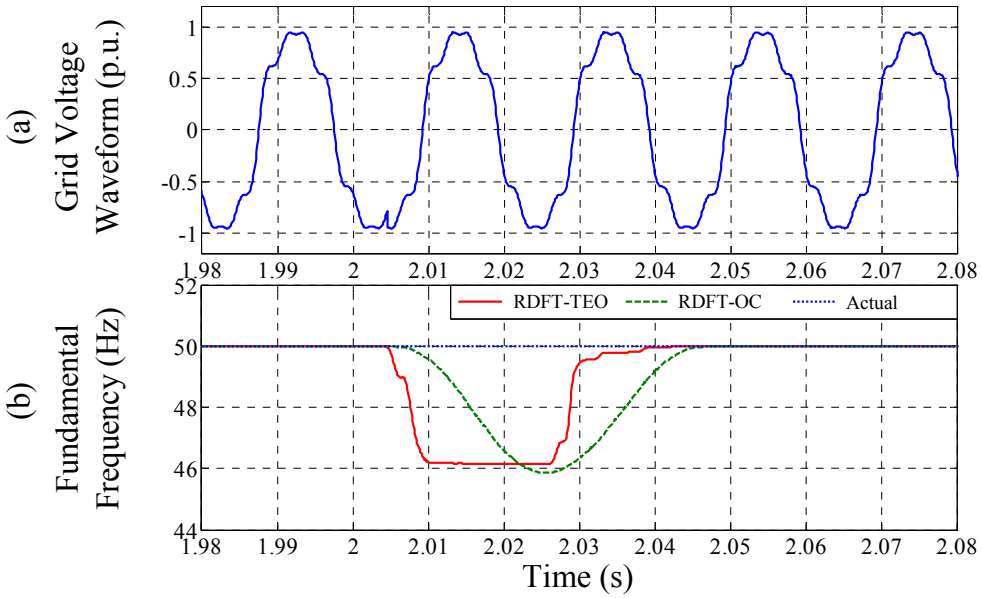

Fig. 3.12 Case-6: Phase jump (-30°) and harmonics. (a) Grid voltage waveform. (b) Fundamental Frequency.

3.4 Performance and Computational Effort Comparisons of the RDFT-TEO and RDFT-OC Techniques

Table 3.3 shows a summary of the performance and computational effort comparisons of the RDFT-TEO and RDFT-OC techniques. As it can be seen, the RDFT-OC technique does not contain interdependent loop and the frequency estimation is less affected by the voltage flicker and voltage sag when compared with the RDFT-TEO one. However, the proposed RDFT-TEO one is simpler and computationally efficient as compared to the RDFT-OC technique. For computational performance comparison, turnaround time is one of the measures and can be defined as the time delay between the submission of a task for processing and the return of the complete output. In the DS1103 control board platform, the RDFT-TEO and RDFT-OC techniques take 2.96 μs and 6.14 μs turnaround time, respectively, for providing the real-time frequency estimation. However, the acutaul turnaround time may vary, as the DSP techniques are implemented on a digital signal processor platform for real-time applications. The RDFT-TEO technique can also provide improved estimation of fundamental frequency under DC offset, harmonics, frequency step, frequency sweep and phase jump when compared with the RDFT-OC one, as it can also be noticed from Table 3.3.

Table 3.3 Performance and computational effort comparisons of the RDFT-TEO and RDFT-OC techniques

Comparison Cases	RDFT-TEO	RDFT-OC
Simplicity	√	
Interdependent loop		√
Computational burden	√	
DC offset	√	
Harmonics	√	
Frequency step	√	
Frequency sweep	√	
Voltage flicker		√
Voltage sag		√
Phase jump	√	

√ symbol denotes which technique performs better with respect to the other one for the cases provided in the left column of Table 3.3.

3.5 Conclusions

A single-phase grid voltage fundamental frequency estimation technique has been reported in this chapter. The technique relies on a Teager energy operator and a band-pass filter. The three consecutive samples based Teager energy operator is used to estimate the fundamental frequency. The band-pass filter is implemented based on the recursive discrete Fourier Transform and inverse recursive discrete Fourier Transform. The proposed technique is computationally efficient and can also estimate a wide range of fundamental frequency variation accurately under the DC offset and harmonics. The proposed technique also requires less computational effort, can provide faster estimation and is less affected by harmonics as compared to a technique relying on the recursive discrete Fourier Transform based decomposition of a single-phase system into orthogonal components. The presented simulation and experimental results have confirmed the effectiveness of the proposed technique for grid voltage fundamental frequency estimation.

Chapter 4

Newton-Type Algorithm Based Technique

This chapter presents a technique based on a Newton-type algorithm and an infinite-impulse-response differentiation filter to estimate the single-phase grid voltage fundamental frequency. The technique is described in Section 4.1. Section 4.2 contains the simulation results of the technique. Selected experimental results are presented in Section 4.3. Finally, the conclusions of the work are summarized in Section 4.4.

4.1 Power System Frequency Estimation using A Newton-Type Algorithm and Differentiation Filter Based Technique

A Newton-type algorithm (NTA) and differentiation filter (DF) based (NTA-DF) technique is documented in this section for estimating the single-phase grid voltage fundamental frequency under distorted grid conditions. The block diagram of the proposed NTA-DF technique is shown in Fig. 4.1, where v is the grid voltage, n is the sampling instant, v_1 is the fundamental voltage component, $\psi_1(n) = \Delta\omega(n)nT_s + \theta_1(n)$ is the initial phase angle (θ_1) plus instantaneous phase angle $\{\Delta\omega(n)nT_s\}$ corresponding to fundamental angular frequency deviation $(\Delta\omega)$, $\Delta\hat{\omega}$ is the estimated fundamental angular frequency deviation, ω_0 is the nominal fundamental angular frequency, $\hat{\omega}$ is the estimated fundamental angular frequency and $\hat{f}$ is the estimated fundamental frequency. As it can be seen, the DC offset is removed from the grid voltage by using a band-pass filter (BPF). The NTA is then used to obtain the phase angle, which is differentiated using the DF to estimate the angular frequency deviation and added with the nominal value to get the actual fundamental angular frequency.

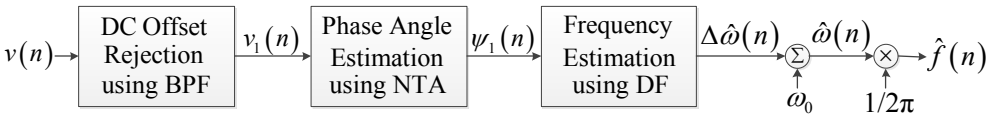

Fig. 4.1 Block diagram of the proposed NTA-DF technique for the estimation of single-phase grid voltage fundamental frequency.

4.1.1 DC Offset Rejection

For simplicity, the single-phase grid voltage waveform can be expressed by

$$v(n) = v_0(n) + v_1(n) \tag{4.1}$$

where v_0 is the DC offset and the fundamental voltage component can be expressed by

$$v_1(n) = A_1(n)\sin\{\omega_0 n T_s + \psi_1(n)\}$$

where A_1 is the fundamental amplitude and T_s is the sampling period.

A second-order infinite-impulse-response (IIR) BPF is used to reject the DC offset from the grid voltage waveform. The discrete transfer function of the BPF is given by [191]

$$T_1(z) = \frac{0.5(1-z^{-2})}{1-\cos(2\pi f_c T_s)z^{-1}} \tag{4.2}$$

where f_c is the centre frequency at which the BPF has unity magnitude and also introduces 0° phase shift. The Bode plot of $T_1(z)$ for f_c=50 Hz and 1.6 kHz sampling frequency is shown in Fig. 4.2. As it can be noticed, the BPF can remove the DC offset from the input grid voltage. The BPF also gives unity amplitude and 0° phase shift at the frequency f_c. Moreover, the BPF can attenuate the amplitude of the high frequency disturbances present in the grid voltage. However, the BPF cannot reject lower order harmonics effectively. The implementation of the BPF is shown in Fig. 4.3.

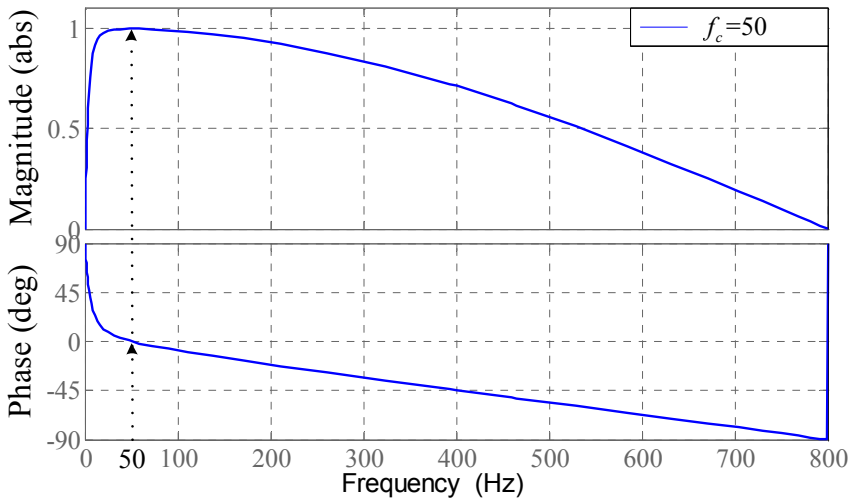

Fig. 4.2 Bode plot of the BPF as given by (4.2).

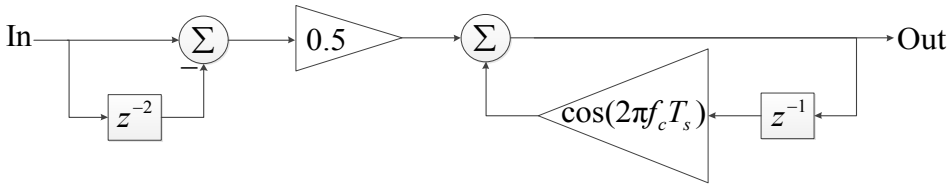

Fig. 4.3 Implementation of the BPF as given by (4.2).

In the proposed technique, the BPF is tuned at grid voltage nominal fundamental frequency i.e. f_c=50 Hz. The BPF tuned at nominal fundamental frequency introduces a leading/lagging phase angle when the grid frequency is smaller/higher than the nominal value, respectively, as can be seen from Fig. 4.2. The leading/lagging phase angle is a constant value when the grid frequency drift is constant. The constant leading/lagging phase angle introduces zero stead-state error in the frequency estimation by differentiation operation. On the other hand, the leading/lagging phase is time-varying when the grid frequency varies continuously. Thus, the estimated frequency by differentiation operation contains an error due to the time-varying phase angle introduced by the BPF during frequency transients. However, the grid voltage frequency varies slowly due to the large inertia of the rotating shafts of power generators and hence the estimated frequency error due to the differentiation of the slowly changing phase angle introduced by the BPF is small and thus can be neglected. On the other hand, the fundamental voltage amplitude is also attenuated by the BPF due to the deviation of fundamental frequency from its nominal value, as it can be noticed from Fig. 4.2. However, the attenuation of the fundamental voltage amplitude does not affect the estimation of frequency, as it is estimated from the instantaneous phase angle. Therefore, the output of the BPF can be approximated by

$$v_1(n) = A_1(n)\sin\{\omega_0 n T_s + \psi_1(n)\} \tag{4.3}$$

4.1.2 Instantaneous Phase Angle Estimation

Based on the NTA, the grid voltage fundamental component, as obtained by (4.3), can be expressed by

$$v_1(n) = \eta_{NTA}(X_n) \tag{4.4}$$

where η_{NTA} and X_n are the estimation function and the estimation vector of the NTA, respectively. For the proposed technique, the estimation function and vector at the n sampling instant can be defined by (4.5) and (4.6), respectively.

$$\eta_{NTA}\left(X_n\right) = A_1\left(n\right)\sin\left\{\omega_0 nT_s + \psi_1\left(n\right)\right\} \tag{4.5}$$

$$X_n = \left[A_1\left(n\right) \quad \psi_1\left(n\right)\right]^{\square} \tag{4.6}$$

where $\square$ denotes transpose operation. The estimation error of the NTA can be obtained by

$$e_v\left(n\right) = \eta_{NTA}\left(X_n\right) - v_1\left(n\right) \tag{4.7}$$

An error vector is also defined as given by

$$E\left(X_n\right) = \left[e_v\left(n\right) \quad e_v\left(n-1\right)\right]^{\square} = 0_{2\times 1} \tag{4.8}$$

where $0_{2\times1}$ is a 2×1 zeros vector. For the estimation vector X_{n+1} at the (n+1) sampling instant, there is an unknown estimation correction vector (ΔX_n) such that

$$E\left(X_{n+1}\right) = E\left(X_n + \Delta X_n\right) = 0_{2\times 1} \tag{4.9}$$

where

$$\Delta X_n = \left[\Delta A_1\left(n\right) \quad \Delta\psi_1\left(n\right)\right]^{\square}$$

The following linear relation can be obtained using the Taylor series expansion of $E(X_n+\Delta X_n)$ in the close neighbourhood of X_n [119].

$$E\left(X_n + \Delta X_n\right) = E\left(X_n\right) + J_{NTA}\Delta X_n \tag{4.10}$$

where J_{NTA} is the Jacobian matrix and can be defined as

$$J_{NTA} = \begin{bmatrix} \dfrac{\partial e_v\left(n\right)}{\partial A_1\left(n\right)} & \dfrac{\partial e_v\left(n\right)}{\partial \psi_1\left(n\right)} \\ \dfrac{\partial e_v\left(n-1\right)}{\partial A_1\left(n-1\right)} & \dfrac{\partial e_v\left(n-1\right)}{\partial \psi_1\left(n-1\right)} \end{bmatrix} = \begin{bmatrix} a_n & b_n \\ a_{n-1} & b_{n-1} \end{bmatrix} \tag{4.11}$$

where

$$a_n = \frac{\partial e_v\left(n\right)}{\partial A_1\left(n\right)} = \sin\left\{\omega_0 nT_s + \psi_1\left(n\right)\right\}$$

$$b_n = \frac{\partial e_v(n)}{\partial \psi_1(n)} = A_1(n)\cos\{\omega_0 n T_s + \psi_1(n)\}$$

To estimate ΔX_n, the following relation can be obtained from (4.9) and (4.10).

$$J_{NTA}\Delta X_n = -E(X_n) \tag{4.12}$$

The estimation correction vector can be obtained from (4.12) and is given by [116-119]

$$\Delta X_n = -\left(J_{NTA}^{\square} J_{NTA}\right)^{-1} J_{NTA}^{\square} E(X_n) \tag{4.13}$$

Equation (4.13) can be simplified by putting the values of J_{NTA} and $E(X_n)$, and is expressed by

$$\Delta X_n = \begin{bmatrix} \dfrac{(a_n b_n + a_{n-1}b_{n-1})(b_n e_n + b_{n-1}e_{n-1}) - (b_n^2 + b_{n-1}^2)(a_n e_n + a_{n-1}e_{n-1})}{(a_n b_{n-1} - a_{n-1}b_n)^2} \\ \dfrac{(a_n b_n + a_{n-1}b_{n-1})(a_n e_n + a_{n-1}e_{n-1}) - (a_n^2 + a_{n-1}^2)(b_n e_n + b_{n-1}e_{n-1})}{(a_n b_{n-1} - a_{n-1}b_n)^2} \end{bmatrix} \tag{4.14}$$

Expression (4.14) helps to avoid matrix multiplication and inversion operations required for the NTA, thus reducing computational burden for real-time implementation. However, expression (4.14) has to satisfy the following condition.

$$(a_n b_{n-1} - a_{n-1}b_n)^2 \neq 0 \tag{4.15}$$

Based on an assumption $A_1(n)=A_1(n\text{-}1)$, the following condition is obtained from (4.15) after replacing the values of a_n, b_n, $a_{n\text{-}1}$ and $b_{n\text{-}1}$.

$$A_1(n)\sin\{\omega(n)T_s\} \neq 0 \tag{4.16}$$

Therefore, the proposed NTA can be used when $A_1(n)\neq 0$. This condition is also obtained in [119] for removing the matrix singularities of the NTA. To avoid possible matrix singularities in cases of abrupt changes, $(J_{NTA}^{\square} J_{NTA})^{-1}$ in (4.13) can be replaced by a scalar value of equal to 0.2 when $A_1(n)$ is equal or close to zero [119]. For this case, the estimation correction vector in the proposed NTA can be expressed by

$$\Delta X_n = -0.2\begin{bmatrix} a_n e_n + a_{n-1}e_{n-1} \\ b_n e_n + b_{n-1}e_{n-1} \end{bmatrix} \tag{4.17}$$

After obtaining ΔX_n, the estimation vector at the (n+1) sampling instant can be expressed by

$$X_{n+1} = X_n + \Delta X_n \tag{4.18}$$

4.1.3 Fundamental Frequency Estimation

The grid voltage fundamental angular frequency deviation can be estimated using a differentiation operation from the phase angle obtained by the NTA and is expressed by

$$\Delta\omega(n) = \frac{\psi_1(n) - \psi_1(n-1)}{T_s} \tag{4.19}$$

However, the time-varying frequency estimation using (4.19) is not suitable when the instantaneous phase angle is distorted by high frequency disturbances. Based on (4.19), $\Delta\omega$ for the n, (n-1),$\cdots$,(n-N_w/2+1) sampling instants can also be obtained from a window size of N_w/2 samples of the instantaneous phase angle and is given by

$$\left.\begin{aligned} \Delta\omega_{N_w/2}(n) &= \frac{\psi_1(n) - \psi_1(n - N_w/2)}{T_s N_w/2} \\ \Delta\omega_{N_w/2}(n-1) &= \frac{\psi_1(n-1) - \psi_1(n - N_w/2 - 1)}{T_s N_w/2} \\ &\vdots \\ \Delta\omega_{N_w/2}(n - N_w/2+1) &= \frac{\psi_1(n - N_w/2+1) - \psi_1(n - N_w + 1)}{T_s N_w/2} \end{aligned}\right] \tag{4.20}$$

To reject the negative effects caused by high frequency disturbances, the average angular frequency deviation at the n sampling instant over a window size, T_w=$N_w T_s$, of N_w samples of the instantaneous phase angle can be obtained from (4.20) and is expressed by

$$\Delta\omega(n) = \frac{\Delta\omega_{N_w/2}(n) + \Delta\omega_{N_w/2}(n-1) + \cdots + \Delta\omega_{N_w/2}(n - N_w/2 + 1)}{N_w/2} = \frac{4}{N_w^2 T_s}\Big[\psi_1(n) + \psi_1(n-1)$$

$$+ \cdots + \psi_1(n - N_w/2 + 1) - \big\{\psi_1(n - N_w/2) + \psi_1(n - N_w/2 - 1) + \cdots + \psi_1(n - N_w + 1)\big\}\Big] \tag{4.21}$$

By replacing n with n-1, expression (4.21) can also be written as

$$\Delta\omega(n-1)=\frac{4}{N_w^2T_s}\Big[\psi_1(n-1)+\psi_1(n-2)+\cdots+\psi_1(n-N_w/2) \\ -\{\psi_1(n-N_w/2-1)+\psi_1(n-N_w/2-2)+\cdots+\psi_1(n-N_w)\}\Big] \tag{4.22}$$

After subtracting (4.22) from (4.21), the following recursive expression is obtained.

$$\Delta\omega(n)=\Delta\omega(n-1)+\frac{4}{N_w^2T_s}\Big[\psi_1(n)-2\psi_1(n-N_w/2)+\psi_1(n-N_w)\Big] \tag{4.23}$$

The recursive expression, as given by (4.23), can be used to estimate the time-varying fundamental frequency from the instantaneous phase angle over a window size equal to T_w. However, irrespective of the size of the window, only three samples of instantaneous phase angle are used for frequency estimation using (4.23) and hence the computational burden is constant. The transfer function of (4.23) in z-domain can be expressed by

$$T_2(z)=\frac{\Delta\omega(z)}{\psi_1(z)}=\frac{4}{N_w^2T_s}\left[\frac{1-2z^{-N_w/2}+z^{-N_w}}{1-z^{-1}}\right] \tag{4.24}$$

The magnitude responses of $T_2(z)$ for different window size are shown in Fig. 4.4. As it can be seen, $T_2(z)$ behaves like a DF with high frequency disturbance rejection capability. The even harmonics can be rejected from the estimated frequency when the window size is one fundamental time period. On the other hand, odd and even harmonics including the fundamental oscillations can be removed from the estimated frequency when the window size is two fundamental time periods. The proposed recursive DF can reject the oscillations at integer multiples of frequency of $2/T_w$. The high frequency disturbance rejection capability is also improved when the window size is increased. However, if the window

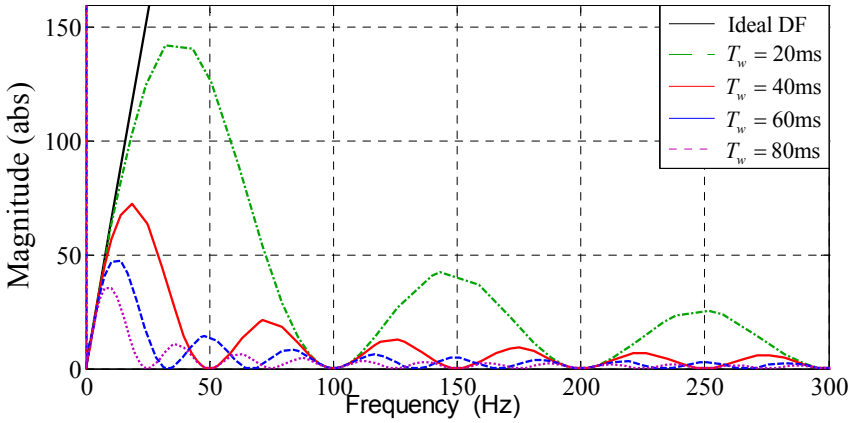

Fig. 4.4 Magnitude responses of the transfer function $T_2(z)$ for different values of T_w.

size is fixed and the frequency is time-varying, the estimated frequency may contain ripple under harmonics. Therefore, a low-pass filter (LPF) can be cascaded with the fixed size window based recursive DF for better attenuation of the ripple from the estimated time-varying fundamental frequency at the expense of a slower dynamic response. A computationally efficient IIR LPF can be used for this purpose.

The implementation of the NTA-DF technique is shown in Fig. 4.5. As it can be seen, a second-order IIR BPF, NTA, DF and second-order IIR LPF are cascaded in series to estimate the fundamental frequency. Expressions (4.14), (4.17) and (4.18) are implemented in the NTA block, as shown Fig. 4.5. In contrast with the NTA-DF, the NTA and least-squares (LS) based (NTA-LS) technique presented in [119] uses a sixth-order IIR BPF to reject harmonics from the input grid voltage waveform. The NTA is then used to obtain the DC offset, fundamental voltage amplitude and phase angle, where J_{NTA} is a 3×3 matrix and ΔX_n is obtained by matrix multiplication and inversion operations. A moving window based LS principle is applied to estimate the frequency from the phase angle. The computational burden of the LS is increased with the increasing size of the window and vice versa. When compared with the NTA-LS technique [119], the proposed NTA reduces matrix dimensions and avoids matrix inversion operation. The DF also requires less computational effort as compared to the LS. Therefore, based on a same sampling frequency, the NTA-DF technique is computationally efficient for real-time implementation when compared with the NTA-LS one.

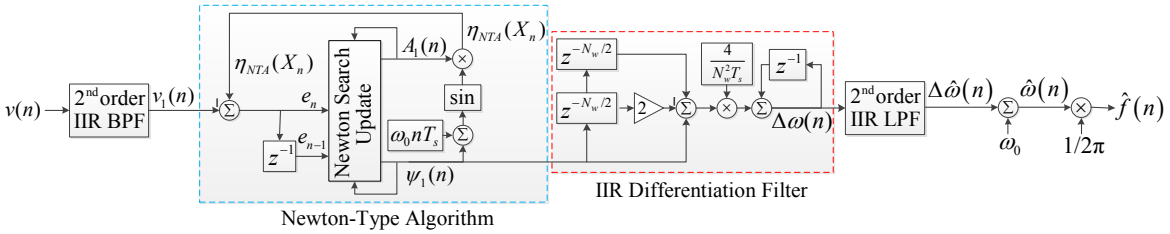

Fig. 4.5 Proposed NTA-DF technique to estimate the single-phase grid voltage fundamental frequency.

4.2 Simulation Results

The simulation performance of the proposed NTA-DF technique is reported in this section. The sampling frequency is chosen as 1.6 kHz, since the minimum sampling frequency, to capture the microscopic features of the load signature for nonintrusive load

monitoring in smart meters, can be used as 1.2-2.0 kHz [35, 37]. The window size of the recursive DF and cut-off frequency of the second-order IIR LPF are chosen as 40 ms and 15 Hz, respectively. For evaluating the performance of the NTA-DF technique, the fundamental component of the grid voltage is distorted by harmonics, as given in Table 3.1 of Chapter 3. The estimation of the fundamental frequency steps ±7.5 Hz using the NTA-DF technique is shown in Fig. 4.6, where the grid voltage waveform contains 1.0 p.u. fundamental voltage amplitude, harmonics, as given in Table 3.1, and the frequency variation range is considered based on the IEC standard 61000-4-30 [85]. As it can be observed from Fig. 4.6, the settling time of the NTA-DF technique is around 3.5 fundamental cycles and is lower than 0.2 s, which is the maximum phasor estimation time specified by the IEC standard 61000-4-7 [254].

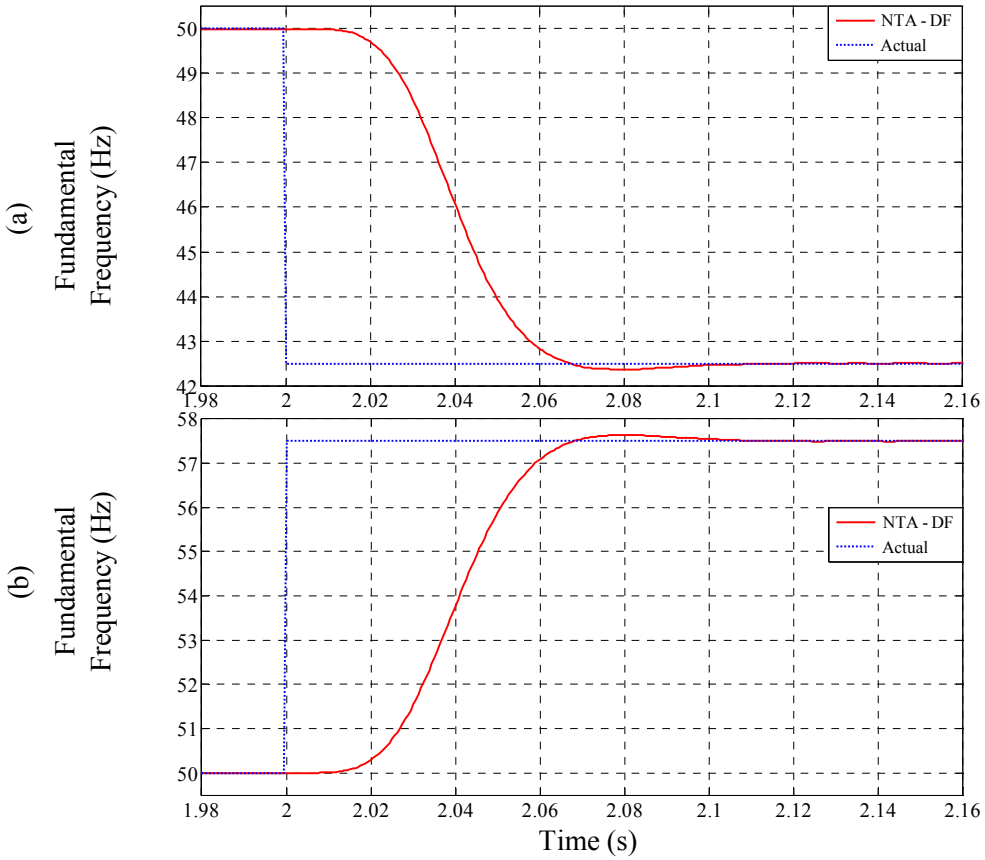

Fig. 4.6 Frequency step estimation under harmonics, as given in Table 3.1. (a) -7.5 Hz (50 Hz to 42.5 Hz). (b) +7.5 Hz (50 Hz to 57.5 Hz).

The steady-state error of the estimated fundamental frequency using the NTA-DF technique is shown in Fig. 4.7, where the grid voltage contains 1.0 p.u. fundamental amplitude, harmonics, as given in Table 3.1, and the fundamental frequency is varied from

42.5 Hz to 57.5 Hz. As it can be noticed, the NTA-DF technique can provide accurate estimation of nominal fundamental frequency. It can also be noticed that the estimation error increases as the deviation of fundamental frequency from its nominal value increases. However, the relative error of the estimated fundamental frequency range of 42.5 Hz to 57.5 Hz under 14.58% THD, as given in Table 3.1, remains inside the acceptable range (less than 0.03%) specified by the IEC standard 61000-4-7, where the relative error can be defined by (3.25).

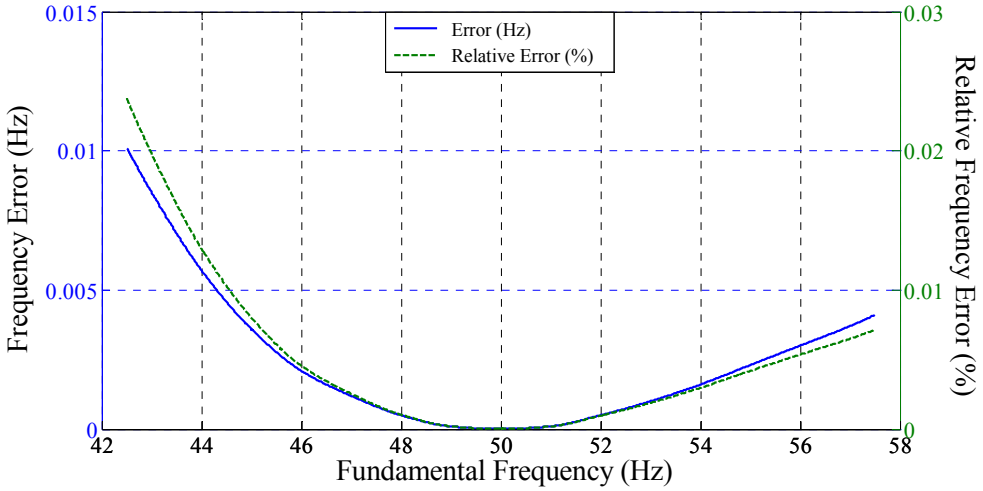

Fig. 4.7 Steady-state frequency estimation error under harmonics, as given in Table 3.1.

4.3 Real-Time Experimental Results

The experimental performance of the proposed NTA-DF technique is compared with the NTA-LS one [119]. The experimental setup is presented in Section 1.3 of Chapter 1. The parameters of the NTA-DF and the NTA-LS techniques are given in Table 4.1. The settling time of the NTA-LS technique is around 13 fundamental cycles as reported in [119], however, is tuned to provide similar dynamics when compared with the NTA-DF one.

Table 4.1 Parameters of the NTA-DF and NTA-LS techniques

NTA-DF	NTA-LS
IIR BPF: f_c =50 Hz and order=2. DF: T_w =40 ms. IIR LPF: order=2 and cut-off frequency=15 Hz. T_s=1/1600 s.	IIR BPF: f_c =50 Hz, order = 6 and bandwidth = 20 Hz. LS: T_w = 40 ms. T_s=1/1600 s.

The performance of the NTA-DF and NTA-LS techniques is documented under following real-time case studies:

i. Steady-state with DC offset and harmonics (Case-1)
ii. Frequency step and harmonics (Case-2)
iii. Frequency sweep and harmonics (Case-3)
iv. Voltage sag and harmonics (Case-4)
v. Voltage flicker and harmonics (Case-5)
vi. Phase jump and harmonics (Case-6)
vii. Notches, spikes and harmonics (Case-7)

The fundamental component of the grid voltage waveforms presented in all the above case studies is distorted by harmonics, as given in Table 3.1.

4.3.1 Case-1: Steady-State with DC Offset and Harmonics

A steady-state grid voltage is distorted by 5% DC offset and harmonics, as given in Table 3.1. The grid voltage waveform and the estimation of the fundamental frequency using the NTA-DF and NTA-LS techniques are shown in Fig. 4.8(a) and (b), respectively. As it can be seen, both NTA-DF and NTA-LS techniques can provide accurate estimation of fundamental frequency in steady-state operation with DC offset and harmonics.

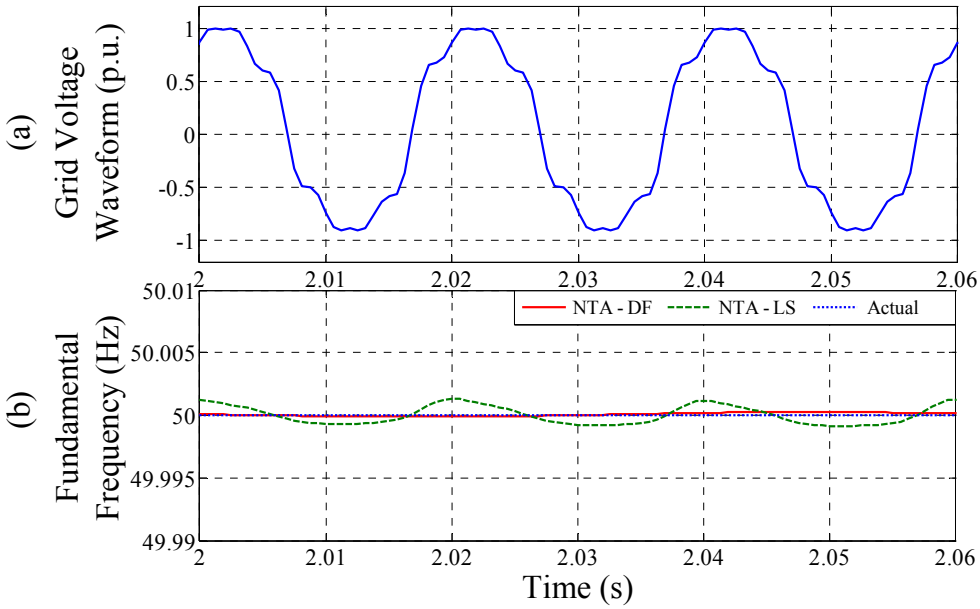

Fig. 4.8 Case-1: Steady-state with DC offset (5%) and harmonics. (a) Grid voltage waveform. (b) Fundamental frequency.

4.3.2 Case-2: Frequency Step and Harmonics

In this case, the performance of the NTA-DF and NTA-LS techniques is compared under frequency step. A frequency step of -7.5 Hz (50 Hz to 42.5 Hz) is considered into a grid voltage waveform distorted by harmonics, as given in Table 3.1. Fig. 4.9 shows the estimation of the fundamental frequency step using the NTA-DF and NTA-LS techniques. As it can be noticed, the NTA-DF technique takes around 3.5 fundamental cycles settling time for tracking the frequency step and is similar to the simulation result presented in Table 4.1. Moreover, the NTA-DF technique generates less ripple in the estimation of fundamental frequency of 42.5 Hz when compared with the NTA-LS one, as can be seen from the magnified plot in Fig. 4.9. The steady-state relative error of the estimated fundamental frequency of 42.5 Hz obtained using the NTA-DF and NTA-LS techniques are 0.024% and 0.105%, respectively. As it can be seen, the NTA-DF technique meets the relative error criteria specified by the IEC standard 61000-4-7.

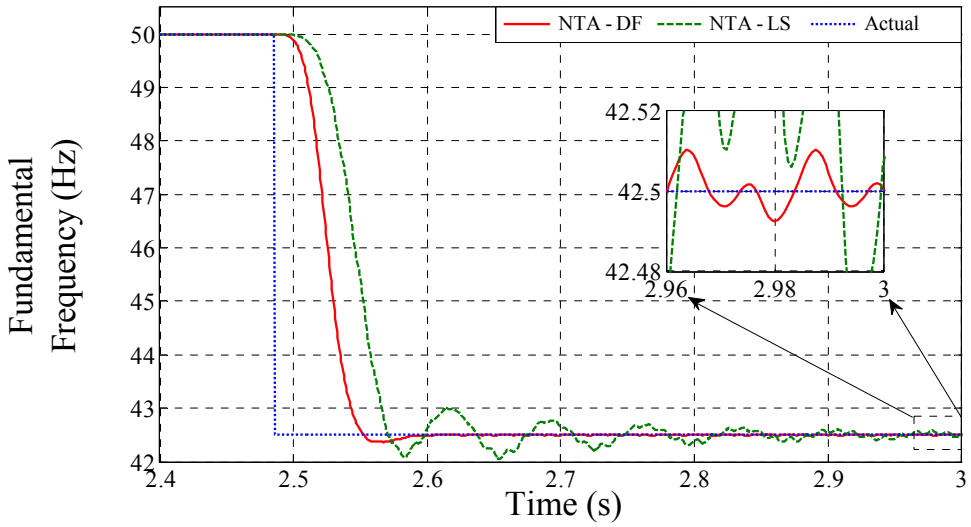

Fig. 4.9 Case-2: Frequency step (-7.5 Hz: 50 Hz to 42.5 Hz) and harmonics.

4.3.3 Case-3: Frequency Sweep and Harmonics

For this case, the grid voltage contains frequency sweep and harmonics, as given in Table 3.1. A frequency sweep of +10 Hz/s up to 55 Hz is considered. The estimation of frequency sweep using the NTA-DF and NTA-LS techniques is shown in Fig. 4.10. As it can be noticed, both techniques can track the frequency sweep. However, it can be seen from the magnified plot in Fig. 4.10 that the NTA-DF technique shows less sensitivity to the presence of harmonics at steady-state for the estimation of 55 Hz as compared to the

NTA-LS technique. The steady-state relative error of the estimated fundamental frequency of 55 Hz obtained using the NTA-DF and NTA-LS techniques are 0.005% and 0.033%, respectively. As it can be observed, the NTA-DF technique can estimate the fundamental frequency of 55 Hz with a relative error less than 0.03%.

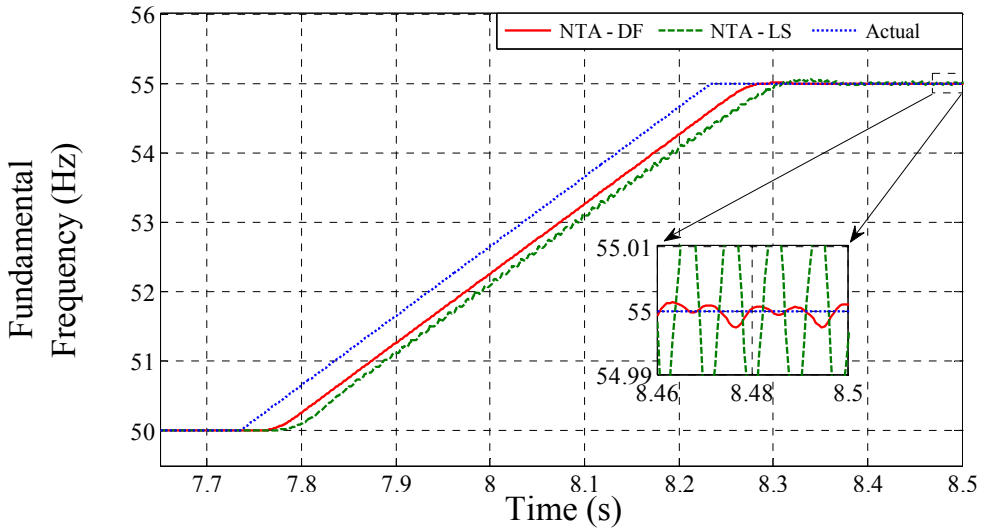

Fig. 4.10 Case-3: Frequency sweep (+10 Hz/s: 50 Hz to 55 Hz) and harmonics.

4.3.4 Case-4: Voltage Sag and Harmonics

A grid voltage sag of 50% and harmonics, as given in Table 3.1, is shown in Fig. 4.11(a). The performance of the NTA-DF and NTA-LS techniques for the estimation of fundamental frequency during voltage sag is shown in Fig. 4.11(b). As it can be noticed, the performance of both techniques for fundamental frequency estimation is affected by voltage sag. However, the NTA-DF technique presents less undershoot/overshoot and converges more quickly to the actual value during voltage sag when compared with the NTA-LS technique, as can be noticed from Fig. 4.11(b).

4.3.5 Case-5: Voltage Flicker and Harmonics

In this case, the grid voltage is distorted by 2.5 Hz, ±0.10 p.u. triangular voltage flicker and harmonics, as given in Table 3.1. The distorted grid voltage waveform is shown in Fig. 4.12(a). The estimation of the fundamental frequency using the NTA-DF and NTA-LS techniques under voltage flicker and harmonics is presented in Fig. 4.12(b). As it can be observed, the performance of both techniques is slightly affected by voltage flicker.

However, the performance of the proposed NTA-DF technique is less affected as compared to the NTA-LS one.

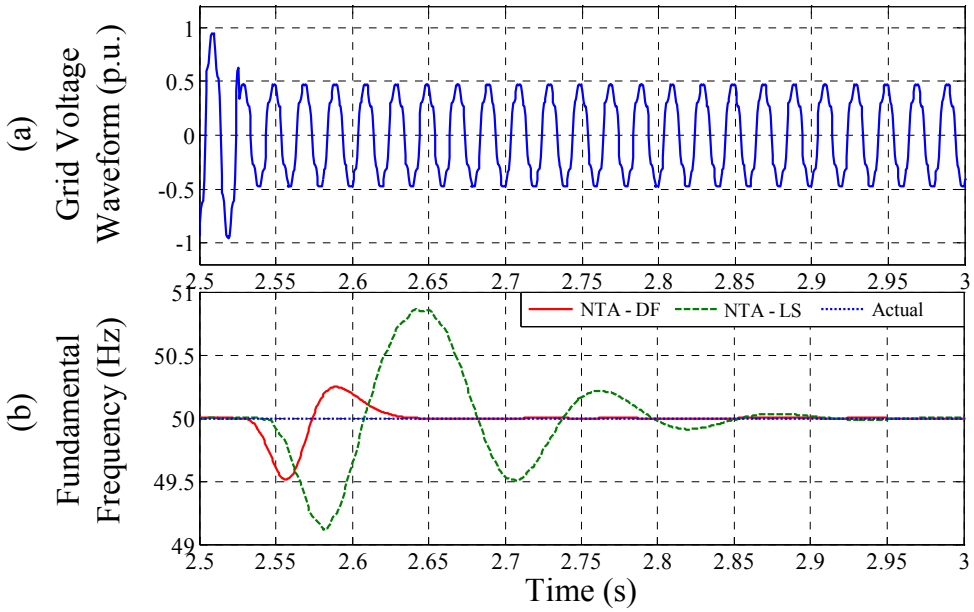

Fig. 4.11 Case-4: Voltage sag (50%) and harmonics. (a) Grid voltage waveform. (b) Fundamental frequency.

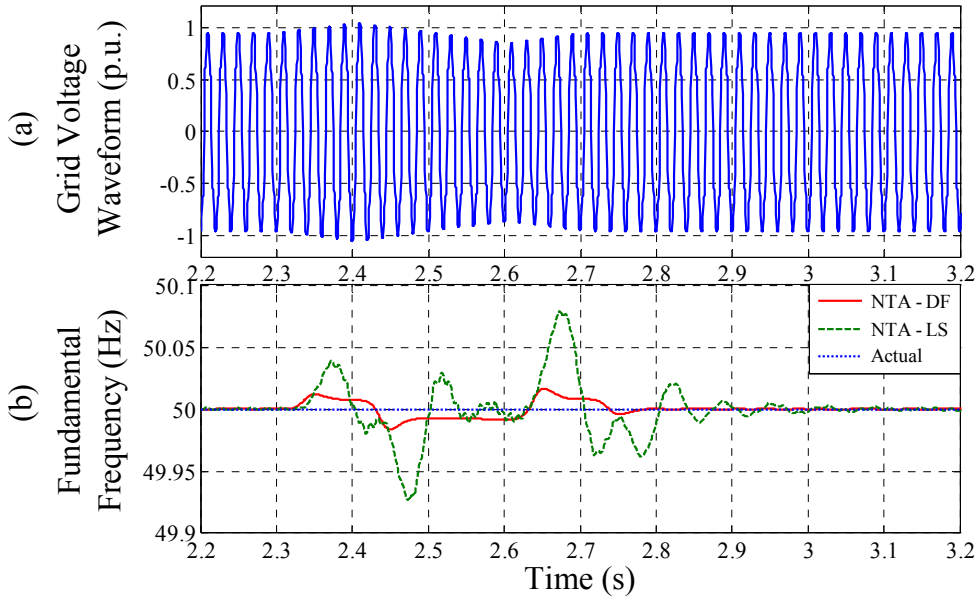

Fig. 4.12 Case-5: Voltage flicker (±10%) and harmonics. (a) Grid voltage waveform. (b) Fundamental frequency.

4.3.6 Case-6: Phase Jump and Harmonics

The grid voltage waveform, as shown in Fig. 4.13(a), contains a -30° phase jump and harmonics, as given in Table 3.1. For this case, the estimation of the fundamental frequency is shown in Fig. 4.13(b). As it can be observed, the performance of both the NTA-DF and NTA-LS techniques is affected by phase jump.

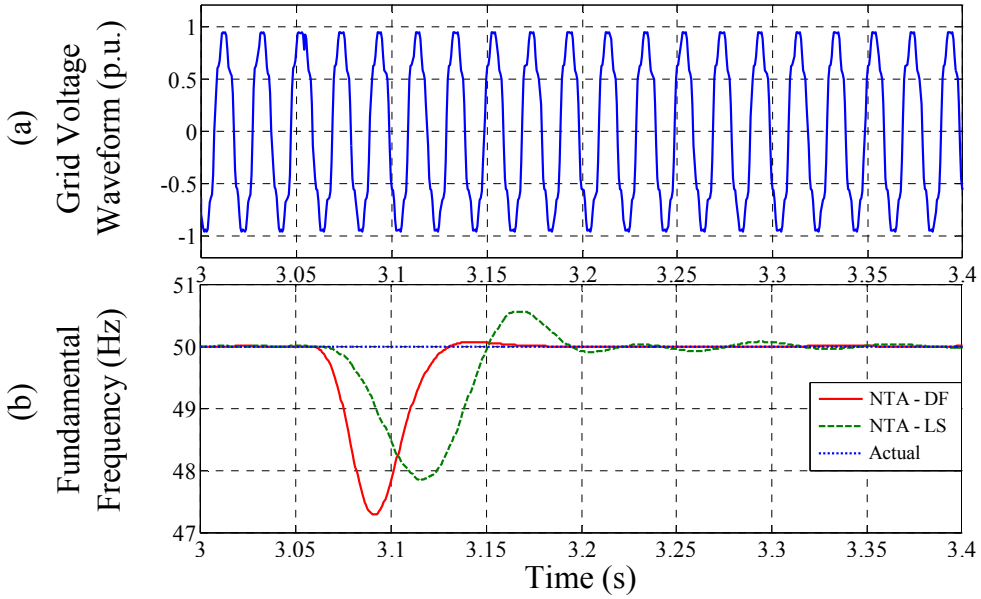

Fig. 4.13 Case-6: Phase jump (-30°) and harmonics. (a) Grid voltage waveform. (b) Fundamental frequency.

4.3.7 Case-7: Notches, Spikes and Harmonics

The grid voltage waveform, as shown in Fig. 4.14(a), contains notches, spikes and harmonics, as given in Table 3.1. The fundamental frequency estimation using the NTA-DF and NTA-LS techniques is shown in Fig. 4.14(b). As it can be noticed, both techniques can provide accurate estimation of frequency during voltage notches and spikes.

4.3.8 Computational Time

In the DS1103 control board platform, the NTA-DF and NTA-LS techniques take 2.55 μs and 3.45 μs turnaround time, respectively, for providing the real-time frequency estimation. Thus, the proposed NTA-DF technique takes 26.10% less time when compared with the NTA-LS one.

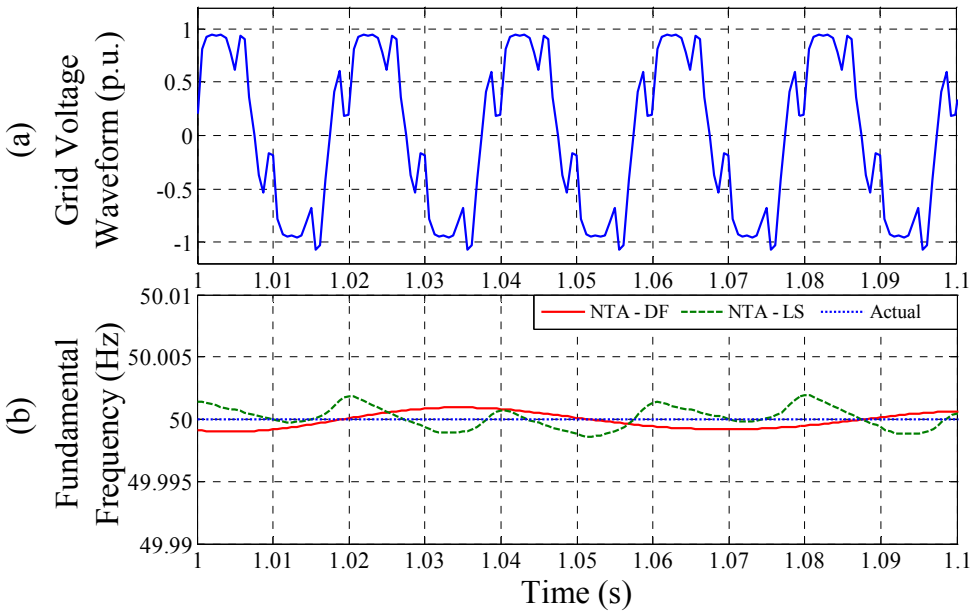

Fig. 4.14 Case-7: Notches, spikes and harmonics. (a) Grid voltage waveform. (b) Fundamental frequency.

4.4 Conclusions

A single-phase grid voltage fundamental frequency estimation technique has been reported in this chapter. The technique relies on a Newton-type algorithm and an infinite-impulse-response differentiation filter. The proposed technique reduces matrix dimensions, avoids matrix inversion operation, is computationally efficient and also shows less sensitivity to the presence of harmonics when compared with the Newton-type algorithm and least-squares based technique. The technique can reject the negative effects caused by the presence of the DC offset and harmonics. It can also provide the estimation of a wide range of frequency variation and also meets the estimation error criteria specified by the standard. The presented experimental results have confirmed the effectiveness of the proposed technique for real-time fundamental frequency estimation.

Chapter 5
Modulation and/or Demodulation Based Techniques

This chapter presents three techniques based on modulation and/or demodulation to estimate the single-phase grid voltage fundamental frequency and/or amplitude. A fundamental frequency estimation technique relying on a voltage modulation and an algorithm based on three consecutive samples is presented in Section 5.1. Section 5.2 describes a demodulation and a differentiation filter based technique for the estimation of fundamental frequency. A modified demodulation based technique to estimate the fundamental voltage amplitude and frequency is described in Section 5.3. Selected simulation and/or experimental results are presented after the description of each technique. Finally, the conclusions are presented in Section 5.4.

5.1 Power System Frequency Estimation using A Voltage Modulation and Three Consecutive Samples Based Technique

A technique based on three consecutive samples (3CS) of a modulated voltage waveform is described in this section to estimate the single-phase grid voltage fundamental frequency under distorted grid conditions. The block diagram of the proposed fundamental frequency estimation technique is shown in Fig. 5.1, where v is the grid voltage, n is the sampling instant, v^m is the modulated grid voltage and $\hat{f}$ is the estimated fundamental frequency. As it can be seen, the grid voltage waveform is modulated by using a modulating function (MF) strategy for rejecting the negative effects caused by DC offset and harmonics. The 3CS of the modulated voltage waveform is then used to estimate the fundamental frequency.

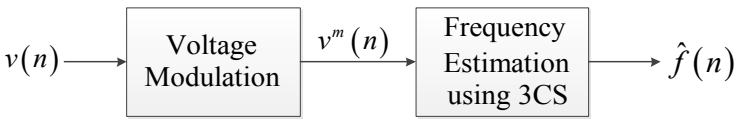

Fig. 5.1 Block diagram of the proposed 3CS based frequency estimation technique.

5.1.1 3CS Based Frequency Estimation

For simplicity, the single-phase grid voltage waveform can be expressed by

$$v(n) = v_0(n) + v_1(n) \tag{5.1}$$

where v_0 is the DC offset, v_1 is the fundamental voltage component and is expressed by

$$v_1(n) = A_1(n)\sin\left\{\omega(n)nT_s + \theta_1(n)\right\}$$

where A_1 is the fundamental voltage amplitude, $\omega=2\pi f$ is the fundamental angular frequency, f is the fundamental frequency, T_s is the sampling period and θ_1 is the initial phase angle.

The following relation can be obtained from (5.1) when the DC offset is zero ($v_0=0$) and the parameters are constant within the 3CS of the fundamental voltage component [78, 127, 236, 237].

$$v(n) + v(n-2) = 2v(n-1)\cos(2\pi fT_s)$$

$$\Rightarrow c(n) = d(n)r \tag{5.2}$$

where

$$c(n) = v(n) + v(n-2)$$

$$d(n) = 2v(n-1)$$

$$r = \cos(2\pi fT_s)$$

The above relation based on the 3CS of the grid voltage fundamental component can be used to estimate the value of r and f [78, 127, 236, 237]. However, the relation (5.2) is not true when the grid voltage fundamental component contains nonzero DC offset (i.e. $v_0\neq0$). Nevertheless, the following relation is always true whether the grid voltage fundamental component contains zero or nonzero DC offset.

$$c^{(1)}(n) = d^{(1)}(n)r \tag{5.3}$$

where

$$c^{(1)}(n) = v^{(1)}(n) + v^{(1)}(n-2)$$

$$d^{(1)}(n) = 2v^{(1)}(n-1)$$

and superscript '1' indicates first-order derivative with respect to time. Equation (5.3) can be used to estimate the value of r and f from the grid voltage fundamental component with/without DC offset. However, the estimation of f using (5.3) is sensitive to the change of the fundamental parameters within the 3CS of the grid voltage [78, 127, 236, 237]. Equation (5.3) is also ill-conditioned when $v^{(1)}(n\text{-}1)=0$. Moreover, the estimation of frequency using (5.3) is not suitable for the grid voltage containing disturbances such as harmonics and noise [78, 127, 236, 237]. Additionally, the differentiation operation increases the negative effects caused by the presence of high frequency disturbances. The above shortcomings of the 3CS based fundamental frequency estimation technique can be rejected by using an integration based MF strategy [246, 248].

5.1.2 Proposed 3CS Based Frequency Estimation Technique

The MF can be denoted by $\varphi(t)$, where t indicates time in continuous domain. The MF can be differentiated S times $\{\varphi_S(t)\}$. The ℓ^{th} derivative of the MF over a finite time interval $[0, T_w]$ satisfies the following condition.

$$\varphi_S^{(\ell)}(0) = \varphi_S^{(\ell)}(T_w) = 0 \tag{5.4}$$

where $\ell=0,1,2,\ldots,S\text{-}1$ and T_w is the size of the window. The continuous time grid voltage, as denoted by $v(t)$, can be modulated by taking the inner product with the MF. The modulated grid voltage over the time window (T_w) can be expressed by

$$\langle v, \varphi_S \rangle = \int_0^{T_w} v(t)\varphi_S(t)\,dt \tag{5.5}$$

The modulation relation, as given by (5.5), also holds for the ℓ^{th} derivative of the grid voltage $\{v^{(\ell)}(t)\}$ and can be expressed by [246, 248]

$$\langle v^{(\ell)}, \varphi_S \rangle = \int_0^{T_w} v^{(\ell)}(t)\varphi_S(t)\,dt \tag{5.6}$$

The above integration based MF strategy can reject the negative effects caused by the high frequency disturbances present in the grid voltage. The high frequency disturbance rejection capability is also improved when the window size is increased. After the modulation, the boundary conditions of the grid voltage are set by the terminal conditions

of the MF, which make it possible to transfer the differentiation operation from the grid voltage on to the MF. The interchange of differentiation operation between the grid voltage and the MF can be expressed by

$$\left\langle v^{(\ell)}, \varphi_S \right\rangle = (-1)^{\ell} \left\langle v, \varphi_S^{(\ell)} \right\rangle \tag{5.7}$$

The interchange of the differentiation operation from the grid voltage on to the MF, as given by (5.7), helps to eliminate the requirement of differentiating the grid voltage distorted by high frequency disturbances.

In continuous time domain, equation (5.3) can be expressed as

$$c^{(1)}(t) = rd^{(1)}(t) \tag{5.8}$$

Therefore, based on (5.6), equation (5.8) can be modulated and is expressed by

$$\int_0^{T_w} c^{(1)}(t)\varphi_S(t)\,dt = r\int_0^{T_w} d^{(1)}(t)\varphi_S(t)\,dt \tag{5.9}$$

Based on (5.7), equation (5.9) can also be expressed by

$$\int_0^{T_w} c(t)\varphi_S^{(1)}(t)\,dt = r\int_0^{T_w} d(t)\varphi_S^{(1)}(t)\,dt \tag{5.10}$$

For implementing on a digital signal processor, the continuous time domain integration based MF strategy, as given by (5.10), can be expressed in discrete domain, where t can be discretised by $t = nT_s$. Therefore, the simplified discrete form of (5.10) can be written as

$$\sum_{l=0}^{N_w-1} c(n+l)\varphi_S^{(1)}(l) = r\sum_{l=0}^{N_w-1} c(n+l)\varphi_S^{(1)}(l)$$

$$\Rightarrow C(n) = rD(n) \tag{5.11}$$

where

$$C(n) = \sum_{l=0}^{N_w-1} c(n+l)\varphi_S^{(1)}(l)$$

$$D(n) = \sum_{l=0}^{N_w-1} d(n+l)\varphi_S^{(1)}(l)$$

and $N_w=T_w/T_s$ is the number of samples in the integration window of time duration T_w. It can be seen form (5.11) that a first-order time derivative $(\ell = 1)$ of the MF is required and hence the value of S has to satisfy the condition $S\geq 2$.

The value of r and f can be obtained from (5.11), which can reject the negative effects caused by the DC offset and harmonics present in the grid voltage. However, equation (5.11) is ill-conditioned to estimate the frequency when the instantaneous value of $D(n)$ is zero [78, 127, 236, 237]. To avoid this shortcoming of (5.11), a recursive algorithm can be used and is presented below [246].

The value of r at the n sampling instant (r_n) can be obtained by minimizing an index function Γ_n given by

$$\Gamma_n = \frac{1}{2}\sum_{a=0}^{n} \rho^{n-a} \left\{C(a) - r_n D(a)\right\}^2 \tag{5.12}$$

where ρ is a constant parameter in the interval [0,1]. The parameter ρ represents a forgetting factor to exponentially discard the old data in the recursive scheme, which means that the most recent measurements have a higher weight as compared to that of the old measurements. The low value of ρ increases the dynamic capability of the technique to track the time-varying fundamental frequency [246]. The value of r_n which minimizes J_n can be obtained from the following condition

$$\frac{d}{dr_n}\Gamma_n = 0 \tag{5.13}$$

The differentiation of the index function Γ_n with respect to r_n can be expressed by

$$\frac{d}{dr_n}\Gamma_n = \sum_{a=0}^{n} \rho^{n-a} \left\{C(a) - r_n D(a)\right\} D(a) \tag{5.14}$$

Based on the condition (5.13), the value of r_n can be obtained from (5.14) and is given by

$$r_n = \frac{\sum_{a=0}^{n} \rho^{n-a} C(a) D(a)}{\sum_{a=0}^{n} \rho^{n-a} \left\{D(a)\right\}^2} \tag{5.15}$$

Equation (5.15) can also be represented as a recursive form and is given by

$$r_n = \frac{\rho\lambda_{n-1} r_{n-1} + C(n) D(n)}{\lambda_n} \tag{5.16}$$

where

$$\lambda_n = \sum_{a=0}^{n} \rho^{n-a} \left\{ D(a) \right\}^2 = \rho \lambda_{n-1} + \left\{ D(n) \right\}^2$$

The grid voltage fundamental frequency at the n sampling instant can be estimated by

$$\hat{f}(n) = \frac{\cos^{-1}(r_n)}{2\pi T_s} \tag{5.17}$$

Equation (5.17) can be used to estimate the time-varying fundamental frequency from a non-periodic single-phase grid voltage distorted by DC offset and harmonics. The implementation of (5.17) is shown in Fig. 5.2. As it can be noticed, $C(n)$ and $D(n)$ are the outputs of two discrete-time finite-impulse-response (FIR) filters, where the inputs of the filters are $c(n)$ and $d(n)$, respectively. The coefficients of the FIR filters are the same and determined by the MF $\varphi_S^{(1)}(l)$, where l=0,1,2,…,N_w-1 and S≥2. As the coefficients of the FIR filters are the same, and $c(n)$ and $d(n)$ are also linearly related with the grid voltage samples $v(n)$, hence only one FIR filter can be used to filter $v(n)$ instead of filtering $c(n)$ and $d(n)$ separately. Therefore, the simplified form of the proposed 3CS based frequency estimation technique is presented in Fig. 5.3.

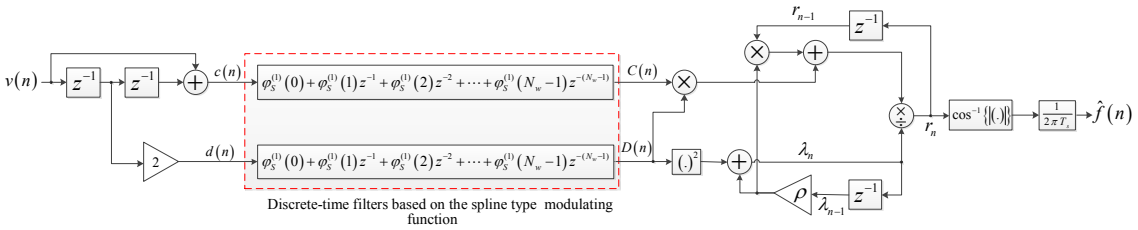

Fig. 5.2 Proposed 3CS based technique for the estimation of single-phase grid voltage fundamental frequency.

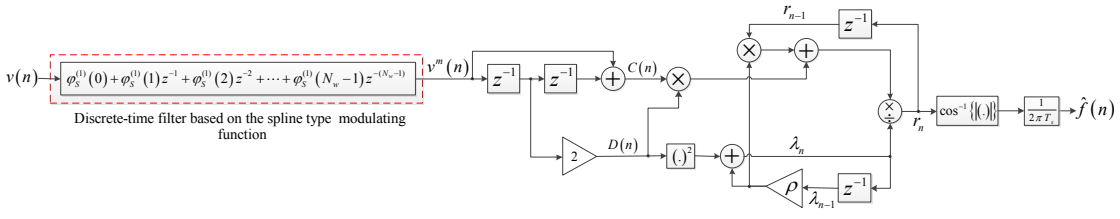

Fig. 5.3 Simplified form of the proposed 3CS based technique, as shown in Fig. 5.2, for the estimation of single-phase grid voltage fundamental frequency.

The coefficients of the FIR filter are obtained from a spline type MF. The ℓ^{th} derivative of the spline function with maximum derivative order S and characteristics time $T_c=T_w/S$ can be expressed by [246]

$$\varphi_S^{(\ell)}(l)=\begin{cases}\sum_{b=0}^{S}(-1)^b\binom{S}{b}g_{b\ell}\left(lT_s-bT_c\right) & \text{for } \ell=0,1,...,S\text{-}1\\ \sum_{b=0}^{S}(-1)^b\binom{S}{b}\delta\left(lT_s-bT_c\right) & \text{for } \ell=S\end{cases} \tag{5.18}$$

where

$$g_{b\ell}\left(lT_s-bT_c\right)=\begin{cases}\dfrac{1}{(S-\ell-1)!}\left(lT_s-bT_c\right)^{S-\ell-1} & \text{for } lT_s\ \varepsilon\ \left[bT_c,T_w\right]\\ 0 & \text{otherwise}\end{cases}$$

and $\delta(lT_s)$ is the Dirac delta function.

5.1.3 Simulation Results

The simulation performance of the proposed 3CS based technique is documented in this subsection. The parameters of the technique are given in Table 5.1. The estimations of ± 7.5 Hz fundamental frequency steps using the proposed technique are shown in Fig. 5.4, where the grid voltage contains 1.0 p.u. fundamental voltage amplitude and 10.67% total harmonic distortion (THD), as given in Table 5.2. The harmonics, as given in Table 5.2, are chosen in accordance with the European standard EN-50160 [78, 255]. As it can be noticed from Fig. 5.4, the proposed 3CS based technique takes around two fundamental cycles as settling times for tracking the -7.5 Hz and +7.5 Hz frequency steps, respectively.

The steady-state performance of the proposed technique for fundamental frequency estimation is shown in Fig. 5.5, where the grid voltage waveform contains 1.0 p.u. fundamental voltage amplitude, 10.67% THD, as given in Table 5.2, and the fundamental frequency is varied from 42.5 Hz to 57.5 Hz based on the specification of IEC standard 61000-4-30 [85]. As it can be noticed, the estimation error increases when the negative deviation of fundamental frequency increases from its nominal value. However, the estimation error decreases as the positive deviation of fundamental frequency increases from its nominal value. The relative error of the estimated fundamental frequency range of 42.5 Hz to 57.5 Hz is less than 0.03% and remains inside the acceptable range, as specified by the IEC standard 61000-4-7 [254], where the relative error can be defined by (3.25).

Table 5.1 Parameters of the proposed 3CS based technique

T_w=40ms	f_s=5.0 kHz	N_w=200	S=6	ρ = 0.96

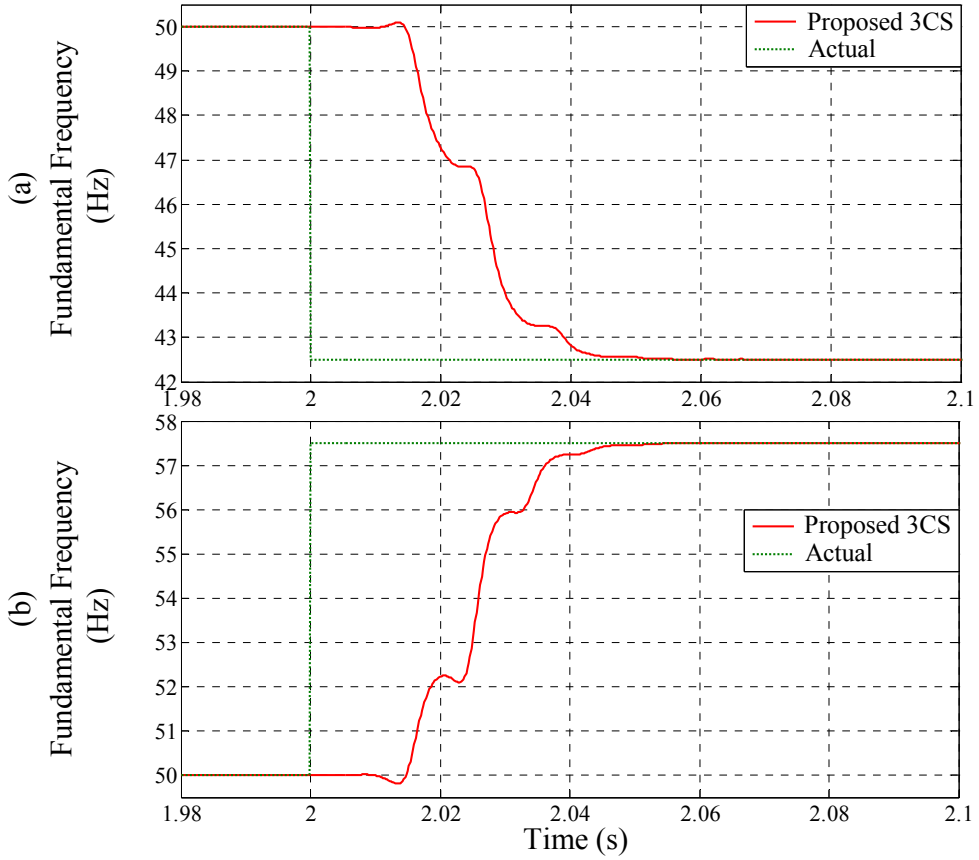

Fig. 5.4 Frequency steps estimation under harmonics, as given in Table 5.2. (a) -7.5 Hz (50 Hz to 42.5 Hz). (b) +7.5 Hz (50 Hz to 57.5 Hz).

Table 5.2 Harmonic as a percentage of fundamental component in accordance with the European standard EN-50160

Harmonics								THD
3rd	5th	7th	9th	11th	13th	15th	17th	10.67%
5.0%	6.0%	5.0%	1.5%	3.5%	3.0%	0.5%	2.0%	

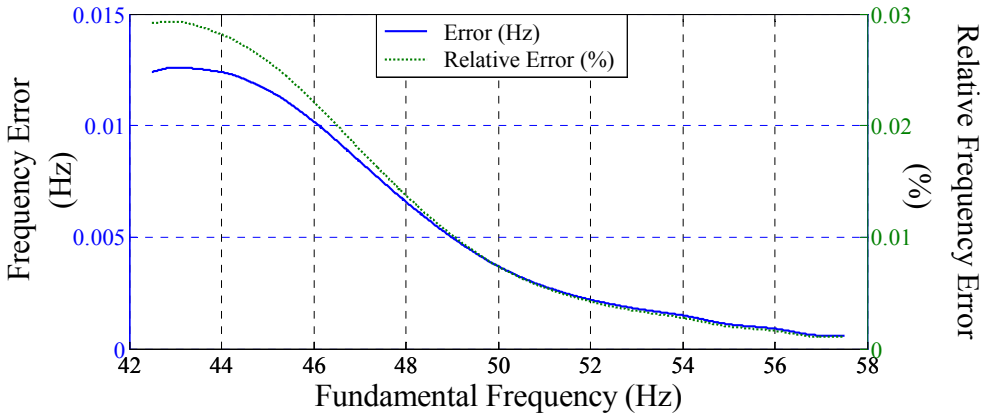

Fig. 5.5 Frequency error estimation at steady-state operation with harmonics, as given in Table 5.2.

Fig. 5.6 shows a +7.5 Hz frequency step estimation under harmonics, as given in Table 5.2, using the conventional 3CS based technique reported in [78], where a high-order FIR filter is designed at f_s=5 kHz and a threshold value of ±0.005 p.u. for the middle sample is considered for removing the ill-condition of the technique. As it can be seen, the technique presents unwanted oscillations during frequency step. However, a low-pass filter (LPF) can be used to reduce these oscillations, as can be noticed in Fig. 5.6, where the LPF-1 is an infinite-impulse response (IIR) filter of second-order and cut-off frequency of 100 Hz. A more accurate frequency estimation can be obtained by reducing the cut-off frequency of the LPF at the expense of slower dynamic response, as it can also be seen in Fig. 5.6, where the cut-off frequency of the second-order IIR LPF-2 is 40 Hz. The conventional technique with LPF-2 takes around two fundamental cycles as settling time during

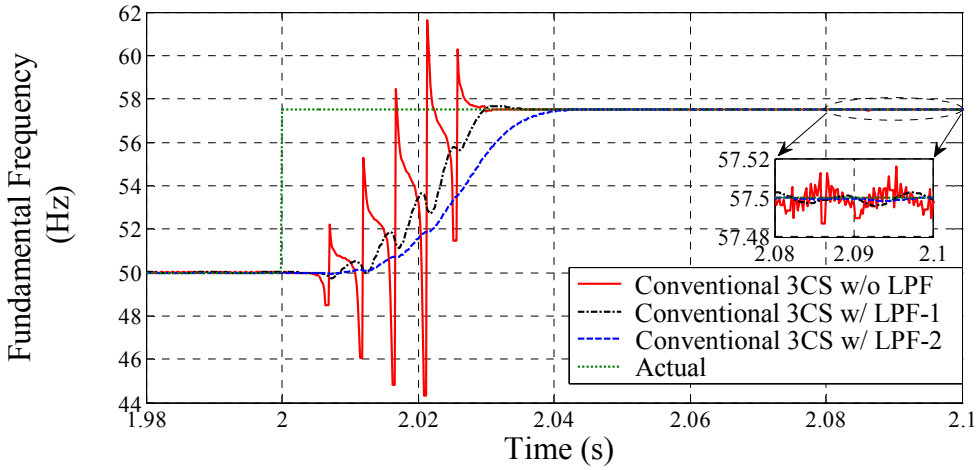

Fig. 5.6 Frequency step (+7.5 Hz: 50 Hz to 57.5 Hz) estimation under harmonics, as given in Table 5.2, using the conventional 3CS based technique.

frequency step and is used in the next section for experimental performance comparison with the proposed technique under similar frequency dynamic condition.

5.1.4 Real-Time Experimental Results

In this subsection, the performance of the proposed technique is compared with the conventional one [78] on a real-time experimental setup. The experimental setup is presented in Section 1.3 of Chapter 1. The performance of the proposed and conventional 3CS based techniques is compared under following case studies:

i. Steady-state with DC offset and harmonics (Case-A1)
ii. Frequency step and harmonics (Case-A2)
iii. Frequency sweep and harmonics (Case-A3)
iv. Voltage sag and harmonics (Case-A4)
v. Voltage flicker and harmonics (Case-A5)
vi. Phase jump and harmonics (case-A6)
vii. Notches, spikes and harmonics (case-A7)

In all the above case studies, the grid voltage fundamental component contains 10.67% THD, as given in Table 5.2.

5.1.4.1 Case-A1: Steady-State with DC Offset and Harmonics

The grid voltage waveform, as shown in Fig. 5.7(a), contains 5% DC offset and 10.67% THD, as given in Table 5.2. The fundamental frequency estimation using the proposed and conventional 3CS based techniques is shown in Fig. 5.7(b). As it can be seen, the conventional technique generates low frequency ripple in the frequency estimation due to the presence of DC offset. On the other hand, the proposed technique is less affected by DC offset and harmonics when compared with the conventional one. The relative error of the nominal fundamental frequency estimation using the proposed technique is 0.008% and is less than the acceptable error threshold specified by the standard IEC 61000-4-7.

5.1.4.2 Case-A2: Frequency Step and Harmonics

In this case, the performance of the proposed and conventional 3CS based techniques is documented for a fundamental frequency step including 10.67% THD, as given in Table 5.2. A +7.5 Hz fundamental frequency step is considered in a harmonically distorted grid

voltage waveform. The estimation of the fundamental frequency step using the proposed and conventional 3CS based techniques is depicted in Fig. 5.8. As it can be observed, both techniques provide similar dynamics. However, the proposed technique offers more accurate estimation of off-nominal frequency (57.5 Hz) at steady-state when compared with the conventional one, as it can be noticed from the magnified plot in Fig. 5.8. Similar to the simulation result presented in Fig. 5.5, the steady-state relative errors of the fundamental frequency of 50 Hz and 57.5 Hz estimation under harmonics using the proposed technique are 0.008% and 0.0019%, respectively, and are less than the error threshold set by the standard IEC 61000-4-7.

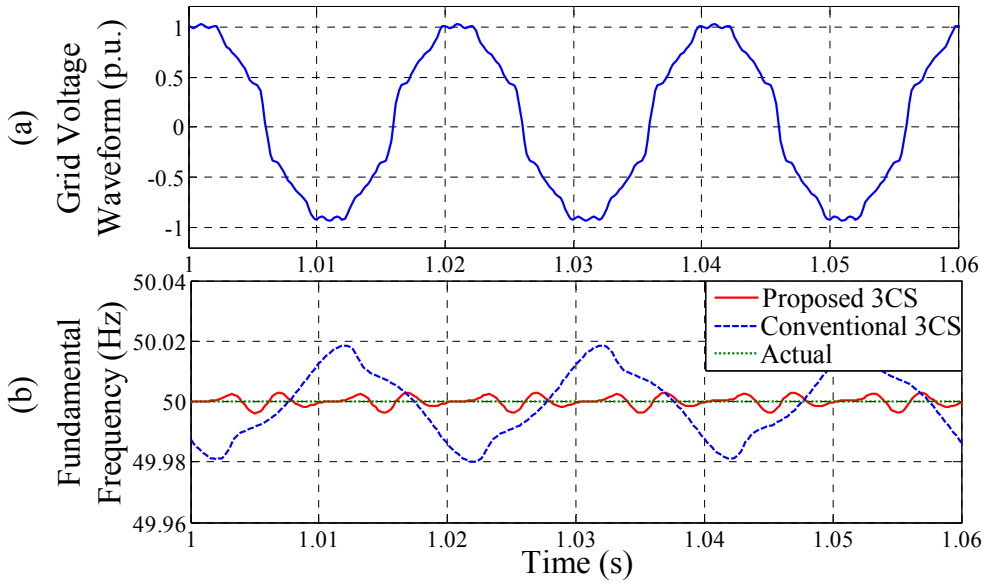

Fig. 5.7 Case-A1: steady-state with DC offset (5%) and harmonics. (a) Grid voltage waveform. (b) Fundamental Frequency.

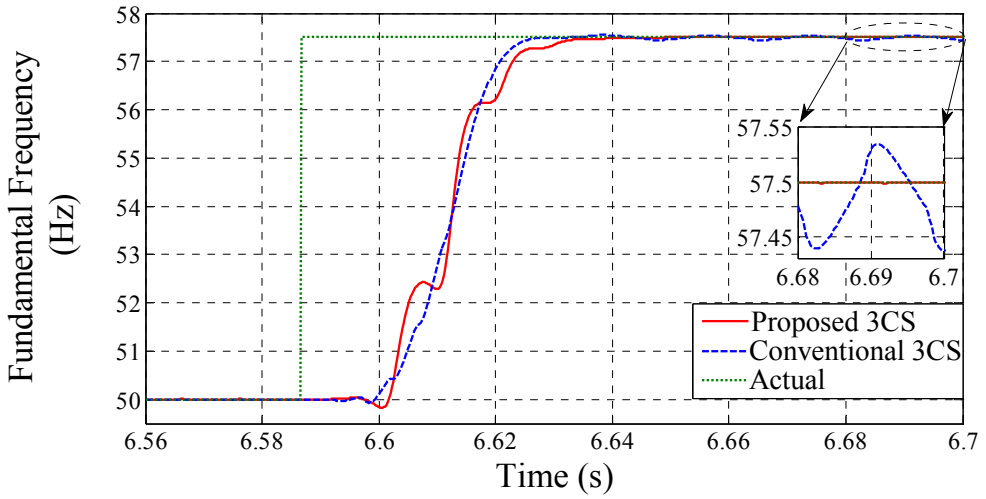

Fig. 5.8 Case-A2: frequency step (+7.5 Hz: 50 Hz to 57.5 Hz) and harmonics.

5.1.4.3 Case-A3: Frequency Sweep and Harmonics

A -10 Hz/s fundamental frequency sweep down to 42.5 Hz is considered into a grid voltage waveform distorted by harmonics, as given in Table 5.2. The estimation of the fundamental frequency sweep using the proposed and conventional 3CS based techniques is shown in Fig. 5.9. As it can be observed, both proposed and conventional techniques can track the frequency sweep under harmonics. Nevertheless, when compared with the conventional technique, the proposed one provides more accurate estimation of 42.5 Hz at steady-state, which is depicted by the magnified plot in Fig. 5.9. Similar to the simulation result presented in Fig. 5.5, the steady-state relative error of the fundamental frequency of 42.5 Hz estimation under harmonics using the proposed technique is 0.0299% and meets the error criteria specified by the standard IEC 61000-4-7.

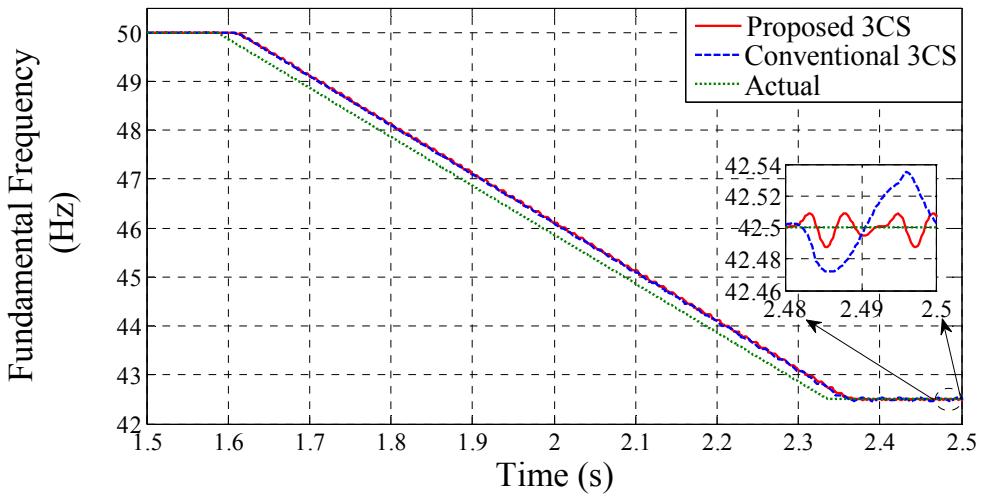

Fig. 5.9 Case-A3: frequency sweep (-10 Hz/s: 50 Hz to 42.5 Hz) and harmonics.

5.1.4.4 Case-A4: Voltage Sag and Harmonics

The performance of the proposed and conventional 3CS based techniques under a 50% voltage sag and 10.67% THD, as given in Table 5.2, is presented in Fig. 5.10(b), where the corresponding grid voltage waveform is shown in Fig. 5.10(a). As it can be seen, the conventional technique is more sensitive to the voltage sag and presents large oscillations in the estimation of fundamental frequency as compared to the proposed one.

5.1.4.5 Case-A5: Voltage Flicker and Harmonics

The performance of the proposed and conventional 3CS based techniques under voltage flicker and harmonics, as given in Table 5.2, is shown in Fig. 5.11(b). The grid voltage

waveform, as shown in Fig. 5.11(a), contains 2.5 Hz and ±0.05 p.u. triangular voltage flicker and 10.67% THD. As it can be seen, the conventional technique presents a steady-state error during the voltage flicker while the proposed one only generates some ripple.

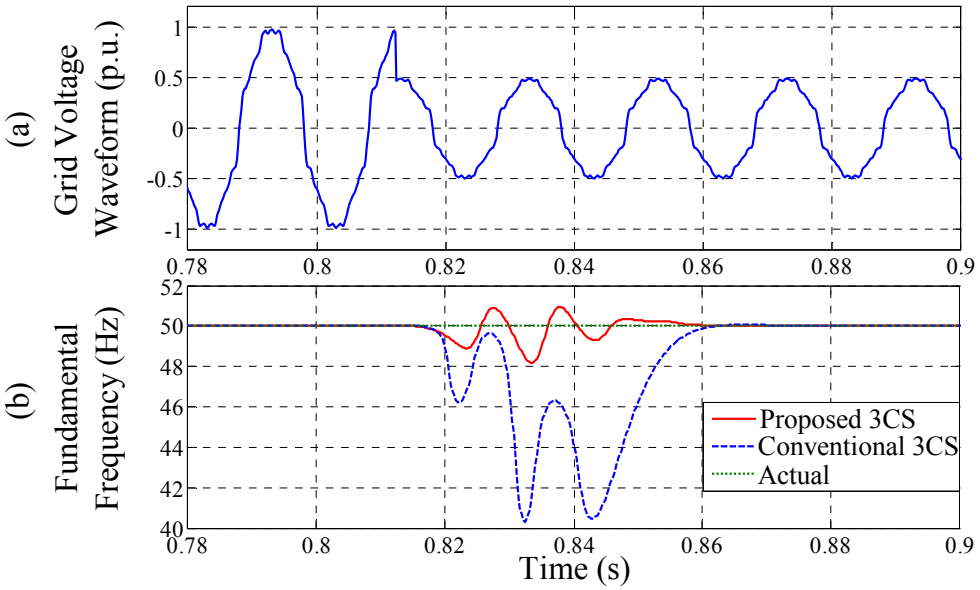

Fig. 5.10 Case-A4: voltage sag (50%) and harmonics. (a) Grid voltage waveform. (b) Fundamental Frequency.

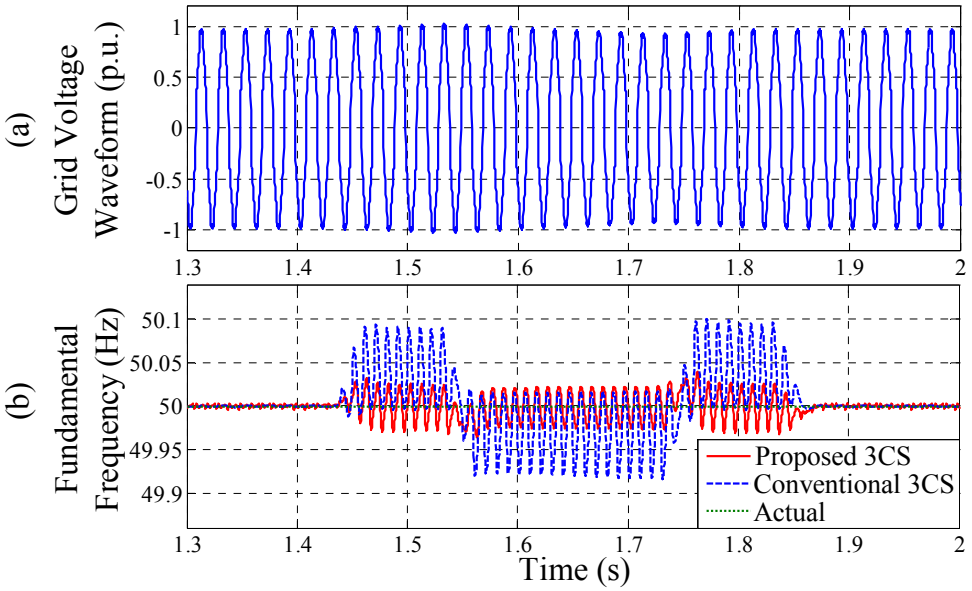

Fig. 5.11 Case-A5: voltage flicker (±5%) and harmonics. (a) Grid voltage waveform. (b) Fundamental Frequency.

5.1.4.6 Case-A6: Phase Jump and Harmonics

The grid voltage waveform, as shown in Fig. 5.12(a), contains a -30° phase jump and harmonics, as given in Table 5.2. The estimation of the fundamental frequency using both proposed and conventional 3CS based techniques is shown in Fig. 5.12(b). As it can be noticed, both proposed and conventional techniques are affected by the phase jump and present undershoot in the estimation of frequency.

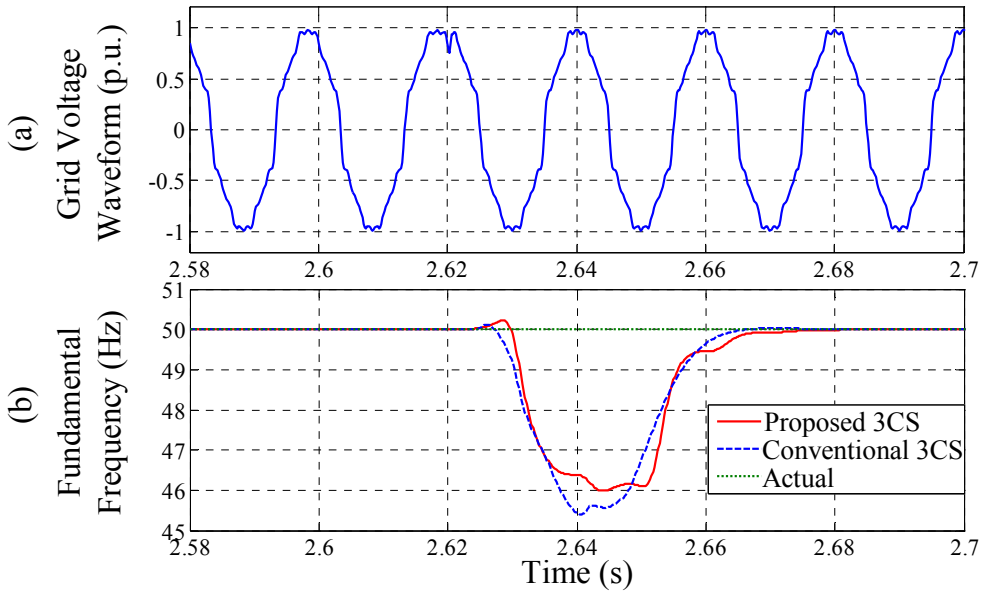

Fig. 5.12 Case-A6: phase jump (-30°) and harmonics. (a) Grid voltage waveform. (b) Fundamental Frequency.

5.1.4.7 Case-A7: Notches, Spikes and Harmonics

The grid voltage waveform, as shown in Fig. 5.13(a), contains notches, spikes and harmonics, as given in Table 5.2. For this case, the performance of the proposed and conventional techniques is shown in Fig. 5.13(b). As it can be observed, the performance of the proposed technique is not affected by the notches and spikes. On the other hand, the conventional technique provides a steady-state error in the estimation of frequency.

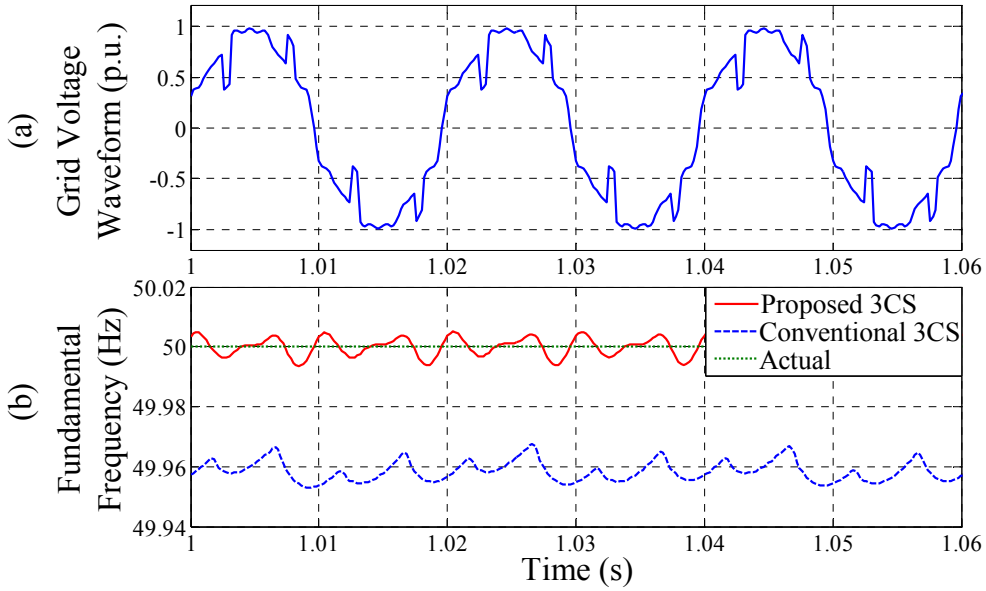

Fig. 5.13 Case-A7: notches, spikes and harmonics. (a) Grid voltage waveform. (b) Fundamental Frequency.

5.2 Power System Frequency Estimation using A Demodulation and Differentiation Filter Based Technique

In this section, a demodulation and a differentiation filter (DF) based technique is documented for estimating the single-phase grid voltage fundamental frequency under distorted grid conditions. The block diagram of the proposed fundamental frequency estimation technique is shown in Fig. 5.14, where $\psi_1(n) = \Delta\omega(n)nT_s + \theta_1(n)$ is the initial phase angle (θ_1) plus instantaneous phase angle $\{\Delta\omega(n)nT_s\}$ corresponding to fundamental angular frequency deviation $(\Delta\omega)$, $\Delta\hat{\omega}$ is the estimated fundamental angular frequency deviation, ω_0 is the nominal fundamental angular frequency and $\hat{\omega}$ is the estimated fundamental angular frequency. As it can be seen, the demodulation method is used to obtain the phase angle and is then differentiated using a FIR DF to estimate the

Fig. 5.14 Block diagram of the proposed demodulation and DF based technique for single-phase grid voltage fundamental frequency estimation.

fundamental angular frequency deviation. The estimated angular frequency deviation is added with the nominal value to obtain the actual fundamental angular frequency.

5.2.1 Instantaneous Phase Angle Estimation

The generalised expression of a single-phase grid voltage distorted DC offset and harmonics is expressed by

$$v(n) = v_0(n) + \sum_{i=1,2,..}^{M} A_i(n)\sin\left\{i\omega_0 nT_s + \psi_i(n)\right\} \tag{5.19}$$

where M is the maximum order of harmonics, and A_i and $\psi_i(n) = i\Delta\omega(n)nT_s + \theta_i(n)$ are the amplitude and initial phase angle (θ_i) plus instantaneous phase angle $\{i\Delta\omega(n)nT_s\}$ corresponding to angular frequency deviation $i\Delta\omega$ of the $i\omega$ (i=1,2,..,M) angular frequency component, respectively. The grid voltage, as expressed by (5.19), can be demodulated by the trigonometric functions $\sin(\omega_0 n\mathrm{T_s})$ and $\cos(\omega_0 n\mathrm{T_s})$, respectively, at the nominal fundamental frequency [203, 204, 212]. The demodulated grid voltage can be expressed by (5.20) and (5.21), respectively.

$$v_{1S}(n) = v(n)\sin(\omega_0 nT_s) = \frac{A_1(n)}{2}\cos\left\{\psi_1(n)\right\} + D_{1S}\left\{\omega_0, \omega_0 + 2\Delta\omega,\ 2\omega_0 + \Delta\omega, 2\omega_0 + 3\Delta\omega, ...\right\} \tag{5.20}$$

$$v_{1C}(n) = v(n)\cos(\omega_0 nT_s) = \frac{A_1(n)}{2}\sin\left\{\psi_1(n)\right\} + D_{1C}\left\{\omega_0, \omega_0 + 2\Delta\omega,\ 2\omega_0 + \Delta\omega, 2\omega_0 + 3\Delta\omega, ...\right\} \tag{5.21}$$

where D_{1S} and D_{1C} are functions of oscillations at angular frequencies $\omega_0, \omega_0 + 2\Delta\omega,\ 2\omega_0 + \Delta\omega, 2\omega_0 + 3\Delta\omega, \ldots$. Both D_{1S} and D_{1C} contain oscillation at angular frequency $2\omega_0+\Delta\omega$ with amplitude $A_1/2$ due to the demodulation of fundamental voltage component. On the other hand, the presence of the DC offset and harmonics introduce oscillations at angular frequencies ω_0 and $h(\omega_0+\Delta\omega)\pm\omega_0$ with amplitudes v_0 and $A_h/2$, respectively, where A_h is the amplitude of the h^{th} harmonic component and h=2,3,..,M. Thus, two LPFs with a cut-off frequency less than $\omega_0 + 2\Delta\omega$ $(\Delta\omega < 0)$ can be used to reject the oscillations D_{1S} and D_{1C}, respectively. Therefore, the outputs of the LPFs can be approximated by (5.22) and (5.23), respectively.

$$v_{1SF}(n) = \frac{A_1(n)}{2}\cos\{\psi_1(n)\} \tag{5.22}$$

$$v_{1CF}(n) = \frac{A_1(n)}{2}\sin\{\psi_1(n)\} \tag{5.23}$$

The instantaneous phase angle can be obtained from (5.22) and (5.23), and is expressed by

$$\psi_1(n) = \tan^{-1}\left\{\frac{v_{1CF}(n)}{v_{1SF}(n)}\right\}_{\text{unwrapped}} \tag{5.24}$$

where the subscript "unwrapped" indicates that the estimated sawtooth phase angle is unwrapped.

5.2.2 Fundamental Frequency Estimation

The deviation of fundamental angular frequency can be obtained from the estimated instantaneous phase angle using a differentiation operation and is given by [130, 204, 205]

$$\Delta\omega(t) = \frac{d}{dt}\psi_1(t) = \psi_1^{(1)}(t) \tag{5.25}$$

However, the frequency estimation using (5.25) is sensitive to the presence of high frequency disturbances in the instantaneous phase angle [205]. The MF strategy, as presented in Subsection 5.1.2, can also be applied on (5.25) to reject the negative effects caused by high frequency disturbances present in the instantaneous phase angle [246-248]. Therefore, based on (5.6), expression (5.25) can be modulated and is expressed by

$$\int_0^{T_w}\Delta\omega(t)\varphi_S(t)\,dt = \int_0^{T_w}\psi_1^{(1)}(t)\varphi_S(t)\,dt \tag{5.26}$$

Based on (5.7), equation (5.26) can be written as

$$\int_0^{T_w}\Delta\omega(t)\varphi_s(t)\,dt = -\int_0^{T_w}\psi_1(t)\varphi_S^{(1)}(t)\,dt \tag{5.27}$$

Let us assume that $\Delta\omega(t)$ is a constant value within a time window (T_w) and the discrete form of (5.27) can be expressed by

$$\Delta\omega(n)\sum_{l=0}^{N_w-1}\varphi_s(l) = -\sum_{l=0}^{N_w-1}\psi_1(n+l)\varphi_S^{(1)}(l) \tag{5.28}$$

The instantaneous fundamental angular frequency deviation can be estimated from (5.28) and is given by

$$\Delta\hat{\omega}(n) = -\frac{\sum_{l=0}^{N_w-1} \psi_1(n+l)\varphi_S^{(1)}(l)}{\sum_{l=0}^{N_w-1} \varphi_s(l)} \tag{5.29}$$

Based on a moving window of fixed length T_w, equation (5.29) can also be expressed as

$$\Delta\hat{\omega}(n) = \sum_{l=0}^{N_w-1} \psi_1(n-l)T_3(l) \tag{5.30}$$

where

$$T_3(l) = -\frac{\varphi_S^{(1)}(N_w-1-l)}{\sum_{l=0}^{N_w-1} \varphi_s(l)} \quad \text{for } l = 0,1,2,...,N_w-1$$

It can be seen from (5.30) that $\Delta\hat{\omega}(n)$ is the output of a FIR DF whose coefficients are determined by $T_3(l)$, l=0,1,2,…,N_w-1, where the input of the DF is $\psi_1(n)$. Thus, the actual time-varying fundamental frequency can be estimated by

$$\hat{f}(n) = \frac{\hat{\omega}(n)}{2\pi} = \frac{\omega_0 + \Delta\hat{\omega}(n)}{2\pi} \tag{5.31}$$

A spline type MF, as given by (5.18), is used to get the coefficients of the FIR DF. For different values of T_w, S and T_c, the magnitude responses of the proposed and ideal DFs are shown in Fig. 5.15 and Fig. 5.16, respectively. As it can be seen, the performance of the ideal DF will be affected due to the high frequency disturbances present in the instantaneous phase angle. However, it can be seen that the proposed DF can reject the high frequency disturbances from the phase angle. Moreover, multiple notches are observed in the magnitude responses of the proposed DF. The positions of the notches are determined by the characteristics time T_c of the MF. The positions of the notches occur at multiples of the frequency $1/T_c$. Fig. 5.16 shows that for a constant characteristics time T_c=20ms but different values of S and T_w, the notches occur at multiples of 50 Hz (=1/0.02). Therefore, all the harmonics including the fundamental oscillations at nominal frequencies can be rejected completely from the estimated frequency using the proposed FIR DF with T_c=20ms. During the time-varying frequency cases, the fundamental and

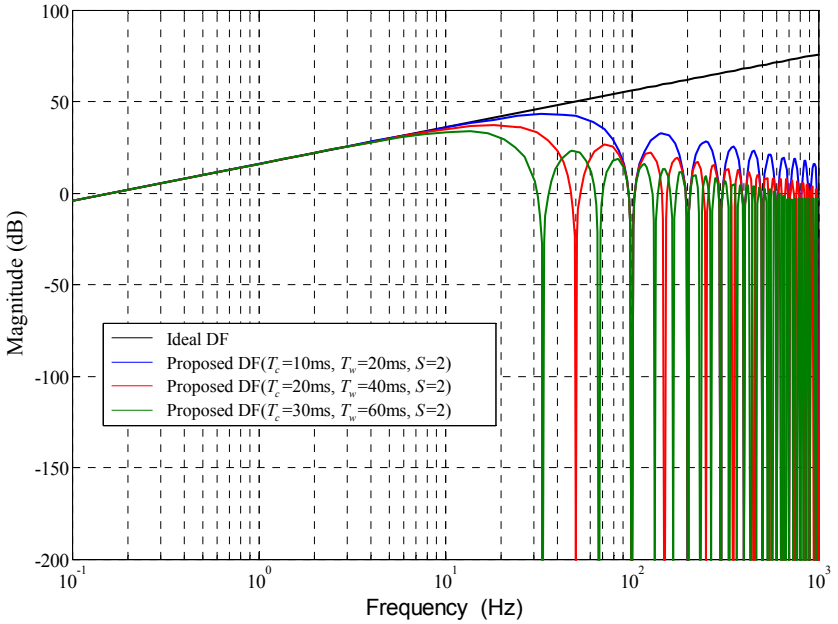

Fig. 5.15 Magnitude responses of the ideal and proposed DFs for different values of T_c and T_w, where S is constant and T_s=0.1ms.

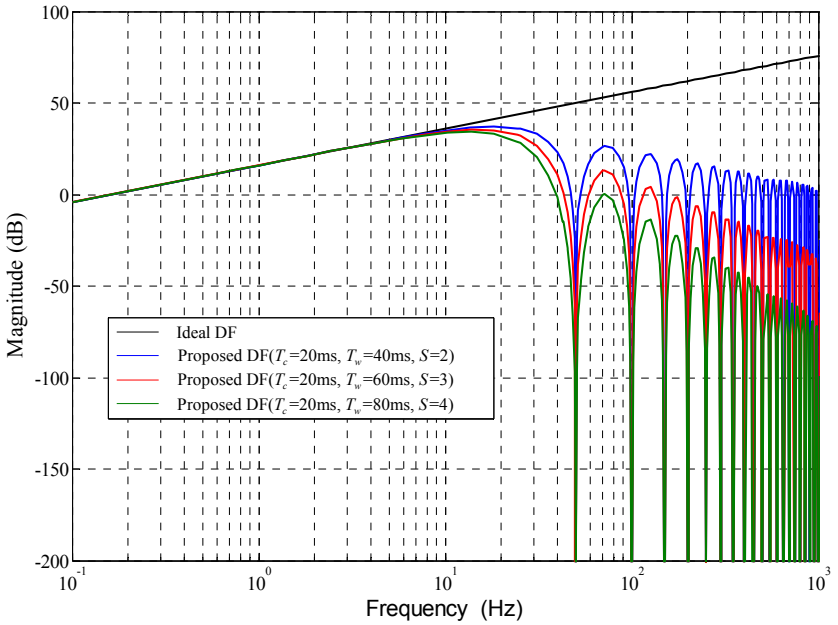

Fig. 5.16 Magnitude responses of the ideal and proposed DFs for constant value of T_c and different values of T_w, where S is varied and T_s=0.1ms.

harmonic oscillations can also be rejected completely if the value of T_c is updated and made equal to the actual fundamental time period. Moreover, as the value of T_w is

increased, the high frequency disturbance rejection capability is improved, as can be seen in Fig. 5.15 and Fig. 5.16. However, the high value of T_w causes a slower dynamic response and also increases the computational burden of the proposed DF.

The magnitude responses of a conventional FIR DF [205] for different values of T_w are shown in Fig. 5.17. As it can be seen, similar to the proposed DF, the high frequency disturbance rejection capability of the conventional DF is enhanced as the value of T_w is increased. Moreover, multiple notches are observed in the magnitude response of the conventional DF. The position of the initial notch occur at 71.52 Hz, 35.76 Hz and 23.84 Hz for the window size of T_w=20ms, 40ms and 60ms, respectively, as can be noticed in Fig. 5.17. The frequency difference between two consecutive notches is equal to $1/T_w$. Therefore, the positions of the notches are occurred at $71.52+\chi/T_w$ Hz, $35.76+\chi/T_w$ Hz and $23.84+\chi/T_w$ Hz, where χ=0,1,2,3…., for T_w=20ms, 40ms and 60ms, respectively. However, unlike the proposed DF, the positions of the notches in the magnitude response of the conventional DF are not at the integer multiples of $1/T_w$. As the positions of the notches in the magnitude response of the conventional DF are not at the fundamental and harmonic frequencies, a large value of T_w has to be chosen to reject the disturbances at fundamental and harmonic frequencies present in the phase angle, thus increasing the computational burden and slower the dynamic response of the conventional DF based technique.

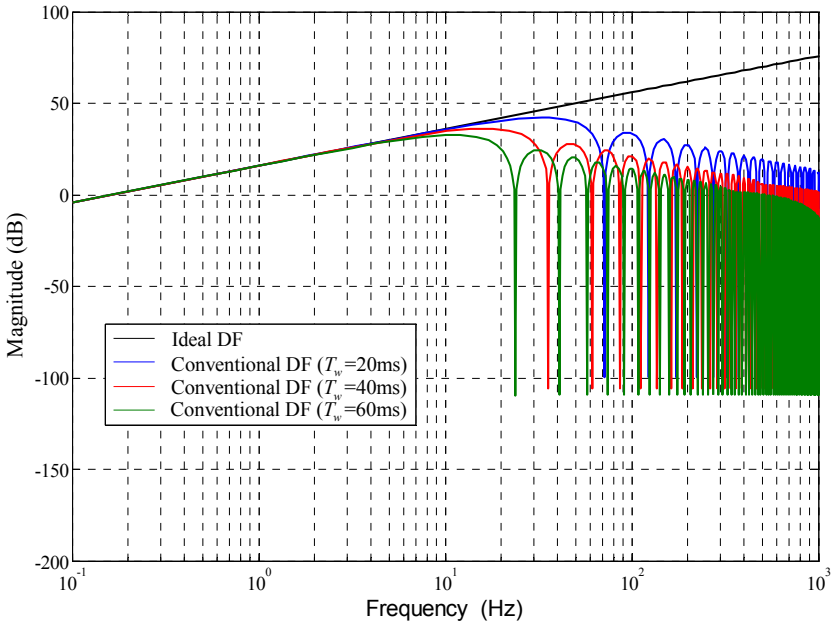

Fig. 5.17 Magnitude responses of the ideal and conventional DFs for T_s=0.1ms and different values of T_w.

The implementation of the proposed fundamental frequency estimation technique is shown in Fig. 5.18. As it can be seen, the unwrapped instantaneous phase angle corresponding to the fundamental angular frequency deviation is estimated using the demodulation method. The DF is then used to estimate the fundamental angular frequency deviation. It can be seen from Fig. 5.18 that there are no interdependent loops, thus leading to a robust frequency estimation technique.

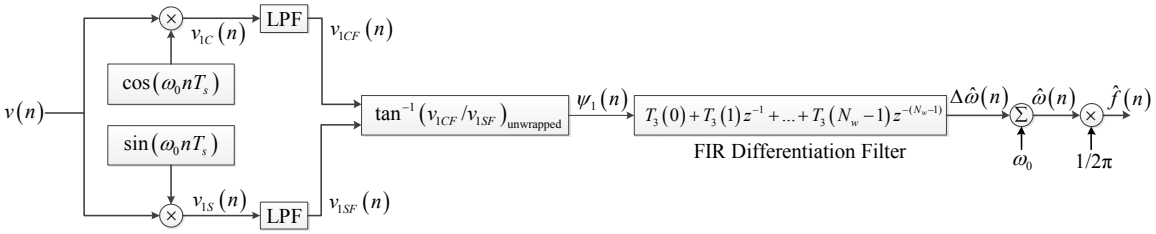

Fig. 5.18 Proposed demodulation and DF based single-phase grid voltage fundamental frequency estimation technique.

5.2.3 Simulation Results

The performance of the proposed technique is documented for a frequency step in the grid voltage fundamental component. The cut-off frequency and order of two IIR LPFs are chosen as 30 Hz and 2, respectively. According to the European standard EN-50160 [255], under normal operating conditions the mean value of the fundamental frequency measured over 10 s shall be within a range of 50 Hz -6/+4 % (i.e. 47 Hz to 52 Hz) during 100 % of the time, for systems with synchronous connection to an interconnected system. The estimations of +2 Hz and -3 Hz fundamental frequency steps using the proposed technique for different fixed size window (T_w=40ms, 60ms and 80ms, respectively) with same characteristics time (T_c=20ms) of the DF are shown in Fig. 5.19. The settling times for the +2 Hz and -3 Hz frequency steps and the estimated errors at frequencies 50 Hz, 52 Hz and 47 Hz are also given in Table 5.3. As it can be noticed, the proposed technique can provide accurate estimation of nominal fundamental frequency for three different window sizes respectively. On the other hand, the proposed technique with smaller size window can provide faster estimation of frequency step and vice versa. However, the error of the estimated off-nominal frequency increases as the window size decreases and vice versa.

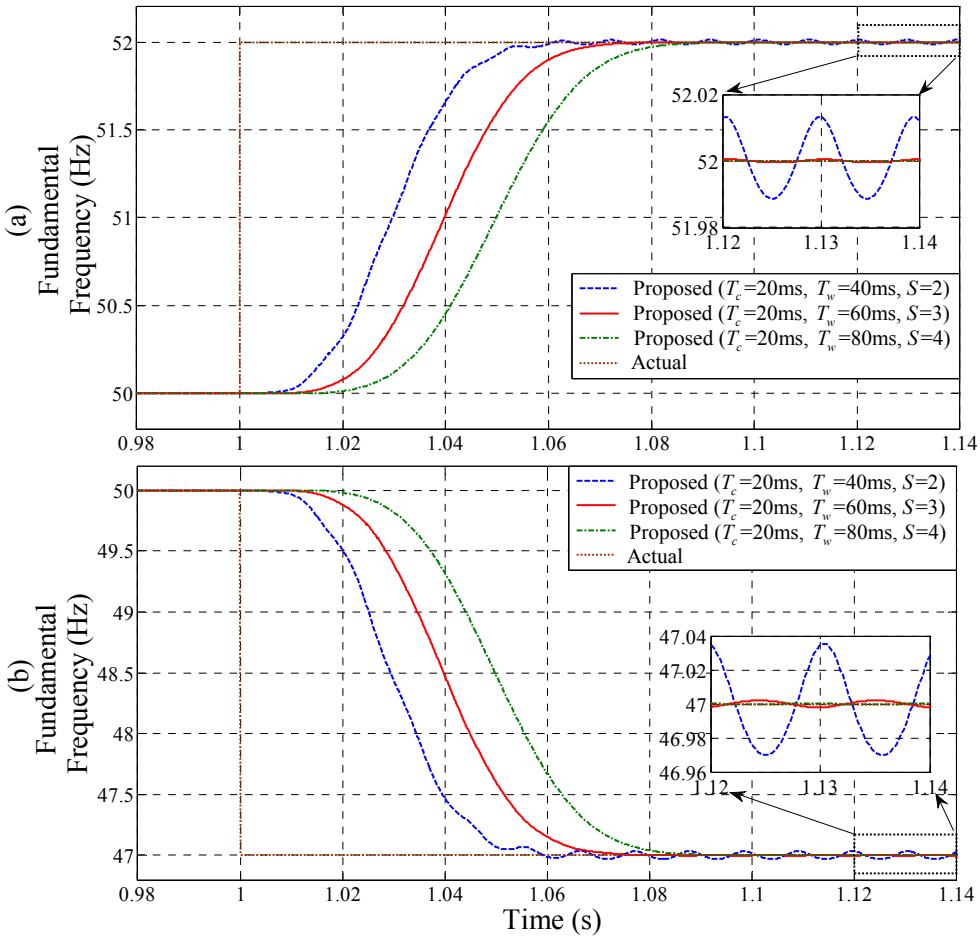

Fig. 5.19 Estimation of fundamental frequency steps (a) +2 Hz (50 Hz to 52 Hz) and (b) -3 Hz (50 Hz to 47 Hz) using the proposed demodulation and DF based technique, where T_s=0.1ms, IIR LPFs cut-off frequency=30 Hz and order=2.

Table 5.3 Settling time for +2 Hz (50 Hz to 52 Hz) and -3 Hz (50 Hz to 47 Hz) frequency steps and estimated errors at frequencies 50 Hz, 52 Hz and 47 Hz

Window Size (ms)	Settling Time (ms)		Frequency Error (Hz)		
	+2 Hz (50 Hz to 52 Hz)	-3 Hz (50 Hz to 47 Hz)	50 Hz	52 Hz	47 Hz
40	2.5 fundamental cycles		0.0000	0.0132	0.0353
60	3.25 fundamental cycles		0.0000	0.0005	0.0022
80	4.0 fundamental cycles		0.0000	0.0000	0.0001

The error of the estimated fundamental frequency at steady-state using the proposed technique for different window size (T_w=40 ms, 60 ms and 80 ms, respectively) of the DF is shown in Fig. 5.20, where the fundamental voltage amplitude is 1.0 p.u. and the fundamental frequency is varied from 45 Hz to 55 Hz based on the specification of the IEEE standard C.37.118.1 for phasor measurement units (PMUs) [29, 31, 32]. As it can be noticed, the proposed technique with DF window size equal to 80 ms can be used to estimate the fundamental frequency range of 45 Hz to 55 Hz with an error less than 0.005 Hz. Moreover, the proposed technique with DF window size equal to 60 ms can be used to estimate the fundamental frequency range of 47 Hz to 52 Hz, as specified by the standard EN-50160, with an error less than 0.005 Hz, as can be seen in Fig. 5.20.

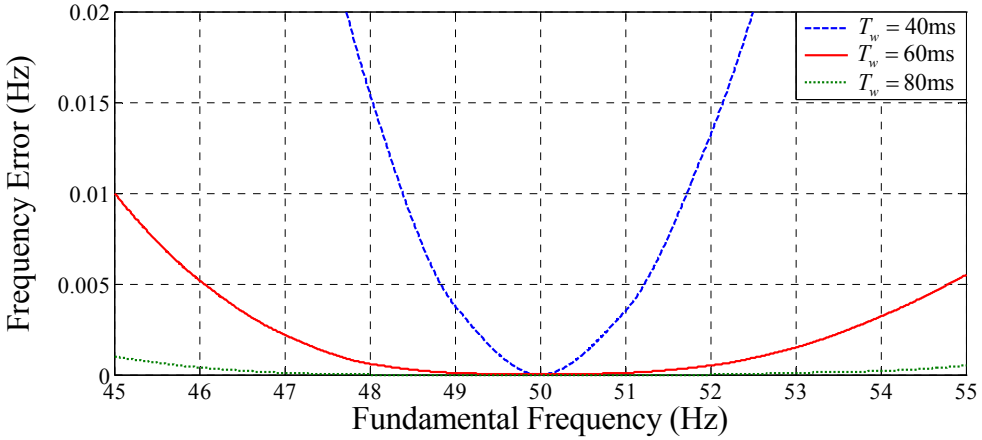

Fig. 5.20 Frequency estimation error using the proposed technique for different window size (T_w=40ms, 60ms and 80ms, respectively) of the DF.

The performance comparison of the proposed DF, the conventional DF [205] and a Kay filter [29, 31, 256] based techniques with a window size of equal to 60 ms for fundamental frequency estimation is shown in Fig. 5.21, where the instantaneous phase angle for all the techniques is obtained using the demodulation method presented in Subsection 5.2.1. As it can be seen, the conventional DF and Kay filter based techniques provide similar results. However, when compared with the conventional DF and Kay filter based techniques, the proposed DF based one can provide improved estimation of fundamental frequency except around 54 Hz, as can also be noticed in Fig. 5.21.

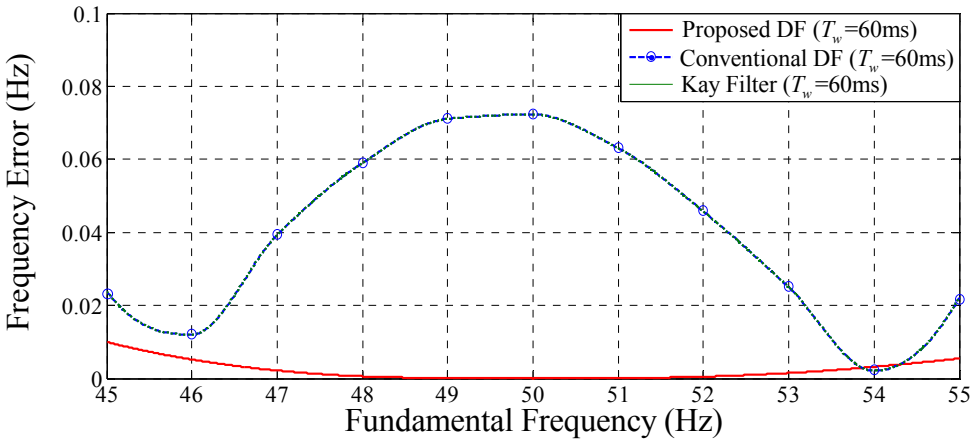

Fig. 5.21 Frequency estimation error using the proposed DF, conventional DF and Kay filter based techniques with T_w=60 ms, where the phase angle is estimated by using the same demodulation method.

5.2.4 Real-Time Experimental Results

The experimental performance of the proposed technique is compared with the conventional DF based technique [205]. The experimental setup is described in Section 1.3 of Chapter 1. The instantaneous phase angle i.e. the inputs of both proposed and conventional DFs are estimated using the same demodulation method for single-phase voltage system. The parameters of both techniques are given in Table 5.4.

Table 5.4 Parameters of the proposed and conventional DF based techniques

Proposed DF based Technique	Conventional DF based Technique
T_w=60ms, T_s=0.1ms, N_w=600, S=3 and T_c=20ms	T_w=60ms, T_s=0.1ms and N_w=600
Demodulation method: IIR LPFs cut-off frequency=30 Hz and order=2	

The performance of both techniques is documented under the following case studies.

i. Steady-state with harmonics (Case-B1)
ii. Steady-state with DC offset and harmonics (Case-B2)
iii. Frequency step and harmonics (Case-B3)
iv. Frequency sweep and harmonics (Case-B4)
v. Voltage sag and harmonics (Case-B5)

vi. Voltage flicker and harmonics (Case-B6)

vii. Phase jump and harmonics (Case-B7)

The fundamental component of the grid voltage waveform presented in the above case studies is distorted by harmonics, as given in Table 5.5. The harmonics, as given in Table 5.5, introduce 7.42% THD into the grid voltage fundamental component.

Table 5.5 Harmonics as a percentage of fundamental component

Harmonics					THD
3^{rd}	5^{th}	7^{th}	9^{th}	11^{th}	7.42%
5.0%	4.0%	3.0%	2.0%	1.0%	

5.2.4.1 Case-B1: Steady-State with Harmonics

A steady-state real-time grid voltage waveform containing harmonics, as given in Table 5.5, is shown in Fig. 5.22(a). The estimation of the fundamental frequency at steady-state using the proposed and conventional DF based techniques is shown in Fig. 5.22(b). As it

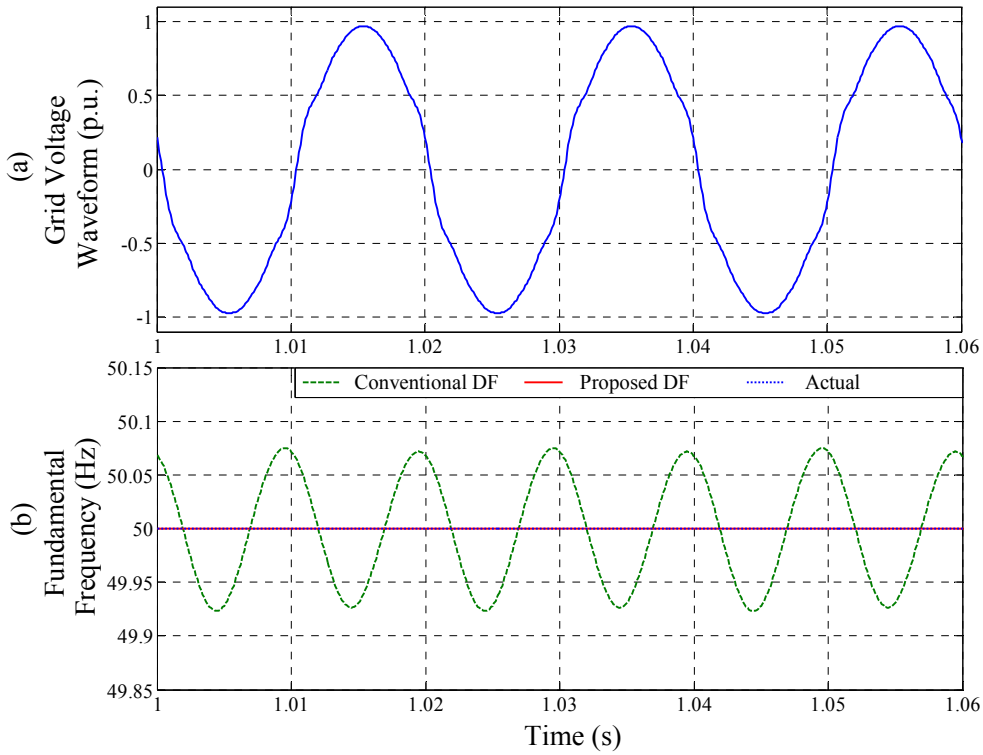

Fig. 5.22 Case-B1: Steady-state with harmonics. (a) Grid voltage waveform. (b) Fundamental frequency.

can be noticed, the conventional DF is affected by the oscillations introduced by the demodulation method at around double the fundamental frequency. On the other side, the proposed DF based technique provides accurate estimation of nominal fundamental frequency as the notch characteristics have been tuned to reject all the nominal harmonic oscillations present in the phase angle.

5.2.4.2 Case-B2: Steady-State with DC Offset and Harmonics

Fig. 5.23(a) shows a grid voltage waveform distorted by 5% DC offset and harmonics, as given in Table 5.5. The estimation of the fundamental frequency using the proposed and conventional DF based techniques is shown in Fig. 5.23(b). The demodulation of the DC offset produces oscillation at the same frequency as the nominal fundamental frequency. As it can be seen from Fig. 5.23(b), the proposed technique can reject this oscillation due to a notch tuned at the nominal fundamental frequency. On the other hand, after comparing the results between Fig. 5.22(b) and Fig. 5.23(b), it can be noticed that the performance of the conventional DF is affected by the oscillation caused by the DC offset.

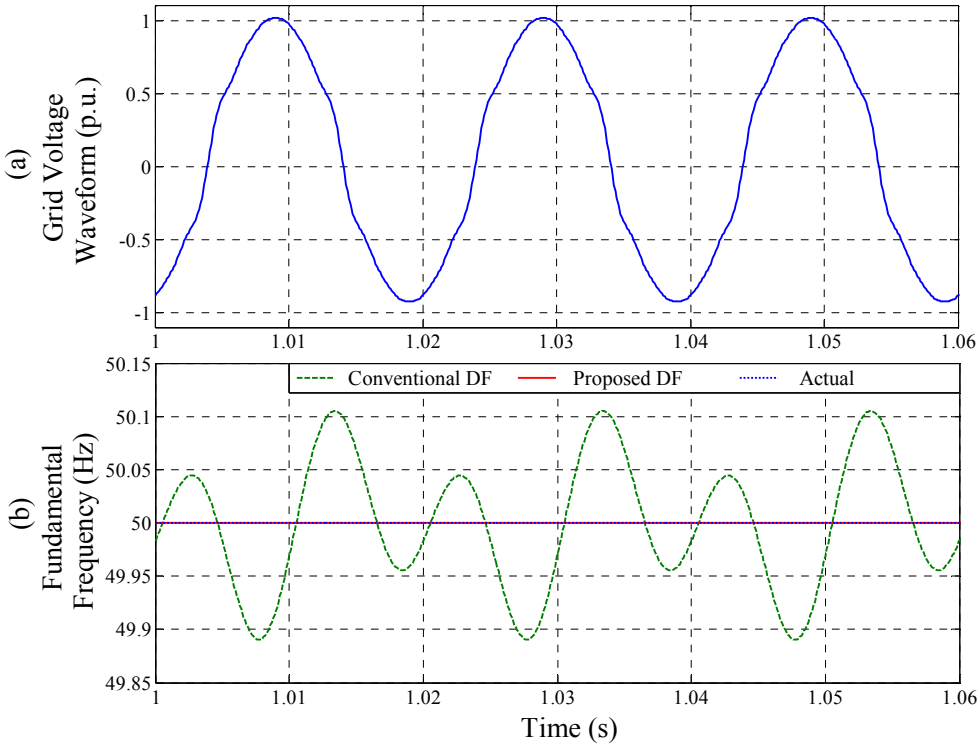

Fig. 5.23 Case-B2: Steady-state with DC offset (5%) and harmonics. (a) Grid voltage waveform. (b) Fundamental frequency.

5.2.4.3 Case-B3: Frequency Step and Harmonics

In this case, the dynamic performances of the proposed and conventional DF based techniques are compared for a fundamental frequency step of +2 Hz and harmonics, as given in Table 5.5. Fig. 5.24 depicts the estimation of the frequency step. As it can be observed, the settling time and the estimation error of the proposed technique are around 3.25 fundamental cycles and 0.0006 Hz, respectively, which are similar to the simulation results provided in Table 5.3 for a window size of 60 ms. As compared to the conventional DF based technique, the proposed technique takes equal settling time for tracking the frequency step while being less affected by the oscillations caused by the demodulation.

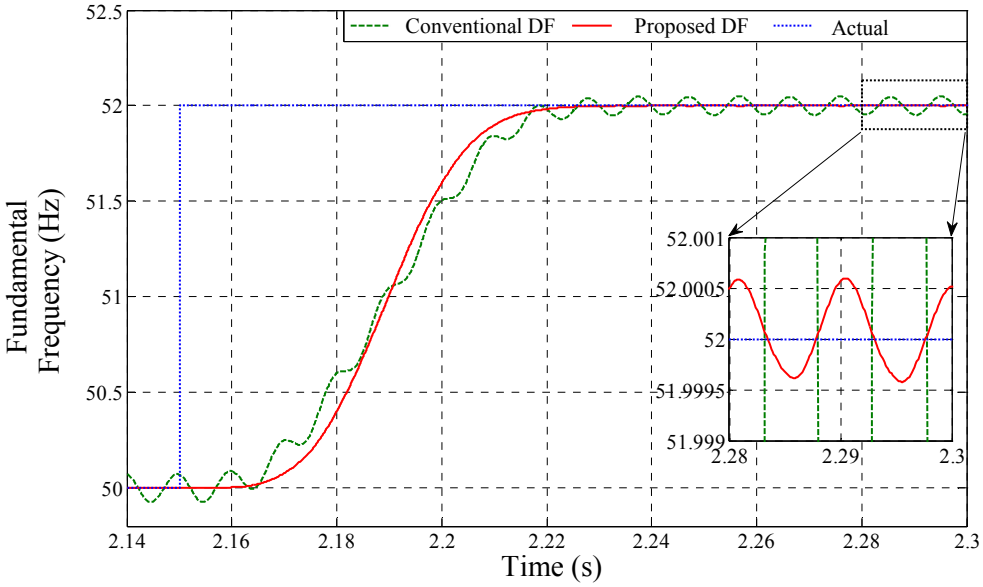

Fig. 5.24 Case-B3: Frequency step (+2 Hz: 50 Hz to 52 Hz) and harmonics.

5.2.4.4 Case-B4: Frequency Sweep and Harmonics

For this case, the grid voltage contains harmonics, as given in Table 5.5, and a frequency sweep of -10 Hz/s down to 47 Hz is considered. The estimation of the frequency using both proposed and conventional DF based techniques is shown in Fig. 5.25. As it can be seen, both techniques can track the frequency sweep. Similar to the frequency step, both techniques provide similar dynamics for tracking the frequency sweep. It can be noticed that the proposed technique presents 0.0023 Hz error at the frequency of 47 Hz, which is also similar to the simulation results presented in Table 5.3 for a window size of 60 ms.

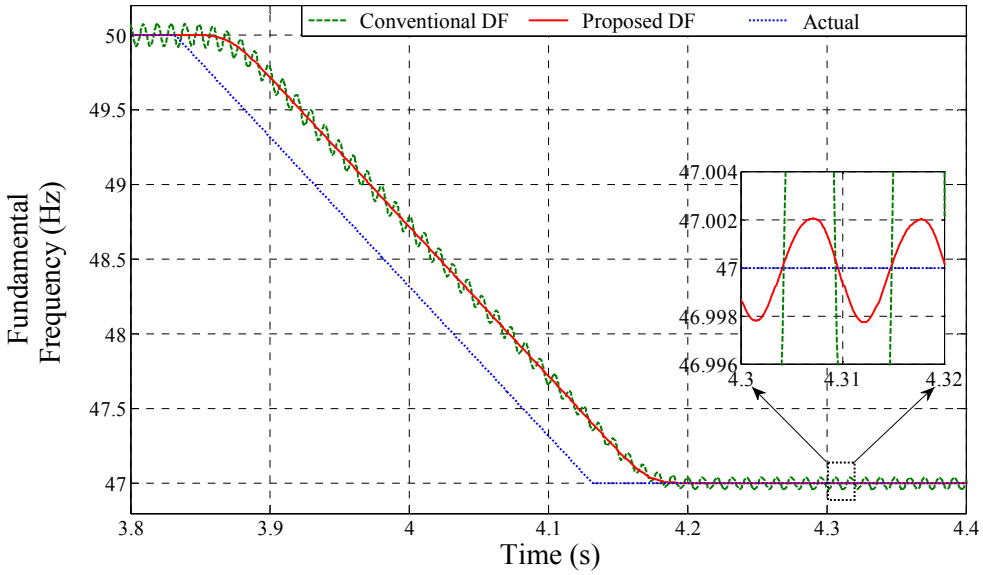

Fig. 5.25 Case-B4: Frequency sweep (-10 Hz/s: 50 Hz to 47 Hz) and harmonics.

5.2.4.5 Case-B5: Voltage Sag and Harmonics

The performance of the proposed and conventional DF based techniques under 50% voltage sag and harmonics, as given in Table 5.5, is shown in Fig. 5.26(b), where the

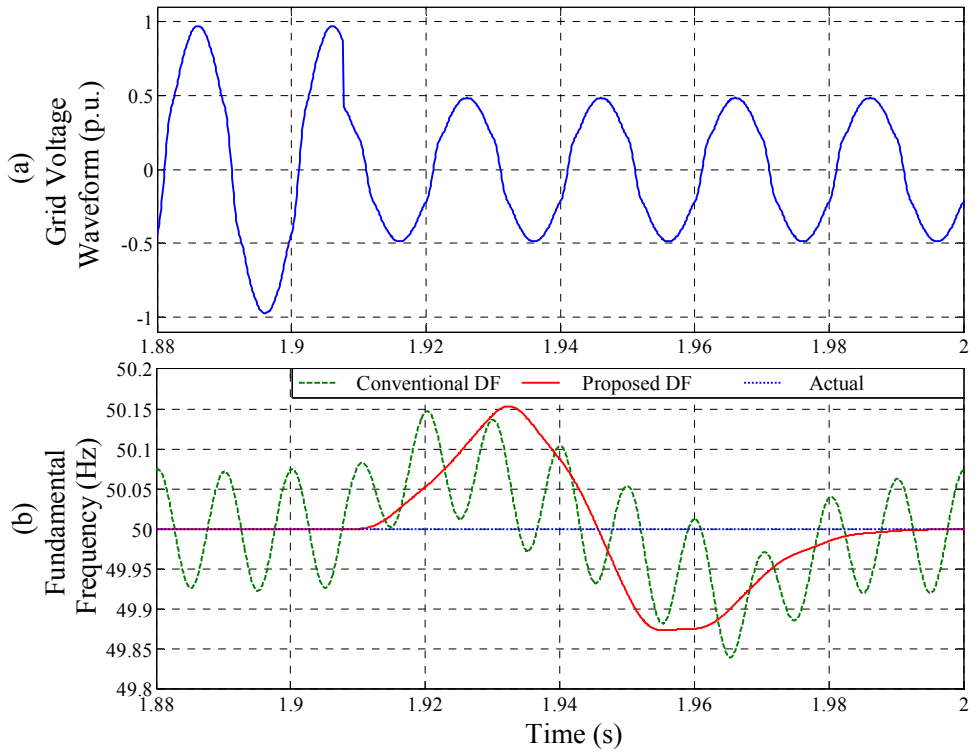

Fig. 5.26 Case-B5: Voltage sag (50%) and harmonics. (a) Grid voltage waveform. (b) Fundamental frequency.

corresponding grid voltage waveform is depicted in Fig. 5.26(a). As it can be observed, both proposed and conventional techniques are only slightly affected by the voltage sag.

5.2.4.6 Case-B6: Voltage Flicker and Harmonics

In this case, the grid voltage waveform, as shown in Fig. 5.27(a), contains a triangular voltage flicker and harmonics, as given in Table 5.5. The frequency and amplitude of the triangular voltage flicker are 2.5 Hz and ±0.05 p.u., respectively. The estimation of fundamental frequency using both proposed and conventional DF based techniques is shown in Fig. 5.27(b). As it can be seen, the performance of the proposed technique is only slightly affected by the voltage flicker.

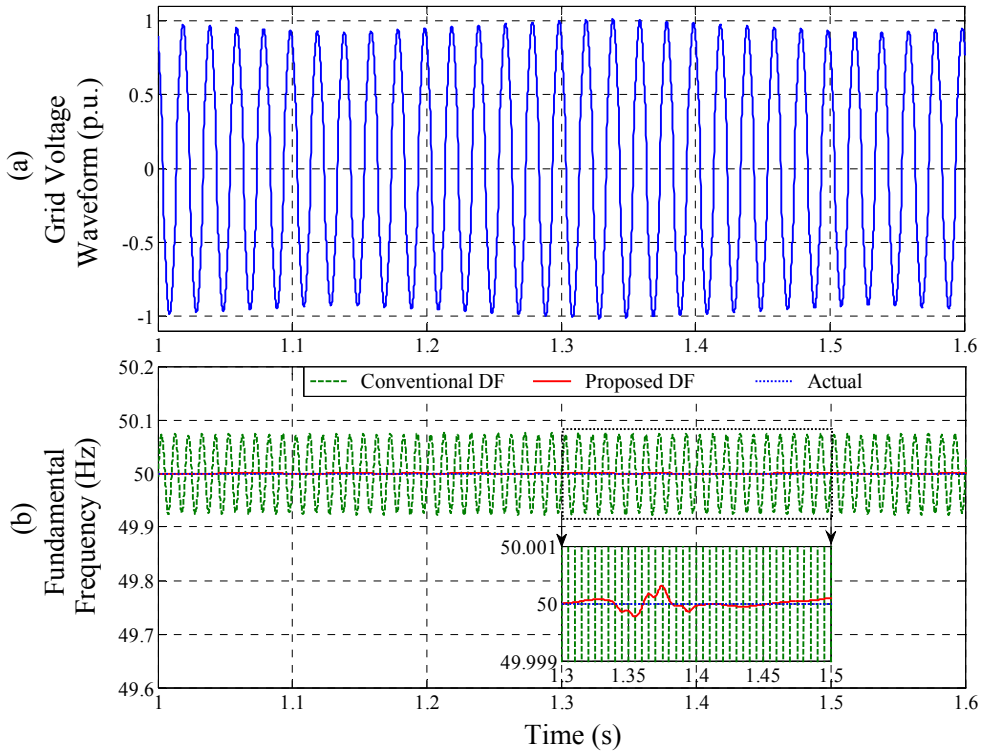

Fig. 5.27 Case-B6: Voltage flicker (±5%) and harmonics. (a) Grid voltage waveform. (b) Fundamental frequency.

5.2.4.7 Case-B7: Phase Jump and Harmonics

The grid voltage waveform, as shown in Fig. 5.28(a), contains a -30° phase jump and harmonics. The harmonic contents are given in Table 5.5. For this case, the estimation of fundamental frequency is shown in Fig. 5.28(b). As it can be seen, both proposed and conventional DF based techniques present undershoot in the frequency estimation under the phase jump.

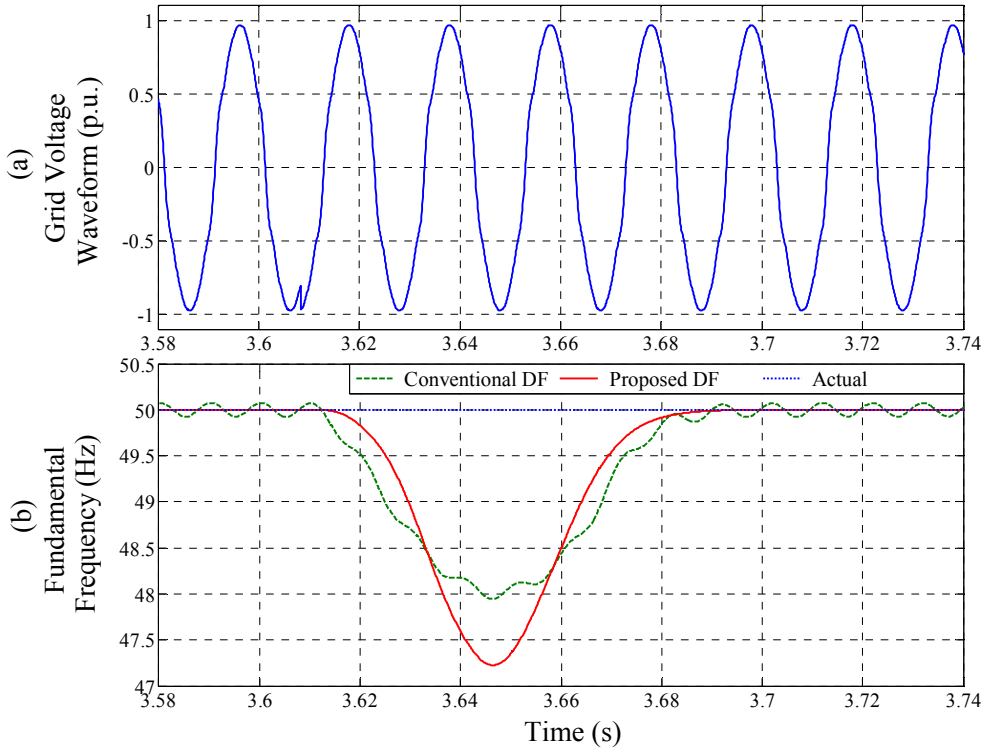

Fig. 5.28 Case-B7: Phase jump (-30°) and harmonics. (a) Grid voltage waveform. (b) Fundamental frequency.

5.3 Power System Fundamental Voltage Amplitude and Frequency Estimation using A Modified Demodulation Based Technique

5.3.1 Conventional Demodulation Based Technique

A conventional demodulation based technique for tracking of the single-phase grid voltage fundamental amplitude and frequency is shown in Fig. 5.29 [203-205, 211, 212], where $\hat{A}_1$ is the estimated fundamental voltage amplitude and ψ_1' is the low-pass filtered value of ψ_1. In this case, the demodulated grid voltages, as given by (5.20) and (5.21), can also be expressed by (5.32) and (5.33), respectively.

$$v_{1S}(n) = \frac{A_1(n)}{2}\cos\{\psi_1(n)\} - \frac{A_1(n)}{2}\cos\{2\omega_0 nT_s + \psi_1(n)\} + D_S\{\omega_0, \omega_0 + 2\Delta\omega,\ 2\omega_0 + 3\Delta\omega, \ldots\} \tag{5.32}$$

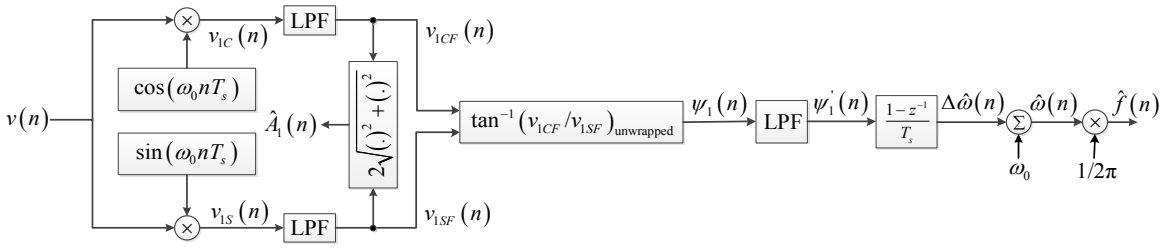

Fig. 5.29 Conventional demodulation based technique for tracking of the single-phase grid voltage fundamental amplitude and frequency.

$$v_{1C}(n) = \frac{A_1(n)}{2}\sin\{\psi_1(n)\} + \frac{A_1(n)}{2}\sin\{2\omega_0 nT_s + \psi_1(n)\} + D_C\{\omega_0, \omega_0 + 2\Delta\omega,\ 2\omega_0 + 3\Delta\omega, \ldots\} \tag{5.33}$$

where the demodulated fundamental voltage component contains oscillations with amplitude $A_1/2$ at angular frequencies $\Delta\omega$ and $2\omega_0+\Delta\omega$, respectively, and the oscillation terms, as expressed by D_S and D_C, are generated by the DC offset and harmonics present in (5.19) [203-205, 211, 212]. Two LPFs are used to reject the oscillations with frequency components higher than $\Delta\omega$, and the outputs of the LPFs are approximated by (5.22) and (5.23), respectively. v_{1SF} and v_{1CF}, as obtained by (5.22) and (5.23) respectively, can be used to estimate the values of A_1 and ψ_1. The phase angle is also passed through a LPF, as shown Fig. 5.29, to smooth the estimated value [212]. The phase angle is then differentiated to obtain the fundamental angular frequency deviation. However, it can be seen from (5.32) and (5.33) that the oscillation components at frequency $2\omega_0+\Delta\omega$ have amplitude equal to half of the fundamental voltage amplitude. The amplitude of this low frequency component is higher when compared with the other oscillations, as expressed by D_S and D_C, generated by the demodulation of the DC offset and harmonics. Therefore, LPFs with high attenuation rate have to be considered to reject the high amplitude oscillations at the frequency $2\omega_0+\Delta\omega$. Thus, high-order LPFs are required which can lead to poor dynamics. On the other hand, two adaptive notch filters (ANFs) tuned at $2\omega_0+\Delta\omega$ can also be combined with low-order LPFs in order to reject the oscillations [181]. Nevertheless, the ANFs require the estimation of fundamental angular frequency deviation and also degrade the dynamic response. However, if there are no oscillations at the frequency $2\omega_0+\Delta\omega$ in (5.32) and (5.33), two low-order LPFs can be used to reject the

oscillations D_S and D_C generated by the demodulation of the DC offset and harmonics present in (5.19).

5.3.2 Proposed Demodulation Based Technique

The proposed modified demodulation based technique for single-phase grid voltage fundamental amplitude and frequency estimation is shown in Fig. 5.30, where an oscillator is integrated with the conventional demodulation based technique. The proposed frequency adaptive oscillator is shown in Fig. 5.31. As it can be seen, the oscillator uses the quadrature components at the angular frequency $\Delta\omega$ $[v'_{1SF}(n) = 0.5A_1(n)\cos\{\psi_1(n)\}$ and $v'_{1CF}(n) = 0.5A_1(n)\sin\{\psi_1(n)\}]$, and the quadrature components at the nominal second harmonic $\{\sin(2\omega_0 nT_s)$ and $\cos(2\omega_0 nT_s)\}$. The proposed oscillator, as shown in Fig. 5.31, is simple to implement and generates orthogonal waveforms at the frequency $2\omega_0+\Delta\omega$ with amplitude $A_1/2$. The outputs of the oscillator $(S_2$ and $C_2)$ can be expressed by (5.34) and (5.35), respectively.

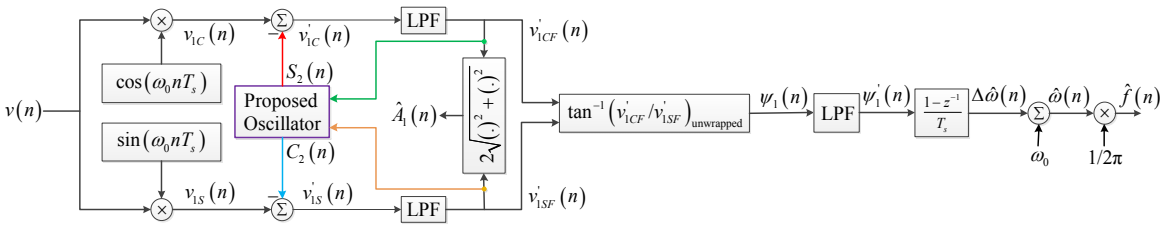

Fig. 5.30 Proposed modified demodulation based technique for tracking of the single-phase grid voltage fundamental amplitude and frequency.

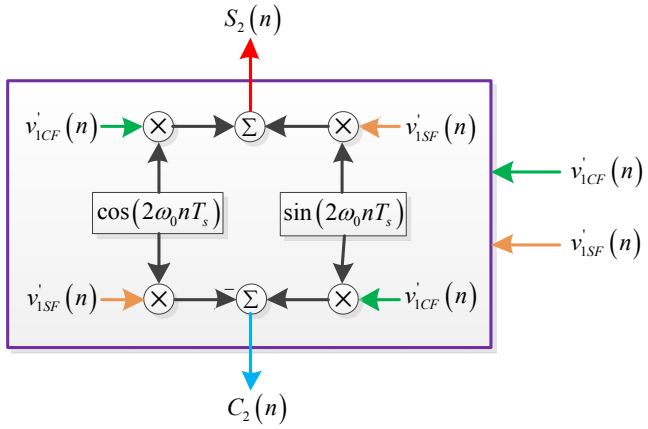

Fig. 5.31 Proposed frequency adaptive oscillator tuned at the frequency $2\omega_0+\Delta\omega$.

$$S_2(n) = v'_{1SF}(n)\sin(2\omega_0 nT_s) + v'_{1CF}(n)\cos(2\omega_0 nT_s)$$

$$= \frac{A_1(n)}{2}\cos\{\psi_1(n)\}\sin(2\omega_0 nT_s) + \frac{A_1(n)}{2}\sin\{\psi_1(n)\}\cos(2\omega_0 nT_s) \quad (5.34)$$

$$= \frac{A_1(n)}{2}\sin\{2\omega_0 nT_s + \psi_1(n)\}$$

$$C_2(n) = -v'_{1SF}(n)\cos(2\omega_0 nT_s) + v'_{1CF}(n)\sin(2\omega_0 nT_s)$$

$$= -\frac{A_1(n)}{2}\cos\{\psi_1(n)\}\cos(2\omega_0 nT_s) + \frac{A_1(n)}{2}\sin\{\psi_1(n)\}\sin(2\omega_0 nT_s) \quad (5.35)$$

$$= -\frac{A_1(n)}{2}\cos\{2\omega_0 nT_s + \psi_1(n)\}$$

The outputs of the oscillator are then subtracted from v_{1S} and v_{1C}, respectively, as can be seen in Fig. 5.30. Therefore, the inputs of the LPFs after the demodulation stage can be expressed by (5.36) and (5.37), respectively.

$$v'_{1S}(n) = v_{1S}(n) - C_2(n) = \frac{A_1(n)}{2}\cos\{\psi_1(n)\} + D_S\{\omega_0, \omega_0 + 2\Delta\omega,\ 2\omega_0 + 3\Delta\omega, ...\} \quad (5.36)$$

$$v'_{1C}(n) = v_{1C}(n) - S_2(n) = \frac{A_1(n)}{2}\sin\{\psi_1(n)\} + D_C\{\omega_0, \omega_0 + 2\Delta\omega,\ 2\omega_0 + 3\Delta\omega, ...\} \quad (5.37)$$

It can be seen that (5.36) and (5.37) do not contain the high amplitude oscillation at the frequency $2\omega_0+\Delta\omega$. The outputs of the LPFs after the demodulation stage can be approximated by (5.38) and (5.39), respectively.

$$v'_{1SF}(n) = \frac{A_1(n)}{2}\cos\{\psi_1(n)\} \quad (5.38)$$

$$v'_{1CF}(n) = \frac{A_1(n)}{2}\sin\{\psi_1(n)\} \quad (5.39)$$

The integration of the proposed oscillator allows the use of low-order LPFs with same cut-off frequency and hence faster response can be obtained when compared with the conventional demodulation based technique. On the other hand, based on LPFs of the same order and cut-off frequency, the outputs of all the LPFs in the proposed technique shown in Fig. 5.30 contain less ripple as compared to the conventional technique shown in Fig. 5.29. Therefore, by using the proposed demodulation based technique relying on the oscillator,

an improved estimation of the time-varying fundamental parameters can be obtained as compared to the conventional demodulation based one.

5.3.4 Real-Time Experimental Results

Three second-order IIR LPFs with a cut-off frequency equal to 30 Hz are used for both proposed and conventional demodulation based techniques, as shown in Fig. 5.29 and Fig. 5.30, respectively. The sampling frequency and the grid voltage nominal frequency are chosen as 10 kHz and 50 Hz, respectively. The experimental setup is described in Section 1.3 of Chapter 1. The performance comparison of both techniques is carried out under the following real-time case studies.

i. Steady-state (Case-C1)
ii. Steady-state with harmonics (Case-C2)
iii. Frequency sweep and harmonics (Case-C3)
iv. Frequency step and harmonics (Case-C4)
v. Voltage swell and harmonics (Case-C5)
vi. Voltage flicker and harmonics (Case-C6)

The fundamental component of the grid voltage waveforms presented in the case studies C2 to C6 contain 7.42% THD, where harmonic contents are given in Table 5.5.

5.3.4.1 Case-C1: Steady-State

The steady-state grid voltage waveform, as shown in Fig. 5.32(a), contains only fundamental component. The estimation of the fundamental voltage amplitude and frequency using the proposed and conventional demodulation based techniques are depicted in Fig. 5.32(b) and (c), respectively. As it can be seen, the performance of the proposed technique is less affected by the second harmonic caused by the demodulation method as compared to the conventional one.

5.3.4.2 Case-C2: Steady-State with Harmonics

A harmonically distorted real-time grid voltage waveform is shown in Fig. 5.33(a), where the harmonic contents are given in Table 5.5. The estimated fundamental voltage amplitude and frequency is also shown in Fig. 5.33(b) and (c), respectively. As it can be

seen, the proposed demodulation based technique presents a small ripple in the estimation of fundamental voltage amplitude and frequency due to the presence of harmonics.

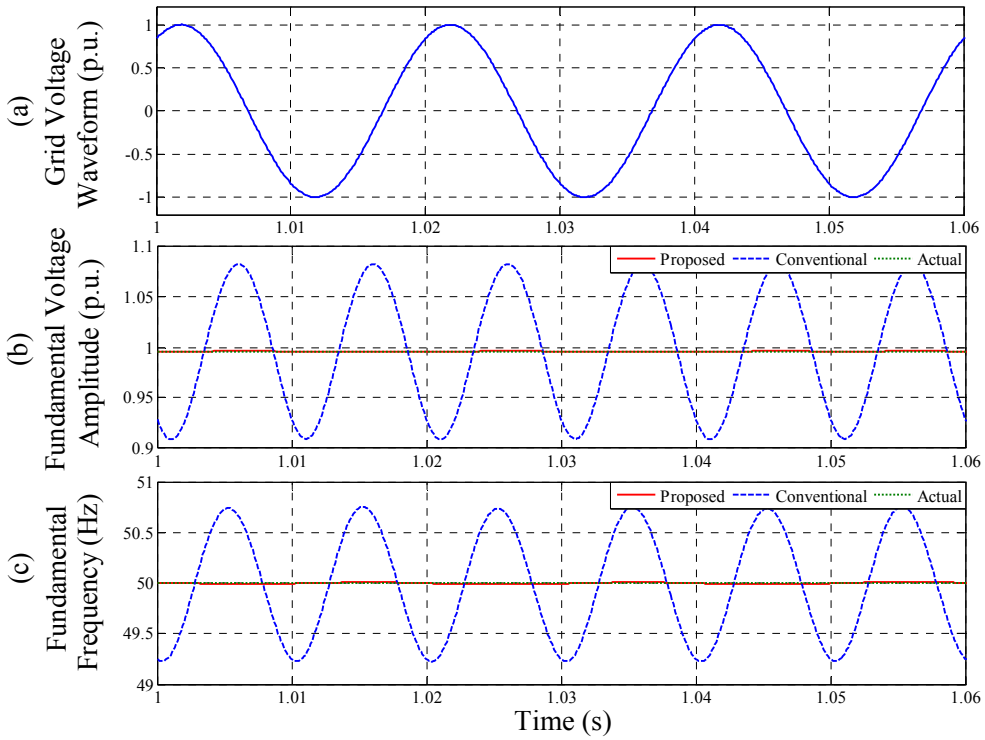

Fig. 5.32 Case-C1: Steady-state. (a) Grid voltage waveform. (b) Fundamental voltage amplitude. (c) Fundamental frequency.

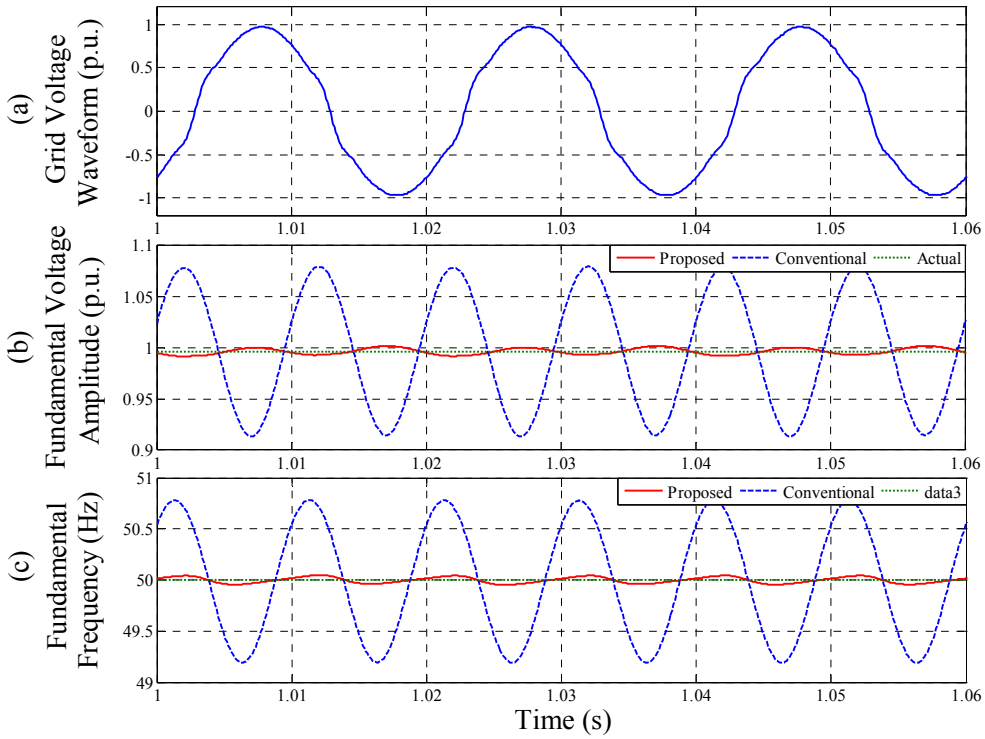

Fig. 5.33 Case-C2: Steady-state with harmonics. (a) Grid voltage waveform. (b) Fundamental voltage amplitude. (c) Fundamental frequency.

5.3.4.3 Case-C3: Frequency Sweep and Harmonics

A +10 Hz/s fundamental frequency sweep with duration of 0.1s is considered into a grid voltage waveform distorted by harmonics, as given in Table 5.5. For this case, the estimation of the fundamental voltage amplitude and frequency sweep using the proposed and conventional demodulation based techniques are shown in Fig. 5.34. As it can be noticed, both techniques can track the frequency sweep. However, the fundamental voltage amplitude and frequency estimation using the proposed technique is more accurate as compared to the conventional one.

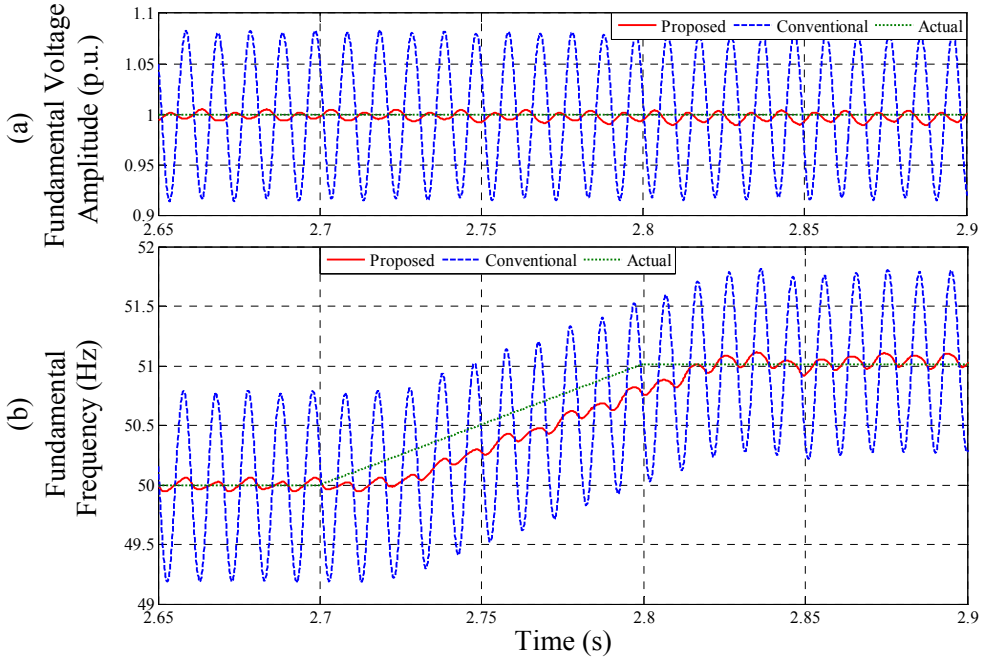

Fig. 5.34 Case-C3: Frequency sweep (+10 Hz/s: 50 Hz to 51 Hz) and harmonics. (a) Fundamental voltage amplitude. (b) Fundamental frequency.

5.3.4.4 Case-C4: Frequency Step and Harmonics

A frequency step is considered in this case for comparing the performance of the proposed and conventional demodulation based techniques. Fig. 5.35 illustrates the estimation of the fundamental voltage amplitude and +1 Hz fundamental frequency step using the presented techniques under harmonics, as given in Table 5.5. It can be seen in Fig. 5.35(b) that both techniques show similar dynamics for tracking the frequency step. However, the proposed technique provides improved estimation of the fundamental voltage amplitude and frequency when compared with the conventional one.

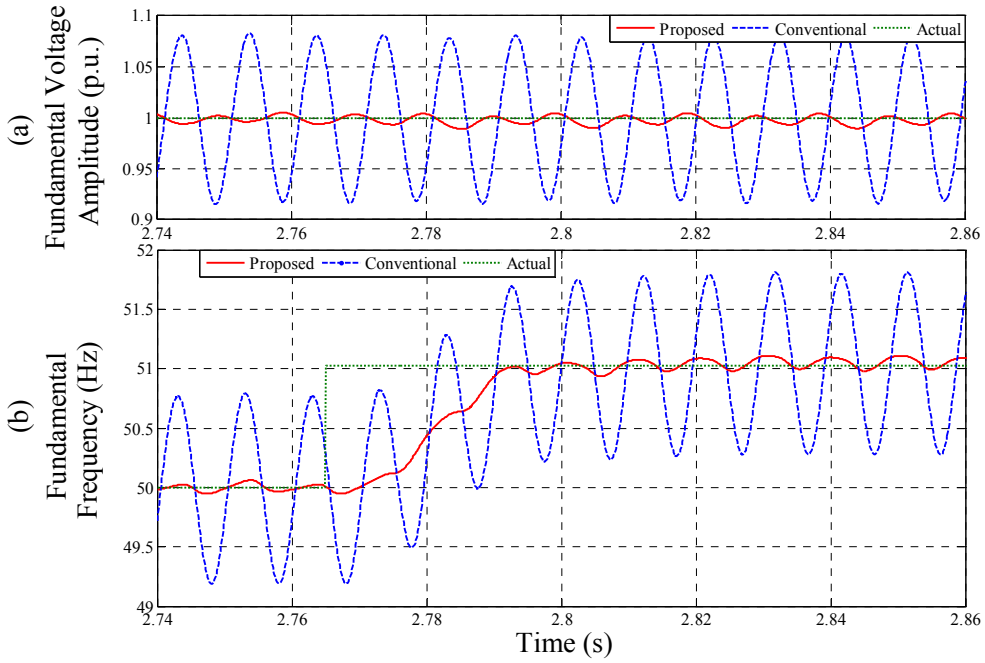

Fig. 5.35 Case-C4: Frequency step (+1 Hz: 50 Hz to 51 Hz) and harmonics. (a) Fundamental voltage amplitude. (b) Fundamental frequency.

5.3.4.5 Case-C5: Voltage Swell and Harmonics

A grid voltage swell of 50% and harmonics, as given in Table 5.5, is shown in Fig. 5.36(a). The estimation of the fundamental voltage amplitude and frequency are also shown in Fig. 5.36(b) and (c), respectively. As it can be seen in Fig. 5.36(b), both proposed and conventional demodulation based techniques show similar dynamics for tracking the voltage swell. However, the proposed one provides less ripple in both amplitude and frequency estimation when compared with the conventional one.

5.3.4.6 Case-C6: Voltage Flicker and Harmonics

In this case, a triangular voltage flicker is considered into a grid voltage waveform distorted by harmonics, as given in Table 5.5. The corresponding distorted grid voltage waveform is shown in Fig. 5.37(a). The frequency and amplitude of the triangular voltage flicker are 2.5 Hz and ±0.10 p.u., respectively. The estimation of the fundamental voltage amplitude and frequency are shown in Fig. 5.37(b) and (c), respectively. As it can be seen in Fig. 5.37(b), both proposed and conventional demodulation based techniques can track the voltage flicker.

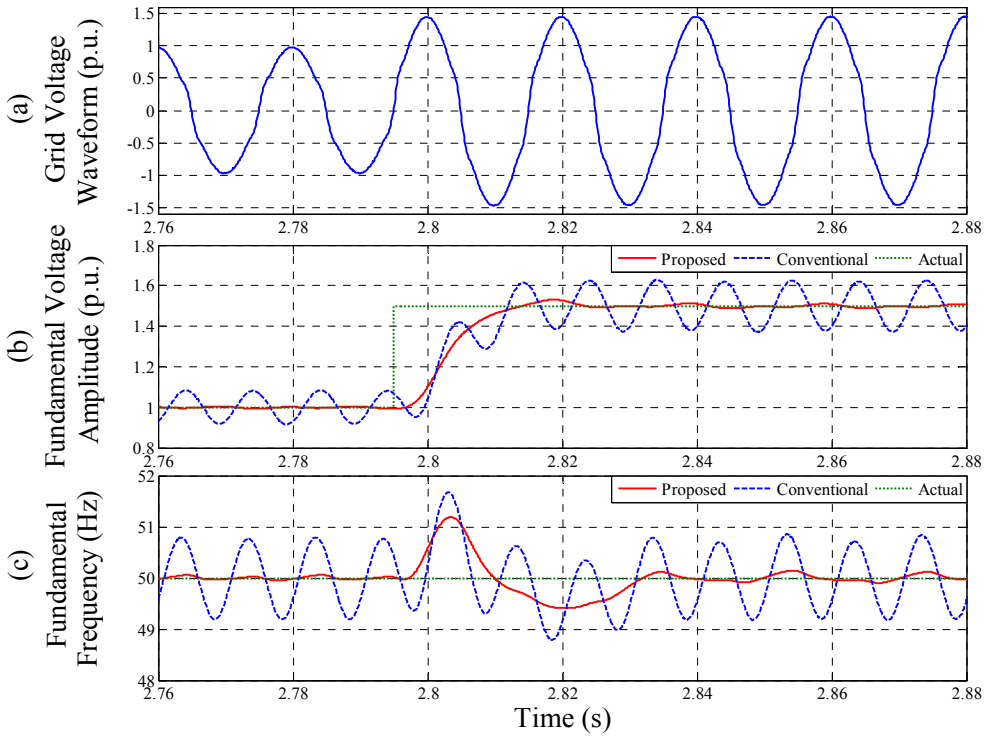

Fig. 5.36 Case-C5: Voltage swell (50%) and harmonics. (a) Grid voltage waveform. (b) Fundamental voltage amplitude. (c) Fundamental frequency.

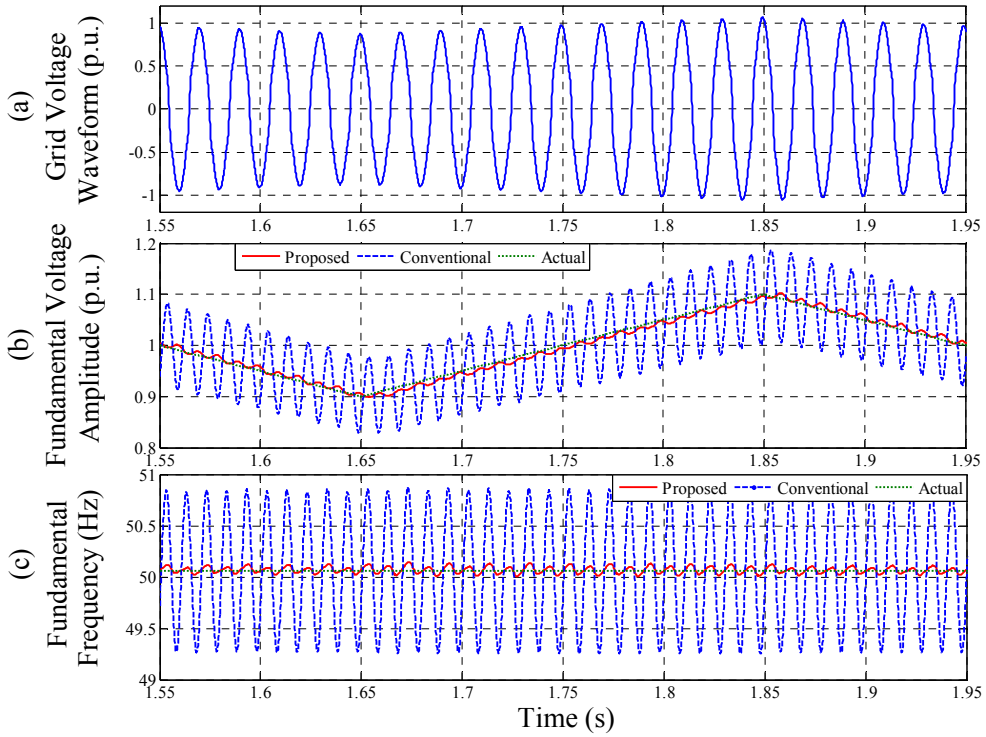

Fig. 5.37 Case-C6: Voltage flicker (±10%) and harmonics. (a) Grid voltage waveform. (b) Fundamental voltage amplitude. (c) Fundamental frequency.

5.4 Conclusions

Three techniques based on modulation and/or demodulation to estimate the single-phase grid voltage fundamental amplitude and/or frequency has been reported in this chapter.

The first proposed technique relies on an algorithm based on three consecutive samples and a voltage modulation strategy to estimate the grid voltage fundamental frequency. The technique is robust, can reject the negative effects caused by the presence of the DC offset, harmonics, notches and spikes, and can also provide the estimation of a wide range of fundamental frequency variation under harmonics with an acceptable error specified by the standard. The technique does not need to set a threshold value of the middle sample of three consecutive samples for removing the ill-condition when compared with a conventional technique based on three consecutive samples and a finite-impulse-response filter. In addition, based on similar frequency dynamics, the proposed technique is less affected by the DC offset, voltage sag, voltage flicker, notches, spikes and also provides improved estimation of the off-nominal frequency under harmonics as compared to the conventional technique. Moreover, unlike the conventional one, the proposed technique does not require additional low-pass filter. The presented real-time experimental results have confirmed the effectiveness of the proposed technique for real-time frequency estimation.

The second proposed technique is based on a demodulation method and a finite-impulse-response differentiation filter to estimate the grid voltage fundamental frequency. A frequency domain analysis for designing the differentiation filter has been presented. It has been shown that the proposed technique can reject the negative effects caused by the presence of the DC offset and harmonics. The performance of the proposed differentiation filter is less affected by the presence of the oscillations caused by the demodulation method as compared to a similar finite-impulse-response differentiation filter. Selected experimental results have been presented to confirm the effectiveness and capability of the proposed demodulation and differentiation filter based technique for real-time frequency estimation.

The third proposed technique consists of a modified demodulation method for tracking of the single-phase grid voltage fundamental amplitude and frequency. An oscillator has been integrated with a conventional demodulation based technique in order to reject the oscillation at around second harmonic caused by the demodulation of the input fundamental voltage component. The proposed technique is simple and can also provide an

accurate estimation of fundamental voltage amplitude and frequency under distorted grid conditions. Based on low-pass filters of the same order and cut-off frequency, the integration of the oscillator with the demodulation based technique does not alter the dynamic response of the estimated fundamental voltage amplitude and frequency as compared to the conventional one. Moreover, when compared with the conventional one, the proposed demodulation technique improves the amplitude and frequency estimation accuracy significantly by removing the second harmonic oscillation generated by the demodulation of the fundamental voltage component. The presented experimental results have confirmed the benefits of the proposed technique for real-time frequency estimation.

Chapter 6
Quadrature Signal Generator Based Techniques

This chapter presents three techniques based on quadrature signal generator to estimate the single-phase grid voltage fundamental amplitude and frequency. The discrete Fourier Transform based frequency adaptive quadrature signal generator relying on a second-order generalized integrator is described in Section 6.1. Section 6.2 presents a fixed frequency tuned second-order generalized integrator based quadrature signal generator technique to estimate the grid voltage fundamental amplitude and frequency. On the other hand, a frequency adaptive quadrature signal generator based on an anticonjugate decomposition and a cascaded delayed signal cancellation is described in Section 6.3. Selected simulation and/or experimental results are presented after the description of each technique. The conclusions of the proposed techniques are documented in Section 6.4.

6.1 Power System Fundamental Voltage Amplitude and Frequency Estimation using A Frequency Adaptive Tuned Second-Order Generalized Integrator Based Technique

A frequency adaptive quadrature signal generator (QSG) based on a second-order generalized integrator (SOGI) is documented in this section for single-phase grid voltage fundamental amplitude and frequency estimation under distorted grid conditions. The fundamental frequency information required by the QSG-SOGI is obtained by using the discrete Fourier Transform (DFT). The DFT and QSG-SOGI based (DFT-SOGI) technique is shown in Fig. 6.1, where v is the grid voltage, n is the sampling instant, $\hat{f}$ is the estimated fundamental frequency, ω_r is the tuning angular frequency of the SOGI, v_1' is the estimated in-phase fundamental voltage component, qv_1' is the estimated in-quadrature fundamental voltage component, $\hat{A}_1$ is the estimated fundamental voltage amplitude, and

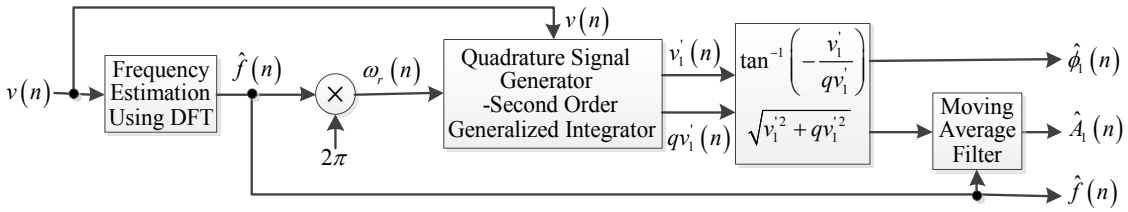

Fig. 6.1 The block diagram of the DFT-SOGI technique for tracking of the single-phase grid voltage fundamental amplitude and frequency.

$\hat{\phi}_1$ is the estimated instantaneous phase angle of the fundamental voltage component. As it can be seen, the QSG-SOGI provides the orthogonal components of the fundamental voltage waveform at the tuning frequency estimated by the DFT. A moving average filter (MAF) is used to remove the ripple from the estimated fundamental voltage amplitude. The window size of the MAF is updated using the estimated frequency. The proposed DFT-SOGI technique is designed for monitoring the voltage of the distribution electricity network where the fundamental frequency does not vary significantly from its nominal value. According to the European standard EN-50160 [255], the fundamental frequency shall be within a range of 50 Hz -6/+4% (i.e. 47 Hz to 52 Hz) during 100% of the time. Therefore, the DFT-SOGI technique is used to estimate the fundamental voltage amplitude and frequency under a frequency variation range of 47 Hz to 52 Hz.

For estimating the fundamental voltage amplitude and frequency using the DFT-SOGI technique, the single-phase grid voltage distorted by DC offset and harmonics can be expressed by

$$v(n) = v_0(n) + \sum_{i=1,2,\ldots}^{M} A_i(n)\sin\left\{i\omega(n)nT_s + \theta_i(n)\right\} \tag{6.1}$$

where v_0 is the DC offset, M is the maximum order of harmonics, $\omega=2\pi f$ is the fundamental angular frequency, $f=f_0+\Delta f$ is the fundamental frequency, f_0 is the nominal fundamental frequency, Δf is the fundamental frequency deviation, T_s is the sampling period, $f_s=1/T_s$ is the sampling frequency, and A_i and θ_i are the amplitude and initial phase angle of the $i\omega$ (i=1,2,…,M) angular frequency component, respectively.

6.1.1 Fundamental Frequency Estimation

A fixed-size window with a fixed sampling frequency is used in the DFT operation for tracking of the time-varying grid voltage fundamental frequency. The length of the window is selected based on nominal fundamental frequency. During the time-varying cases, the picket fence effect and the spectral leakage occur in the fixed window DFT operation and hence inaccurate spectral results are obtained [96]. The spectral leakage is due to the time domain truncation of the grid voltage waveform by the fixed-size window. The spectral leakage causes the actual spectrum of one frequency to spread its energy to its neighbour frequencies. However, this spectral leakage information can be used to track the time-varying fundamental frequency [98, 99, 257]. To estimate the frequency by using the spectral leakage property of the DFT, short range of leakage is preferred as it spreads energy in a short range of neighbour frequencies [98, 99]. For long range of leakage, large errors may occur due to the interference caused by the neighbour harmonics [98, 99]. Therefore, a Hanning window, which gives a smooth truncation of the analysed portion of the grid voltage waveform, can be used to avoid the long range leakage. The DFT of the Hanning windowed grid voltage waveform can be expressed by [98, 99]

$$V_k(n) = \frac{2}{N_w} \sum_{l=n-(N_w-1)}^{n} W_{Han}(l)\, v(l)\, e^{-j\frac{2\pi kl}{N_w}} \tag{6.2}$$

where $N_w=mf_s/f_0$ is the number of voltage samples present in a window, m is the number of nominal fundamental voltage cycles present in the window, $\Delta_f=f_0/m$ is the frequency resolution, $k=0,1,2,\ldots,N_w-1$ is the frequency index, j is the complex operator and $W_{Han}(l)$ is the Hanning window as given by

$$W_{Han}(l) = 0.5\left\{1-\cos\left(\frac{2\pi l}{N_w}\right)\right\}, \quad l = n-(N_w-1), n-(N_w-2), \ldots, n \tag{6.3}$$

From the DFT operation, as given by (6.2), the spectral amplitude corresponding to the nominal fundamental frequency ($f_0=m\Delta_f$) and two neighbour frequencies such as $f_0-\Delta_f=(m-1)\Delta_f$ and $f_0+\Delta_f=(m+1)\Delta_f$ are calculated. These three amplitudes can be used to track the time-varying actual fundamental frequency and can be expressed by [98, 99, 257]

$$\hat{f}(n) = f_0 + \delta_1(n)\Delta_f \tag{6.4}$$

where

$$\delta_1(n) = \frac{1.5\hat{a}_{f_0}(n)\left[\hat{a}_{f_0+\Delta_f}(n) - \hat{a}_{f_0-\Delta_f}(n)\right]}{\left[\hat{a}_{f_0}(n) + \hat{a}_{f_0+\Delta_f}(n)\right]\left[\hat{a}_{f_0}(n) + \hat{a}_{f_0-\Delta_f}(n)\right]},$$

$\hat{a}_{f_0}$ is the estimated amplitude corresponding to the frequency f_0, $\hat{a}_{f_0+\Delta_f}$ is the estimated amplitude corresponding to the frequency $f_0+\Delta_f$ and $\hat{a}_{f_0-\Delta_f}$ is the estimated amplitude corresponding to the frequency $f_0-\Delta_f$. The mathematical derivation of $\delta_1(n)$ for the window size of N_w samples [n-(N_w-1), n-(N_w-2),…,(n-1), n] is reported in [98, 257]. The actual fundamental frequency will be higher than the nominal value if the spectral line at frequency $f_0+\Delta_f$ is higher than the spectral line at frequency $f_0-\Delta_f$ and vice versa, as shown in cases I and II of Fig. 6.2, respectively. In the DFT operation with fixed-size window, the frequency deviation tracking range can be expressed by $-\Delta_f/2<\delta_1\Delta_f<+\Delta_f/2$ [98]. The frequency tracking range can also be increased by incorporating more neighbour spectral lines at the expense of a higher computational burden [98].

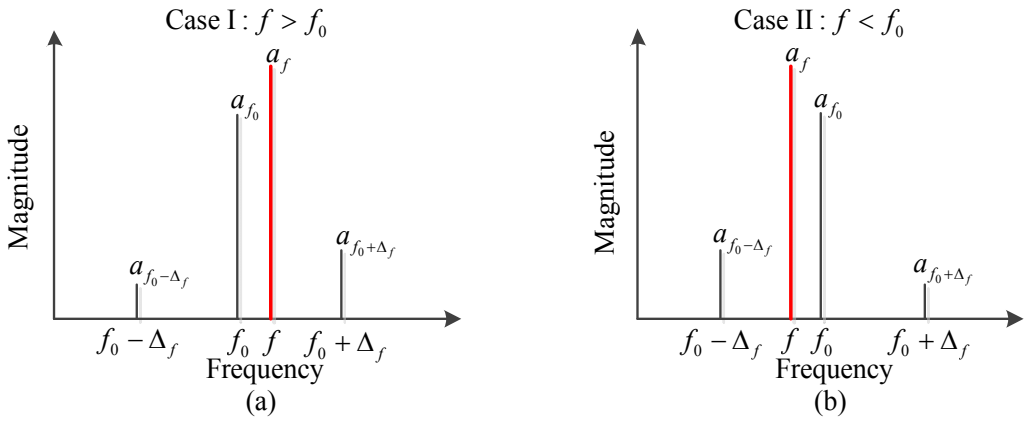

Fig. 6.2 Spectral leakage property of the fixed window DFT operation during the time-varying cases.

As the size of the window is fixed, hence the trigonometric functions required for the DFT operation can be estimated offline and can be stored for real-time application. Therefore, the DFT operation, as given by (6.2), can also be expressed as

$$V_k(n) = \sum_{l=n-(N_w-1)}^{n} y(k, n-l)v(l) \tag{6.5}$$

where

$$y(k,n-l)=\frac{2}{N_w}W_{Han}(n-l)e^{-j\frac{2\pi k(n-l)}{N_w}}=\frac{1}{N_w}\left\{1-\cos\left(\frac{2\pi(n-l)}{N_w}\right)\right\}e^{-j\frac{2\pi k(n-l)}{N_w}}$$

and n-l=0,1,2,…,N_w-1. For constant values of k and N_w, $V_k(n)$, as expressed by (6.5), can be considered as the output of a digital filter with N_w constant coefficients given by $y(k,n-l)$. The implementation of the fixed-size window based DFT operation for tracking of the grid voltage frequency is shown in Fig. 6.3, where three DFT based digital filter are used to track the three spectral amplitudes, respectively. As it can be noticed, the computational complexity of the presented frequency estimation technique mainly depends on the implementation of three DFT based digital filter with N_w constant coefficients.

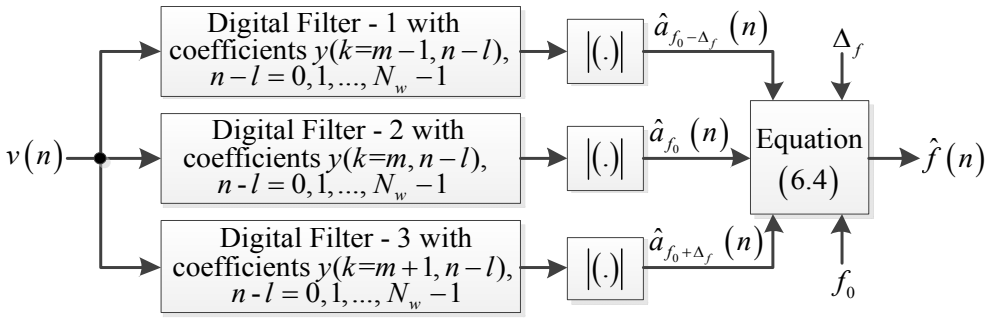

Fig. 6.3 Digital filter implementation of the fixed window DFT operation for fundamental frequency estimation.

The presented DFT based frequency tracking strategy requires a fixed-size memory buffer to store the samples of the grid voltage waveform. A sliding window strategy is followed to estimate the instantaneous fundamental frequency and hence the memory buffer is updated at every new acquired sample and the oldest one is discarded. The use of a large fixed-size window improves the frequency resolution. However, it requires large size memory buffer and the frequency tracking zone is reduced and also increases the computational burden. Moreover, the large size window causes a narrower bandwidth of the DFT operation, as shown in Fig. 6.4, and hence it degrades the dynamic response. On the other hand, a small size window improves the dynamic response due to the higher bandwidth of the DFT operation and decreases the computational burden, but it degrades the frequency resolution. Moreover, for the small size window, harmonics interference may occur due to the spectral line next to the frequency f_0 which might be corresponding to some harmonic components and hence estimation may contain erroneous results [98, 99]. The choice of the window size also depends on the expected variation zone of the

fundamental frequency. Therefore, a compromise is required for choosing the window size of the DFT operation to track the time-varying grid voltage frequency adaptively.

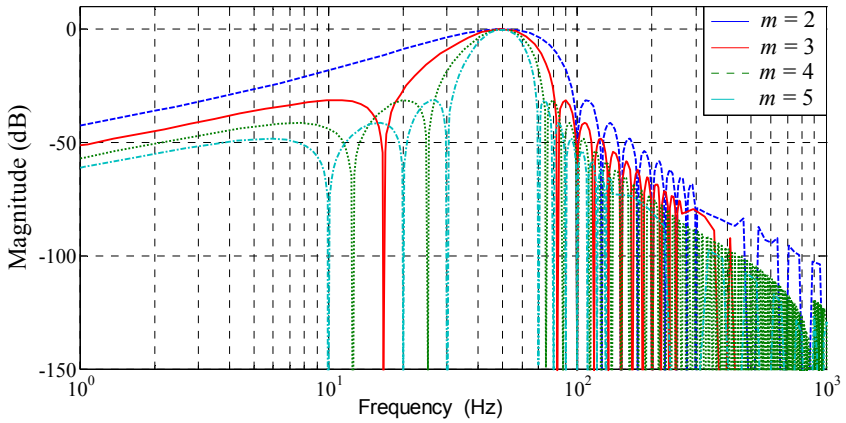

Fig. 6.4 Magnitude responses of the different fixed-size window based DFT operation at nominal fundamental frequency (50 Hz).

6.1.2 Fundamental Voltage Amplitude Estimation

In the DFT-SOGI technique, the fundamental voltage amplitude is estimated by a QSG-SOGI system whose tuning frequency is provided by the DFT operation as described earlier. The QSG-SOGI is shown in Fig. 2.4, where e_v is the error voltage and σ is the gain of the SOGI. The transfer functions of the SOGI, in-phase and in-quadrature components of the QSG-SOGI can be expressed by (6.6), (6.7) and (6.8), respectively.

$$T_4(s) = \frac{v_1'(s)}{\sigma e_v(s)} = \frac{s\omega_r}{s^2 + \omega_r^2} \tag{6.6}$$

$$T_5(s) = \frac{v_1'(s)}{v(s)} = \frac{\sigma\omega_r s}{s^2 + \sigma\omega_r s + \omega_r^2} \tag{6.7}$$

$$T_6(s) = \frac{qv_1'(s)}{v(s)} = \frac{\sigma\omega_r^2}{s^2 + \sigma\omega_r s + \omega_r^2} \tag{6.8}$$

The Bode plots of (6.7) and (6.8) are shown in Fig. 6.5(a) and (b), respectively. As it can be seen, the transfer functions, as given by (6.7) and (6.8), behave like a band-pass filter (BPF) and a low-pass filter (LPF), respectively. It can also be seen that the tuning frequency (ω_r) sets the resonance frequency of the SOGI and the gain (σ) determines the

bandwidth of the in-phase component and the static gain of the in-quadrature component [183, 193, 197, 198]. A trade-off is required between good dynamics and harmonics rejection capability when choosing the value of σ, where $\sigma = 2\xi$ and ξ denotes the damping factor of the QSG-SOGI [183, 193, 197, 198].

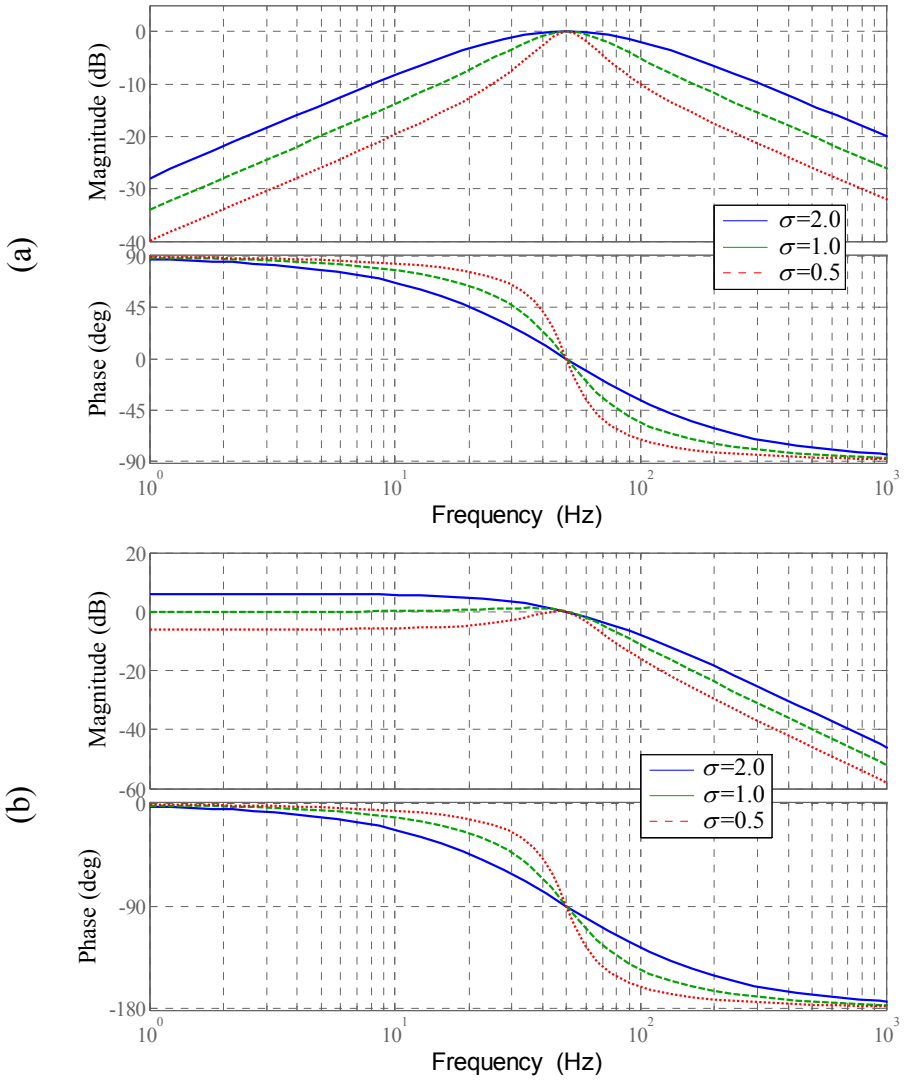

Fig. 6.5 Bode plots of the (a) in-phase transfer function (T_5) and (b) in-quadrature transfer function (T_6) of the QSG-SOGI, where $\omega_r = 2\pi 50$ rad/s.

The discrete implementation of the SOGI is presented in Fig. 2.4, where the integrator blocks are replaced by third-order integrator shown in Fig. 6.6. The QSG-SOGI based on third-order integrators provides more accurate results as compared to the QSG-SOGI relying on Euler, Tustin or second-order integrators and hence the third-order integrators are used for discrete implementation of the SOGI [183, 195, 258].

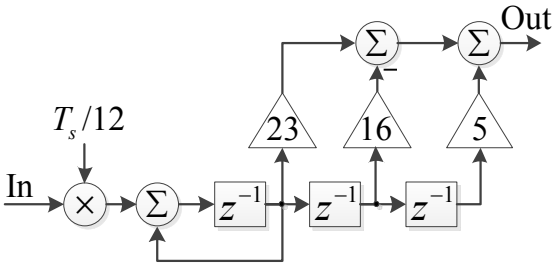

Fig. 6.6 Discrete implementation of a third-order integrator.

The estimation of the fundamental voltage amplitude and instantaneous phase angle using the QSG-SOGI can be expressed by (6.9) and (6.10), respectively.

$$\hat{A}_1(n) = \sqrt{v_1'^2(n) + q v_1'^2(n)} \tag{6.9}$$

$$\hat{\phi}_1(n) = \tan^{-1}\left\{-\frac{v_1'(n)}{q v_1'(n)}\right\} \tag{6.10}$$

The estimation of the fundamental voltage amplitude using (6.9) may contain ripple due to the presence of harmonics and DC offset. The MAF, as shown in Fig. 6.7(a), is used to remove the ripple from the estimated amplitude, where $N_{MAF}=f_s/F$ and F determines the window size (N_{MAF} samples) of the MAF. The Bode plots of the MAF for F=50 and 100 are shown in Fig. 6.7(b). In the presented technique, the value of F is made equal to the grid voltage fundamental frequency in order to reject the fundamental and harmonics ripple adaptively. The third-order integrator, as shown in Fig. 6.6, is used for discrete

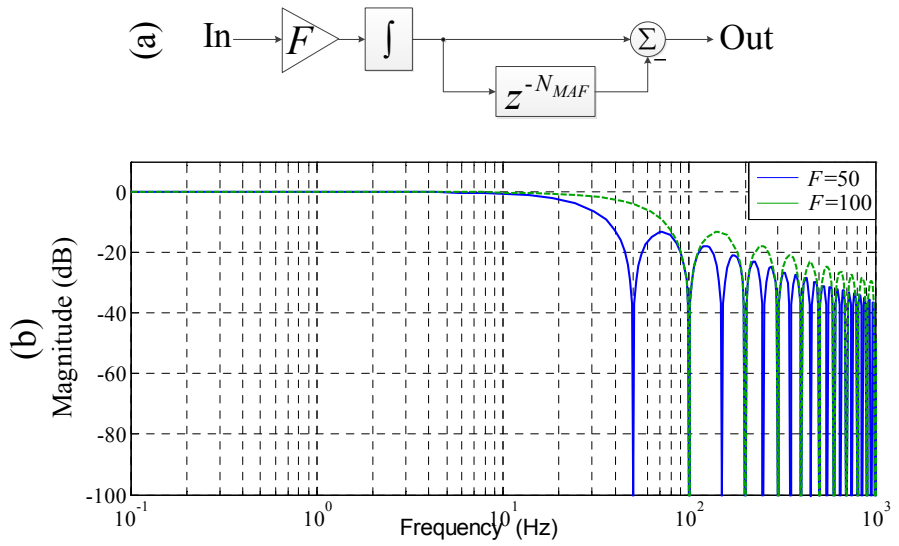

Fig. 6.7 (a) Block diagram of the MAF. (b) Bode plots of the MAF.

implementation of the MAF. The value of N_{MAF} in the MAF can be integer or non-integer, i.e. $L_2 \leq N_{MAF} < L_2+1$ where L_2 is a positive integer, L_2=floor(N_{MAF}), $b_2=N_{MAF}-L_2$ and $0 \leq b_2 < 1$, then linear interpolation can be used to get the value of $z^{-N_{MAF}}$ and is given by [78]

$$z^{-N_{MAF}} = (1-b_2)z^{-L_2} + b_2 z^{-L_2-1} \tag{6.11}$$

6.1.3 Simulation Results

A step change of frequency is considered in the grid voltage fundamental component for evaluating the performance of the fixed-size window based DFT operation. The effect of the different fixed-size window in the DFT operation for frequency estimation is shown in Fig. 6.8, where +1 Hz step change of frequency is occurred at time=1s. As it can be seen, the presented DFT operation provides faster response for the smaller size window and vice versa. However, the DFT operation with smaller size window produces higher ripple for off-nominal frequency estimation, as depicted by the magnified plot in Fig. 6.8.

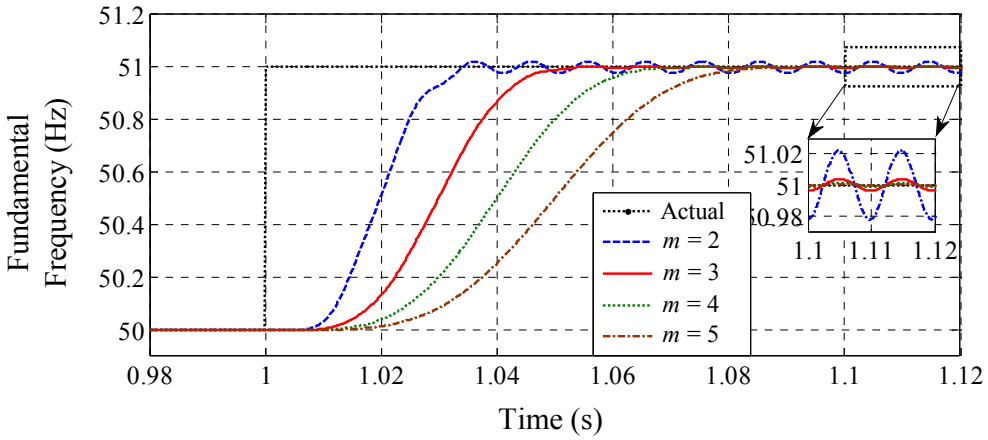

Fig. 6.8 Frequency step (+1 Hz: 50 Hz to 51 Hz) estimation using the DFT operation with different fixed-size window.

The IEEE standard C37.118.1 specifies a frequency range of 50 Hz ± 5 Hz (45 Hz to 55 Hz) for M class phasor measurement unit (PMU) [29, 31, 32]. The estimated frequency error for the frequency range of 45 Hz to 55 Hz using the DFT operation with different window size is shown in Fig. 6.9. As it can be noticed, the DFT operation with window size equal to 4 and 5 nominal fundamental cycles can be used to estimate the fundamental frequency range of 45 Hz to 55 Hz with an error less than 0.01 Hz and 0.005 Hz, respectively. On the other hand, the DFT operation with window size equal to 3 nominal

fundamental voltage cycles can be used to estimate the frequency range of 47 Hz to 52 Hz, as specified by the standard EN-50160, with an error less than 0.01 Hz, as can also be seen from Fig. 6.9.

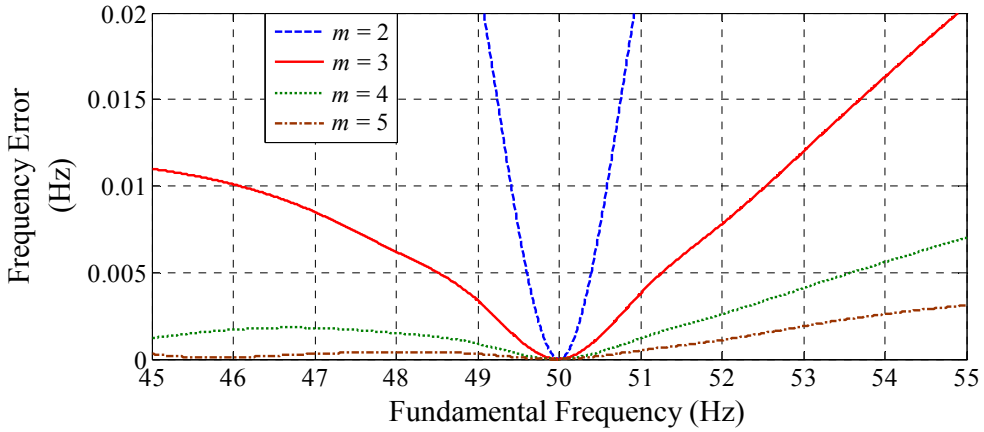

Fig. 6.9 Steady-state error of the estimated frequency using the DFT operation with different fixed-size window.

In the presented DFT-SOGI technique, the QSG-SOGI provides errors in the amplitude and phase angle estimation during an inaccurate tuning frequency. Fig. 6.10 and Fig. 6.11 show the amplitude and phase angle estimation errors due to the inaccurate tuning frequency of the SOGI for + 2 Hz and -3 Hz frequency steps, respectively, where $\sigma=\sqrt{2}$, m=3 and $F=\hat{f}$. As it can be seen, the DFT operation takes some time to estimate the frequency steps and hence the tuning frequency of the SOGI is not equal to the input voltage frequency during transients. It can also be observed that the errors disappear when the tuning frequency of the SOGI estimated by the DFT operation is equal to the input voltage frequency. However, the MAF introduces additional delay to remove the amplitude errors, as can also be noticed from Fig. 6.10(b) and Fig. 6.11(b), respectively.

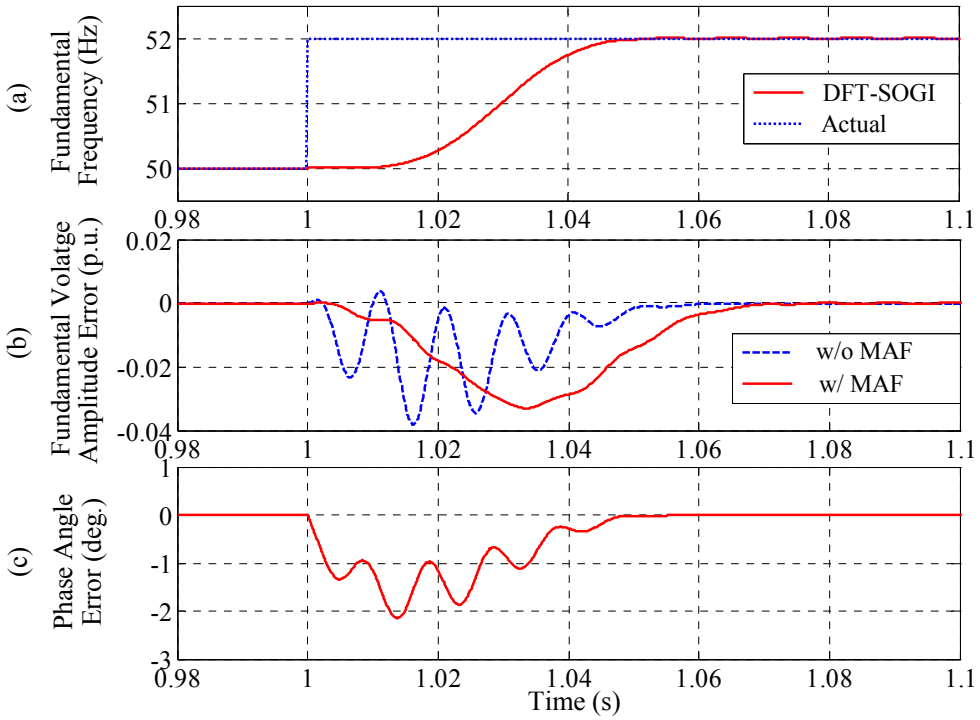

Fig. 6.10 Effects of the inaccurate frequency tracking on the amplitude and phase angle estimation. (a) Frequency step (+2 Hz: 50 Hz to 52 Hz). (b) Fundamental voltage amplitude error. (c) Phase angle error.

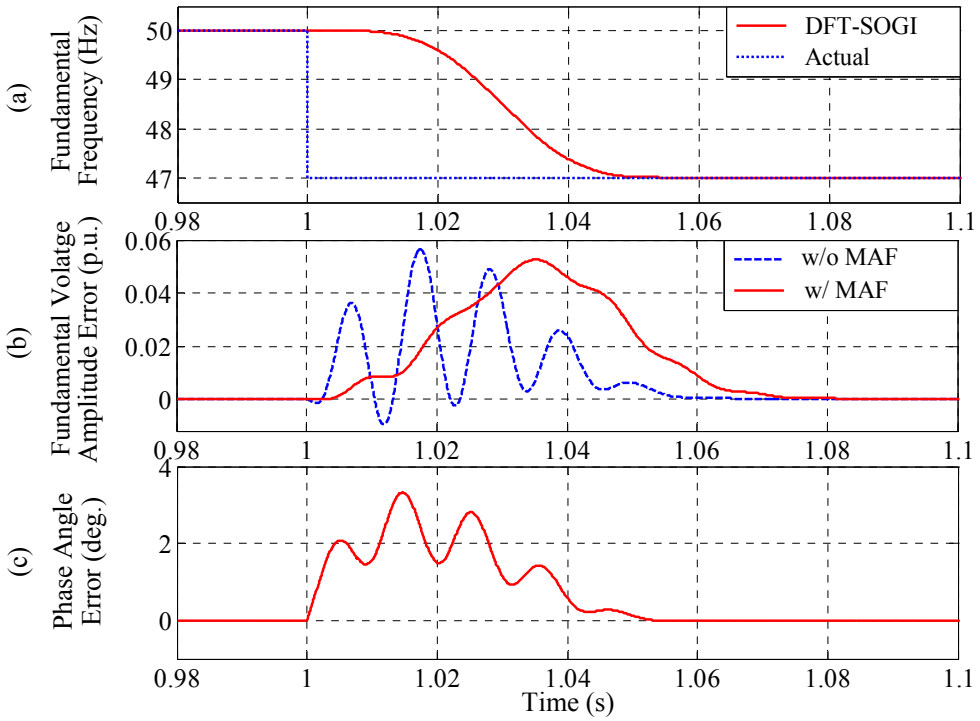

Fig. 6.11 Effects of the inaccurate frequency tracking on the amplitude and phase angle estimation. (a) Frequency step (-3 Hz: 50 Hz to 47 Hz). (b) Fundamental voltage amplitude error. (c) Phase angle error.

6.1.4 Real-Time Experimental Results

The performance of the DFT-SOGI technique is compared with the QSG-SOGI based frequency-locked loop (SOGI-FLL) [198] and phase-locked loop (SOGI-PLL) [182] techniques on a real-time experimental setup, as described in Section 1.3 of Chapter 1. Similar to the DFT-SOGI technique, a frequency adaptive MAF filter is included in the SOGI-FLL and SOGI-PLL techniques for rejecting ripple of the estimated fundamental voltage amplitude. The parameters, as specified in Table 6.1, are tuned so that approximately an equal settling time is obtained for the presented techniques. The sampling frequency is chosen as 10 kHz.

Table 6.1 Parameters of the DFT-SOGI, SOGI-FLL and SOGI-PLL techniques

DFT-SOGI	SOGI-FLL	SOGI-PLL
$\sigma = \sqrt{2},\ m = 3\ \&\ F = \hat{f}$	$\sigma = \sqrt{2},\ \gamma$=50 $\&\ F = \hat{f}$	$\sigma = \sqrt{2},\ k_p = k_i = 50\ \&\ F = \hat{f}$

The following real-time case studies are performed for evaluating the performance of the DFT-SOGI, SOGI-FLL and SOGI-PLL techniques.

i. Steady-state with harmonics (Case-A1)
ii. Steady-state with DC offset and harmonics (Case-A2)
iii. Frequency sweep and harmonics (Case-A3)
iv. Frequency step and harmonics (Case-A4)
v. Voltage flicker and harmonics (Case-A5)
vi. Voltage sag and harmonics (Case-A6)

In the above case studies, the grid voltage fundamental component contains 10% total harmonic distortion (THD), as given in Table 6.2.

Table 6.2 Harmonics as a percentage of fundamental component

Harmonics				THD
3^{rd}	5^{th}	7^{th}	9^{th}	10.0%
5.0%	5.0%	5.0%	5.0%	

6.1.4.1 Case-A1: Steady-State with Harmonics

The steady-state grid voltage waveform, as shown in Fig. 6.12(a), contains 10% THD. The harmonic contents are given in Table 6.2. The estimation of the fundamental voltage amplitude, frequency and phase angle error using the DFT-SOGI, SOGI-FLL and SOGI-PLL techniques are depicted in Fig. 6.12(b), (c) and (d), respectively. As it can be seen, the amplitude and frequency estimations at steady-state using the DFT-SOGI technique are less affected by the harmonic contents as compared to the SOGI-FLL and SOGI-PLL techniques. As the SOGI-FLL and SOGI-PLL techniques provide large ripple in the frequency estimation, hence the MAF cannot reject the amplitude ripple effectively as compared to the DFT-SOGI one which can be noticed in Fig. 6.12(b). On the other hand, the presented techniques provide a little phase angle error due to the presence of harmonics, as can be observed in Fig. 6.12(d).

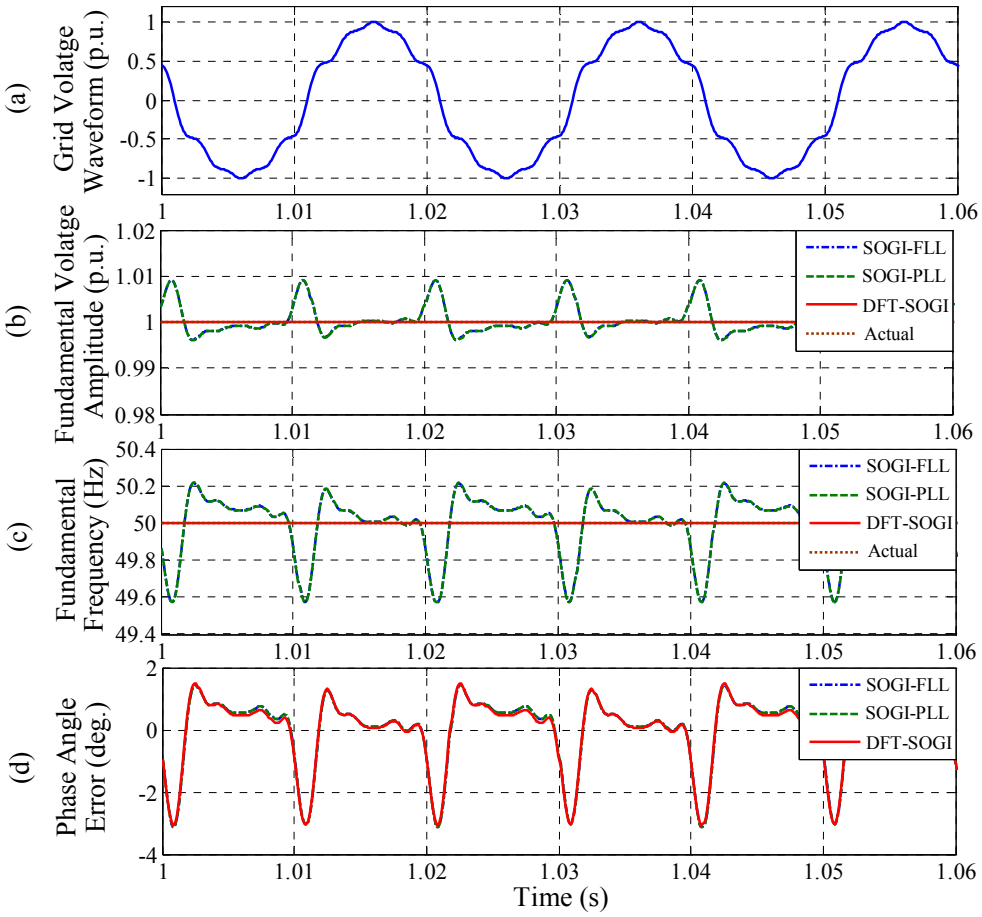

Fig. 6.12 Case-A1: Steady-state with harmonics. (a) Grid voltage waveform. (b) Fundamental voltage amplitude. (c) Fundamental frequency. (d) Phase angle error.

6.1.4.2 Case-A2: Steady-State with DC Offset and Harmonics

In this case, a +5% DC offset is added with a grid voltage waveform containing 10% THD and is shown in Fig. 6.13(a). The harmonic contents are presented in Table 6.2. The estimated fundamental voltage amplitude, frequency and phase angle error using the presented techniques are depicted in Fig. 6.13(b), (c) and (d), respectively. As it can be seen, the performance of the DFT-SOGI technique for amplitude and frequency estimation is less sensitive to the presence of the DC offset and harmonics as compared to the SOGI-FLL and SOGI-PLL techniques. However, it can be observed from Fig. 6.13(d) that the phase angle estimation using the presented techniques is affected due to the presence of DC offset and harmonics.

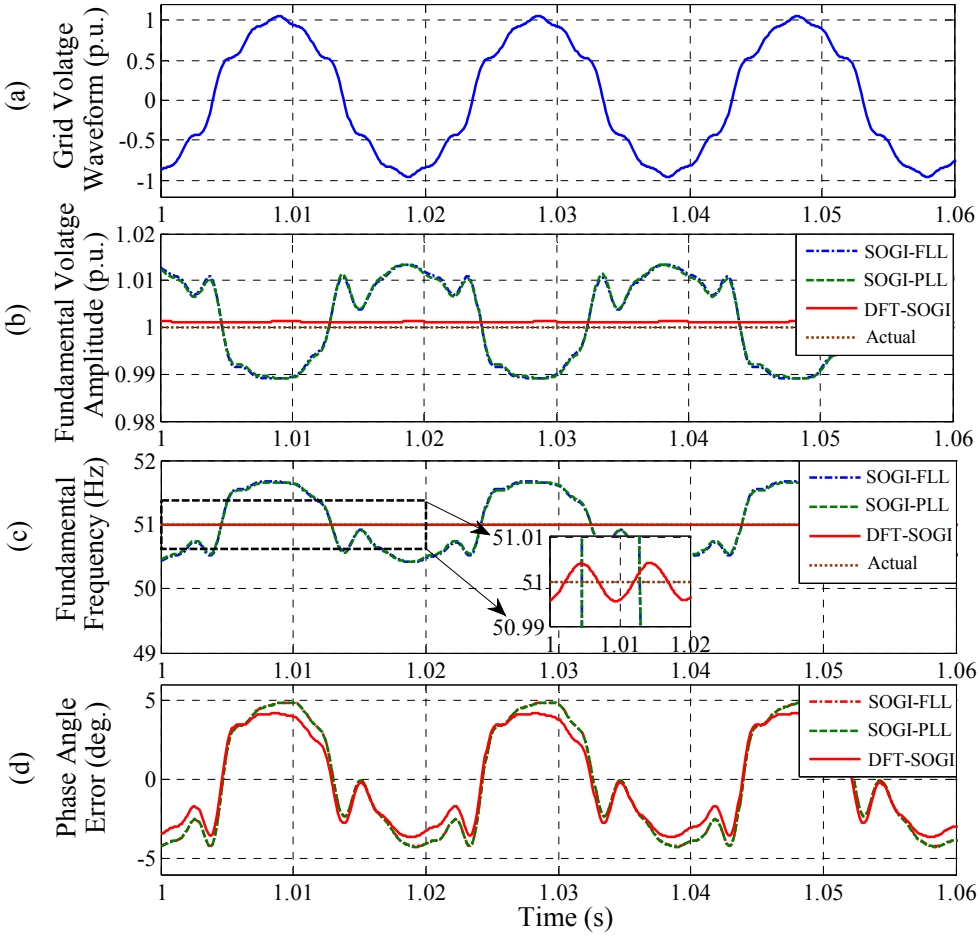

Fig. 6.13 Case-A2: Steady-state with DC offset (+5%) and harmonics. (a) Grid voltage waveform. (b) Fundamental voltage amplitude. (c) Fundamental frequency. (d) Phase angle error.

6.1.4.3 Case-A3: Frequency Sweep and Harmonics

A +10 Hz/s frequency sweep with a duration of 0.2s is considered in the grid voltage waveform containing 10% THD, as given in Table 6.2. The estimation of the fundamental voltage amplitude, frequency sweep and phase angle error using the investigated techniques are shown in Fig. 6.14. As it can be noticed, the DFT-SOGI technique can track the frequency sweep accurately while being less affected by harmonics as compared to the SOGI-FLL and SOGI-PLL techniques. On the other hand, all the presented techniques provide a small amplitude error due to the inaccurate tuning frequency of the QSG-SOGI during the frequency sweep condition. The estimated phase angle errors are similar for the presented techniques, as can be noticed in Fig. 6.14(c).

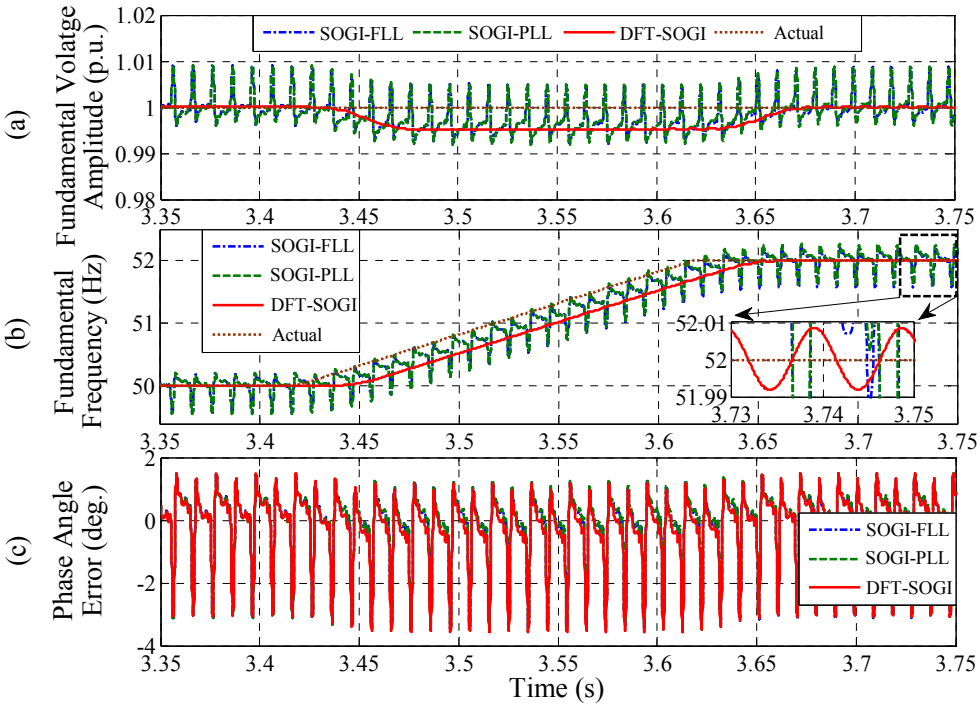

Fig. 6.14 Case-A3: Frequency sweep (+10 Hz/s: 50 Hz to 52 Hz) and harmonics. (a) Fundamental voltage amplitude. (b) Fundamental frequency. (c) Phase angle error.

6.1.4.4 Case-A4: Frequency Step and Harmonics

A frequency step is considered for comparing the performance of the DFT-SOGI, SOGI-FLL and SOGI-PLL techniques. Fig. 6.15 shows the estimation of fundamental voltage parameters using the presented techniques, where the grid voltage waveform contains 10% THD, as given in Table 6.2. It can be seen in Fig. 6.15(b) that the DFT-SOGI technique takes equal settling time for tracking the frequency step and is less disturbed by harmonics

as compared to the SOGI-FLL and SOGI-PLL techniques. Similar to simulation results presented in Fig. 6.11(b), the DFT-SOGI technique provides 0.05 p.u. amplitude error during -3 Hz frequency step, as can be noticed in Fig. 6.15(a). On the other hand, the phase angle estimation is affected due to the frequency step for all the presented techniques.

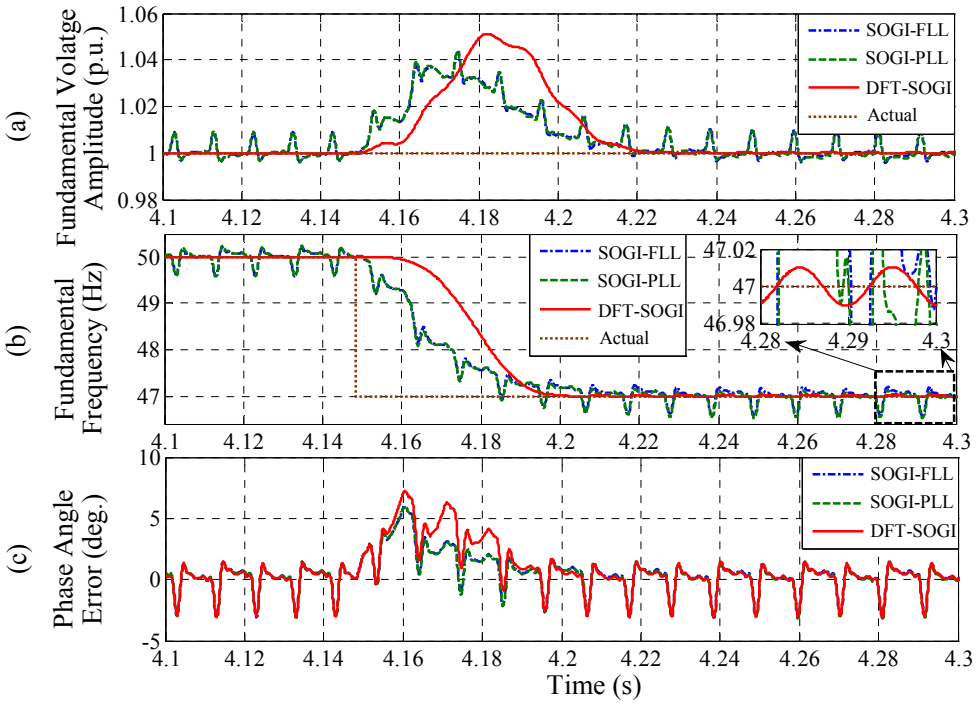

Fig. 6.15 Case-A4: Frequency step (-3 Hz: 50 Hz to 47 Hz) and harmonics. (a) Fundamental voltage amplitude. (b) Fundamental frequency. (c) Phase angle error.

6.1.4.5 Case-A5: Voltage Flicker and Harmonics

In this case, a triangular voltage flicker is introduced into the grid voltage waveform containing 10% THD, as shown in Fig. 6.16(a). The harmonics are presented in Table 6.2. The frequency and amplitude of the triangular voltage flicker are 2.5 Hz and ±5% of the fundamental voltage amplitude, respectively. The estimation of fundamental voltage amplitude, frequency and phase angle error are shown in Fig. 6.16(b), (c) and (d), respectively. As it can be seen, the presented techniques can track the voltage flicker. However, the performance of the DFT-SOGI one for amplitude and frequency estimation is less affected by harmonics as compared to the SOGI-FLL and SOGI-PLL techniques. It can be noticed from Fig. 6.16(d) that the presented techniques provide similar phase angle estimation error during the voltage flicker and harmonics.

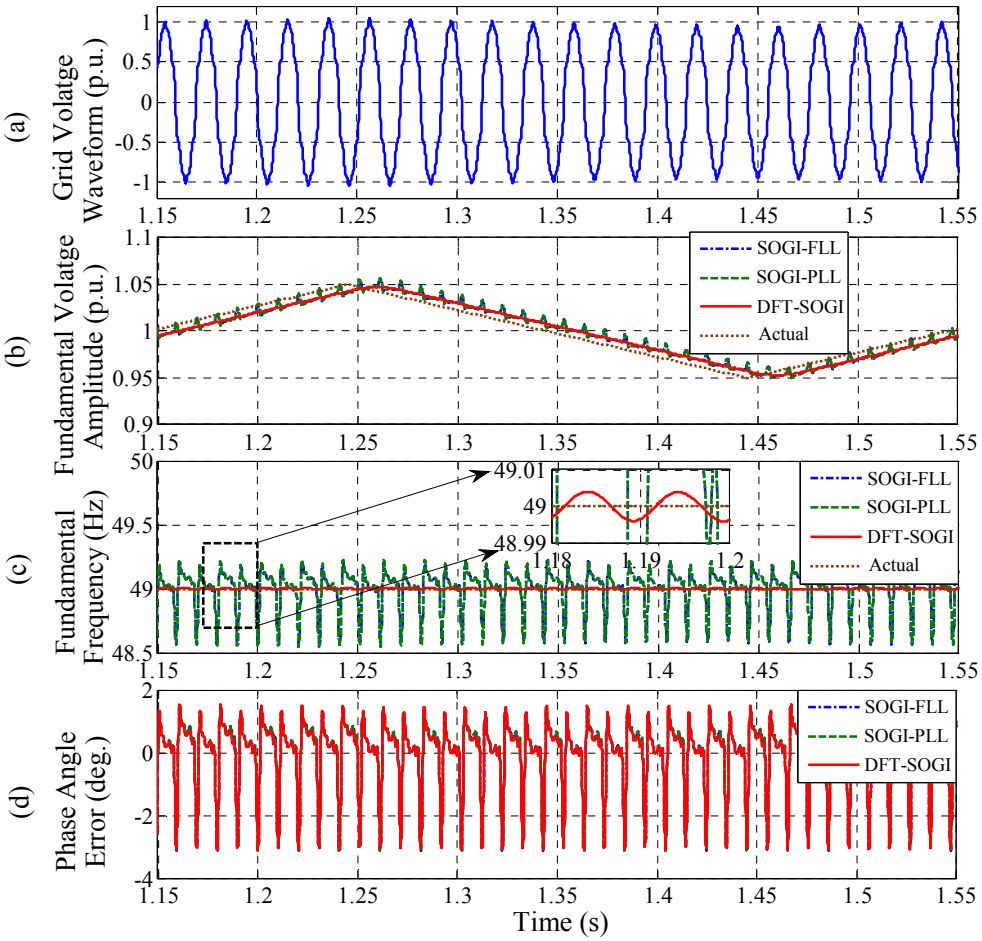

Fig. 6.16 Case-A5: Voltage flicker (±5%) and harmonics. (a) Grid voltage waveform. (b) Fundamental voltage amplitude. (c) Fundamental frequency. (d) Phase angle error.

6.1.4.6 Case-A6: Voltage Sag and Harmonics

A grid voltage waveform containing 50% voltage sag and 10% THD is shown in Fig. 6.17(a). The harmonics are given in Table 6.2. The estimation of fundamental voltage amplitude, frequency and phase angle error using the DFT-SOGI, SOGI-FLL and SOGI-PLL techniques are shown in Fig. 6.17(b), (c) and (d), respectively. As it can be noticed, the presented techniques can track the voltage sag. However, it can be noticed from Fig. 6.17(c) that the DFT-SOGI technique presents less overshoot/undershoot in the frequency estimation during the voltage sag as compared to the SOGI-FLL and SOGI-PLL techniques. On the other hand, the performance of the presented techniques for phase angle estimation is affected by the voltage sag, as can be observed in Fig. 6.17(d).

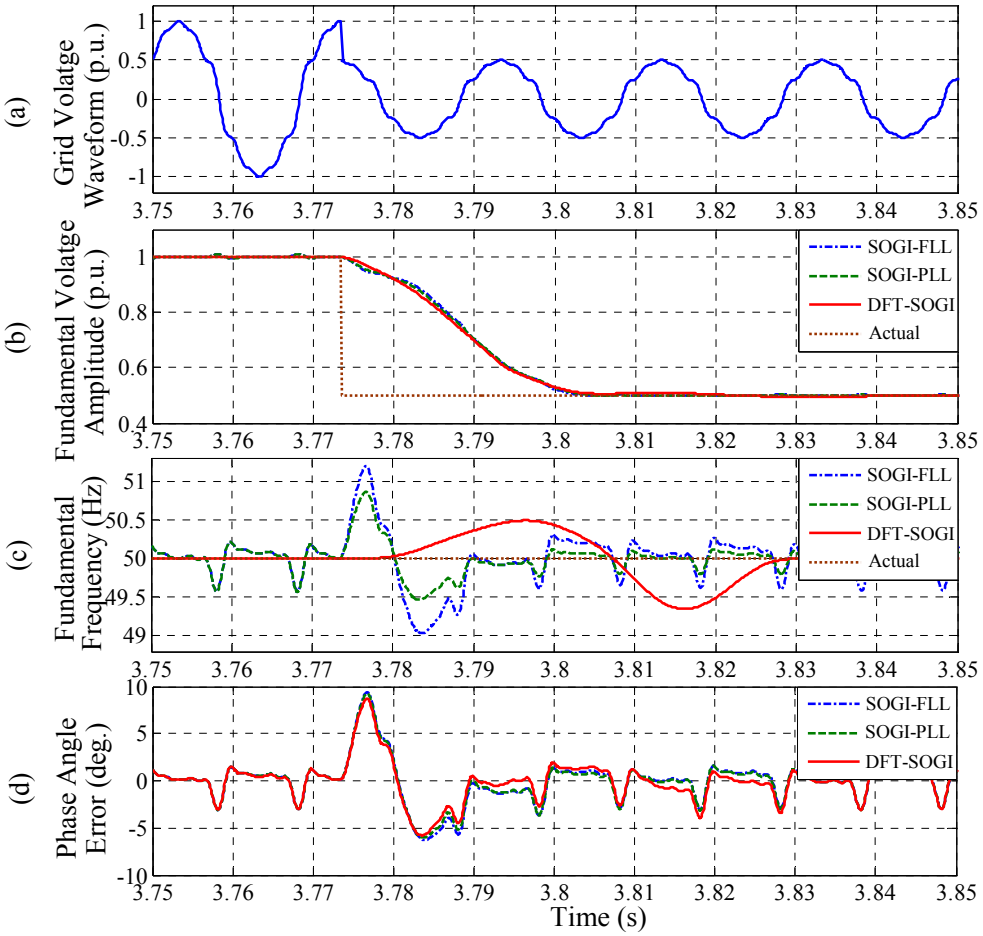

Fig. 6.17 Case-A6: Voltage sag (50%) and harmonics. (a) Grid voltage waveform. (b) Fundamental voltage amplitude. (c) Fundamental frequency. (d) Phase angle error.

6.1.4.7 Computational Burden Comparison

It can be seen from the experimental results presented in case studies A1-A6 that the performance of the DFT-SOGI technique for frequency estimation is less affected by the presence of harmonics as compared to the SOGI-FLL and SOGI-PLL techniques. In addition, the DFT-SOGI technique avoids the use of the interdependent loops, which offers easy tuning process. All these advantages of using the DFT-SOGI technique come to the expense of more computationally demanding as compared to the SOGI-FLL and SOGI-PLL techniques. Although the presented fixed-size window based DFT operation does not require the evaluation of trigonometric functions in real-time, the use of three high-order DFT filters increases the computational burden of the DFT-SOGI technique as compared to the SOGI-FLL and SOGI-PLL techniques. Therefore, a compromise is made between high accuracy frequency estimation and digital resources consumption.

6.2 Power System Fundamental Voltage Amplitude and Frequency Estimation using A Fixed Frequency Tuned Second-Order Generalized Integrator Based Technique

In this section, a technique based on SOGI tuned at a fixed frequency is described for estimating the single-phase grid voltage fundamental amplitude and frequency under distorted grid conditions. The block diagram of the proposed technique is shown in Fig. 6.18. As it can be seen, the QSG-SOGI is used to obtain the orthogonal waveforms of the grid voltage fundamental component, which are then used to estimate the fundamental voltage amplitude and frequency.

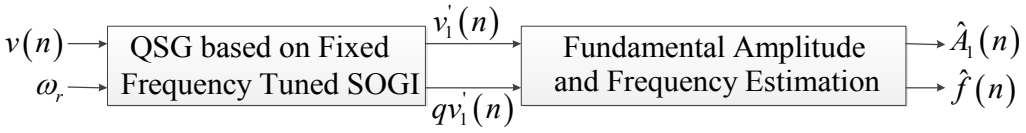

Fig. 6.18 Block diagram of the proposed technique using a QSG based on a SOGI tuned at fixed frequency for estimating the single-phase grid voltage fundamental amplitude and frequency.

6.2.1 Fundamental Voltage Amplitude Estimation

Based on a fixed value of ω_r, the steady-state fundamental voltage orthogonal waveforms obtained by the QSG-SOGI, as shown in Fig. 2.4, can be approximated by (6.12) and (6.13), respectively [193, 197, 198].

$$v_1'(n) = A_1(n)\left|T_5\left\{j\omega(n)\right\}\right|\sin\left[\omega_0 nT_s + \psi_1(n) + \angle T_5\left\{j\omega(n)\right\}\right] \tag{6.12}$$

$$qv_1'(n) = -A_1(n)\left|T_5\left\{j\omega(n)\right\}\right|\left\{\frac{\omega_r}{\omega(n)}\right\}\cos\left[\omega_0 nT_s + \psi_1(n) + \angle T_5\left\{j\omega(n)\right\}\right] \tag{6.13}$$

where

$$\left|T_5\left\{j\omega(n)\right\}\right| = \frac{\sigma\omega(n)\omega_r}{\sqrt{\left\{\sigma\omega(n)\omega_r\right\}^2 + \left\{\omega^2(n) - \omega_r^2\right\}^2}}$$

$$\angle T_5\left\{j\omega(n)\right\} = \tan^{-1}\left\{\frac{\omega_r^2 - \omega^2(n)}{\sigma\omega(n)\omega_r}\right\}$$

and $\psi_1(n) = \Delta\omega(n)nT_s + \theta_1(n)$ is the initial phase angle (θ_1) plus instantaneous phase angle $\{\Delta\omega(n)nT_s\}$ corresponding to fundamental angular frequency deviation $(\Delta\omega)$. It can be seen from (6.12) and (6.13) that v_1' always leads qv_1' by 90° irrespective of the values of σ and ω_r. For the condition $\omega_r = \omega$, the amplitudes of v_1' and qv_1' are equal to the amplitude of v_1, since $\left|T_5\{j\omega(n)\}\right| = 1$ and $\angle T_5\{j\omega(n)\} = 0$ when $\omega_r = \omega$. On the other hand, for the condition $\omega_r \neq \omega$, the amplitudes of v_1' and qv_1' are different and also not equal to the amplitude of v_1. However, if the values of ω_r and ω are known, the fundamental voltage amplitude can also be estimated from (6.12) and (6.13), respectively, and is given by

$$\hat{A}_1(n) = \frac{1}{\left|T_5\left\{j\omega(n)\right\}\right|}\sqrt{v_1'^2(n) + \frac{\omega^2(n)}{\omega_r^2}qv_1'^2(n)} \tag{6.14}$$

In the proposed technique, the QSG-SOGI is tuned at a fixed angular frequency and the grid voltage fundamental angular frequency is estimated separately. The grid voltage fundamental amplitude is then estimated using (6.14). A MAF, as shown in Fig. 6.7(a), is also used to remove the ripple from the estimated fundamental voltage amplitude. An integrator based on backward Euler method, as shown in Fig. 6.19, is used for discrete implementation of the MAF. The linear interpolation operation, as given by (6.11), is also used when the number of samples in the window size of the MAF is not an integer value.

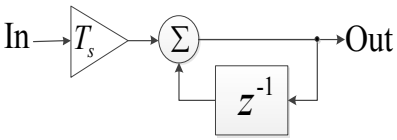

Fig. 6.19 Discrete integrator based on the backward Euler method.

6.2.2 Fundamental Frequency Estimation

In the proposed technique, the actual fundamental angular frequency is estimated by

$$\hat{\omega}(n) = \omega_0 + \Delta\hat{\omega}(n) \tag{6.15}$$

where $\Delta\hat{\omega}$ can be obtained by differentiating $\psi_1(n)$ with respect to time and is expressed by

$$\Delta\hat{\omega}(n) = \frac{d}{dt}\psi_1(t)\Big|_{t=nT_s} \tag{6.16}$$

where t is time in continuous domain and is discretised by $t = nT_s$, and $\psi_1(n)$ can be obtained by

$$\psi_1(n) = \tan^{-1}\left\{-\frac{v_1'(n)}{qv_1'(n)}\right\}_{\text{unwrapped}} - \omega_0 nT_s \tag{6.17}$$

where the subscript 'unwrapped' indicates that the estimated sawtooth phase angle waveform is unwrapped. However, due to the condition $\omega_r \neq \omega$, the instantaneous phase angle, as obtained by (6.17), will contain two types of phase angle error i.e. an error introduced by $\angle T_5\{j\omega(n)\}$ and an estimation error occurs due to the factor ω_r / ω, as can be noticed from (6.12) and (6.13). Moreover, the lower order harmonics may introduce significant distortions into the estimated phase angle.

6.2.2.1 Error Introduced by $\angle T_5\{j\omega(n)\}$

The plots of $\angle T_5\{j\omega(n)\}$ for different values of σ and $\omega_r = 2\pi 50$ rad/s are shown in the phase response of Fig. 6.5(a). Due to the differentiation operation, the angular frequency error $(\omega_{\angle T_5})$ introduced by $\angle T_5\{j\omega(n)\}$ can be obtained by

$$\omega_{\angle T_5} = \frac{d}{dt}\angle T_5\left\{j\omega(t)\right\} = \begin{cases} 0 & \text{for } \omega_r = \omega \\ \dfrac{-\sigma\omega_r\left\{\omega^2(t) + \omega_r^2\right\}}{\sigma^2\omega^2(t)\omega_r^2 + \left\{\omega^2(t) - \omega_r^2\right\}^2}\dfrac{d}{dt}\omega(t) & \text{for } \omega_r \neq \omega \end{cases} \tag{6.18}$$

It can be seen from (6.18) that $\omega_{\angle T_5}$ is zero when $\omega_r = \omega$. The plots of $\omega_{\angle T_5}$ for $\omega_r \neq \omega$ are shown in Fig. 6.20. As it can be seen, $\omega_{\angle T_5}$ is also zero when ω is constant i.e. the rate of the frequency change (*df*/*dt*) is zero. However, the variation of frequency will introduce an error whose magnitude depends on the rate of the frequency change. The grid frequency

varies slowly and hence the estimated frequency error introduced by $\angle T_5\{j\omega(n)\}$ will be small and thus can be neglected.

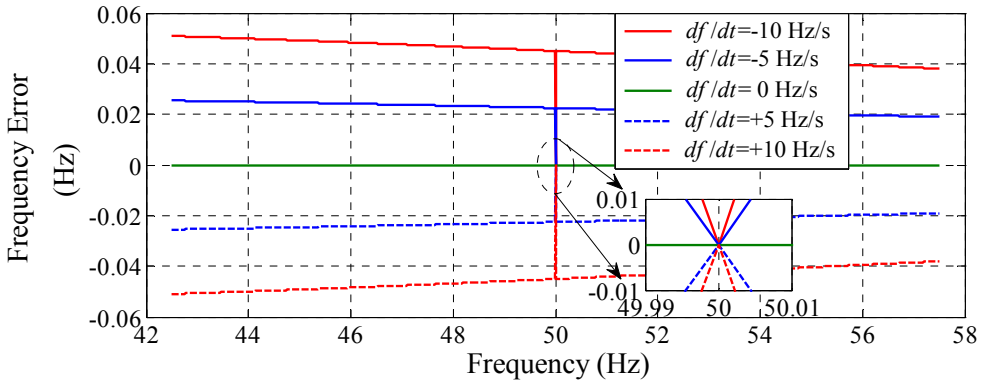

Fig. 6.20 Frequency error caused by $\angle T_5\{j\omega(n)\}$ due to the differentiation of the instantaneous phase angle, where $\sigma=\sqrt{2}$ and ω_r=2π50 rad/s.

6.2.2.2 Error Introduced by ω_r / ω

The following relation can be written from the orthogonal voltage waveforms obtained by (6.12) and (6.13), respectively.

$$-\frac{v_1'(n)}{qv_1'(n)}=\frac{\omega(n)}{\omega_r}\tan\left[\omega_0 nT_s+\psi_1(n)+\angle T_5\{j\omega(n)\}\right] \tag{6.19}$$

Expression (6.19) can also be written as

$$\omega_0 nT_s+\psi_1(n)+\angle T_5\{j\omega(n)\}=\tan^{-1}\left\{-\frac{\omega_r}{\omega(n)}\cdot\frac{v_1'(n)}{qv_1'(n)}\right\} \tag{6.20}$$

Thus, the estimated phase angle using v_1' and qv_1' can be expressed by

$$\omega_0 nT_s+\psi_1(n)+\angle T_5\{j\omega(n)\}+\theta_{er}(n)=\tan^{-1}\left\{-\frac{v_1'(n)}{qv_1'(n)}\right\} \tag{6.21}$$

where $\theta_{er}(n)$ is the estimated phase angle error introduced by the factor ω_r / ω. The following expression can be obtained from (6.19) and (6.21).

$$\frac{\omega(n)}{\omega_r}\tan\left[\omega_0 nT_s+\psi_1(n)+\angle T_5\{j\omega(n)\}\right]=\tan\left[\omega_0 nT_s+\psi_1(n)+\angle T_5\{j\omega(n)\}+\theta_{er}(n)\right] \tag{6.22}$$

For calculating the estimated phase angle error $\theta_{er}(n)$, expression (6.22) can be simplified using the following relation

$$\tan\left[\omega_0 nT_s + \psi_1(n) + \angle T_5\left\{j\omega(n)\right\} + \theta_{er}(n)\right]$$

$$= \frac{\tan\left[\omega_0 nT_s + \psi_1(n) + \angle T_5\left\{j\omega(n)\right\}\right] + \tan\left\{\theta_{er}(n)\right\}}{1 - \tan\left[\omega_0 nT_s + \psi_1(n) + \angle T_5\left\{j\omega(n)\right\}\right]\tan\left\{\theta_{er}(n)\right\}}$$

After some mathematical calculations, $\theta_{er}(n)$ can be expressed by

$$\theta_{er}(n) = \tan^{-1}\frac{0.5\left\{\frac{\omega(n)}{\omega_r} - 1\right\}\sin\left[2\omega_0 nT_s + 2\psi_1(n) + 2\angle T_5\left\{j\omega(n)\right\}\right]}{1 + 0.5\left\{\frac{\omega(n)}{\omega_r} - 1\right\}\left[1 - \cos\left[2\omega_0 nT_s + 2\psi_1(n) + 2\angle T_5\left\{j\omega(n)\right\}\right]\right]} \tag{6.23}$$

The plot of $\theta_{er}(n)$ is shown in Fig. 6.21. As it can be seen, $\theta_{er}(n)$ is zero when $\omega_r = \omega$. Otherwise, $\theta_{er}(n)$ is a second harmonic oscillation of the actual fundamental frequency. Thus, a LPF is required to reject the second harmonic oscillation caused by the factor ω_r / ω from the estimated phase angle.

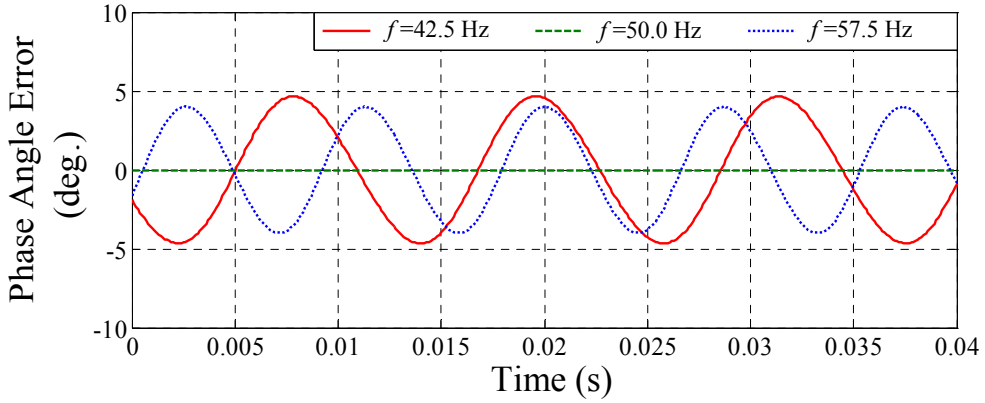

Fig. 6.21 Phase angle error $\{\theta_{er}(n)\}$ introduced by the factor ω_r / ω, where $\sigma = \sqrt{2}$, $\omega_r = 2\pi 50$ rad/s and $\theta_1 = 0$.

6.2.2.3 Frequency Estimation using Differentiation Filter

An infinite-impulse-response (IIR) differentiation filter (DF) for estimating the frequency from the instantaneous phase angle has been derived in Subsection 4.1.3 of Chapter 4. Same IIR DF, as expressed by $T_2(z)$ in (4.24), is also used in the proposed fixed frequency tuned SOGI based technique. An IIR LPF is also cascaded with the fixed size

window based IIR DF for better attenuation of the ripple from the estimated time-varying frequency at the cost of a slower dynamic response.

The implementation of the proposed QSG-SOGI and DF based (SOGI-DF) technique is shown in Fig. 6.22. As it can be seen, the instantaneous phase angle is estimated using the orthogonal voltage waveforms obtained by the QSG based on the fixed frequency tuned SOGI. The fundamental frequency deviation is then estimated by differentiating the unwrapped instantaneous phase angle and is added with the nominal value to obtain the actual frequency. The estimated frequency is also used to obtain the actual fundamental voltage amplitude. The harmonics ripple of the estimated fundamental voltage amplitude is rejected using a frequency adaptive MAF. It can be noticed from Fig. 6.22 that the proposed technique does not include interdependent loops between the orthogonal voltage system and the frequency estimation, thus making the technique robust and offering an easy tuning process as compared to the QSG-SOGI based techniques including interdependent loops such as SOGI-FLL [198] or SOGI-PLL [182]. The proposed SOGI-DF technique is also computationally efficient when compared with the DFT-SOGI technique, as described earlier in Section 6.1 of this chapter.

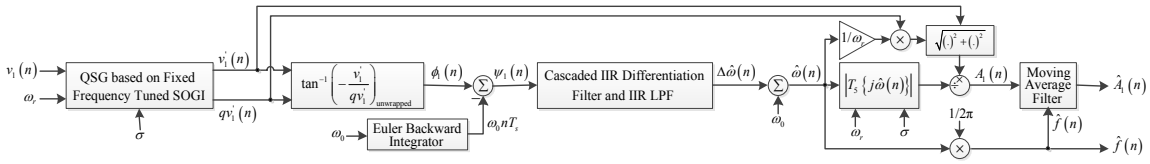

Fig. 6.22 Proposed SOGI-DF technique for the estimation of single-phase grid voltage fundamental amplitude and frequency.

6.2.3 Simulation Results

The performance of the proposed SOGI-DF technique is compared with a QSG relying on the fixed frequency tuned SOGI and least-squares based (SOGI-LS) technique [259]. The parameters of both techniques, as given in Table 6.3, are tuned so that approximately equal dynamics are obtained, where $\square$ indicates transpose operation. Similar to the SOGI-DF technique, same IIR LPF and MAF are used for the SOGI-LS technique to filter the estimated fundamental frequency and amplitude, respectively. The response of the SOGI-DF and SOGI-LS techniques during a -7.5 Hz frequency step is presented in Fig. 6.23, where the grid voltage waveform contains only fundamental component with 1.0 p.u. amplitude. As it can be seen from the magnified plots in Fig. 6.23(b), the SOGI-LS

technique can provide accurate estimation of nominal and off-nominal fundamental frequency under undistorted condition. On the other hand, the SOGI-DF technique can provide accurate estimation of nominal frequency. However, due to the second harmonic oscillation of θ_{er} for $\omega_r \neq \omega$, as shown in Fig. 6.21, the proposed technique generates second harmonic ripple at steady-state off-nominal fundamental frequency (42.5 Hz) estimation, which can be seen from the magnified plot in Fig. 6.23(b). The frequency step estimation time is less than the maximum phasor estimation time (0.2s), as specified by the standard IEC 61000-4-7 [254]. It can be noticed from Fig. 6.23(a) that both techniques based on the fixed frequency tuned SOGI can provide accurate and similar estimation of fundamental voltage amplitude during nominal and off-nominal frequency conditions.

Table 6.3 Parameters of the SOGI-DF and SOGI-LS techniques

SOGI-DF	SOGI-LS
QSG-SOGI: $\sigma=\sqrt{2}$, $\omega_r=\omega_0$ DF: T_w=40 ms	QSG-SOGI: $\sigma=\sqrt{2}$, $\omega_r=\omega_0$ LS: λ_{LS}=70, $\theta_{0-LS}=[\omega_0^2 \quad \omega_0^2]^{\square}$
f_s=10 kHz. IIR LPF: order = 2, cut-off frequency = 15Hz. MAF: $F=\hat{f}$	

The steady-state relative errors of the estimated fundamental voltage amplitude and frequency using the SOGI-DF and SOGI-LS techniques under harmonics and frequency variation is presented in Fig. 6.24, where the relative error can be defined by (3.25). In this case, the fundamental voltage amplitude is 1.0 p.u., fundamental frequency is varied from 42.5 Hz to 57.5, as specified by the standard IEC 61000-4-30 [85], and 14.58% THD, as given in Table 3.1 of Chapter 3. As it can be seen from Fig. 6.24, the proposed SOGI-DF technique can provide improved estimation of fundamental voltage amplitude and frequency under harmonics as compared to the SOGI-LS technique. The SOGI-DF technique can also meet the estimated frequency error criteria, since the relative frequency error is less than 0.03% which is the maximum acceptable value, as specified by the IEC standard 61000-4-7.

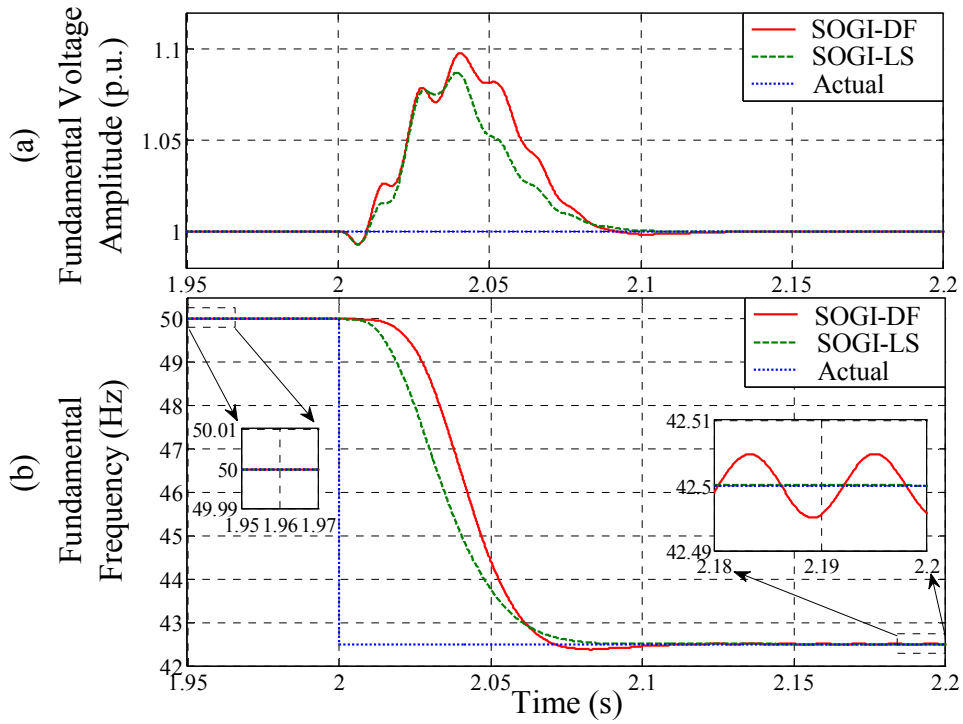

Fig. 6.23 Dynamic performance of the SOGI-DF and SOGI-LS techniques during -7.5 Hz (50 Hz to 42.5 Hz) frequency step. (a) Fundamental voltage amplitude. (b) Fundamental frequency.

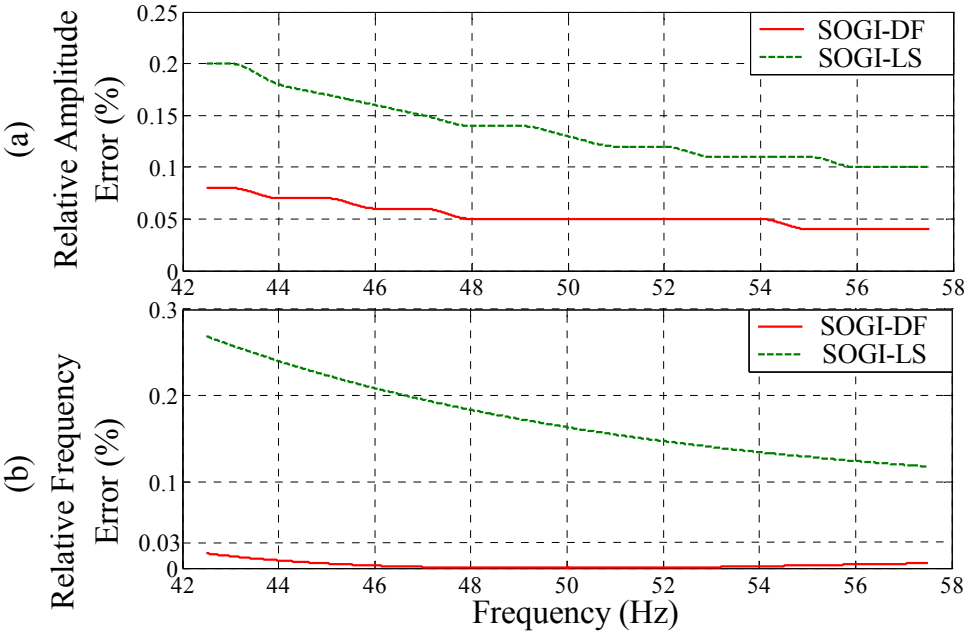

Fig. 6.24 Steady-state performance of the SOGI-DF and SOGI-LS techniques under harmonics, as given in Table 3.1. (a) Relative fundamental voltage amplitude error. (b) Relative frequency error.

6.2.4 Real-Time Experimental Results

The performance of the SOGI-DF and SOGI-LS techniques is compared using real-time experimental results. The experimental setup is described in Section 1.3 of Chapter. The parameters of the SOGI-DF and SOGI-LS techniques are given in Table 6.3. The performance is compared under the following real-time case studies:

i. Steady-state with DC offset and harmonics (Case-B1)
ii. Frequency sweep and harmonics (Case-B2)
iii. Frequency step and harmonics (Case-B3)
iv. Voltage sag and harmonics (Case-B4)
v. Voltage flicker and harmonics (Case-B5)

The fundamental component of the grid voltage waveforms presented in all the above case studies contains 14.58% THD, as given in Table 3.1.

6.2.4.1 Case-B1: Steady-State with DC Offset and Harmonics

A grid voltage waveform containing 5% DC offset and 14.58% THD, as given in Table 3.1, is shown in Fig. 6.25(a). The estimation of the fundamental voltage amplitude and frequency using the SOGI-DF and SOGI-LS techniques are shown in Fig. 6.25(b) and (c), respectively. As it can be seen, the SOGI-DF technique can provide accurate estimation of fundamental frequency, however, generates a steady-state error in the amplitude estimation under DC offset and harmonics. On the other hand, the SOGI-LS technique produces a steady-state error in the estimation of both fundamental voltage amplitude and frequency due to the presence of DC offset and harmonics.

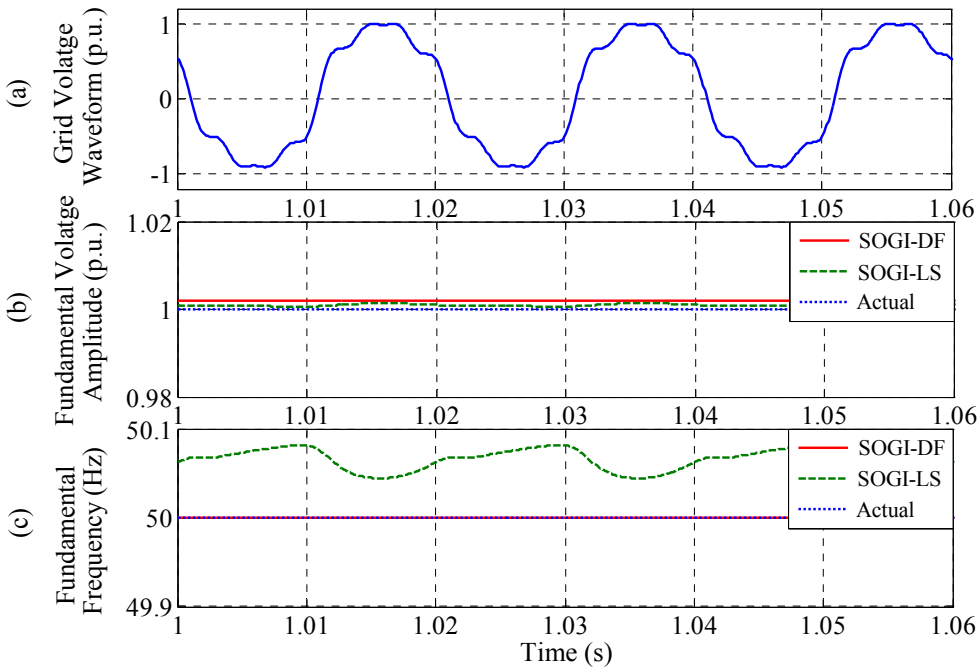

Fig. 6.25 Case-B1: Steady-state with DC offset (5%) and harmonics. (a) Grid voltage waveform. (b) Fundamental voltage amplitude. (c) Fundamental frequency.

6.2.4.2 Case-B2: Frequency Sweep and Harmonics

A fundamental frequency sweep of +10 Hz/s up to 57.5 Hz is considered into the grid voltage containing 14.58% THD, as given in Table 3.1. The estimation of the fundamental voltage amplitude and frequency sweep is shown in Fig. 6.26. As it can be noticed, both techniques can track the frequency sweep. However, the SOGI-LS technique presents an offset error for the estimation of 50 Hz and 57.5 Hz under harmonics, as can be seen from the magnified plots in Fig. 6.26(b). On the other hand, both techniques produce small steady-state errors in the estimation of fundamental voltage amplitude during the frequency sweep, as can be seen in Fig. 6.26(a).

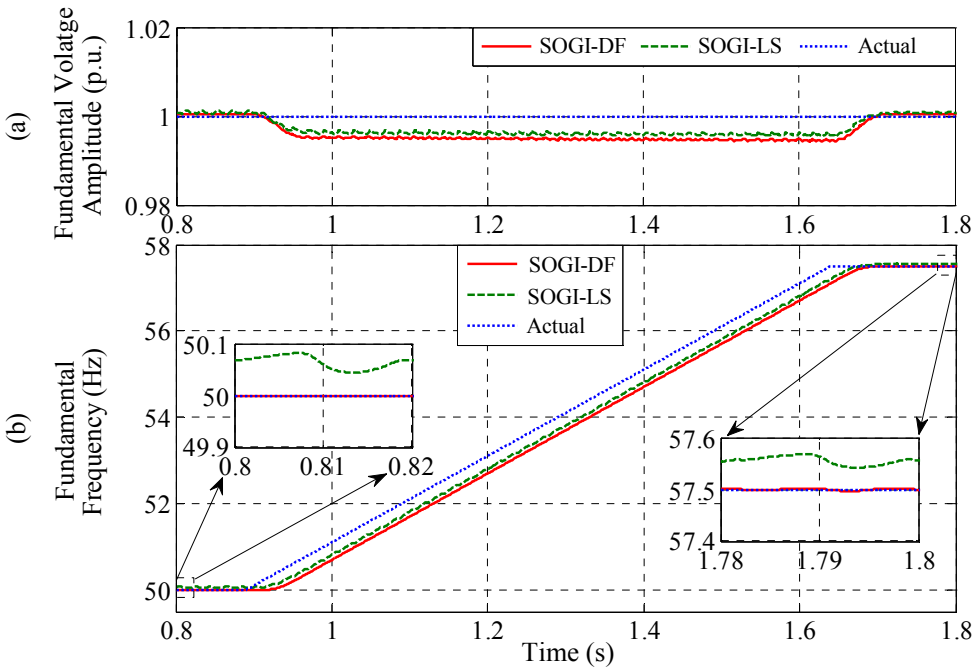

Fig. 6.26 Case-B2: Frequency sweep (+10 Hz/s: 50 Hz to 57.5 Hz) and harmonics. (a) Fundamental voltage amplitude. (b) Fundamental frequency.

6.2.4.3 Case-B3: Frequency Step and Harmonics

A fundamental frequency step of -7.5 Hz is considered into the grid voltage waveform containing 14.58% THD, as given in Table 3.1. The fundamental voltage amplitude and frequency estimation is shown in Fig. 6.27. As it can be seen, both techniques can track the frequency step. However, the SOGI-LS technique presents an offset error for the estimation of 42.5 Hz under 14.58% THD given in Table 3.1. The fundamental voltage amplitude estimation using both techniques is also affected by the frequency step, as noticed in Fig. 6.27(a).

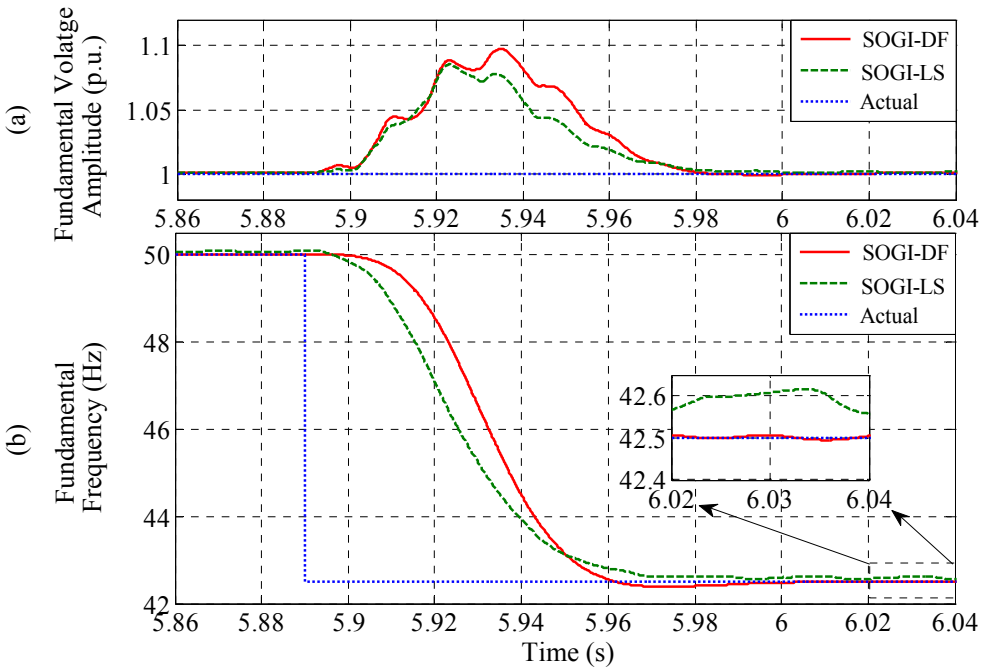

Fig. 6.27 Case-B3: Frequency step (-7.5 Hz: 50 Hz to 42.5 Hz) and harmonics. (a) Fundamental voltage amplitude. (b) Fundamental frequency.

6.2.4.4 Case-B4: Voltage Sag and Harmonics

The estimation of the fundamental voltage amplitude and frequency using the SOGI-DF and SOGI-LS techniques are depicted in Fig. 6.28, where the grid voltage waveform

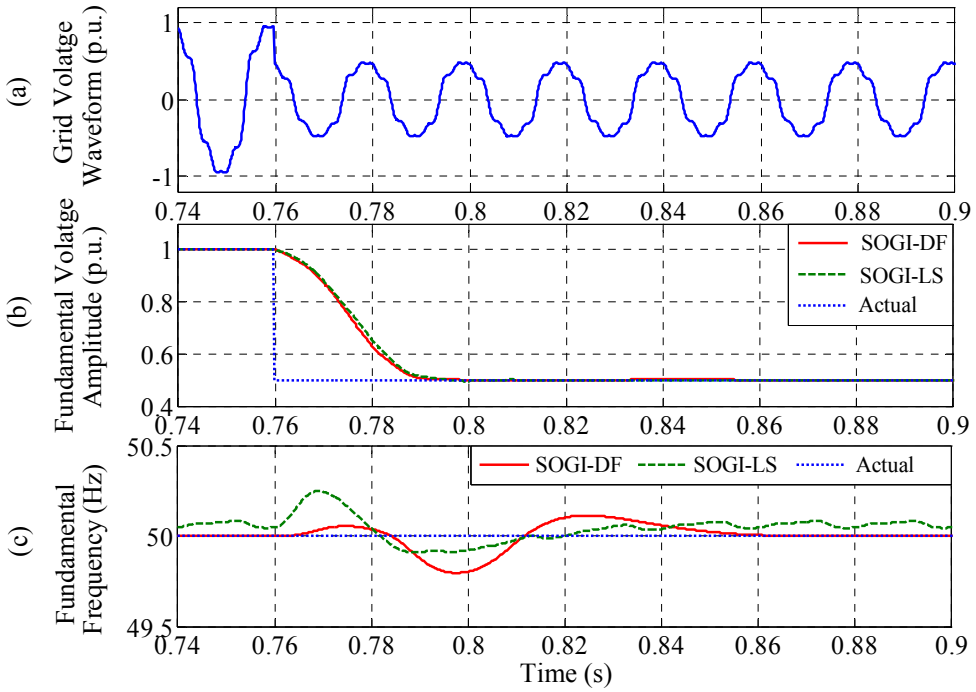

Fig. 6.28 Case-B4: Voltage sag (50%) and harmonics. (a) Grid voltage waveform. (b) Fundamental voltage amplitude. (c) Fundamental frequency.

contains 50% voltage sag and 14.58% THD, as given in Table 3.1. As it can be observed, both techniques can track the voltage sag accurately. However, the frequency estimation of both techniques is affected by the voltage sag.

6.2.4.5 Case-B5: Voltage Flicker and Harmonics

In this case, the grid voltage waveform contains voltage flicker and 14.58% THD, as given in Table 3.1. The frequency and amplitude of the voltage flicker are 2.5 Hz and ±0.10 p.u., respectively. The fundamental voltage amplitude and frequency estimation using the techniques are shown in Fig. 6.29. As it can be seen, both techniques can track the voltage flicker. On the other hand, the frequency estimation using both techniques is slightly affected by the voltage flicker.

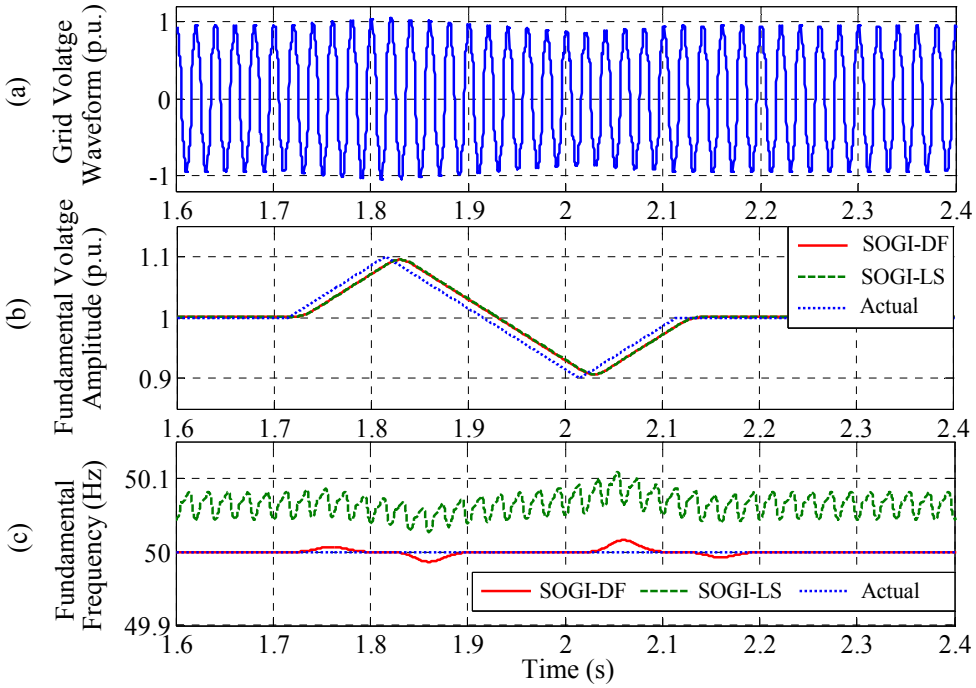

Fig. 6.29 Case-B5: Voltage flicker (±10%) and harmonics. (a) Grid voltage waveform. (b) Fundamental voltage amplitude. (c) Fundamental frequency.

6.3 Power System Fundamental Voltage Amplitude and Frequency Estimation using A Cascaded Delayed Signal Cancellation Based Technique

In this section, a frequency adaptive QSG relying on an anticonjugate decomposition (ACD) process and a cascaded delayed signal cancellation (CDSC) strategy based technique is reported for estimating the single-phase grid voltage fundamental amplitude and frequency under distorted grid conditions. The proposed technique is shown in Fig. 6.30. As it can be seen, the fundamental voltage amplitude is estimated from the orthogonal voltage waveforms generated by the QSG. The orthogonal voltage waveforms are also used as inputs for the estimation of frequency. The value of N_w is used as the number of voltage samples present in one fundamental period and is updated adaptively at every sample using the estimated fundamental frequency, as can also be seen in Fig. 6.30.

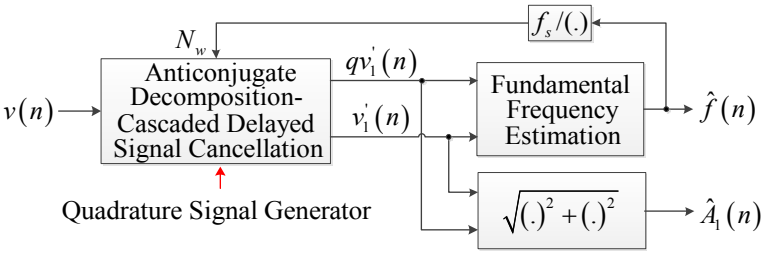

Fig. 6.30 Block diagram of the proposed technique for single-phase grid voltage fundamental amplitude and frequency estimation.

6.3.1 Fundamental Voltage Orthogonal Waveforms Generation

According to the ACD process, the single-phase voltage system can be considered from two space vectors: a positive-sequence one and a negative-sequence one [186]. The decomposition is called anticonjugate because both vectors are symmetrical about the imaginary axis (vectors are symmetrical about the real axis in conjugate decomposition) [186]. The amplitudes of both vectors are half of the single-phase voltage amplitude. The positive-sequence component is in-phase with the input single-phase voltage waveform. The real and imaginary parts of the vectorial sum of both vectors are zero and input single-phase voltage, respectively. Therefore, the vectorial sum can be decomposed back to the anitconjugate pair and hence can be used to estimate the amplitude and phase angle of the single-phase voltage system. The detail of the ACD process for single-phase voltage

system is reported in [186]. The ACD process can be combined with the CDSC strategy (ACDSC) to reject the negative effects caused by harmonics and DC offset [186]. Therefore, the ACDSC can be used to produce clean fundamental voltage orthogonal waveforms from a distorted single-phase grid voltage waveform with known fundamental frequency and hence is named as QSG-ACDSC.

The QSG-ACDSC for the single-phase voltage system is shown in Fig. 6.31 [186]. The inputs of the CDSC are used as v and qv, where qv is the in-quadrature component of v. According to the ACD process, the value of qv is equal to zero. Multiple delayed signal cancellation (DSC) operators, such as $\mathrm{DSC}_{\mathrm{p}_1}, \mathrm{DSC}_{\mathrm{p}_2}, \mathrm{DSC}_{\mathrm{p}_3}$ and so on, are cascaded in series to form $\mathrm{CDSC}_{\mathrm{p}_1,\mathrm{p}_2,\mathrm{p}_3,\ldots..}$ The subscript p_1 of the operator $\mathrm{DSC}_{\mathrm{p}_1}$ indicates that the input orthogonal voltages are delayed by T/p_1, where T is the grid voltage fundamental time period. The principle of the CDSC is to delay the input voltages and then processed to reject harmonics and DC offset [186, 252, 260, 261]. The operating principle of the $\mathrm{DSC}_{\mathrm{p}_1}$ can be expressed by [186]

$$\begin{bmatrix} qv_{out}(n) \\ v_{out}(n) \end{bmatrix} = 0.5\begin{bmatrix} qv_{in}(n) \\ v_{in}(n) \end{bmatrix} + 0.5\begin{bmatrix} \cos\left(\frac{2\pi}{\mathrm{p}_1}\right) & \sin\left(\frac{2\pi}{\mathrm{p}_1}\right) \\ -\sin\left(\frac{2\pi}{\mathrm{p}_1}\right) & \cos\left(\frac{2\pi}{\mathrm{p}_1}\right) \end{bmatrix}\begin{bmatrix} qv_{in}\left(n-\frac{N_w}{\mathrm{p}_1}\right) \\ v_{in}\left(n-\frac{N_w}{\mathrm{p}_1}\right) \end{bmatrix} \tag{6.24}$$

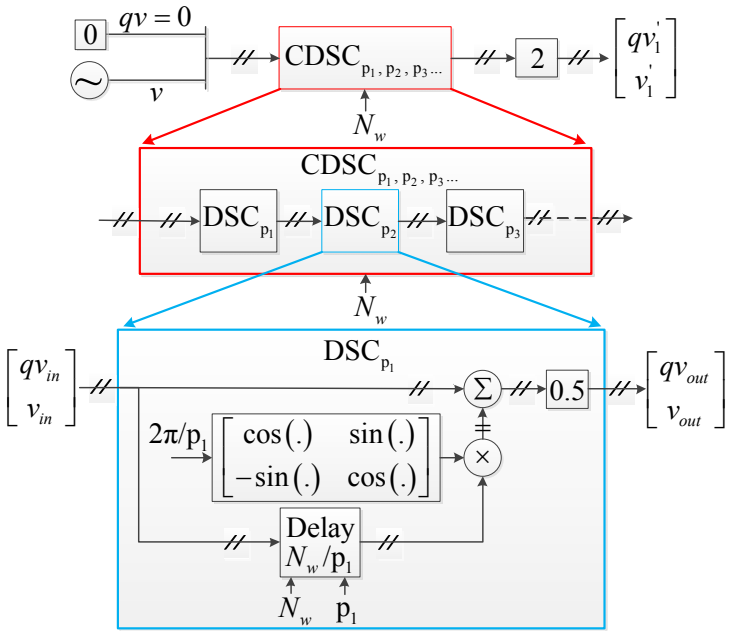

Fig. 6.31 QSG-ACDSC.

where $qv_{out}(n)$ and $qv_{in}(n)$ are the in-quadrature components, $v_{out}(n)$ and $v_{in}(n)$ are the in-phase components and the subscripts *in* and *out* indicate the input and output variables of the DSC_{p_1}, respectively. In (6.24), $2\pi/p_1$ is a constant phase angle and hence the matrix formed by the trigonometric functions is a constant matrix. The implementation of the operator DSC_{p_1} is also shown by the blue block in Fig. 6.31. As it can be seen, only simple transport delay, multiplication and summation operations are to be handled by the digital signal processor [186]. For discrete implementation of DSC_{p_1}, the value of N_w/p_1 can be integer or non-integer i.e. $L_3 \leq N_w/p_1 < L_3+1$, where L_3 is a positive integer and $L_3=\mathrm{floor}(N_w/p_1)$, then a linear interpolation operation can be performed between the samples $v_{in}(n-L_3)$ and $v_{in}(n-L_3-1)$ to obtain the value of $v_{in}(n-N_w/p_1)$ [78]. The linear interpolation operation can also be performed between the samples $qv_{in}(n-L_3)$ and $qv_{in}(n-L_3)$ to get the value of $qv_{in}(n-N_w/p_1)$.

The magnitude responses of the operator DSC_{p_1} for different values of p_1 and two CDSC structures ($\mathrm{CDSC}_{2,4,8,16,32}$ and $\mathrm{CDSC}_{4,8,16,32}$) are shown in Fig. 6.32. As it can be seen in Fig. 6.32(g), the $\mathrm{CDSC}_{2,4,8,16,32}$ can reject all the even and odd harmonics including the DC offset from the estimated fundamental voltage orthogonal waveforms. However, during the dynamic conditions, the delay provided by the $\mathrm{CDSC}_{2,4,8,16,32}$ is $0.97N_w$ ($=N_w/2+N_w/4+N_w/8+N_w/16+N_w/32$). On the other hand, it can be seen in Fig. 6.32(f) that the $\mathrm{CDSC}_{4,8,16,32}$ can reject the odd harmonics from the estimated fundamental voltage orthogonal waveforms. Nevertheless, during the dynamic conditions, the delay provided by the $\mathrm{CDSC}_{4,8,16,32}$ is $0.47N_w$ ($=N_w/4+N_w/8+N_w/16+N_w/32$). The ACD and $\mathrm{CDSC}_{4,8,16,32}$ is used in the proposed technique to track the fundamental voltage orthogonal components from a grid voltage waveform distorted by odd harmonics at the expense of a dynamic delay equal to 47% ($0.47N_w$) of the fundamental time period.

The fundamental voltage in-phase and in-quadrature components generated by the QSG-ACDSC, as shown in Fig. 6.31, can be expressed by (6.25) and (6.26), respectively.

$$v_1'(n) = A_1(n)\sin\{\omega(n)nT_s + \theta_1(n)\} \tag{6.25}$$

$$qv_1'(n) = A_1(n)\cos\{\omega(n)nT_s + \theta_1(n)\} \tag{6.26}$$

Therefore, the fundamental voltage amplitude can be estimated by

$$\hat{A}_1(n) = \sqrt{v_1'^2(n) + qv_1'^2(n)} \tag{6.27}$$

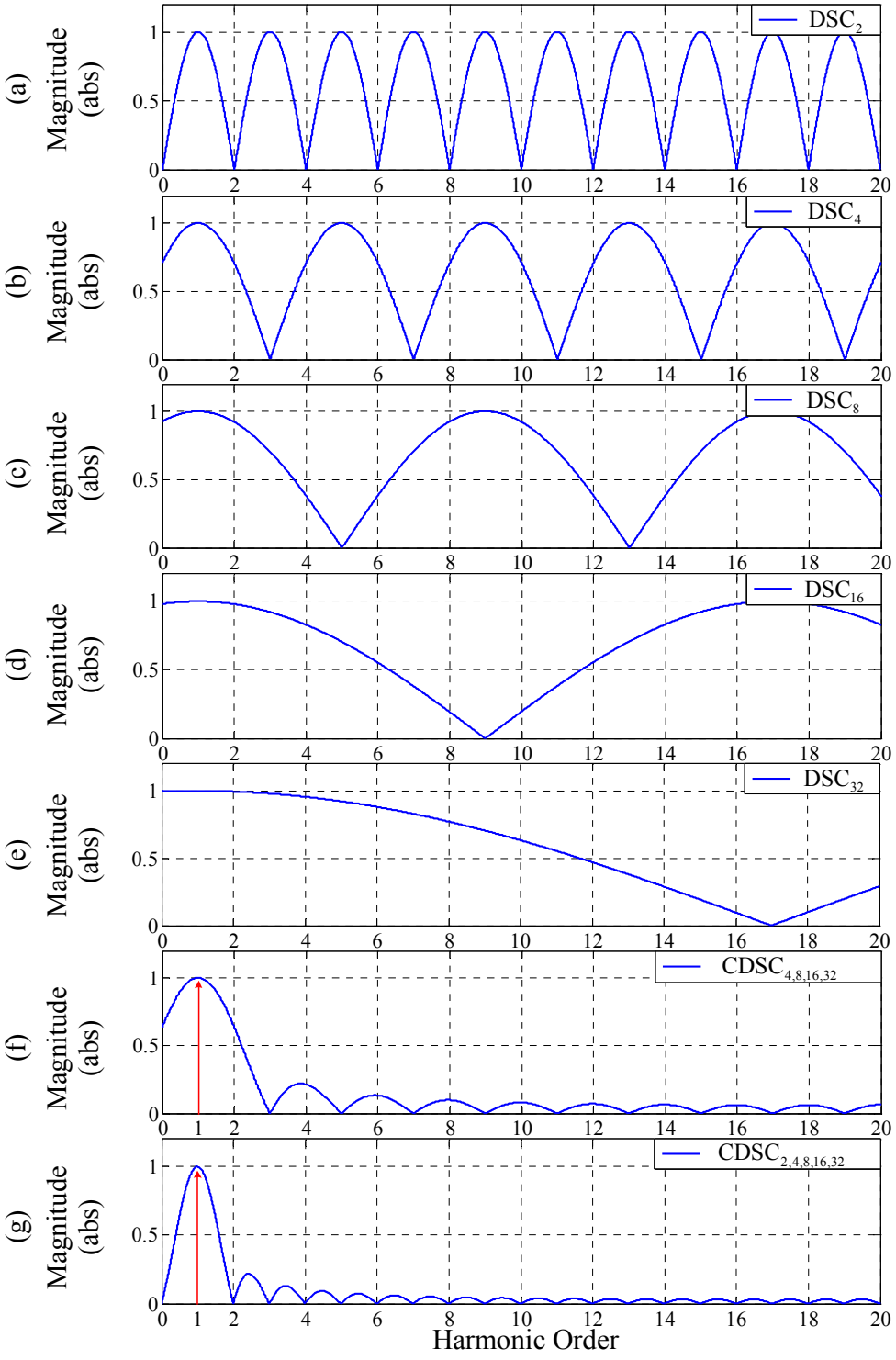

Fig. 6.32 Magnitude responses of the operators DSC_{p_1} and $CDSC_{p_1, p_2, p_3, \ldots\ldots}$

6.3.2 Fundamental Frequency Estimation

The following relation can be obtained when the fundamental voltage parameters are constant within the two consecutive samples of (6.25) and (6.26) [82].

$$\sin\{\omega(n)T_s\} = \frac{v_1'(n)qv_1'(n-1) - v_1'(n-1)qv_1'(n)}{A_1^2(n)} \tag{6.28}$$

Based on a small variation of the grid voltage fundamental frequency, $\sin\{\omega(n)T_s\}$ can be expressed by

$$\begin{aligned}\sin\{\omega(n)T_s\} &= \sin\{\omega_0 T_s + \Delta\omega(n)T_s\} = \sin(\omega_0 T_s)\cos\{\Delta\omega(n)T_s\} + \sin\{\Delta\omega(n)T_s\}\cos(\omega_0 T_s) \\ &\cong \sin(\omega_0 T_s) + \Delta\omega(n)T_s\cos(\omega_0 T_s)\end{aligned} \tag{6.29}$$

where $\cos\{\Delta\omega(n)T_s\} \cong 1$ and $\sin\{\Delta\omega(n)T_s\} \cong \Delta\omega(n)T_s$. Therefore, from (6.28) and (6.29), the deviation of fundamental frequency from its nominal value can be obtained by

$$\Delta\hat{f}(n) = \frac{\dfrac{v_1'(n)qv_1'(n-1) - v_1'(n-1)qv_1'(n)}{A_1^2(n)} - \sin(\omega_0 T_s)}{2\pi T_s\cos(\omega_0 T_s)} \tag{6.30}$$

The actual fundamental frequency can be estimated by

$$\hat{f}(n) = f_0 + \Delta\hat{f}(n) \tag{6.31}$$

The implementations of (6.30) and (6.31) for tracking of the fundamental frequency are shown in Fig. 6.33. As it can be noticed, the technique requires two successive samples of the fundamental voltage orthogonal waveforms to estimate the frequency. However, due to the presence of the interdependent loop, as shown in Fig. 6.30, the faster tracking of fundamental frequency as compared to the orthogonal voltage waveforms estimation will affect the stability of the proposed technique. Therefore, a time delay is used for the loop providing the estimated frequency and a first-order IIR LPF is used for this purpose, as can be seen in Fig. 6.33 [179, 252, 261]. The angular cut-off frequency of the LPF is ω_{cut}. The

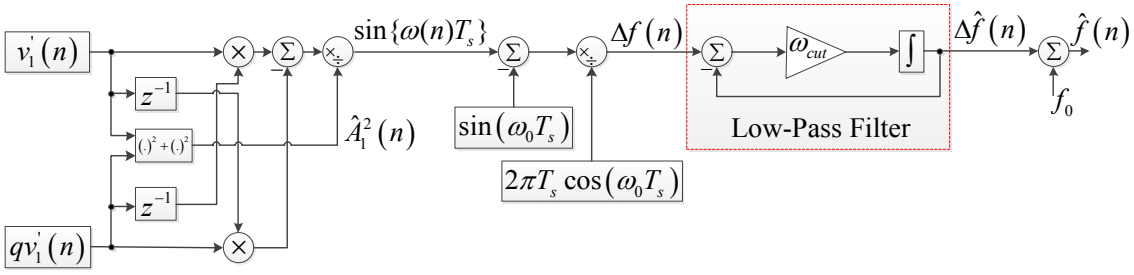

Fig. 6.33 Fundamental frequency estimation based on the fundamental voltage orthogonal waveforms obtained by the QSG-ACDSC.

stability of the technique depends on the tuning of ω_{cut}. A slower dynamics can be obtained by using a low value of ω_{cut}. The optimal tuning of the LPF's cut-off frequency in the outer frequency estimation loop is reported in [252, 261] as $\omega_{cut} = \omega_0/3$ and is also used in the proposed technique.

6.3.3 Simulation Results

The performance of the QSG-ACDSC technique is compared with the SOGI-FLL one [198]. The parameters of both techniques, as given in Table 6.4, are tuned to provide similar dynamics for the fundamental voltage amplitude and frequency estimation. The sampling and nominal grid voltage fundamental frequencies are chosen as 10 kHz and 50 Hz, respectively. The following case studies are carried out for performance comparison.

i. Steady-state with harmonics (Case-C1)
ii. Frequency step and harmonics (Case-C2)
iii. Frequency sweep and harmonics (Case-C3)
iv. Voltage sag and harmonics (Case-C4)
v. Voltage swell and harmonics (Case-C5)
vi. Voltage flicker and harmonics (Case-C6)

The fundamental component of the grid voltage waveforms presented in all the above case studies are distorted by harmonics, as given in Table 5.5 of Chapter 5, thus leading to a THD of 7.42%.

Table 6.4 Parameters of the QSG-ACDSC and SOGI-FLL techniques

QSG-ACDSC	SOGI-FLL
$\mathrm{CDSC}_{4,8,16,32}$ & $\omega_{cut} = \omega_0 / 3$	$\sigma = \sqrt{2}$ & $\gamma = \omega_0 / 3$

6.3.3.1 Case-C1: Steady-State with Harmonics

A distorted grid voltage waveform containing 7.42% THD is shown in Fig. 6.34(a). The harmonic contents are given in Table 5.5. The estimation of the fundamental voltage amplitude and frequency at steady-state using the proposed QSG-ACDSC and SOGI-FLL

techniques are depicted in Fig. 6.34(b) and (c), respectively. As it can be seen, the estimation of fundamental voltage amplitude and frequency using the proposed technique is accurate. Moreover, the performance of the proposed technique is less affected by harmonics as compared to the SOGI-FLL one.

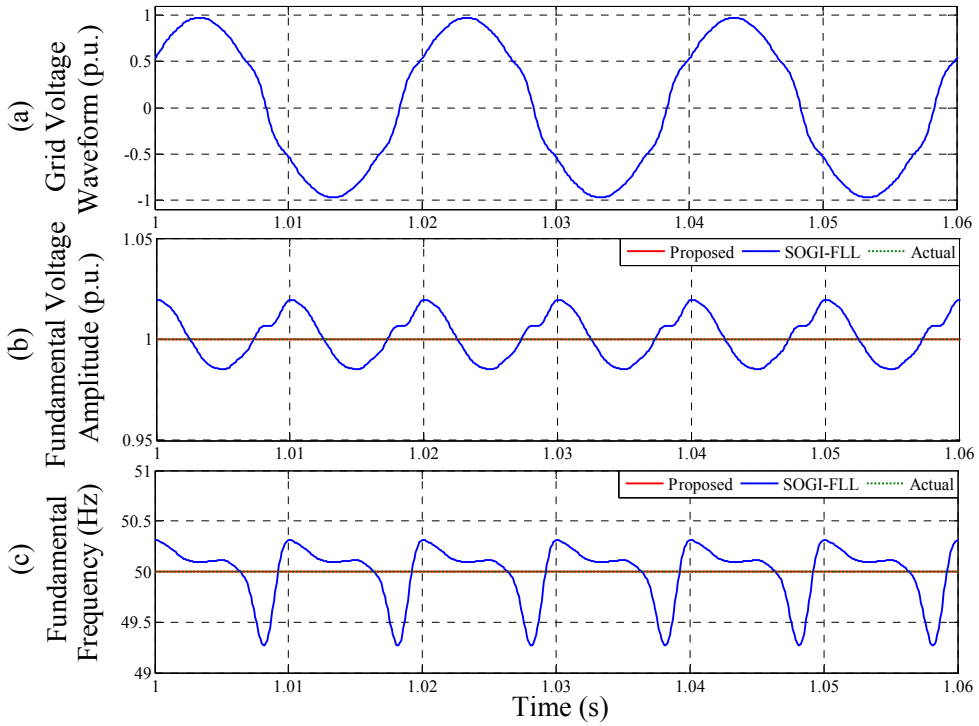

Fig. 6.34 Case-C1: Steady-state with harmonics. (a) Grid voltage waveform. (b) Fundamental voltage amplitude. (c) Fundamental frequency.

6.3.3.2 Case-C2: Frequency Step and Harmonics

A worst case scenario of grid frequency variation such as a step change is considered for comparing the performance of the proposed QSG-ACDSC and SOGI-FLL techniques. Fig. 6.35 illustrates the estimation of the fundamental voltage amplitude and +1 Hz fundamental frequency step using the presented techniques under 7.42% THD, as given in Table 5.5. As it can be noticed in Fig. 6.35(b), the proposed technique takes around one fundamental cycle as a settling time for tracking the frequency step.

6.3.3.3 Case-C3: Frequency Sweep and Harmonics

A frequency sweep of -10 Hz/s down to 49 Hz and 7.42% THD, as given in Table 5.5, are considered for this case study. The estimation of the fundamental voltage amplitude and frequency sweep using the proposed QSG-ACDSC and SOGI-FLL techniques are

shown in Fig. 6.36. It can be noticed that the proposed technique can track the frequency sweep more accurately as compared to the SOGI-FLL technique. The amplitude estimation using the proposed technique is also more accurate when compared with the SOGI-FLL one, as can be observed in Fig. 6.36(a).

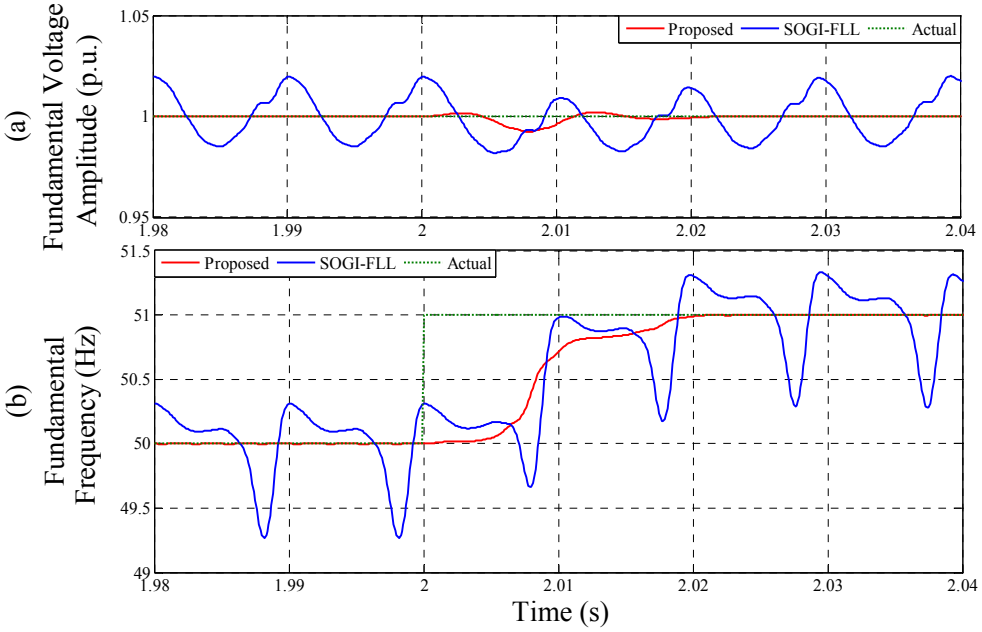

Fig. 6.35 Case-C2: Frequency step (+1 Hz: 50 Hz to 51 Hz) and harmonics. (a) Fundamental voltage amplitude. (b) Fundamental frequency.

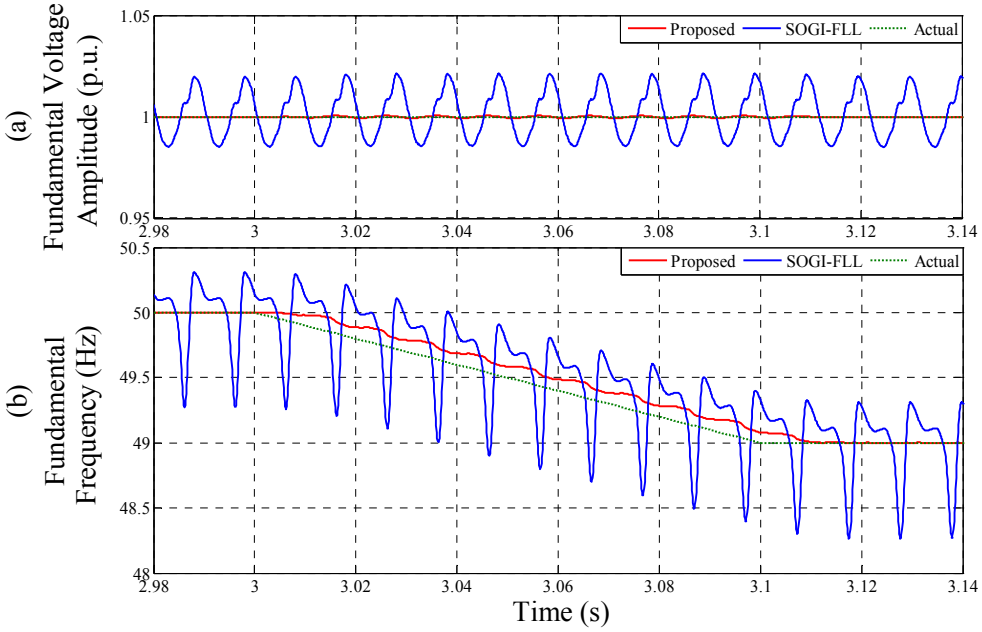

Fig. 6.36 Case-C3: Frequency sweep (-10 Hz/s: 50 Hz to 49 Hz) and harmonics. (a) Fundamental voltage amplitude. (b) Fundamental frequency.

6.3.4.4 Case-C4: Voltage Sag and Harmonics

A grid voltage sag of 30% and harmonics, as given in Table 5.5, is shown in Fig. 6.37(a). As it can be seen from Fig. 6.37(b), the dynamics of the amplitude estimation of both techniques are similar. However, the estimated frequency presents overshoot/undershoot during the voltage sag using both of the techniques, as can be noticed in Fig. 6.37(c).

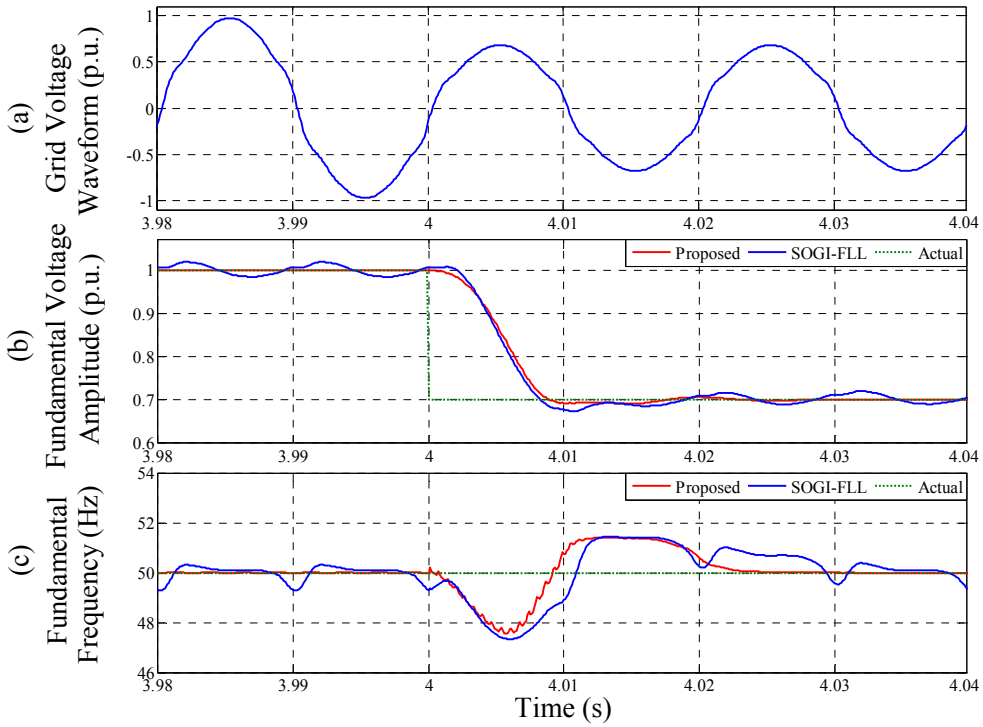

Fig. 6.37 Case-C4: Voltage sag (30%) and harmonics. (a) Grid voltage waveform. (b) Fundamental voltage amplitude. (c) Fundamental frequency.

6.3.3.5 Case-C5: Voltage Swell and Harmonics

A grid voltage swell of 30% and harmonics, as given in Table 5.5, is shown in Fig. 6.38(a). Similar to the voltage sag, the dynamic response of both techniques for amplitude estimation, as shown in Fig. 6.38(b), are comparable. As it can be seen from Fig. 6.38(c), the estimated fundamental frequency also presents overshoot/undershoot during the voltage swell.

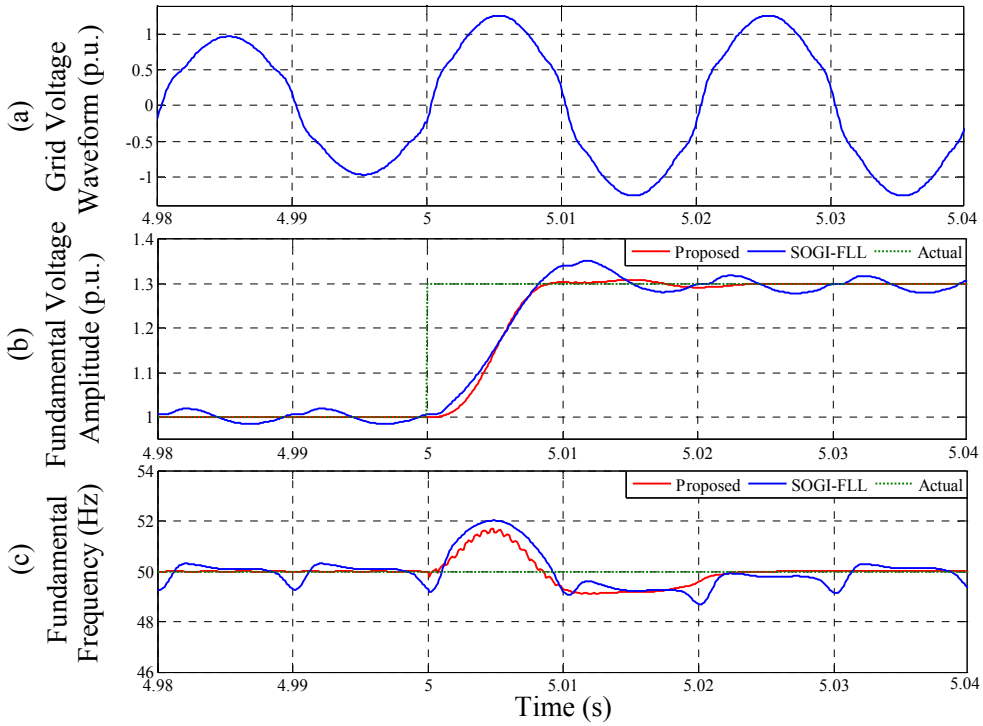

Fig. 6.38 Case-C5: Voltage swell (30%) and harmonics. (a) Grid voltage waveform. (b) Fundamental voltage amplitude. (c) Fundamental frequency.

6.3.3.6 Case-C6: Voltage Flicker and Harmonics

In this case, a 5 Hz and ±0.10 p.u. triangular voltage flicker is considered into a grid voltage waveform containing 7.42% THD, as shown in Fig. 6.39(a). The harmonic contents are presented in Table 5.5. As it can be seen from Fig. 6.39(b), the proposed technique can track the voltage flicker accurately. The frequency estimation is also shown in Fig. 6.39(c). As it can be noticed, the voltage flicker introduces ripple into the frequency estimation of the proposed technique.

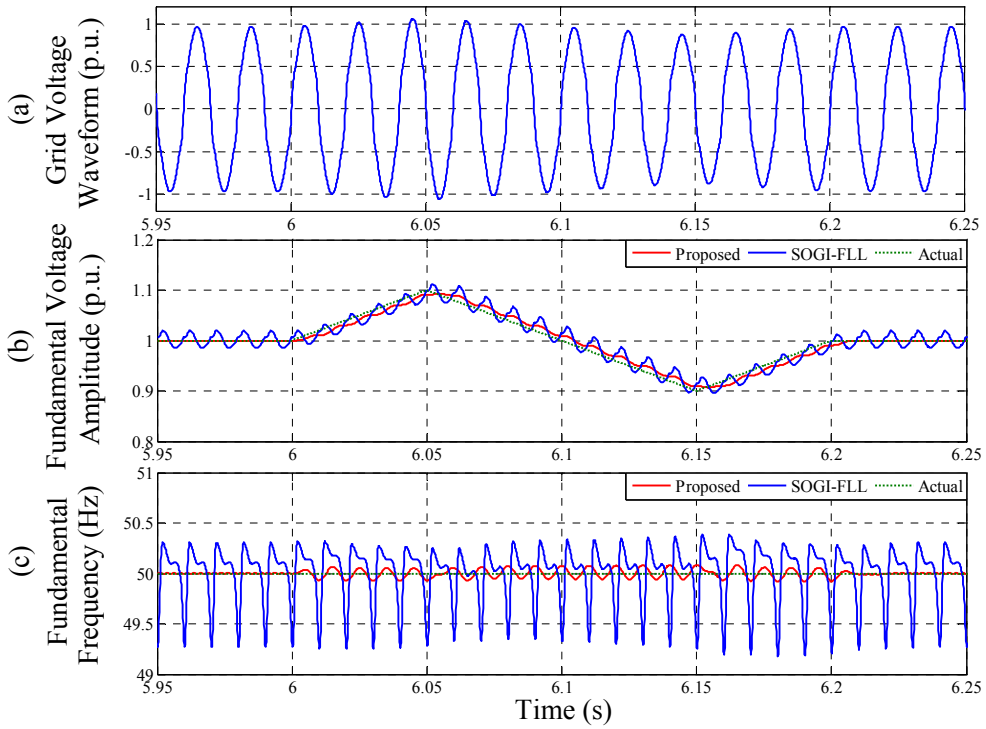

Fig. 6.39 Case-C6: Voltage flicker (±10%) and harmonics. (a) Grid voltage waveform. (b) Fundamental voltage amplitude. (c) Fundamental frequency.

6.4 Conclusions

Three techniques based on quadrature signal generator have been reported in this chapter to estimate the single-phase grid voltage fundamental amplitude and frequency.

The first proposed technique relies on the discrete Fourier Transform and a quadrature signal generator based on a second-order generalized integrator, and has been used to estimate the fundamental voltage amplitude and frequency from a distorted single-phase grid voltage waveform. The presented discrete Fourier Transform operation does not need to adjust the window size corresponding to the actual time-varying frequency. The fixed-size window based on nominal fundamental periods allows offline computation of the trigonometric functions required for the discrete Fourier Transform. The use of three high order discrete Fourier Transform filters increases the computational burden of the proposed technique as compared to a frequency-locked loop/phase-locked loop relying on the quadrature signal generator based on the second-order generalized integrator. However, the frequency estimation using the proposed technique is less sensitive to the presence of harmonics and is also not depending on the generation of the quadrature waveforms when compared with the frequency-locked loop/phase-locked loop. Moreover, unlike the

frequency-locked loop/phase-locked loop, the proposed technique does not create any interdependent loops, thus increasing the overall stability and easing the tuning process. The presented experimental results have confirmed the effectiveness of the proposed technique for real-time estimation of the fundamental voltage amplitude and frequency.

The second proposed technique consists of a quadrature signal generator based on a fixed frequency tuned second-order generalized integrator and an infinite-impulse-response differentiation filter. It does not create any interdependent loop between the orthogonal voltage system and the frequency estimation, thus making the technique robust and offering an easy tuning process. The technique is computationally efficient and can also provide an accurate estimation of fundamental voltage amplitude and frequency under the DC offset, harmonics and a wide range of fundamental frequency variation. The technique shows less sensitivity to the presence of harmonics for frequency estimation as compared to a similar technique relying on the quadrature signal generator based on the fixed frequency tuned second-order generalized integrator and least-squares. The presented experimental results have shown the real-time grid voltage parameters estimation capability of the proposed technique.

The third proposed technique is based on a quadrature signal generator, which relies on an anticonjugate decomposition process and a cascaded delayed signal cancellation strategy. The frequency information required by the quadrature signal generator is updated using a frequency estimation algorithm. The proposed technique estimates the fundamental voltage amplitude and frequency accurately from a grid voltage waveform distorted by harmonics. Moreover, the proposed technique shows less sensitivity to the presence of harmonics when compared with the quadrature signal generator based on a second-order generalized integrator and frequency-locked loop, as confirmed by the simulation results.

Chapter 7

Kalman Filter Based Techniques

This chapter presents Kalman filter based techniques for single-phase grid voltage fundamental and harmonics parameters estimation. A frequency-locked loop with a linear Kalman filter based technique is presented in Section 7.1 to estimate the grid voltage fundamental amplitude and frequency. The technique is also extended in Section 7.2 for the estimation of grid voltage harmonics amplitudes including the fundamental frequency and amplitude. Moreover, an extended Kalman filter is described in Subsection 7.2.3 for tracking of the instantaneous voltage flicker level from the estimated fundamental voltage amplitude. Selected simulation results are presented after the description of each technique. The conclusions of the works are documented in Section 7.3.

7.1 Power System Fundamental Voltage Amplitude and Frequency Estimation using A Kalman Filter Based Technique

A frequency adaptive linear Kalman filter (LKF) is documented in this section for estimating the single-phase grid voltage fundamental amplitude and frequency under distorted grid conditions. In the proposed technique, a frequency-locked loop (FLL) is combined with the LKF (LKF-FLL) for adaptive estimation of the fundamental voltage amplitude and frequency. The proposed LKF-FLL technique is shown in Fig. 7.1, where v is the grid voltage, n is the sampling instant, $\hat{\omega}$ is the estimated fundamental angular frequency, $\hat{f}$ is the estimated fundamental frequency, $\hat{A}_1$ is the estimated fundamental voltage amplitude, K_{LKF} is the Kalman gain, L_{LKF} is the measurement matrix, J_{LKF} is the transition or Jacobian matrix, x_{11} is the state corresponding to the in-phase fundamental voltage component, x_{12} is the state corresponding to the in-quadrature fundamental voltage component, $x_{11} = v_1'$, v_1' is the estimated in-phase fundamental voltage component, $x_{12} = qv_1'$, qv_1' is the estimated in-quadrature fundamental voltage component, x is the

state vector, x_{11}^{-} is the predicted value of x_{11}, x_{12}^{-} is the predicted value of x_{12} and x^{-} is the predicted value of x. As it can be seen, the fundamental voltage angular frequency is estimated adaptively using the FLL and is fed to the LKF. The inputs of the FLL are the fundamental voltage orthogonal components estimated by the LKF and the grid voltage. The amplitude, as estimated from the fundamental voltage orthogonal components obtained by the LKF, is filtered using a frequency adaptive moving average filter (MAF), as it can be noticed in Fig. 7.1.

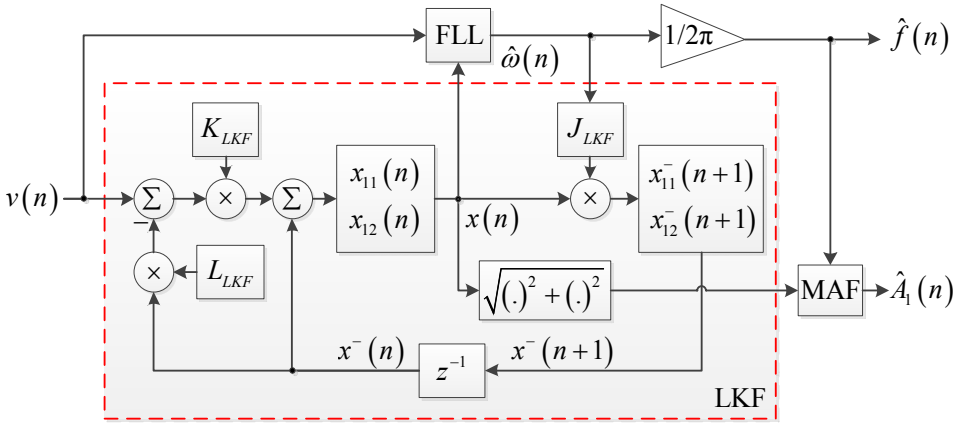

Fig. 7.1 Proposed frequency adaptive LKF technique based on FLL for the estimation of single-phase grid voltage fundamental amplitude and frequency.

7.1.1 Fundamental Voltage Amplitude Estimation

For estimating the grid voltage fundamental amplitude, the LKF can be described by a dynamic process and a measurement relation as given by (7.1) and (7.2), respectively.

$$x(n+1) = J_{LKF}x(n) + d_1 \tag{7.1}$$

$$v(n) = L_{LKF}x(n) + d_2 \tag{7.2}$$

where d_1 is the process noise and d_2 is the measurement noise. The process and measurement noises are assumed to be independent, white and zero mean normal probability distributions. In practice, the process noise covariance matrix (Q_n) and the measurement noise covariance (R_n) may change with each time step and measurement. However, a constant value of Q_n=Q=qI and R_n=R can also be used for the LKF [135, 137, 146, 262], where q is the process noise covariance and I is an identity matrix. Four parameters of the LKF such as q, R, initial state estimate $\{x(0)\}$ and initial estimation error covariance p (P_0=pI, P_0 is the initial error covariance matrix) are assumed *a priori*.

The in-phase and in-quadrature components of the grid voltage fundamental waveform are used as the states of the LKF and are expressed by (7.3) and (7.4), respectively.

$$x_{11}(n) = v_1'(n) = A_1(n)\sin\left\{\omega(n)nT_s + \theta_1(n)\right\} \tag{7.3}$$

$$x_{12}(n) = qv_1'(n) = A_1(n)\cos\left\{\omega(n)nT_s + \theta_1(n)\right\} \tag{7.4}$$

where A_1 is the fundamental voltage amplitude, $\omega=2\pi f$ is the fundamental angular frequency, f is the fundamental frequency, θ_1 is the initial phase angle and T_s is the sampling period. The state vector is obtained by $x(n) = [x_{11}(n) \quad x_{12}(n)]^{\square}$, where $\square$ denotes transpose operation. The state transition between two successive sampling instants can be expressed by (7.5) and (7.6), respectively.

$$x_{11}^{-}(n+1) = x_{11}(n)\cos\left\{\omega(n)T_s\right\} + x_{12}(n)\sin\left\{\omega(n)T_s\right\} \tag{7.5}$$

$$x_{12}^{-}(n+1) = -x_{11}(n)\sin\left\{\omega(n)T_s\right\} + x_{12}(n)\cos\left\{\omega(n)T_s\right\} \tag{7.6}$$

The predicted state vector is obtained by $x^{-}(n+1) = [x_{11}^{-}(n+1) \quad x_{12}^{-}(n+1)]^{\square}$. The state transition matrix of the LKF can be expressed by

$$J_{LKF} = \begin{bmatrix} \cos\left\{\omega(n)T_s\right\} & \sin\left\{\omega(n)T_s\right\} \\ -\sin\left\{\omega(n)T_s\right\} & \cos\left\{\omega(n)T_s\right\} \end{bmatrix} \tag{7.7}$$

The fundamental frequency is provided in (7.7) by the FLL under the assumption that the estimated frequency is equal to the input voltage frequency. The measurement matrix can be expressed by

$$L_{LKF} = [1 \quad 0] \tag{7.8}$$

The steps of the LKF are as follows [134-136]:

Time update stage:

Project the state ahead: $x^{-}(n+1) = J_{LKF}x(n)$

Project the error covariance ahead: $P_{n+1}^{-} = J_{LKF}P_nJ_{LKF}^{\square} + Q$

Measurements update stage:

Compute the Kalman gain: $K_{LKF} = P_n^{-}L_{LKF}^{\square}\left(L_{LKF}P_n^{-}L_{LKF}^{\square} + R\right)^{-1}$

Update estimate: $x(n) = x^{-}(n) + K_{LKF}\left\{v(n) - L_{LKF}x^{-}(n)\right\}$

Update error covariance: $P_n = \left(I - K_{LKF} L_{LKF}\right) P_n^-$

where P_n is the error covariance matrix and P_{n+1}^- is the predicted value of P_n. Therefore, the grid voltage fundamental amplitude can be estimated by

$$\hat{A}_1(n) = \sqrt{x_{11}^2(n) + x_{12}^2(n)} = \sqrt{v_1'^2(n) + q v_1'^2(n)} \tag{7.9}$$

The grid voltage fundamental amplitude estimation using the LKF may contain ripple due to the presence of DC offset and harmonics. The MAF, as shown in Fig. 6.7(a) of Chapter 6, is used to remove the ripple from the estimated amplitude. An integrator based on backward Euler method, as shown in Fig. 6.19, is used for discrete implementation of the MAF. The linear interpolation operation, as given by (6.11), is also used when the number of samples in a window size of the MAF is not an integer value.

7.1.2 Tuning of the LKF Parameters

A frequency domain analysis is presented in this subsection for showing the performance of the LKF under different tuning conditions. For different combinations of the parameters q, R and p, the Bode plots of the in-phase and in-quadrature components of the LKF with respect to the input voltage are presented in Fig. 7.2 and Fig. 7.3, respectively. The tuning frequency of the LKF is chosen as $\hat{\omega} = 2\pi 50$ rad/s. As it can be seen from Fig. 7.2 and Fig. 7.3, the in-phase and in-quadrature structures of the LKF behave like a band-pass filter (BPF) and a low-pass filter (LPF), respectively. With p=0, the frequency responses are similar for a constant value of the ratio q/R i.e. $q/R=q_1/R_1=(q_1/10)/(R_1/10)=(10q_1)/(10R_1)=\beta$, where $q_1=10^{-2.0}$ is a fixed value of q, R_1=1.0 is a fixed value of R, and $\beta=10^{-2.0}$ is the ratio of q_1 and R_1. However, as the value of the ratio q/R decreases i.e. for $q/R=q_1/(10R_1)=0.1\beta$, the bandwidth of the LKF decreases and vice versa. Thus, for a constant value of p, the bandwidth of the LKF is determined by the ratio q/R [137, 145]. Therefore, a lower value of the ratio q/R can be chosen to reject the disturbances from the estimation at the cost of a slower dynamic response and vice versa.

For different values of p and a constant value of the ratio $q/R=q_1/R_1=\beta$, the Bode plots of the in-phase and in-quadrature components of the LKF with respect to the input voltage are also shown in Fig. 7.2 and Fig. 7.3, respectively. In this case, the bandwidth of the LKF

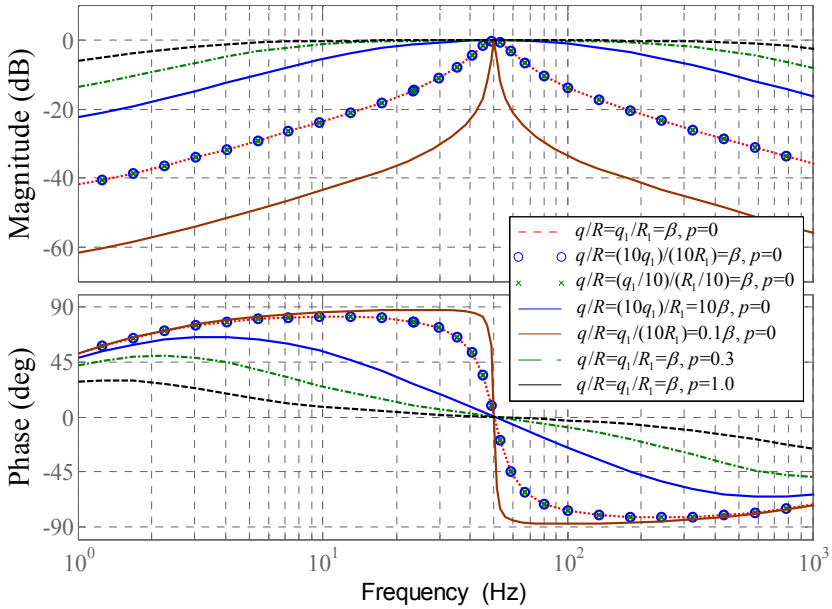

Fig. 7.2 Bode plots of the in-phase component (v_1') of the LKF with respect to the input voltage (v) for a tuning frequency $\hat{\omega} = 2\pi 50$ rad/s and different combinations of the parameters q, R and p.

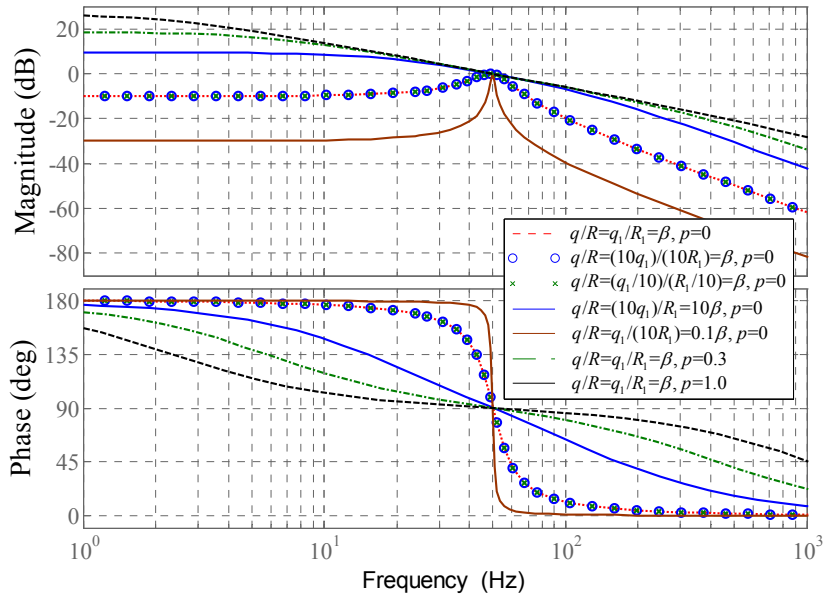

Fig. 7.3 Bode plots of the in-quadrature component (qv_1') of the LKF with respect to the input voltage (v) for a tuning frequency $\hat{\omega} = 2\pi 50$ rad/s and different combinations of the parameters q, R and p.

increases as the value of p increases and vice versa. For the initial start of the LKF, a high value of p is usually chosen to provide a high bandwidth so that a fast tracking of the input voltage is obtained. However, after initial convergence, the value of p and hence the Kalman gain settles to a very small value. Therefore, when a large change occurs in the input voltage, p can be reset to a high value for quickly tracking the changes of the input voltage [139, 141, 143].

7.1.3 Fundamental Frequency Estimation

The estimation error (e_v) of the LKF can be obtained by subtracting the estimated in-phase fundamental voltage component from the input grid voltage i.e. $e_v = v - v_1'$. The Bode plots of the estimation error and the in-quadrature component of the LKF with respect to the input voltage are shown in Fig. 7.4. As it can be observed, the phase difference between the in-quadrature component and the estimation error are 180° and 0° when $\omega < \hat{\omega}$ and $\omega > \hat{\omega}$, respectively. The product of the estimation error signal and the in-quadrature component is negative, zero and positive for the conditions $\omega < \hat{\omega}$, $\omega = \hat{\omega}$ and $\omega > \hat{\omega}$, respectively. Therefore, the product of the estimation error signal and the in-quadrature component can be defined as a frequency error variable (e_f) and can be fed to an integrator with a gain (γ) to track the actual fundamental frequency and the result is the formation of the FLL [193]. The value of γ determines the dynamic speed and disturbance rejection capability of the FLL. The lower value of γ increases the disturbance rejection capability at the expense of a slower dynamic speed and vice versa. Thus, a trade-off is required between the dynamic speed and disturbance rejection capability when choosing the value of γ. On the other hand, the frequency estimation accuracy under distorted grid conditions can also be increased by placing an in-loop LPF inside the FLL at the expense of slower dynamics [188]. A window based MAF can be used inside the FLL to reject the negative effects caused by disturbances present in the grid voltage [188]. The dynamics of the fundamental frequency estimation using the FLL can be expressed by [193, 197, 198]

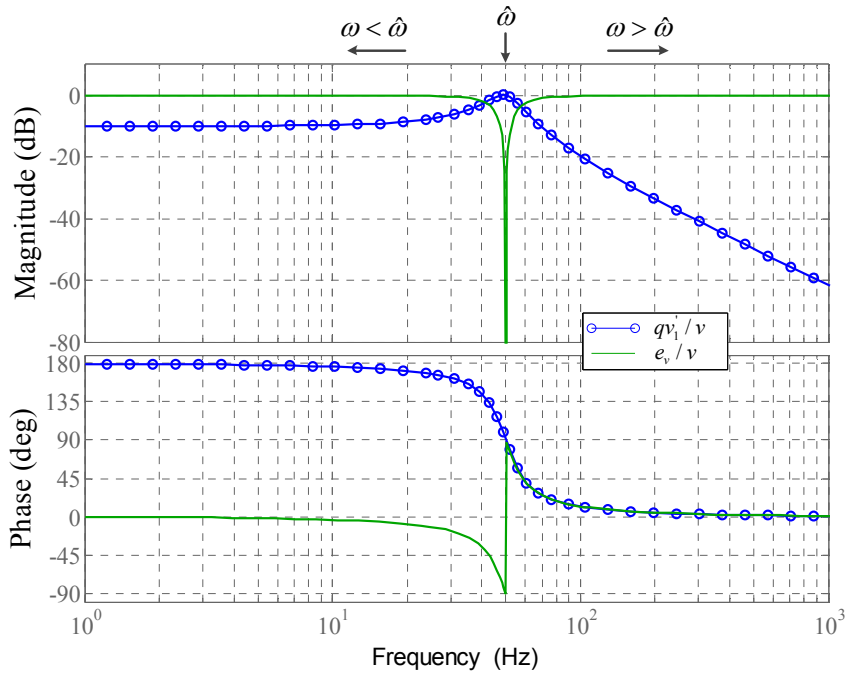

Fig. 7.4 Bode plots of the estimation error $(e_v = v - v_1')$ and the in-quadrature component (qv_1') of the LKF with respect to the input signal (v) for the parameters $\hat{\omega} = 2\pi 50$ rad/s, q=$10^{-2.0}$, R=1.0 and p=0.

$$\dot{\omega}(n) = \gamma e_v(n) q v_1'(n) = \gamma A_1^2(n) \sin\left[\left\{\omega(n) - \hat{\omega}(n)\right\} nT_s\right]$$

$$+ \gamma A_1^2(n) \sin\left[\left\{\omega(n) + \hat{\omega}(n)\right\} nT_s + 2\theta_1(n)\right] - \gamma A_1^2(n) \sin\left\{2\hat{\omega}(n) nT_s + 2\theta_1(n)\right\} \quad (7.10)$$

$$\cong \gamma A_1^2(n) \sin\left[\left\{\omega(n) - \hat{\omega}(n)\right\} nT_s\right]$$

where $\dot{\omega}$ is the fundamental angular frequency dynamics. It can be seen from (7.10) that the tracking speed of the fundamental frequency also depends on the square of the fundamental voltage amplitude and hence the estimation speed is affected by the variation of the amplitude such as the voltage sag, swell and flicker. Therefore, to keep the estimation speed of the frequency dynamics non-sensitive to the change of the fundamental voltage amplitude, the gain of the FLL can be normalized by $A_1^2(n)$ and is given by

$$\dot{\omega}(n) \cong \gamma \sin\left[\left\{\omega(n) - \hat{\omega}(n)\right\} nT_s\right] \quad (7.11)$$

The implementation of the FLL based on the orthogonal voltage waveforms estimated by the LKF is shown in Fig. 7.5. The MAF, as shown in Fig. 6.7(a), is also used in Fig. 7.5. The window size of the MAF is updated adaptively based on the estimated fundamental frequency. In order to avoid an algebraic loop, a discrete forward Euler integrator is used in the FLL. The nominal fundamental angular frequency is also used to increase the initial synchronization process, where $\hat{\omega}=\omega_0+\Delta\hat{\omega}$ and $\Delta\hat{\omega}$ is the estimated fundamental angular frequency deviation, as can be noticed in Fig. 7.5.

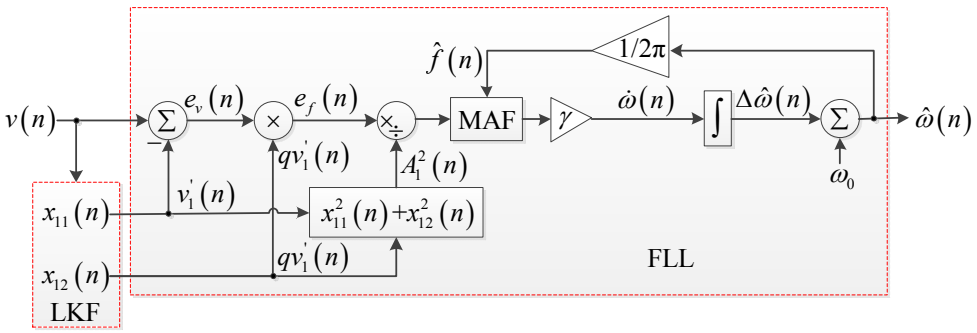

Fig. 7.5 Implementation of the FLL based on the orthogonal voltage waveforms generated by the LKF.

7.1.4 Simulation Results

In this subsection, the performance of the proposed LKF-FLL technique is compared with an extended complex Kalman filter (ECKF) technique [138-143] under several cases as follows:

i. Steady-state with harmonics (Case-A1)
ii. Frequency sweep and harmonics (Case-A2)
iii. Frequency step and harmonics (Case-A3)
iv. Voltage sag and harmonics (Case-A4)
v. Voltage flicker and harmonics (Case-A5)

The parameters of the LKF-FLL and ECKF techniques, as given in Table 7.1, are tuned so that approximately an equal dynamic response is obtained, where $I_{2\times2}$ is a 2×2 identity matrix, $I_{3\times3}$ is a 3×3 identity matrix, j is the complex operator, F is the gain of the MAF, and 'diag' indicates diagonal matrix. Similar to the LKF-FLL technique, a frequency adaptive MAF is used in the ECKF to reject ripple from the estimated fundamental voltage amplitude. The sampling and nominal grid voltage fundamental frequencies are chosen as

10 kHz and 50 Hz, respectively. The fundamental component of the grid voltage presented in all case studies are distorted by 4.0% 3rd and 3.0% 5th harmonics, thus leading to a total harmonic distortion (THD) = 5.0%, as given in Table 7.2.

Table 7.1 Parameters of the LKF-FLL and ECKF techniques

LKF-FLL	ECKF
$x(0)=\begin{bmatrix}0.01 & 0.01\end{bmatrix}^{\square}$, $P_0=10^{3.0}I_{2\times2}$, $R=1.0,\ Q=10^{-2.0}I_{2\times2}$, $\gamma=222\omega_0$, MAFs: $F=\hat{f}$.	$x(0)=\begin{bmatrix}e^{+j\omega_0T_s} & e^{+j(\omega_0T_s+0.001\pi)} & e^{-j(\omega_0T_s+0.001\pi)}\end{bmatrix}^{\square}$, $P_0=10^{3.0}I_{3\times3}$, $R=1.0,\ Q=\mathrm{diag}\left(10^{-6.6},\ 10^{-2.0},\ 10^{-2.0}\right)$, MAF: $F=\hat{f}$.

Table 7.2 Harmonics as a percentage of fundamental component

Harmonics		THD
3rd	5th	5.0%
4.0%	3.0%	

7.1.4.1 Case-A1: Steady-State with Harmonics

The steady-state relative error of the estimated fundamental frequency using the LKF-FLL and ECKF techniques is shown in Fig. 7.6, where the relative error can be defined by (3.25). In this case, the fundamental voltage amplitude is 1.0 p.u., THD is 5%, as given in Table 7.2, and the fundamental frequency is varied from 42.5 Hz to 57.5 Hz, as specified by the IEC standard 61000-4-30 [85]. It can be noticed from Fig. 7.6 that the fundamental

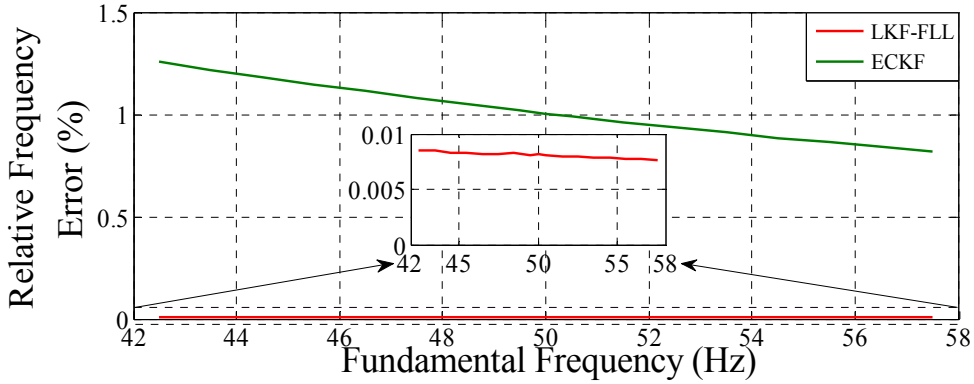

Fig. 7.6 Case-A1: Relative error of the estimated fundamental frequency at steady-state operation with harmonics, as given in Table 7.2.

frequency estimation error using the LKF-FLL technique remains inside the acceptable range (less than 0.03%), as specified by the IEC standard 61000-4-7 [254]. Moreover, the fundamental frequency estimation using the LKF-FLL technique is less affected by harmonics when compared with the ECKF one.

Fig. 7.7 shows the estimated relative error of the fundamental voltage amplitude at steady-state using the LKF-FLL and ECKF techniques, where the fundamental frequency is 50 Hz, THD is 5%, as given in Table 7.2, and the fundamental voltage amplitude is varied from 5% to 200%. As it can be noticed, the LKF-FLL technique can provide more accurate estimation of the fundamental voltage amplitude as compared to the ECKF one.

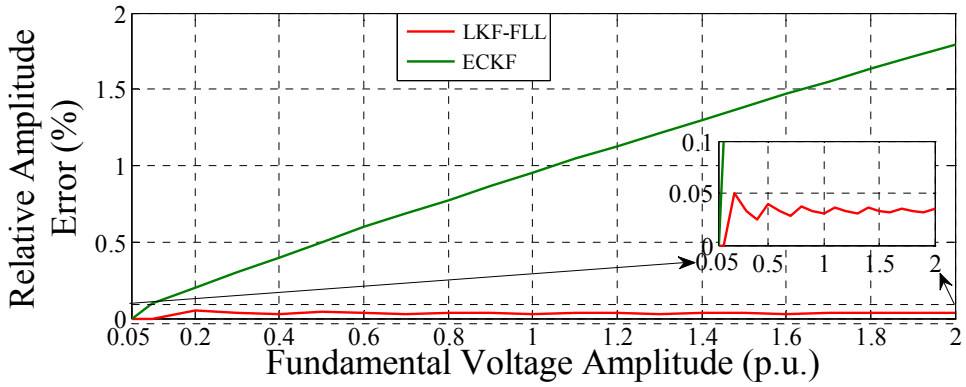

Fig. 7.7 Case-A1: Relative error of the estimated fundamental voltage amplitude at steady-state operation with harmonics, as given in Table 7.2.

7.1.4.2 Case-A2: Frequency Sweep and Harmonics

For this case, a frequency sweep is performed at -10 Hz/s down to 42.5 Hz in the grid voltage distorted by harmonics, as given in Table 7.2. The estimation of the fundamental voltage amplitude and frequency using the LKF-FLL and ECKF techniques are shown in Fig. 7.8. The dynamic performance of both techniques for frequency sweep estimation is the same. On the other hand, the fundamental voltage amplitude estimation using both techniques is slightly affected by the frequency sweep. However, the LKF-FLL technique is less sensitive to the presence of harmonics when compared with the ECKF one, as can be noticed in Fig. 7.8.

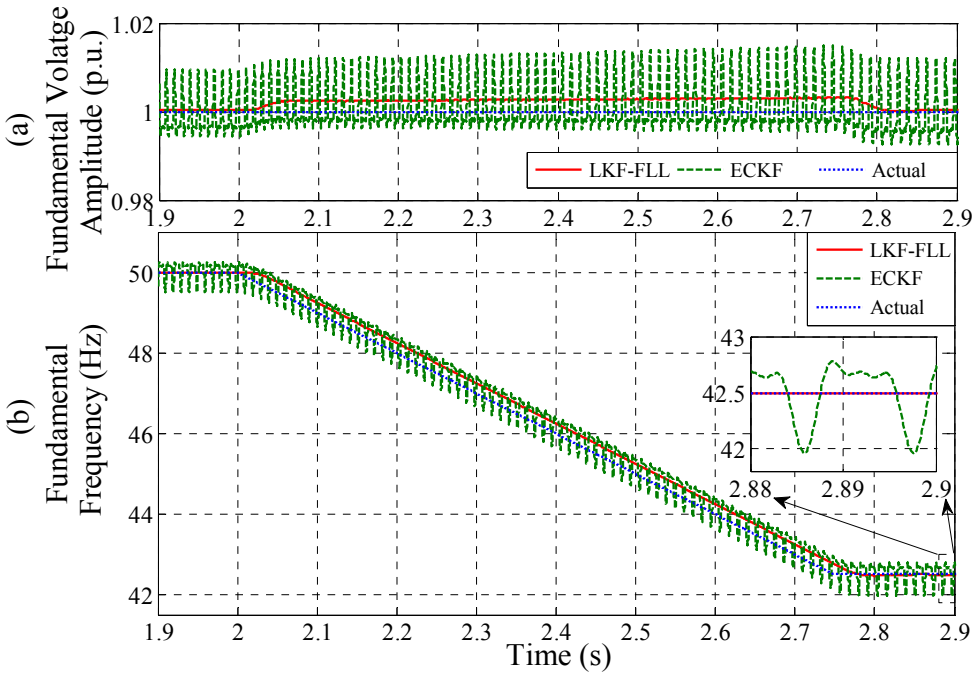

Fig. 7.8 Case-A2: Frequency sweep (-10 Hz/s: 50 Hz to 42.5 Hz) and harmonics. (a) Fundamental voltage amplitude. (b) Fundamental frequency.

7.1.4.3 Case-A3: Frequency Step and Harmonics

A worst case scenario of grid frequency variation such as a step change is considered in this case. Fig. 7.9 shows the estimation of fundamental voltage amplitude and +7.5 Hz (50 Hz to 57.5 Hz) frequency step under harmonics, as given in Table 7.2. As it can be noticed from Fig. 7.9(b), both LKF-FLL and ECKF techniques can track the frequency step. It can also be seen that the settling time for tracking the fundamental frequency step using the LKF-FLL technique is around 2.5 fundamental cycles. On the other hand, the fundamental voltage amplitude estimation using both techniques are affected by the frequency step, as can be observed in Fig. 7.9(a).

7.1.4.4 Case-A4: Voltage Sag and Harmonics

A grid voltage sag of 50% and harmonics, as given in Table 7.2, is shown in Fig. 7.10(a). The performance of the LKF-FLL and ECKF techniques for fundamental voltage amplitude and frequency estimation is shown in Fig. 7.10(b) and (c), respectively. As it can be seen from Fig. 7.10(b), the LKF-FLL and ECKF techniques can track the voltage sag. The settling time for tracking the fundamental voltage amplitude using both techniques is around 1.25 fundamental cycles. On the other hand, both techniques present undershoot in the frequency estimation during the voltage sag, as can be noticed in Fig. 7.10(c).

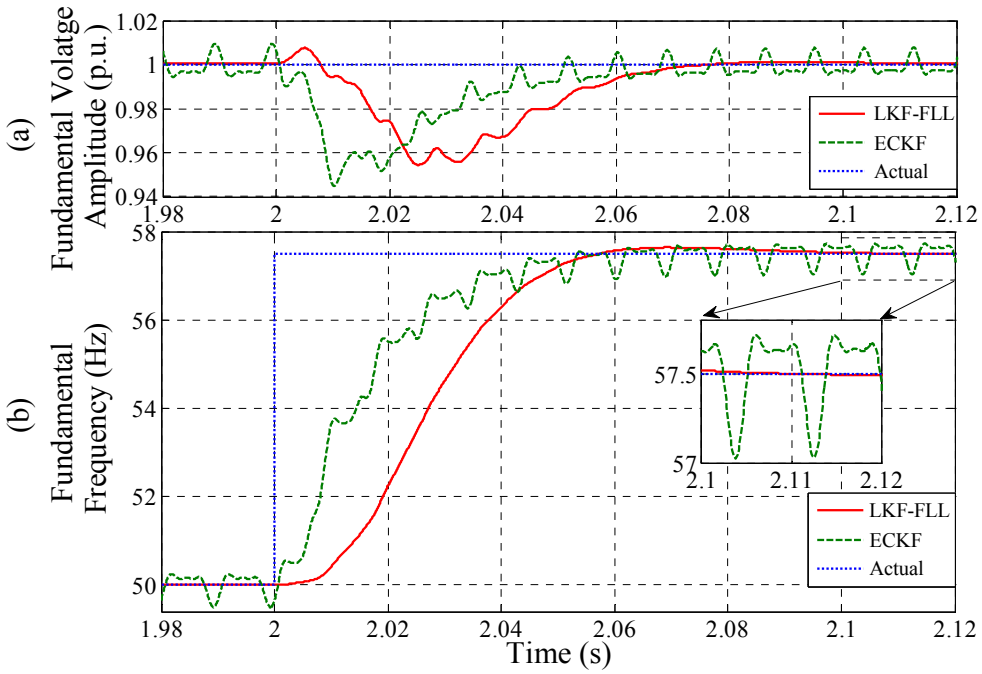

Fig. 7.9 Case-A3: Frequency step (+7.5 Hz: 50 Hz to 57.5 Hz) and harmonics. (a) Fundamental voltage amplitude. (b) Fundamental frequency.

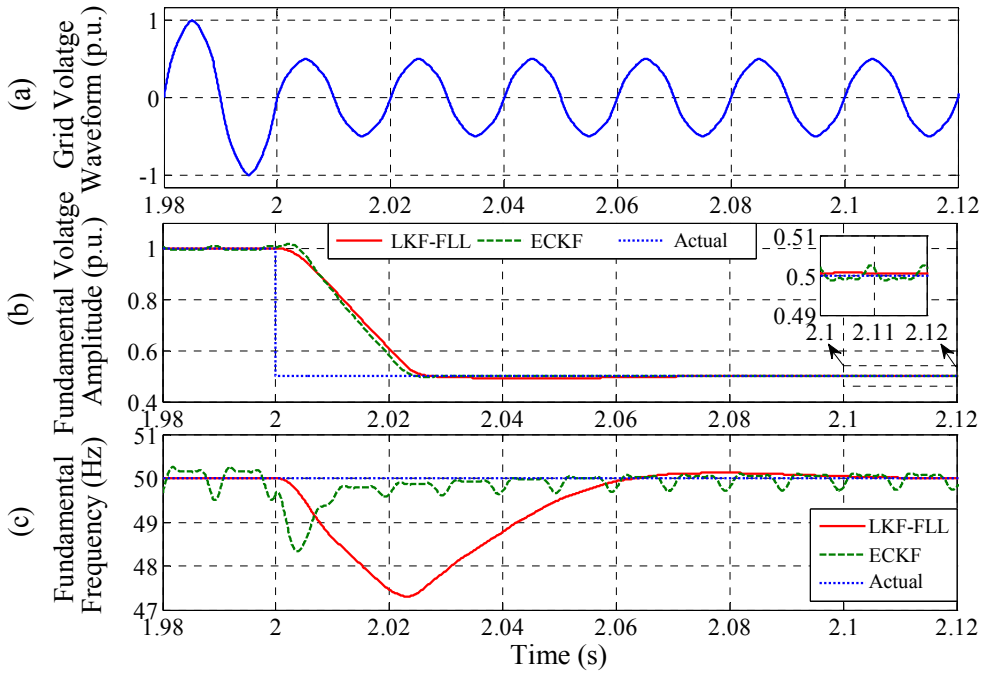

Fig. 7.10 Case-A4: Voltage sag (50%) and harmonics. (a) Grid voltage waveform. (b) Fundamental voltage amplitude. (c) Fundamental frequency.

7.1.4.5 Case-A5: Voltage Flicker and Harmonics

The grid voltage waveform, as shown in Fig. 7.11(a), contains 2.5 Hz, ±0.10 p.u. triangular voltage flicker and harmonics, as given in Table 7.2. In this case, the fundamental voltage amplitude and frequency estimation using the LKF-FLL and ECKF techniques are shown in Fig. 7.11(b) and (c), respectively. As it can be noticed, both techniques can track the voltage flicker. On the other hand, the LKF-FLL technique generates a steady-state error in the estimation of fundamental frequency due to the voltage flicker, as can be observed in Fig. 7.11(c).

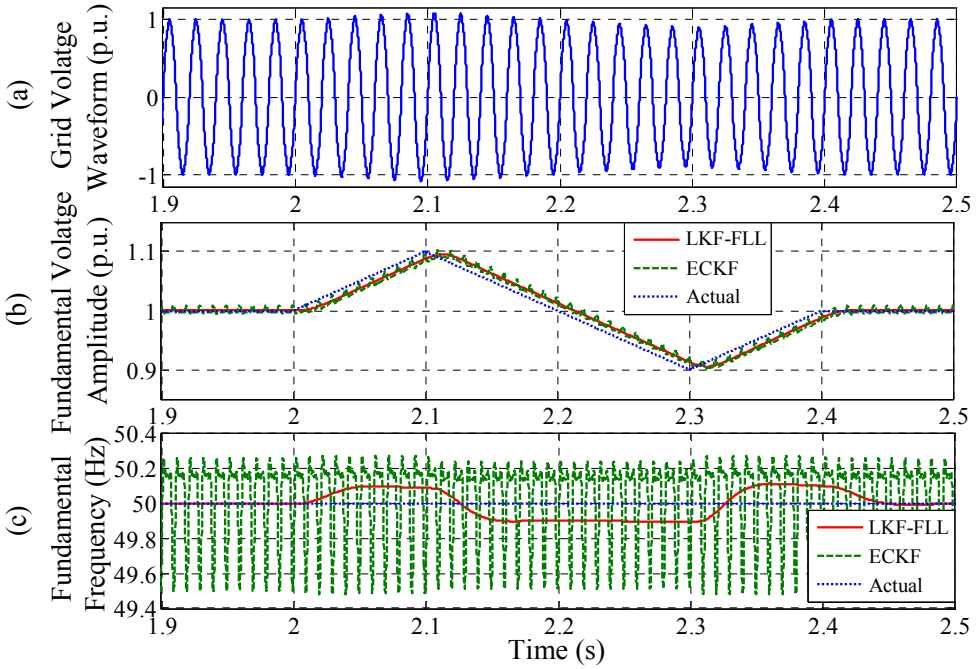

Fig. 7.11 Case-A5: Voltage flicker (±10%) and harmonics. (a) Grid voltage waveform. (b) Fundamental voltage amplitude. (c) Fundamental frequency.

7.2 Power System Harmonics and Flicker Estimation using A Kalman Filter Based Technique

In this section, the LKF-FLL technique is extended for the single-phase grid voltage fundamental amplitude, frequency and harmonics amplitudes estimation. In addition, an extended Kalman filter (EKF) is used to obtain the instantaneous voltage flicker level (IFL) from the estimated fundamental voltage amplitude. The proposed Kalman filter (KF) based technique for the grid voltage fundamental amplitude, frequency, harmonics

amplitudes and IFL estimation is shown in Fig. 7.12, where x_{i1} is the state corresponding to the in-phase component of v_i, x_{i2} is the state corresponding to the in-quadrature component of v_i, v_i is the voltage component at the angular frequency $i\omega$, (i=1,2,3,…,M), M is the maximum order of harmonics, $x_{i1} = v_i'$, v_i' is the estimated in-phase component of v_i, $x_{i2} = qv_i'$, qv_i' is the estimated in-quadrature component of v_i, x_{i1}^- is the predicted value of x_{i1}, x_{i2}^- is the predicted value of x_{i2}, $\hat{A}_i$ is the estimated amplitude of v_i, $\hat{A}_{fund}$ is the estimated fundamental voltage amplitude without IFL and v_F' is the estimated IFL. As it can be seen, the grid voltage fundamental angular frequency is estimated adaptively using the FLL and is forwarded to the LKF for extracting the orthogonal voltage components of the fundamental and harmonics present in the distorted grid voltage waveform. The orthogonal components are then used to obtain the amplitudes of the grid voltage fundamental and harmonics. The estimated fundamental voltage amplitude is passed through a LPF and is then fed to the EKF for extracting the IFL and the actual fundamental voltage amplitude without IFL.

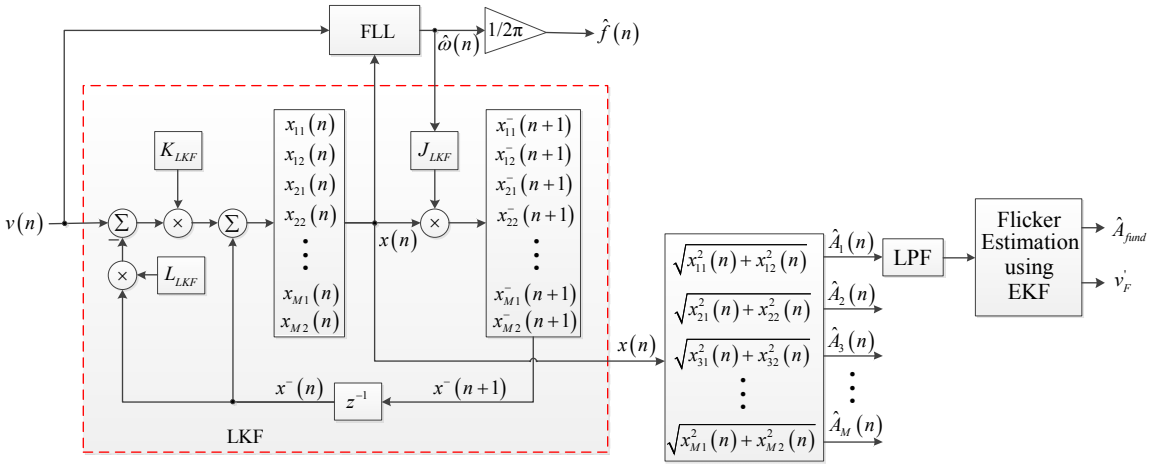

Fig. 7.12 Proposed frequency adaptive KF technique for the single-phase grid voltage fundamental amplitude, frequency, harmonics amplitudes and IFL estimation.

7.2.1 Fundamental and Harmonics Voltage Amplitudes Estimation

The single-phase grid voltage distorted by harmonics can be expressed by

$$v(n) = \sum_{i=1,2,3...}^{M} v_i(n) = \sum_{i=1,2,3...}^{M} A_i(n)\sin\left\{i\omega(n)nT_s + \theta_i(n)\right\} \tag{7.12}$$

where A_i and θ_i are the amplitude and initial phase angle of the $i\omega$ angular frequency component. Let us consider that the states of the in-phase and in-quadrature components of the $i\omega$ angular frequency component are given by (7.13) and (7.14), respectively.

$$x_{i1}(n) = v_i^{'}(n) = A_i(n)\sin\left\{i\omega(n)nT_s + \theta_i(n)\right\} \tag{7.13}$$

$$x_{i2}(n) = qv_i^{'}(n) = A_i(n)\cos\left\{i\omega(n)nT_s + \theta_i(n)\right\} \tag{7.14}$$

In this case, the state vector and the predicted state vector of the LKF can be expressed by (7.15) and (7.16), respectively.

$$x(n) = \left[x_{11}(n) \quad x_{12}(n) \quad x_{21}(n) \quad x_{22}(n) \quad \cdots \quad x_{M1}(n) \quad x_{M2}(n)\right]^{\square} \tag{7.15}$$

$$x^{-}(n+1) = \begin{bmatrix} x_{11}(n)\cos\left\{1\omega(n)T_s\right\} + x_{12}(n)\sin\left\{1\omega(n)T_s\right\} \\ -x_{11}(n)\sin\left\{1\omega(n)T_s\right\} + x_{12}(n)\cos\left\{1\omega(n)T_s\right\} \\ x_{21}(n)\cos\left\{3\omega(n)T_s\right\} + x_{22}(n)\sin\left\{2\omega(n)T_s\right\} \\ -x_{21}(n)\sin\left\{3\omega(n)T_s\right\} + x_{22}(n)\cos\left\{2\omega(n)T_s\right\} \\ \vdots \\ x_{M1}(n)\cos\left\{M\omega(n)T_s\right\} + x_{M2}(k)\sin\left\{M\omega(n)T_s\right\} \\ -x_{M1}(n)\sin\left\{M\omega(n)T_s\right\} + x_{M2}(k)\cos\left\{M\omega(n)T_s\right\} \end{bmatrix} \tag{7.16}$$

Therefore, the state transition or Jacobian matrix can be obtained from (7.15) and (7.16), and is expressed by

$$J_{LKF} = \begin{bmatrix} \cos\left\{1\omega(n)T_s\right\} & \sin\left\{1\omega(n)T_s\right\} & 0 & 0 & \cdots & 0 & 0 \\ -\sin\left\{1\omega(n)T_s\right\} & \cos\left\{1\omega(n)T_s\right\} & 0 & 0 & \cdots & 0 & 0 \\ 0 & 0 & \cos\left\{2\omega(n)T_s\right\} & \sin\left\{2\omega(n)T_s\right\} & \cdots & 0 & 0 \\ 0 & 0 & -\sin\left\{2\omega(n)T_s\right\} & \cos\left\{2\omega(n)T_s\right\} & \cdots & 0 & 0 \\ 0 & 0 & 0 & 0 & \ddots & 0 & 0 \\ 0 & 0 & 0 & 0 & \cdots & \cos\left\{M\omega(n)T_s\right\} & \sin\left\{M\omega(n)T_s\right\} \\ 0 & 0 & 0 & 0 & \cdots & -\sin\left\{M\omega(n)T_s\right\} & \cos\left\{M\omega(n)T_s\right\} \end{bmatrix} \tag{7.17}$$

In this case, the measurement matrix of the LKF can be expressed by

$$L_{LKF} = \left[1 \quad 0 \quad 1 \quad 0 \quad \cdots \quad 1 \quad 0\right] \tag{7.18}$$

The amplitude of the $i\omega$ angular frequency component can be obtained by

$$\hat{A}_i(n)=\sqrt{x_{i1}^2(n)+x_{i2}^2(n)}=\sqrt{v_i^{'2}(n)+qv_i^{'2}(n)} \tag{7.19}$$

The THD present in the grid voltage can also be estimated by

$$\mathrm{THD}(n)=\sqrt{\frac{\sum_{h=2,3,..}^{M} x_{h1}^2(n)+x_{h2}^2(n)}{x_{11}^2(n)+x_{12}^2(n)}}=\sqrt{\frac{\sum_{h=2,3,..}^{M} v_h^{'2}(n)+qv_h^{'2}(n)}{v_1^{'2}(n)+qv_1^{'2}(n)}} \tag{7.20}$$

where x_{h1} is the state corresponding to in-phase component of h^{th} (h=2,3,…,M) harmonic voltage (v_h), x_{h2} is the state corresponding to in-quadrature component of v_h, $v_h^{'}=x_{h1}$, $v_h^{'}$ is the estimated in-phase component of v_h, $qv_h^{'}=x_{h2}$, and $qv_h^{'}$ is the estimated in-quadrature component of v_h.

7.2.2 Fundamental Frequency Estimation

The grid voltage fundamental frequency estimation using the FLL is shown in Fig. 7.13. As it can be seen, the in-phase harmonic voltage components estimated by the LKF are added $(v_H^{'}=\sum_{h=2,3,...,}^{M} v_h^{'})$ and subtracted from the input grid voltage to separate the input voltage fundamental component. An error voltage (e_v) is then obtained by subtracting the fundamental voltage in-phase component estimated by the LKF from the fundamental voltage component of the grid voltage. The error signal and the in-quadrature component of the fundamental frequency estimated by the LKF are fed to the FLL to track the fundamental frequency adaptively and instantaneously, as can be seen in Fig. 7.13. In this case, similar to (7.11), the dynamics of the FLL can also be expressed by [194, 197, 198]

$$\dot{\omega}(n)=\frac{\gamma e_v(n)qv_1^{'}(n)}{A_1^2}=\gamma\sin\left[\left\{\omega(n)-\hat{\omega}(n)\right\}nT_s\right]+\gamma\sin\left[\left\{\omega(n)+\hat{\omega}(n)\right\}nT_s+2\theta_1(n)\right]$$

$$-\gamma\sin\left\{2\omega(n)nT_s+2\theta_1(n)\right\}\cong\gamma\sin\left[\left\{\omega(n)-\hat{\omega}(n)\right\}nT_s\right] \tag{7.21}$$

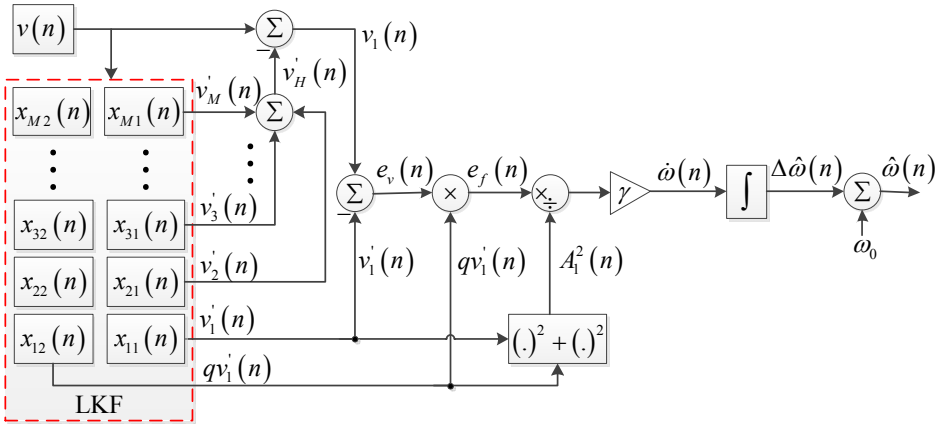

Fig. 7.13 Single-phase grid voltage fundamental frequency estimation using the FLL based on the orthogonal waveforms generated by the LKF.

7.2.3 Instantaneous Voltage Flicker Level (IFL) Estimation

The grid voltage fundamental amplitude estimated by the LKF-FLL technique can be used to extract the IFL (v_F) and the actual fundamental voltage amplitude without IFL (A_{fund}). The EKF can be used for this purpose. The fundamental voltage amplitude extracted by the LKF-FLL technique can be expressed by

$$\hat{A}_1(n) = A_{fund}(n) + v_F(n) = A_{fund}(n) + A_F(n)\sin\left\{2\pi f_F(n) nT_s + \theta_F(n)\right\} \quad (7.22)$$

where A_F, f_F and θ_F are the amplitude, frequency and initial phase angle of the IFL, respectively. The estimated fundamental voltage amplitude is filtered using a LPF and is forwarded to the EKF to extract the IFL. The states of the EKF for the IFL estimation are given by (7.23), (7.24), (7.25) and (7.26), respectively.

$$x_{F1}(n) = A_F(n)\sin\left\{2\pi f_F(n) nT_s + \theta_F(n)\right\} \quad (7.23)$$

$$x_{F2}(n) = A_F(n)\cos\left\{2\pi f_F(n) nT_s + \theta_F(n)\right\} \quad (7.24)$$

$$x_{F3}(n) = f_F(n) \quad (7.25)$$

$$x_{F4}(n) = A_{fund}(n) \quad (7.26)$$

where the states x_{F1} and x_{F2} represent the in-phase and in-quadrature components of the IFL present in the grid voltage. The actual amplitude of the fundamental voltage without

IFL and flicker frequency can be obtained directly from the states x_{F4} and x_{F3}, respectively.

The estimation of the IFL using the EKF is based on the fact that the phasor is rotated by an amount of $2\pi f_F(n)T_s$ at the (n+1) sampling instant. Therefore, the state transition between the n and (n+1) sampling instants for x_{F1} and x_{F2} can be expressed by

$$x_{F1}(n+1)+jx_{F2}(n+1)=\left\{x_{F1}(n)+jx_{F2}(n)\right\}e^{j\left\{2\pi f_F(n)T_s\right\}} \tag{7.27}$$

In this case, the estimation function, state vector, predicted state vector, state transition matrix, and measurement matrix of the EKF can be expressed by (7.28), (7.29), (7.30), (7.31) and (7.32), respectively.

$$g_2\left\{x_F(n)\right\}=x_{F4}(n)+x_{F1}(n)\cos\left\{2\pi x_{F3}(n)T_s\right\}+x_{F2}(n)\sin\left\{2\pi x_{F3}(n)T_s\right\} \tag{7.28}$$

$$x_F(n)=\begin{bmatrix}x_{F1}(n) & x_{F2}(n) & x_{F3}(n) & x_{F4}(n)\end{bmatrix}^{\square} \tag{7.29}$$

$$x_F^-(n+1)=\begin{bmatrix}x_{F1}(n)\cos\left\{2\pi x_{F3}(n)T_s\right\}+x_{F2}(n)\sin\left\{2\pi x_{F3}(n)T_s\right\}\\ -x_{F1}(n)\sin\left\{2\pi x_{F3}(n)T_s\right\}+x_{F2}(n)\cos\left\{2\pi x_{F3}(n)T_s\right\}\\ x_{F3}(n)\\ x_{F4}(n)\end{bmatrix} \tag{7.30}$$

$$J_{EKF}=\begin{bmatrix}\cos\left\{2\pi x_{F3}(n)T_s\right\} & \sin\left\{2\pi x_{F3}(n)T_s\right\} & J_{EKF}(1,3) & 0\\ -\sin\left\{2\pi x_{F3}(n)T_s\right\} & \cos\left\{2\pi x_{F3}(n)T_s\right\} & J_{EKF}(2,3) & 0\\ 0 & 0 & 1 & 0\\ 0 & 0 & 0 & 1\end{bmatrix} \tag{7.31}$$

$$L_{EKF}=\begin{bmatrix}\cos\left\{2\pi x_{F3}(n)T_s\right\} & \sin\left\{2\pi x_{F3}(n)T_s\right\} & L_{EKF}(1,3) & 1\end{bmatrix} \tag{7.32}$$

where

$$J_{EKF}(1,3)=2\pi T_s\left[-x_{F1}(n)\sin\left\{2\pi x_{F3}(n)T_s\right\}+x_{F2}(n)\cos\left\{2\pi x_{F3}(n)T_s\right\}\right]$$

$$J_{EKF}(2,3)=2\pi T_s\left[-x_{F1}(n)\cos\left\{2\pi x_{F3}(n)T_s\right\}-x_{F2}(n)\sin\left\{2\pi x_{F3}(n)T_s\right\}\right]$$

$$L_{EKF}(1,3)=2\pi T_s\left[-x_{F1}(n)\sin\left\{2\pi x_{F3}(n)T_s\right\}+x_{F2}(n)\cos\left\{2\pi x_{F3}(n)T_s\right\}\right]$$

The state transition matrix, as given in (7.31), is obtained by the partial derivative of (7.30) with respect to the states in the vector x_F. The measurement matrix, as given by (7.32), is also obtained by the partial derivative of (7.28) with respect to the states in the vector x_F. The steps of the EKF are similar to the steps of the LKF, as presented in Section 7.1, except x, J_{LKF}, L_{LKF} and v will be replaced by x_F, J_{EKF}, L_{EKF} and $\hat{A}_1$, respectively. The implementation of the EKF for IFL estimation is shown in Fig. 7.14.

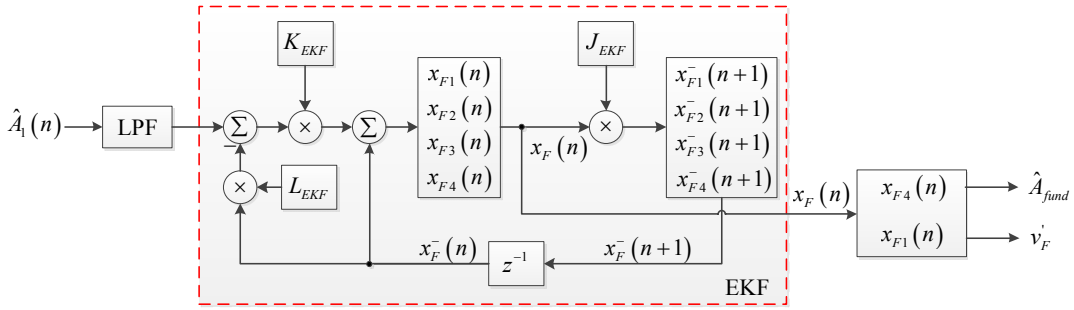

Fig. 7.14 EKF for the estimation of IFL present in the grid voltage fundamental amplitude.

7.2.4 Simulation Results

The simulation performance of the proposed KF based technique is reported in this subsection. The sampling frequency is chosen as 4 kHz. A second-order infinite-impulse-response (IIR) LPF with a cut-off frequency of equal to 25 Hz is used before the EKF in the proposed technique. The following case studies are carried out to evaluate the performance of the proposed technique.

i. Steady-state with harmonics (Case-B1)
ii. Frequency drifts and harmonics (Case-B2)
iii. Voltage sag, harmonics and frequency sweep (Case-B3)
iv. Voltage swell, harmonics and frequency sweep (Case-B4)
v. Phase jump, harmonics and frequency sweep (Case-B5)
vi. Voltage flicker, harmonics and frequency sweep (Case-B6)

The grid voltage fundamental component presented in all the above case studies contains a THD of equal to 22.36%, as given in Table 7.3.

Table 7.3 Harmonics as a percentage of fundamental component

Harmonics		THD
3^{rd}	5^{th}	22.36%
20.0 %	10.0 %	

7.2.4.1 Case-B1: Steady-State with Harmonics

The steady-state estimation of the grid voltage fundamental amplitude, frequency and harmonics amplitudes using the LKF-FLL technique is shown in Fig. 7.15, where the grid voltage contains 3^{rd} and 5^{th} harmonics of THD equal to 22.36% THD, as given in Table 7.3. As it can be noticed, the proposed LKF-FLL technique can provide accurate estimation of the fundamental voltage amplitude, frequency and harmonics amplitudes.

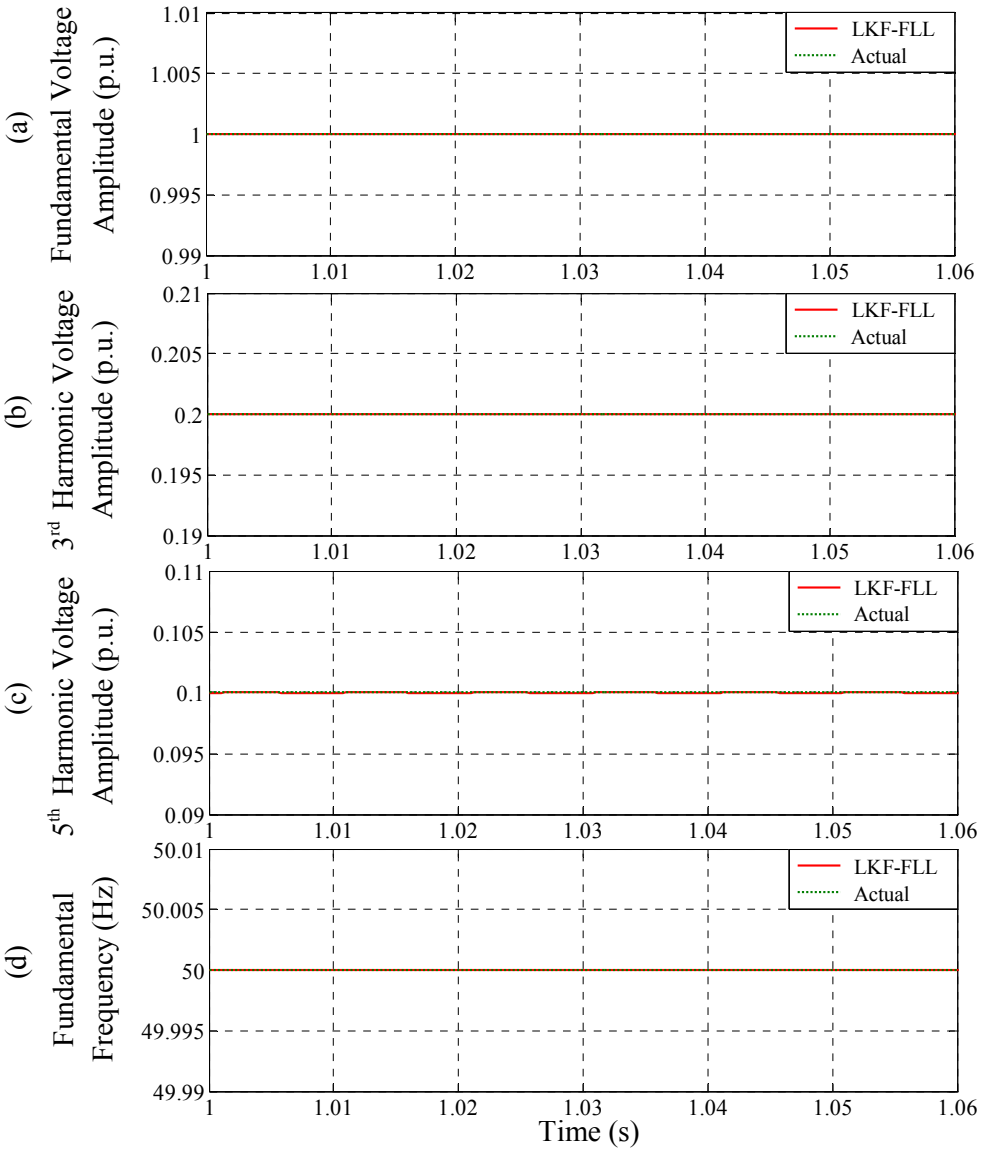

Fig. 7.15 Case-B1: Steady-state with harmonics. (a) Fundamental voltage amplitude. (b) 3rd harmonic voltage amplitude. (c) 5th harmonic voltage amplitude. (d) Fundamental frequency.

7.2.4.2 Case-B2: Frequency Drifts and Harmonics

The performance of the LKF-FLL technique for fundamental frequency estimation under various frequency drift conditions is shown in Fig. 7.16, where the grid voltage contains 22.36% THD, as given in Table 7.3. In this case, sinusoidal, triangular, sawtooth and square variations of the fundamental frequency are considered in the harmonically distorted grid voltage waveforms. As it can be noticed from Fig. 7.16(a) and (b), a slowly varying fundamental frequency such as the sinusoidal and triangular is tracked accurately. On the other hand, the estimation of the step change of fundamental frequency in sawtooth

and square variations takes approximately one fundamental cycle as settling time to attain the actual value, as can be noticed in Fig. 7.16(c) and (d), respectively.

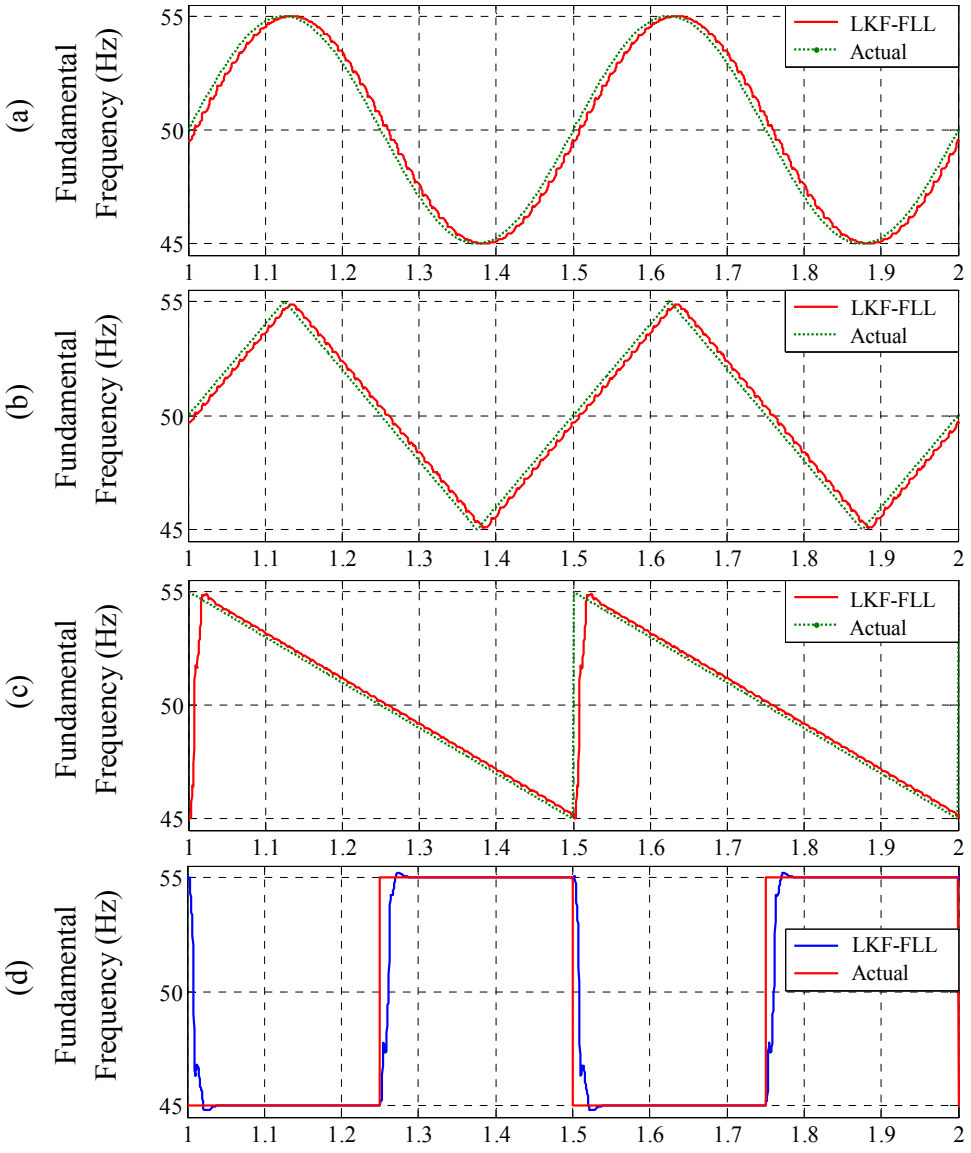

Fig. 7.16 Case-B2: Frequency drifts and harmonics. (a) Sinusoidal variation of the fundamental frequency. (b) Triangular variation of the fundamental frequency. (c) Sawtooth variation of the fundamental frequency. (d) Square variation of the fundamental frequency.

7.2.4.3 Case-B3: Voltage Sag, Harmonics and Frequency Sweep

Fig. 7.17 shows the estimation of the grid voltage fundamental amplitude, frequency and THD using the LKF-FLL under a voltage sag of 50%, 22.36% THD, as given in Table 7.3, and frequency sweep. As it can be noticed from Fig. 7.17(a), the voltage sag is tracked adaptively by the LKF-FLL technique at the expense of approximately one fundamental

cycle settling time. On the other hand, the THD and fundamental frequency estimation are affected during the transient of the voltage sag, as can be seen in Fig. 7.17(b) and (c), respectively.

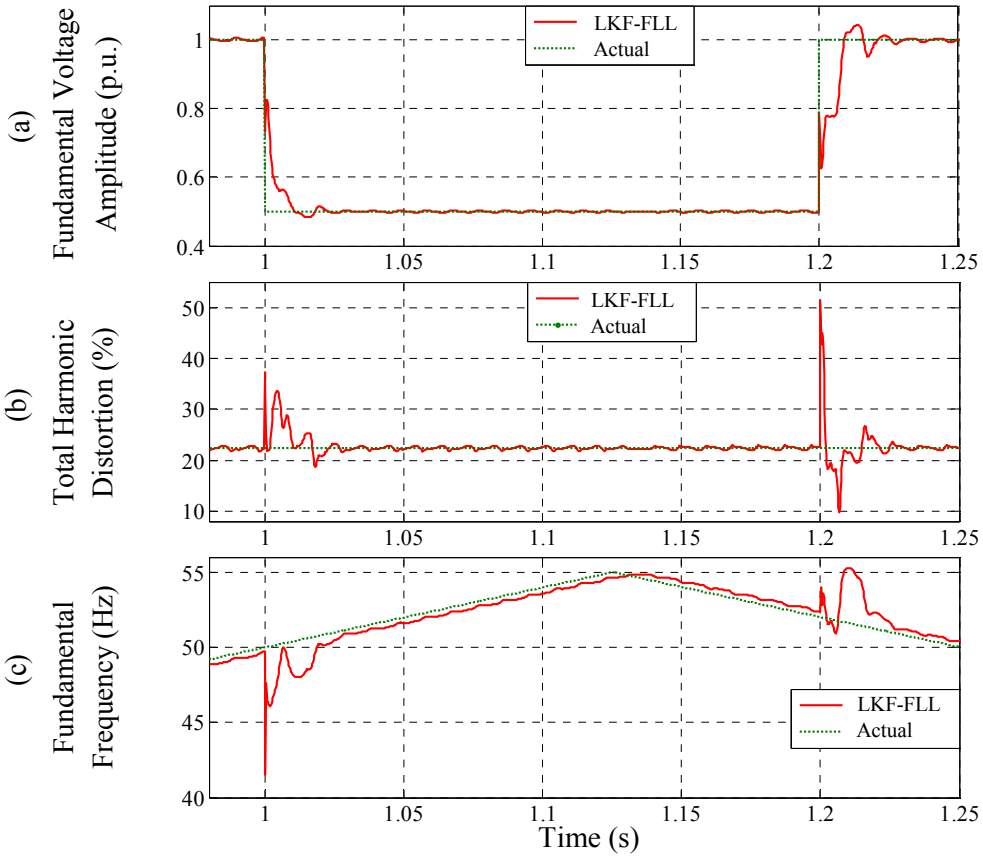

Fig. 7.17 Case-B3: Voltage sag (50%), harmonics and frequency sweep. (a) Fundamental voltage amplitude. (b) Total harmonic distortion. (c) Fundamental frequency.

7.2.4.4 Case-B4: Voltage Swell, Harmonics and Frequency Sweep

The estimation of the grid voltage fundamental amplitude, frequency and THD using the LKF-FLL technique are shown in Fig. 7.18 under a voltage swell of 50%, harmonics, as given in Table 7.3, and frequency sweep. Similar to the voltage sag, the voltage swell is tracked adaptively by the LKF-FLL technique. The estimation of the THD and fundamental frequency is also affected during the transient of the voltage swell, as can be noticed in Fig. 7.18(b) and (c), respectively.

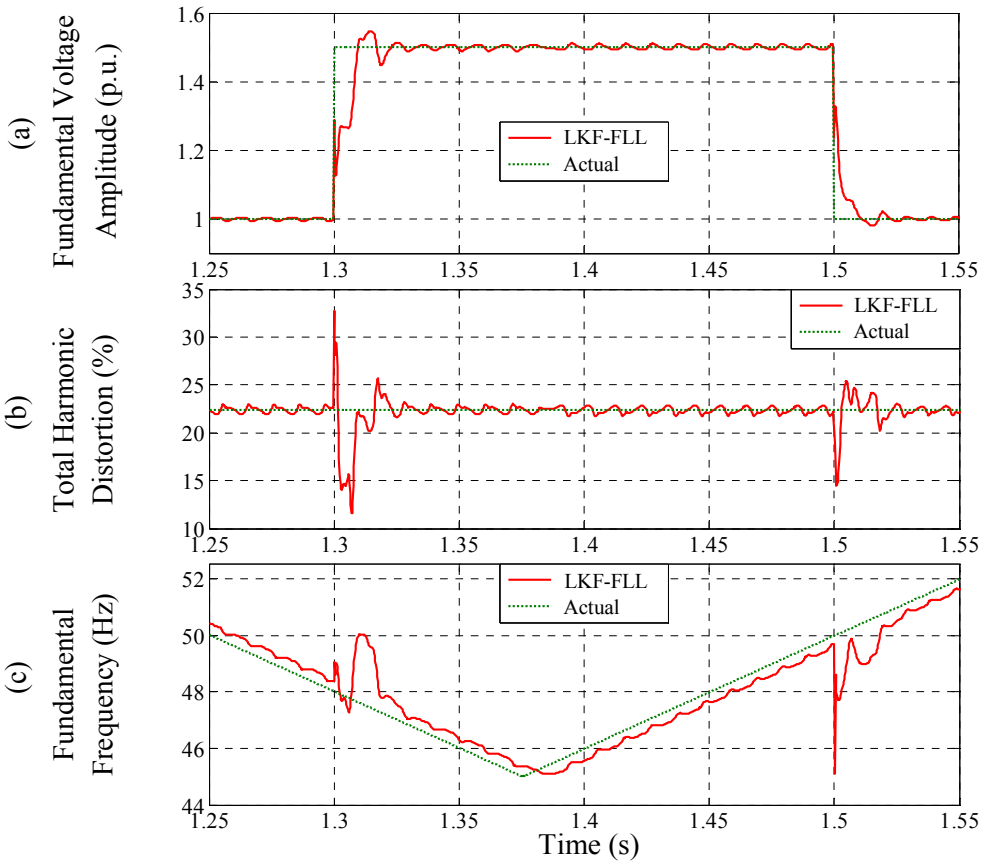

Fig. 7.18 Case-B4: Voltage swell (50%), harmonics and frequency sweep. (a) Fundamental voltage amplitude. (b) Total harmonic distortion. (c) Fundamental frequency.

7.2.4.5 Case-B5: Phase Jump, Harmonics and Frequency Sweep

In this case, 10º phase jump (-10º at time 1s and +10º at time 1.2s) is introduced into a grid voltage waveform containing harmonics, as given in Table 7.3, and frequency sweep. The estimation of the fundamental voltage amplitude, THD and fundamental frequency is shown in Fig. 7.19. As it can be noticed, the estimation is affected during the phase jump. However, after the dynamics, the technique can track the parameters accurately, as can be noticed from Fig. 7.19.

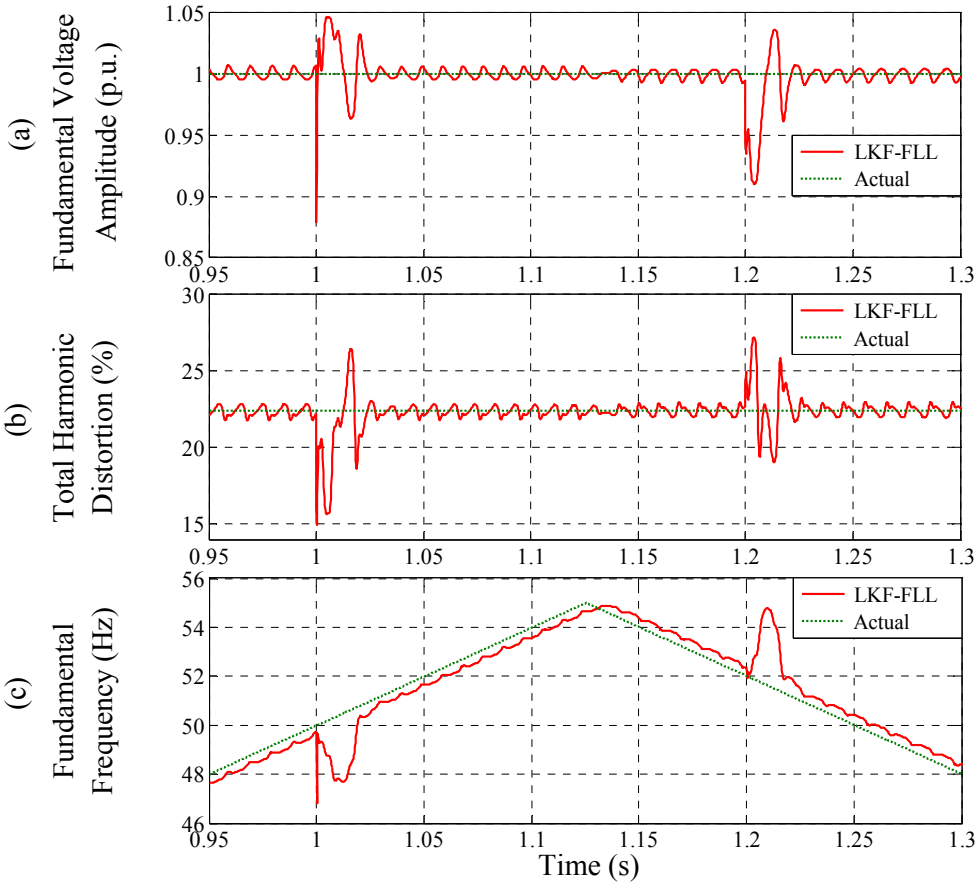

Fig. 7.19 Case-B5: Phase jump (-10º at time 1s and +10º at time 1.2s), harmonics and frequency sweep. (a) Fundamental voltage amplitude. (b) Total harmonic distortion. (c) Fundamental frequency.

7.2.4.6 Case-B6: Voltage Flicker, Harmonics and Frequency Sweep

In this case, the performance of the proposed technique is verified under voltage flicker, harmonics and frequency sweep conditions. Fig. 7.20 shows the estimation of the fundamental voltage amplitude, IFL, THD and fundamental frequency, where the grid voltage contains A_F =0.1 p.u., f_F=5 Hz voltage flicker, 0.2 p.u. 3rd and 0.1 p.u. 5th harmonics and frequency sweep. As it can be seen, the proposed technique can provide accurate estimation of the time-varying grid voltage fundamental amplitude, IFL, THD and fundamental frequency.

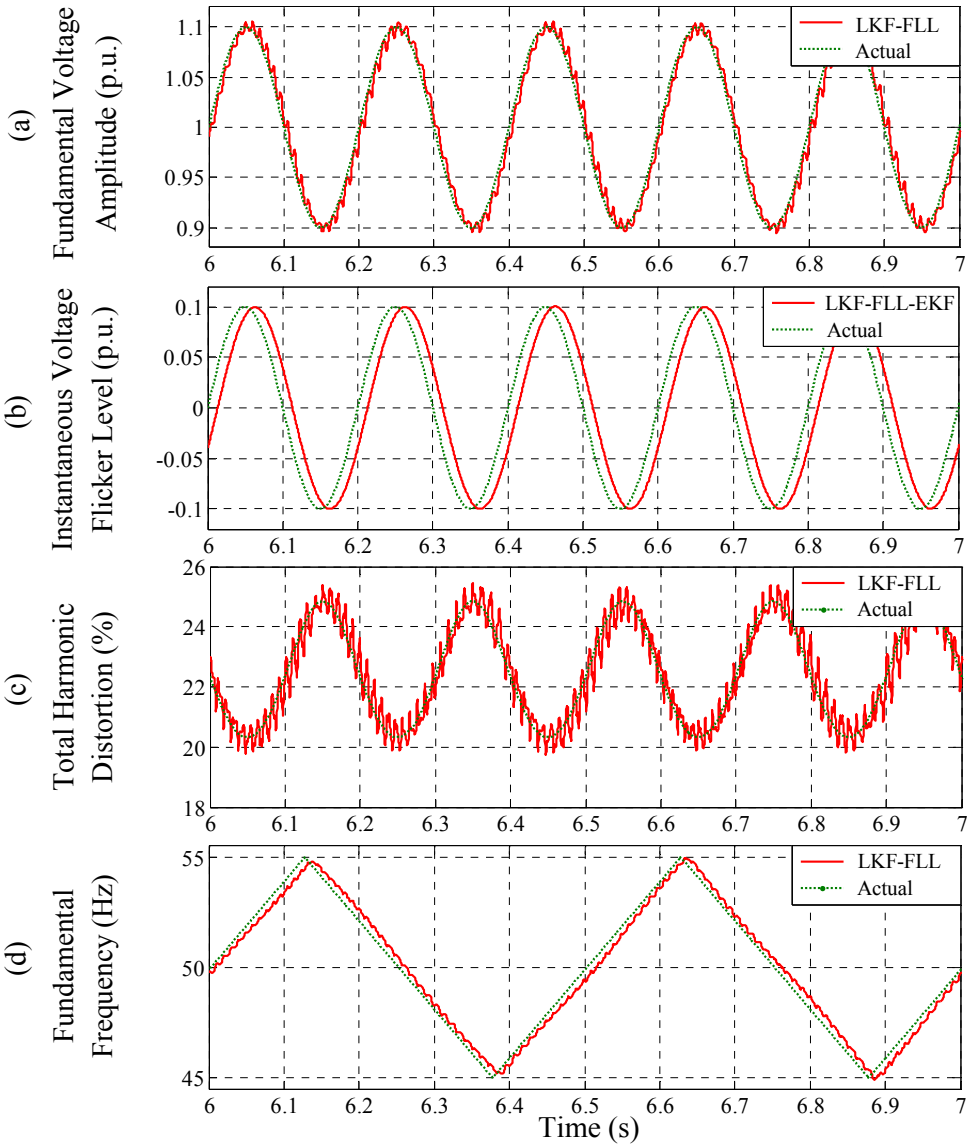

Fig. 7.20 Case-B6: Voltage flicker (A_F =0.1 p.u., f_F=5 Hz), harmonics and frequency sweep. (a) Fundamental voltage amplitude. (b) Instantaneous voltage flicker level. (c) Total harmonic distortion. (d) Fundamental frequency.

Fig. 7.21 and Fig. 7.22 show the estimation of the fundamental voltage amplitude, IFL, THD and fundamental frequency using the proposed technique for the voltage flicker with time-varying parameters such as A_F =0~0.2 p.u., f_F=5 Hz and A_F =0~0.2 p.u., f_F=3~7 Hz, respectively. As it can be noticed, the proposed technique can also track the IFL with time-varying parameters. Moreover, the estimations of fundamental voltage amplitude, frequency and THD are accurate under the IFL with time-varying parameters, as can be seen in Fig. 7.21 and Fig. 7.22.

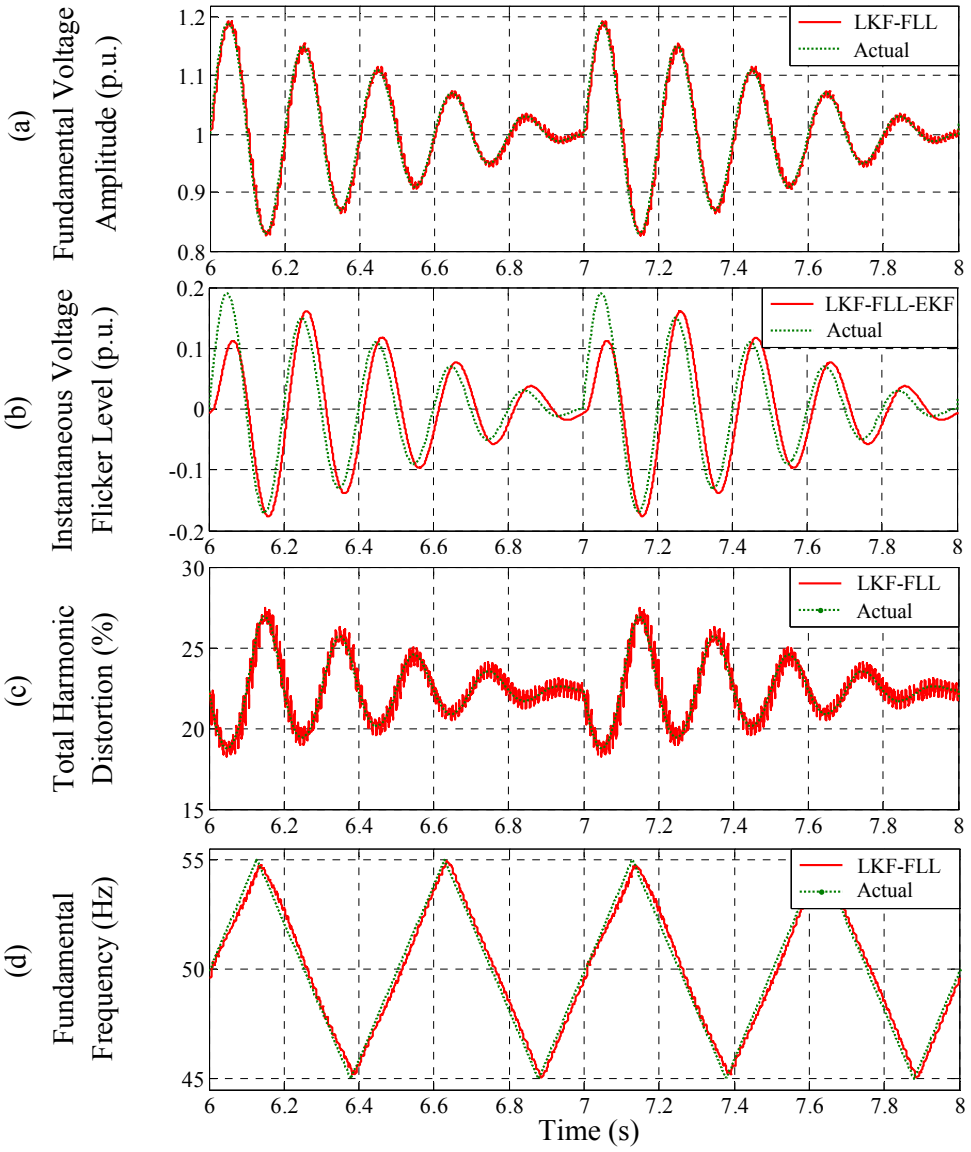

Fig. 7.21 Case-B6: Voltage flicker (A_F =0~0.2 p.u., f_F=5 Hz), harmonics and frequency sweep. (a) Fundamental voltage amplitude. (b) Instantaneous voltage flicker level. (c) Total harmonic distortion. (d) Fundamental frequency.

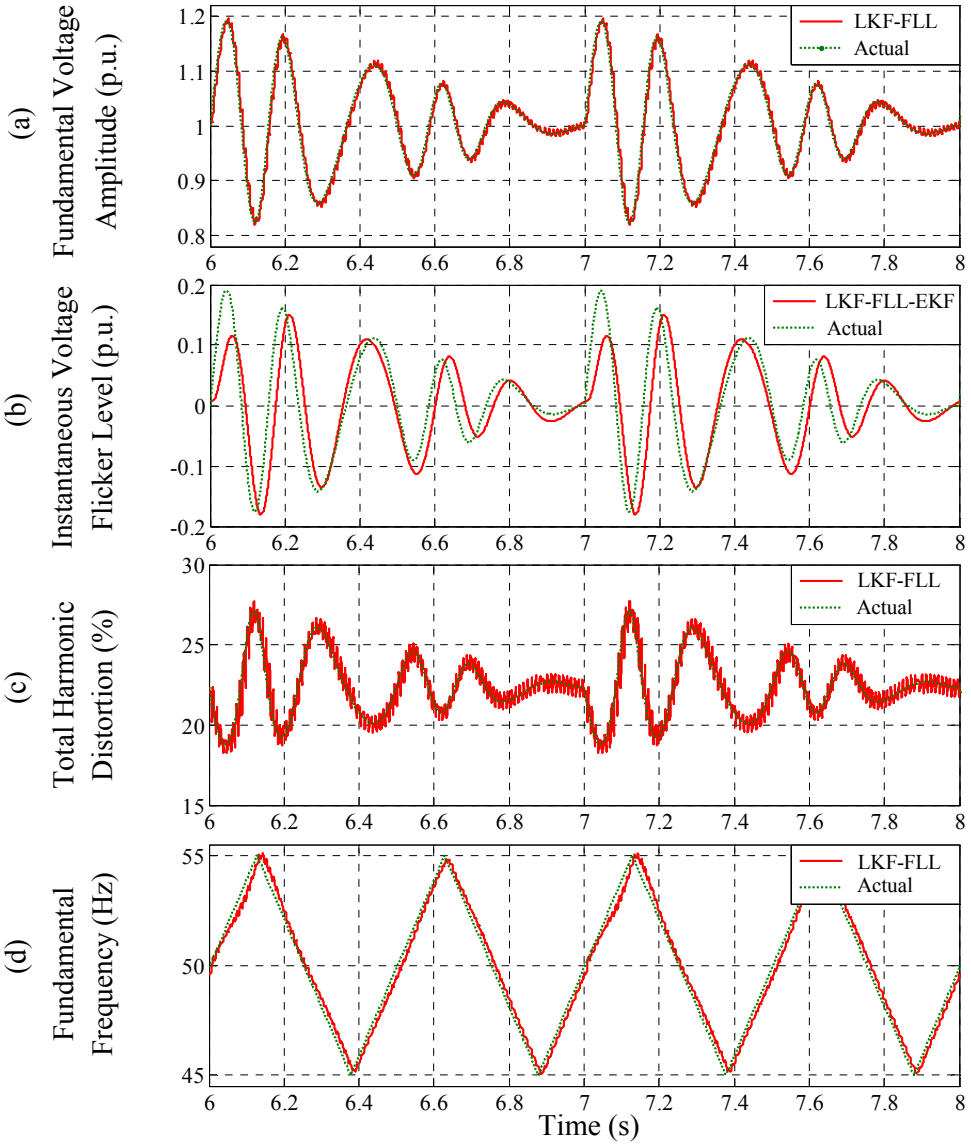

Fig. 7.22 Case-B6: Voltage flicker (A_F =0~0.2 p.u., f_F=3~7 Hz), harmonics and frequency sweep. (a) Fundamental voltage amplitude. (b) Instantaneous voltage flicker level. (c) Total harmonic distortion. (d) Fundamental frequency.

7.3 Conclusions

A frequency adaptive linear Kalman filter technique relying on a frequency-locked loop has been reported in this chapter for single-phase grid voltage fundamental amplitude and frequency estimation. A frequency domain analysis for tuning the LKF parameters has been presented. When compared with a nonlinear Kalman filter such as an extended Kalman filter, the proposed technique offers the following benefits: is linear; avoids the derivatives of the nonlinear functions; does not contain nonlinear terms; and is

computationally less complex. The proposed technique can reject the negative effects caused by harmonics. The fundamental frequency estimation using the proposed technique is less sensitive to the presence of harmonics as compared to an extended complex Kalman filter. Moreover, the proposed technique can estimate a wide range of frequency variation and can also meet the error criteria specified by the standard. The effective application of the proposed technique for fundamental voltage amplitude and frequency estimation has been verified by simulation results.

The frequency adaptive linear Kalman filter technique based on the frequency-locked loop has also been extended for the estimation of single-phase grid voltage fundamental amplitude, frequency and harmonics amplitudes. An extended Kalman filter has also been used to estimate the instantaneous voltage flicker level present in the grid voltage. The frequency-locked loop based linear Kalman filter technique avoids the use of the nonlinear Kalman filter for fundamental and harmonics parameters estimation. However, the technique depends on the extended Kalman filter for voltage flicker estimation. The technique can provide accurate estimation of the grid voltage fundamental amplitude, frequency, harmonics amplitudes and voltage flicker under a wide range of frequency variation. The presented simulation results have confirmed the effective application of the proposed technique for grid voltage fundamental amplitude, frequency, harmonics amplitudes and voltage flicker estimation.

Chapter 8
Conclusions

This chapter concludes all the estimation techniques proposed in this thesis. A summary of each chapter is documented in Section 8.1. A benchmark among the proposed techniques is reported in Section 8.2. Finally, Section 8.3 suggests some directions for future research.

8.1 Summary

The thesis has started with research motivation and objectives in Chapter 1. A review of the technical literature on voltage monitoring techniques has been presented in Chapter 2. A number of digital signal processing (DSP) techniques have been proposed in Chapters 3-7 for single-phase grid voltage fundamental amplitude and/or frequency estimation. Simulation and/or real-time experimental results have also been documented in Chapters 3-7 for showing the effective application of the proposed techniques to estimate the grid voltage parameters. The IEEE, IEC and European standards have been followed to evaluate the performance of the proposed techniques. More specifically, chapters presented in the thesis have offered the followings.

Chapter 1 has documented the objectives along with the background and motivation of the thesis. The methodology and tools used for implementing the proposed estimation techniques have also been documented in this chapter. Moreover, the contributions of the thesis have been reported. Furthermore, a list of publications obtained from the proposed techniques has been presented.

In **Chapter 2**, a comprehensive overview of the commonly used single-phase grid voltage parameters estimation techniques has been presented. The following techniques are reviewed in this chapter: discrete Fourier Transform (DFT), adaptive linear combiner (ADALINE), Newton-type algorithm (NTA), least-squares (LS), Kalman filter (KF), Prony's method (PM), phase-locked loop (PLL), frequency-locked loop (FLL), demodulation, Teager energy operator (TEO), zero crossing detection (ZCD), and three consecutive samples (3CS).

Chapter 3 has presented a technique based on the TEO and a band-pass filter (BPF) for single-phase grid voltage fundamental frequency estimation. The BPF has been implemented based on a recursive DFT (RDFT) and inverse RDFT. The proposed RDFT-TEO technique is relatively simple and computationally efficient. It can also provide the accurate estimation of a wide range of fundamental frequency variation, as specified by the IEC standards 61000-4-7 and 61000-4-30. The RDFT-TEO technique requires less computational effort, can provide faster estimation and is less affected by harmonics as compared to the RDFT based decomposition of a single-phase system into orthogonal components (RDFT-OC) technique. The real-time experimental performance comparison between RDFT-TEO and RDFT-OC techniques has been assessed under DC offset, harmonics, frequency drifts, amplitude excursions and phase jump. The presented experimental results have confirmed the effectiveness of the RDFT-TEO technique for real-time applications.

In summary, the pros and cons of the RDFT-TEO technique are given in the following.

Pros:
- Relatively simple
- Computationally efficient
- Can reject errors caused by DC offset and harmonics
- Can meet standard requirements
- Settling time is around 1.5 fundamental cycles

Cons:
- Contains interdependent loop
- Requires proper tuning of the low-pass filter (LPF) for stability

In **Chapter 4**, a single-phase grid voltage fundamental frequency estimation technique has been proposed. The technique is based on the NTA and an infinite-impulse-response (IIR) differentiation filter (DF). The proposed technique reduces matrix dimensions, avoids matrix inversion operation, is computationally efficient and also shows less sensitivity to the presence of harmonics when compared with the NTA based LS (NTA-LS) technique. The proposed NAT-DF technique can reject the negative effects caused by the presence of DC offset and harmonics, and also meet the estimation error criteria under a large variation of frequency as specified by the IEC standards 61000-4-7 and 61000-4-30. The performance of the NTA-DF and NTA-LS techniques has been evaluated on a real-time digital signal processor. The experimental performance has been tested under DC offset, harmonics, frequency variations, amplitude excursions, phase jump, notches and spikes, and has proved the capability of the proposed technique for real-time frequency estimation.

In summary, the pros and cons of the NTA-DF technique are given in the following.

Pros:
- Computationally efficient
- Can reject errors caused by DC offset and harmonics
- Can meet standard requirements
- No interdependent loop
- Avoids matrix inversion operation

Cons:
- Subject to instability when abrupt changes occur
- Settling time is around 3.5 fundamental cycles

Chapter 5 has introduced three techniques based on a modulation and/or demodulation to estimate the single-phase grid voltage fundamental amplitude and/or frequency.

The first technique relies on the 3CS and a finite-impulse-response (FIR) filter based on a voltage modulation, and is used to estimate the single-phase grid voltage fundamental frequency. The technique is robust and can provide the estimation of a wide range of fundamental frequency variation under harmonics with an acceptable error, as specified by the IEC standards 61000-4-7 and 61000-4-30. The technique does not require setting a threshold value of the middle sample of 3CS for removing the ill-condition when compared with a conventional technique based on the 3CS and a FIR filter. In addition, the proposed technique is less affected by DC offset, voltage sag, voltage flicker, notches and spikes, and also provides improved estimation of off-nominal frequency under harmonics as compared to the conventional one. Moreover, unlike the conventional one, the proposed technique does not require additional LPF. The presented experimental results have shown the accurate and robust performance of the proposed technique for real-time applications.

In summary, the pros and cons of the voltage modulation and 3CS technique are given in the following.

Pros:
- Can reject errors caused by DC offset and harmonics
- Can meet standard requirements
- No interdependent loop
- Does not suffer from ill-condition
- Settling time is around 2.0 fundamental cycles

Cons:
- Requires computationally demanding FIR filter

The second technique is based on the demodulation method and a FIR DF to estimate the single-phase grid voltage fundamental frequency. A frequency domain analysis for designing the DF has been presented. It has been shown that based on a same

computational burden, the performance of the proposed FIR DF is less affected by the presence of oscillations caused by the demodulation method as compared to a similar conventional FIR DF. The proposed technique can also provide accurate estimation of a wide range of fundamental frequency variation, as specified by the IEEE standard C.37.118.1 and European standard EN-50160. Selected experimental case studies such as DC offset, harmonics, frequency drifts, amplitude excursions and phase jump have been presented to confirm the superior performance of the proposed FIR DF based technique when compared with the conventional FIR DF.

In summary, the pros and cons of the demodulation and DF technique are given in the following.

Pros:
- Can reject errors caused by DC offset and harmonics
- Can meet standard requirements
- No interdependent loop

Cons:
- Settling time is around 3.25 fundamental cycles
- Requires computationally demanding FIR filter

The third proposed technique consists of a modified demodulation method for tracking of the single-phase grid voltage fundamental amplitude and frequency. An oscillator has been combined with a conventional demodulation method in order to reject oscillation at around second harmonic caused by the demodulation of the fundamental voltage component. The proposed technique can provide an accurate estimation of real-time fundamental voltage amplitude and frequency, and has been verified under different grid conditions such as harmonics, frequency drifts and amplitude excursions. The proposed technique does not alter the dynamic response and improves the fundamental voltage amplitude and frequency estimation accuracy significantly when compared with the conventional demodulation.

In summary, the pros and cons of the modified demodulation technique are given in the following.

Pros:
- Relatively simple
- Computationally efficient
- Can reject errors caused by harmonics
- No interdependent loop
- Settling time is around 2.0 fundamental cycles

Cons:
- Amplitude and phase estimation may contain errors during off-nominal

frequency condition

- Proposed oscillator cannot reject oscillation at around second harmonic effectively under large frequency deviation
- DC offset rejection can be obtained at the cost of additional delay

Chapter 6 has presented three techniques based on a quadrature signal generator (QSG) to estimate the single-phase grid voltage fundamental amplitude and frequency.

The first proposed technique consists of the DFT and a QSG based on a second-order generalized integrator (DFT-SOGI), and has been used to estimate the fundamental voltage amplitude and frequency of the single-phase grid voltage waveform. The presented DFT operation does not need to adjust the window size corresponding to the actual fundamental frequency. The fixed-size window based on nominal fundamental periods allows offline computation of the trigonometric functions required for the DFT. The technique can provide accurate estimation of the fundamental frequency variation ranges specified by the IEEE standard C.37.118.1 and European standard EN-50160. As a drawback, the use of three high-order DFT filters increases the computational burden of the technique. The frequency estimation using the proposed technique is less sensitive to the presence of harmonics and is also not depending on the generation of quadrature waveforms when compared with QSG-SOGI based FLL (SOGI-FLL) or PLL (SOGI-PLL) techniques. Moreover, unlike these techniques, the DFT-SOGI does not create any interdependent loops, thus increasing the overall stability and easing the tuning process. The improved performance of the DFT-SOGI technique has been verified by real-time experiments in the presence of DC offset, harmonics, frequency variations and amplitude excursions.

In summary, the pros and cons of the DFT-SOGI technique are given in the following.

Pros:
- Frequency adaptive
- Can reject errors caused by DC offset and harmonics
- No interdependent loop
- Can meet standard requirements

Cons:
- Requires computationally demanding high-order FIR filters based on the DFT
- Phase estimation is affected by DC offset

The second technique relies on a QSG based on a fixed frequency tuned SOGI and an IIR DF for estimating the single-phase grid voltage fundamental amplitude and frequency. The SOGI-DF technique is robust and offers easy tuning process, since it does not create any interdependent loop between the orthogonal voltage system and the frequency

estimation. The technique is computationally efficient and can provide an accurate estimation of fundamental voltage amplitude and frequency under harmonics. It can also meet the estimation error criteria under a large variation of frequency as specified by the IEC standards 61000-4-7 and 61000-4-30. The SOGI-DF technique shows less sensitivity to the presence of harmonics as compared to the QSG based on the SOGI tuned at fixed frequency and least-squares (SOGI-LS) technique. Several experimental case studies such as DC offset, harmonics, frequency variations, amplitude excursions and phase jump have been performed to demonstrate the effectiveness of the proposed SOGI-DF technique for real-time fundamental voltage amplitude and frequency estimation.

In summary, the pros and cons of the SOGI-DF technique are given in the following.

Pros:
- Frequency adaptive
- Relatively simple
- Computationally efficient
- Can reject errors caused by DC offset and harmonics
- No interdependent loop
- Can meet standard requirements

Cons:
- Phase estimation contains error during off-nominal frequency condition
- Settling time is around 3.5 fundamental cycles

The third proposed QSG is based on an anticonjugate decomposition process and a cascaded delayed signal cancellation strategy (ACDSC), and has been used to obtain the single-phase grid voltage fundamental amplitude and frequency. The frequency information required by the ACDSC is updated by using a relatively simple frequency estimation algorithm. The technique can estimate the fundamental voltage amplitude and frequency accurately from the grid voltage waveform distorted by harmonics. The proposed technique shows less sensitivity to the presence of harmonics while providing similar dynamic performance when compared with the SOGI-FLL and have been confirmed by the simulation results in MATLAB/Simulink under several cases such as harmonics, frequency drifts and amplitude excursions.

In summary, the pros and cons of the ACDSC technique are given in the following.

Pros:
- Frequency adaptive
- Relatively simple
- Computationally efficient
- Can reject errors caused by harmonics

– Settling time is around 1.0 fundamental cycle

Cons:
– Contains interdependent loop
– DC offset rejection can be obtained at the cost of additional delay
– Requires proper tuning of the LPF for stability

In **Chapter 7**, a frequency adaptive linear KF (LKF) based on the FLL (LKF-FLL) technique has been proposed for single-phase grid voltage fundamental amplitude and frequency estimation. A frequency domain analysis has been presented for showing the effects of the tuning of LKF's parameters. When compared with a nonlinear KF (NLKF) such as an extended KF (EKF), the proposed LKF-FLL technique offers the following benefits: is linear; avoids the derivatives of the nonlinear functions; does not contain nonlinear terms; and is computationally less complex. The LKF-FLL technique can also meet the estimation error criteria under a wide range of frequency deviation, as specified by the IEC standards 61000-4-7 and 61000-4-30. The estimation of the fundamental voltage amplitude and frequency using the LKF-FLL technique is less disturbed by the harmonics as compared to an extended complex KF (ECKF) and has been confirmed by the simulation results in MATLAB/Simulink.

The LKF-FLL technique has also been extended for the estimation of single-phase grid voltage fundamental amplitude, frequency and harmonics amplitudes. In addition, an EKF has been used to estimate the instantaneous voltage flicker level (IFL) present in the grid voltage. The LKF-FLL technique avoids the shortcomings of the NLKF for frequency adaptive fundamental and harmonics amplitudes estimation. However, the proposed technique depends on the NLKF for IFL estimation. The technique can provide accurate estimation of the grid voltage fundamental amplitude, frequency, harmonics amplitudes and IFL under a wide range of fundamental frequency variation. Several simulation case studies such as harmonics, frequency drifts, amplitude excursions and phase jump have been presented to confirm the effectiveness of the proposed technique for grid voltage fundamental amplitude, frequency, harmonics amplitudes and IFL estimation.

In summary, the pros and cons of the LKF-FLL technique are given in the following.

Pros:
– Frequency adaptive
– Can reject errors caused by DC offset and harmonics
– Can meet standard requirements
– Can provide harmonics estimation
– Avoids use of nonlinear model

Cons:
- Complex
- Computationally demanding
- Harmonics modelling increases computational effort

8.2 Benchmark

The thesis has documented nine DSP techniques for single-phase grid voltage fundamental amplitude and/or frequency estimation. Among these techniques, four are proposed for tracking of the fundamental frequency. Table 8.1 presents a benchmark among the four proposed techniques for frequency estimation in terms of simplicity, stability, computational effort and performance in the presence of harmonics, DC offset, frequency variations, amplitude excursions and phase jump. A technique with a higher number of stars (*) is superior with respect to the other one for a case provided in the left column of Table 8.1. On the other hand, two or more techniques with an equal number of stars are similar for the given case. As it can be noticed from Table 8.1, all four techniques can reject the negative effects caused by harmonics and DC offset. Among these techniques, the RDFT-TEO is the simplest one and its performance is superior during the frequency variations, however, worst for the amplitude excursions. Both RDFT-TEO and NTA-DF techniques are computationally efficient but may suffer from stability issues when compared with the other two techniques. The performance of the NTA-DF technique is also less sensitive to the amplitude excursions and phase jump, however, is worse during the frequency variations in comparison with the RDFT-TEO, and voltage modulation and 3CS techniques. The voltage modulation and 3CS, and demodulation and DF techniques are complex and computationally demanding for real-time implementations but more stable when compared with the other two techniques. The voltage modulation and 3CS technique also provides improved estimation during the frequency variations but suffers under the amplitude excursions and phase jump when compared with the NTA-DF, and demodulation and DF. From the above discussions it can be concluded that the RDFT-TEO or NTA-DF is simple and computationally efficient technique for real-time grid voltage fundamental frequency estimation, and can be implemented on a low cost digital signal processor. On the other hand, a more stable technique, such as the voltage modulation and 3CS, or demodulation and DF, can be implemented on a digital signal processor where a computationally demanding high-order FIR filter can be executed.

Table 8.1 Benchmark among four proposed techniques for fundamental frequency estimation

Comparison Cases	RFDT-TEO	NTA-DF	Voltage Modulation and 3CS	Demodulation and DF
Harmonics	***	***	***	***
DC Offset	***	***	***	***
Frequency variations	***	*	**	*
Amplitude excursions	*	***	**	***
Phase jump	**	***	**	***
Simplicity	***	**	*	*
Stability	**	**	***	***
Computational effort	***	***	**	**

The technique with a higher number of stars (*) is superior with respect to the other one for a case provided in the left column of Table 8.1. On the other hand, two or more techniques with an equal number of stars are similar for the given case.

Five other techniques have also been proposed in the thesis for single-phase grid voltage fundamental amplitude and frequency estimation. The benchmark among these five proposed techniques is presented in Table 8.2. As it can be seen, all five techniques can remove the negative effects caused by harmonics and DC offset. The modified demodulation, DFT-SOGI and SOGI-DF are more stable techniques in comparison with the ACDSC and LKF-FLL. The modified demodulation technique is also simple, computationally efficient but is not suitable at off-nominal frequency conditions. However, the DFT-SOGI technique is suitable under frequency variations, however, requires high computational effort for real-time implementation on a digital signal processor. On the other hand, the SOGI-DF technique is simple and computationally efficient for real-time implementation, and can also track the fundamental voltage amplitude and frequency at the cost of slower dynamic performance. The ACDSC technique is also computationally efficient, shows improved estimation under both amplitude and frequency variations. On

Table 8.2 Benchmark among five proposed techniques for fundamental voltage amplitude and frequency estimation

Comparison Cases	Modified Demodulation	DFT-SOGI	SOGI-DF	ACDSC	LKF-FLL
Harmonics	***	***	***	***	***
DC Offset	***	***	***	***	***
Frequency variations	*	***	**	***	**
Amplitude excursions	**	**	**	***	**
Simplicity	***	**	***	**	*
Stability	***	***	***	**	**
Computational effort	***	*	***	***	**

The technique with a higher number of stars (*) is superior with respect to the other one for a case provided in the left column of Table 8.2. On the other hand, two or more techniques with an equal number of stars are similar for the given case.

the other hand, the LKF-FLL is a complex one among the five proposed techniques, however, is computationally efficient when compared with the DFT-SOGI. Therefore, among these five proposed techniques, the SOGI-DF is the most simple, stable and computationally efficient for estimating both fundamental voltage amplitude and frequency under a wide range of voltage excursions. On the other side, the computationally efficient ACDSC technique can also be used when faster dynamics are required.

8.3 Future Work

The following research can be conducted in future in parallel with the application of the proposed DSP techniques reported in Chapters 3-7 for single-phase grid voltage fundamental amplitude and/or frequency estimation.

The RDFT-TEO technique has been documented for grid voltage fundamental frequency estimation. In the proposed technique, the frequency adaptive RDFT can also provide the estimation of the fundamental voltage amplitude and phase angle, however, is affected by

the accumulation error due to the voltage transients. Therefore, by adding a control mechanism in order to reject the accumulation error of the RDFT, the technique can be used not only to estimate the fundamental frequency but also the fundamental voltage amplitude and phase angle under variable frequency conditions.

The NTA-DF technique has been reported to obtain the grid voltage fundamental frequency. The fundamental voltage amplitude and phase angle are also obtained using the NTA following a BPF tuned at nominal grid frequency. The BPF attenuates the fundamental voltage amplitude and also introduces error in the estimation of phase angle during frequency variations. Therefore, based on the frequency response of the BPF, a correction factor for the amplitude and a phase angle offset error can be added to obtain the actual fundamental voltage amplitude and phase angle, and is yet another open field for research.

In the modified demodulation technique, an oscillator has been combined with the conventional demodulation for rejecting the oscillation at around second harmonic generated by the demodulation of the fundamental voltage component. However, during off-nominal fundamental frequency condition, the LPFs after the demodulation stages introduce delays and the amplitude can also be attenuated by the non-ideal characteristics of the filters, thus the proposed oscillator cannot reject the oscillations at around second harmonic effectively and hence the performance of the technique can be significantly affected for a large deviation of fundamental frequency. However, the performance of the modified demodulation technique can be improved by adding a control mechanism so that the output of the oscillator is not affected during off-nominal fundamental frequency and is yet another subject for further investigation.

The spectral leakage information of the DFT is used to obtain the time-varying fundamental frequency in the DFT-SOGI technique. However, the use of three DFT filters with a large size moving window increases the real-time computational burden of the technique. The RDFT can be used to reduce the computational effort of the DFT for estimating the fundamental frequency using the spectral leakage property and is still an opportunity to conduct further research.

The LKF-FLL technique has been presented for estimating the grid voltage fundamental frequency, amplitude and harmonics amplitude. The LKF-FLL technique overcomes the shortcomings of the NLKF for frequency adaptive estimation. However, the grid voltage IFL estimation depends on the NLKF such as EKF. Therefore, developing a platform for IFL estimation using the LKF-FLL technique remains to be investigated.

References

[1] S. M. Amin and B. F. Wollenberg, "Toward a smart grid: Power delivery for the 21st century," *IEEE Power and Energy Mag.,* vol. 3, no. 5, pp. 34-41, Sept./Oct. 2005.

[2] X. Yu, C. Cecati, T. Dillon, and M. G. Simoes, "The new frontier of smart grids," *IEEE Ind. Elect. Mag.,* vol. 5, no. 3, pp. 49-63, Sept. 2011.

[3] V. C. Gungor, D. Sahin, T. Kocak, S. Ergut, C. Buccella, C. Cecati, and G. P. Hancke, "Smart grid and smart homes: Key players and pilot projects," *IEEE Ind. Elect. Mag.,* vol. 6, no. 4, pp. 18-34, Dec. 2012.

[4] F. Cohen, "The smarter grid," *IEEE Security & Privacy,* vol. 8, no. 1, pp. 60-63, 2010.

[5] V. C. Gungor, D. Sahin, T. Kocak, S. Ergut, C. Buccella, C. Cecati, and G. P. Hancke, "A survey on smart grid potential applications and communication requirements," *IEEE Trans. Ind. Inform.,* vol. 9, no. 1, pp. 28-42, Feb. 2013.

[6] G. N. Ericsson, "Cyber security and power system communication-essential parts of a smart grid infrastructure," *IEEE Trans. Power Del.,* vol. 25, no. 3, pp. 1501-1507, July 2010.

[7] M. Anderson, "WiMax for smart grids," *IEEE Spectrum,* vol. 47, no. 7, pp. 14-14, July 2010.

[8] Z. M. Fadlullah, M. M. Fouda, N. Kato, A. Takeuchi, N. Iwasaki, and Y. Nozaki, "Toward intelligent machine-to-machine communications in smart grid," *IEEE Communications Magazine,* vol. 49, no. 4, pp. 60-65, Apr. 2011.

[9] V. C. Gungor, D. Sahin, T. Kocak, S. Ergut, C. Buccella, C. Cecati, and G. P. Hancke, "Smart grid technologies: Communication technologies and standards," *IEEE Trans. Ind. Inform.,* vol. 7, no. 4, pp. 529-539, Nov. 2011.

[10] Y. Yan, Y. Qian, H. Sharif, and D. Tipper, "A survey on smart grid communication infrastructures: motivations, requirements and challenges," *IEEE Comm. Surveys & Tuto.,* vol. PP, no. 99, pp. 1-16, 2012.

[11] L. Husheng, G. Shuping, L. Lifeng, H. Zhu, R. C. Qiu, and Y. Depeng, "Efficient and secure wireless communications for advanced metering infrastructure in smart grids," *IEEE Trans. Smart Grid,* vol. 3, no. 3, pp. 1540-1551, Sept. 2012.

[12] M. A. Rahman, E. Al-shaer, and P. Bera, "A noninvasive threat analyzer for advanced metering infrastructure in smart grid," *IEEE Trans. Smart Grid,* vol. 4, no. 1, pp. 273-287, Mar. 2013.

[13] J. Zhou, R. Hu, and Y. Qian, "Scalable distributed communication architectures to support advanced metering Infrastructure in smart grid," *IEEE Trans. Parallel & Distr. Sys.,* vol. 23, 2012.

[14] Y. Zhang, P. Markham, T. Xia, L. Chen, Y. Ye, Z. Wu, Z. Yuan, L. Wang, J. Bank, J. Burgett, R. W. Conners, and Y. Liu, "Wide-area frequency monitoring network (FNET) architecture and applications," *IEEE Trans. Smart Grid,* vol. 1, no. 2, pp. 159-167, Sept. 2010.

[15] M. Qiu, W. Gao, M. Chen, J.-W. Niu, and L. Zhang, "Energy efficient security algorithm for power grid wide area monitoring system," *IEEE Trans. Smart Grid,* vol. 2, no. 4, pp. 715-723, Dec. 2011.

[16] L. Xie, D.-H. Choi, S. Kar, and H. V. Poor, "Fully distributed state estimation for wide-area monitoring systems," *IEEE Trans. Smart Grid,* vol. 3, no. 3, pp. 1154-1169, Sept. 2012.

[17] P. Seunghyun, K. Hanjoo, M. Hichan, H. Jun, and Y. Sungroh, "Concurrent simulation platform for energy-aware smart metering systems," *IEEE Trans. Consumer Elect.,* vol. 56, no. 3, pp. 1918-1926, Aug. 2010.

[18] B. Stephen and S. J. Galloway, "Domestic load characterization through smart meter advance stratification," *IEEE Trans. Smart Grid,* vol. 3, no. 3, pp. 1571-1572, Sept. 2012.

[19] F. Benzi, N. Anglani, E. Bassi, and L. Frosini, "Electricity smart meters interfacing the households," *IEEE Trans. Ind. Elect.,* vol. 58, no. 10, no. 10, pp. 4487-4494, Oct. 2011.

[20] D. Ming, P. C. M. Meira, X. Wilsun, and W. Freitas, "An event window based load monitoring technique for smart meters," *IEEE Trans. Smart Grid,* vol. 3, no. 2, pp. 787-796, June 2012.

[21] K. Samarakoon, J. Ekanayake, and N. Jenkins, "Investigation of domestic load control to provide primary frequency response using smart meters," *IEEE Trans. Smart Grid,* vol. 3, no. 1, pp. 282-292, Mar. 2012.

[22] I. Sadinezhad and V. G. Agelidis, "Slow sampling on-line harmonics/interharmonics estimation technique for smart meters," *Elsevier Electric Power Sys. Resear.,* vol. 81, pp. 1643–1653, 2011.

[23] A. Albert and R. Rajagopal, "Smart meter driven segmentation: What your consumption says about you," *IEEE Trans. Power Sys.,* vol. 28, no. 4, pp. 4019-4030, Nov. 2013.

[24] I. Kamwa, A. K. Pradhan, and G. Joos, "Adaptive phasor and frequency-tracking schemes for wide-area protection and control," *IEEE Trans. Power Del.,* vol. 26, no. 2, pp. 744-753, Apr. 2011.

[25] I. Kamwa, S. R. Samantaray, and G. Joos, "Compliance analysis of PMU algorithms and devices for wide-area stabilizing control of large power systems," *IEEE Trans. Power Sys.,* vol. 28, no. 2, pp. 1766-1778, May 2013.

[26] I. Kamwa, S. R. Samantaray, and G. Joos, "On the accuracy versus transparency trade-off of data-mining models for fast-response PMU-based catastrophe predictors," *IEEE Trans. Smart Grid,* vol. 3, no. 1, pp. 152-161, Mar. 2012.

[27] I. Kamwa, S. R. Samantaray, and G. Joos, "Optimal integration of disparate C37.118 PMUs in wide-area PSS with electromagnetic transients," *IEEE Trans. Power Sys.,* vol. 28, no. 4, pp. 4760-4770, Nov. 2013.

[28] A. J. Roscoe, I. F. Abdulhadi, and G. M. Burt, "P and M class phasor measurement unit algorithms using adaptive cascaded filters," *IEEE Trans. Power Del.,* vol. 28, no. 3, pp. 1447-1459, July 2013.

[29] I. Kamwa, M. Leclerc, and D. McNabb, "Performance of demodulation-based frequency measurement algorithms used in typical PMUs," *IEEE Trans. Power Del.,* vol. 19, no. 2, pp. 505-514, Apr. 2004.

[30] I. Kamwa and R. Grondin, "PMU configuration for system dynamic performance measurement in large, multiarea power systems," *IEEE Trans. Power Sys.,* vol. 17, no. 2, pp. 385-394, May 2002.

[31] I. Kamwa, S. R. Samantaray, and G. Joos, "Wide frequency range adaptive phasor and frequency PMU algorithms," *IEEE Trans. Smart Grid,* vol. 5, no. 2, pp. 569-579, Mar. 2014.

[32] IEEE Standard C37.118.1, "IEEE standard for synchrophasor measurements for power systems," 2011.

[33] Smart meters and smart meter systems: A metering industry perspective, Edison Electric Institute, Mar. 2011.

[34] R. A. S. Fernandes, I. da Silva, and M. Oleskovicz, "Load profile identification interface for consumer online monitoring purposes in smart grids," *IEEE Trans. Ind. Inform.,* vol. 9, no. 3, pp. 1507-1517, Aug. 2013.

[35] M. Zeifman and K. Roth, "Nonintrusive appliance load monitoring: Review and outlook," *IEEE Trans. Consumer Elect.,* vol. 57, no. 1, pp. 76-84, Feb. 2011.

[36] M. Dong, P. C. M. Meira, W. Xu, and C. Y. Chung, "Non-intrusive signature extraction for major residential loads," *IEEE Trans. Smart Grid,* vol. 4, no. 3, pp. 1421-1430, Sept. 2013.

[37] F. Sultanem, "Using appliance signatures for monitoring residential loads at meter panel level," *IEEE Trans. Power Del.,* vol. 6, no. 4, pp. 1380-1385, Oct. 1991.

[38] W. Chen, X. Wang, J. Petersen, R. Tyagi, and J. Black, "Optimal scheduling of demand response events for electric utilities," *IEEE Trans. Smart Grid,* vol. 4, no. 4, pp. 2309-2319, Dec. 2013.

[39] Z. Baharlouei, M. Hashemi, H. Narimani, and H. Mohsenian-Rad, "Achieving optimality and fairness in autonomous demand response: Benchmarks and billing mechanisms," *IEEE Trans. Smart Grid,* vol. 4, no. 2, pp. 968-975, June 2013.

[40] D. He, W. Lin, N. Liu, R. G. Harley, and T. G. Habetler, "Incorporating non-intrusive load monitoring into building level demand response," *IEEE Trans. Smart Grid,* vol. 4, no. 4, pp. 1870-1877, Dec. 2013.

[41] P. Koponen, R. Seesvuori, and R. Bostman, "Adding power quality monitoring to a smart kWh meter," *IET Power Engg. Journal,* vol. 10, no. 4, pp. 159-163, Aug. 1996.

[42] H. Saari, P. Koponen, E. Tahvanainen, and T. Lindholm, "Remote reading and data management system for kWh meters with power quality monitoring," *IET Power Engg. Journal,* vol. 10, no. 4, pp. 164-168, Aug. 1996.

[43] IEC Smart Grid Standardization Roadmap, SMB Smart Grid Strategic Group (SG3), June 2010.

[44] K. D. McBee and M. G. Simoes, "Utilizing a smart grid monitoring system to improve voltage quality of customers," *IEEE Trans. Smart Grid,* vol. 3, no. 2, pp. 738-743, June 2012.

[45] Y. Xia, S. C. Douglas, and D. P. Mandic, "Adaptive frequency estimation in smart grid applications: Exploiting noncircularity and widely linear adaptive estimators," *IEEE Signal Proc. Mag.,* vol. 29, no. 5, pp. 44-54, Sept. 2012.

[46] M. Adamiak , B. Kasztenny, and W. Premerlani, "Synchrophasors: Definition, measurement, and application," in *59th Ann. Georgia Tech Protective Relaying*, 2005.

[47] B. Singh, N. K. Sharma, A. N. Tiwari, K. S. Verma, and S. N. Singh, "Applications of phasor measurement units (PMUs) in electric power system networks incorporated with FACTS controllers," *Int. Jour. Engg. Sci. Tech.,* vol. 3, no. 3, 64-82 2011.

[48] E. Pouresmaeil, C. Miguel-Espinar, M. Massot-Campos, D. Montesinos-Miracle, and O. Gomis-Bellmunt, "A control technique for integration of DG units to the electrical networks," *IEEE Trans. Ind. Elect.,* vol. 60, no. 7, pp. 2881-2893, July 2013.

[49] S. Alepuz, S. Busquets-Monge, J. Bordonau, J. Gago, D. Gonzalez, and J. Balcells, "Interfacing renewable energy sources to the utility grid using a three-level inverter," *IEEE Trans. Ind. Elect.,* vol. 53, no. 5, pp. 1504-1511, Oct. 2006.

[50] S. Dasgupta, S. N. Mohan, S. K. Sahoo, and S. K. Panda, "Lyapunov function-based current controller to control active and reactive power flow from a renewable energy source to a generalized three-phase microgrid system," *IEEE Trans. Ind. Elect.,* vol. 60, no. 2, pp. 799-813, Feb. 2013.

[51] J. M. Carrasco, L. G. Franquelo, J. T. Bialasiewicz, E. Galvan, R. C. P. Guisado, M. A. M. Prats, J. I. Leon, and N. Moreno-Alfonso, "Power-electronic systems for the grid integration of renewable energy sources: A survey," *IEEE Trans. Ind. Elect.,* vol. 53, no. 4, pp. 1002-1016, Aug. 2006.

[52] F. Blaabjerg, R. Teodorescu, M. Liserre, and A. V. Timbus, "Overview of control and grid synchronization for distributed power generation systems," *IEEE Trans. Ind. Elect.,* vol. 53, no. 5, pp. 1398-1409, Oct. 2006.

[53] S. Dasgupta, S. N. Mohan, S. K. Sahoo, and S. K. Panda, "Application of four-switch-based three-phase grid-connected inverter to connect renewable energy source to a generalized unbalanced microgrid system," *IEEE Trans. Ind. Elect.,* vol. 60, no. 3, pp. 1204-1215, Mar. 2013.

[54] A. Y. Saber and G. K. Venayagamoorthy, "Plug-in vehicles and renewable energy sources for cost and emission reductions," *IEEE Trans. Ind. Elect.,* vol. 58, no. 4, pp. 1229-1238, Apr. 2011.

[55] S. Eftekharnejad, V. Vittal, G. T. Heydt, B. Keel, and J. Loehr, "Small signal stability assessment of power systems with increased penetration of photovoltaic generation: A case study," *IEEE Trans. Sustain. Energy,* vol. 4, no. 4, pp. 960-967, Oct. 2013.

[56] S. Eftekharnejad, V. Vittal, G. T. Heydt, B. Keel, and J. Loehr, "Impact of increased penetration of photovoltaic generation on power systems," *IEEE Trans. Power Sys.,* vol. 28, no. 2, pp. 893-901, May 2013.

[57] R. Teodorescu, M. Liserre, and P. Rodríguez, "Grid converters for photovoltaic and wind power systems," John Wiley & Sons, Ltd, Chichester, UK, 2011.

[58] S.-T. Kim, B.-K. Kang, S.-H. Bae, and J.-W. Park, "Application of SMES and grid code compliance to wind/photovoltaic generation system," *IEEE Trans. Applied Supercond.,* vol. 23, no. 3, June 2013.

[59] M. Garcia-Gracia, N. El Halabi, H. Ajami, and M. P. Comech, "Integrated control technique for compliance of solar photovoltaic installation grid codes," *IEEE Trans. Energy Conv.,* vol. 27, no. 3, pp. 792-798, Sept. 2012.

[60] Y. Bae, T.-K. Vu, and R.-Y. Kim, "Implemental control strategy for grid stabilization of grid-connected PV system based on German grid code in symmetrical low-to-medium voltage network," *IEEE Trans. Energy Conv.,* vol. 28, no. 3, pp. 619-631, Sept. 2013.

[61] IEC Standard 61727, "Photovoltaic (PV) systems-Characteristics of the utility interface," 2004.

[62] W. Baochao, M. Sechilariu, and F. Locment, "Intelligent DC microgrid with smart grid communications: control strategy consideration and design," *IEEE Trans. Smart Grid,* vol. 3, no. 4, pp. 2148-2156, Dec. 2012.

[63] H. Kanchev, L. Di, F. Colas, V. Lazarov, and B. Francois, "Energy management and operational planning of a microgrid with a PV-based active generator for smart grid applications," *IEEE Trans. Ind. Elect.,* vol. 58, no. 10, pp. 4583-4592, Oct. 2011.

[64] H. Bevrani, M. Watanabe, and Y. Mitani, "Power system monitoring and control," John Wiley & Sons, Inc, 2014.

[65] S. X. Chen, H. B. Gooi, and M. Q. Wang, "Sizing of energy storage for microgrids," *IEEE Trans. Smart Grid,* vol. 3, no. 1, pp. 142-151, Mar. 2012.

[66] S.-J. Ahn, J.-w. Park, I.-Y. Chung, S.-I. Moon, S.-h. Kang, and S.-R. Nam, "Power-sharing method of multiple distributed generators considering control modes and configurations of a microgrid," *IEEE Trans. Power Del.,* vol. 25, no. 3, pp. 2007-2016, July 2010.

[67] A. Vaccaro, V. Loia, G. Formato, P. Wall, and V. Terzija, "A self organizing architecture for decentralized smart microgrids synchronization, control and monitoring," *IEEE Trans. Ind. Inform.,* 2014.

[68] Y. W. Li and C.-N. Kao, "An accurate power control strategy for power-electronics-interfaced distributed generation units operating in a low-voltage multibus microgrid," *IEEE Trans. Power Elect.,* vol. 24, no. 12, pp. 2977-2988, Dec. 2009.

[69] A. Vaccaro, M. Popov, D. Villacci, and V. Terzija, "An integrated framework for smart microgrids modeling, monitoring, control, communication, and verification," *Proceedings of the IEEE,* vol. 99, no. 1, pp. 119-132, Jan. 2011.

[70] B. M. Eid, N. A. Rahim, J. Selvaraj, and A. H. El Khateb, "Control methods and objectives for electronically coupled distributed energy resources in microgrids: a review," *IEEE Systems Journal,* 2014.

[71] M. Shahidehpour and M. Khodayar, "Cutting campus energy costs with hierarchical control: the economical and reliable operation of a microgrid," *IEEE Electrification Magazine,* vol. 1, no. 1, pp. 40-56, Sept. 2013.

[72] M. Azizi, A. Fatemi, M. Mohamadian, and A. Y. Varjani, "Integrated solution for microgrid power quality assurance," *IEEE Trans. Energy Conv.,* vol. 27, no. 4, pp. 992-1001, Dec. 2012.

[73] M. Illindala and G. Venkataramanan, "Frequency/sequence selective filters for power quality improvement in a microgrid," *IEEE Trans. Smart Grid,* vol. 3, no. 4, pp. 2039-2047, Dec. 2012.

[74] J. Rocabert, G. M. S. Azevedo, A. Luna, J. M. Guerrero, J. I. Candela, and P. Rodriguez, "Intelligent connection agent for three-phase grid-connected microgrids," *IEEE Trans. Power Elect.,* vol. 26, no. 10, pp. 2993-3005, Oct. 2011.

[75] X. Guo, Z. Lu, B. Wang, X. Sun, L. Wang, and J. M. Guerrero, "Dynamic phasors-based modeling and stability analysis of droop-controlled inverters for microgrid applications," *IEEE Trans. Smart Grid,* 2014.

[76] Y.-Y. Hong, M.-C. Hsiao, Y.-R. Chang, Y.-D. Lee, and H.-C. Huang, "Multiscenario underfrequency load shedding in a microgrid consisting of intermittent renewables," *IEEE Trans. Power Del.,* vol. 28, no. 3, pp. 1610-1617, July 2013.

[77] IEEE Standard 1547, "IEEE standard for interconnecting distributed resources with electric power systems," 2003.

[78] P. Roncero-Sanchez, X. del Toro Garcia, A. P. Torres, and V. Feliu, "Robust frequency-estimation method for distorted and imbalanced three-phase systems using discrete filters," *IEEE Trans. Power Elect.,* vol. 26, no. 4, pp. 1089-1101, Apr. 2011.

[79] W. R. Anis Ibrahim and M. M. Morcos, "Artificial intelligence and advanced mathematical tools for power quality applications: a survey," *IEEE Trans. Power Del.,* vol. 17, no. 2, pp. 668-673, Apr. 2002.

[80] M. V. Ribeiro, J. M. T. Romano, and C. A. Duque, "An improved method for signal processing and compression in power quality evaluation," *IEEE Trans. Power Del.,* vol. 19, no. 2, pp. 464-471, 2004.

[81] C. A. G. Marques, D. D. Ferreira, L. R. Freitas, C. A. Duque, and M. V. Ribeiro, "Improved disturbance detection technique for power-quality analysis," *IEEE Trans. Power Del.,* vol. 26, no. 2, pp. 1286-1287, Apr. 2011.

[82] I. Sadinezhad and V. G. Agelidis, "Frequency adaptive least-squares-Kalman technique for real-time voltage envelope and flicker estimation," *IEEE Trans. Ind. Elect.,* vol. 59, no. 8, pp. 3330-3341, Aug. 2012.

[83] L. Cristaldi and A. Ferrero, "Harmonic power flow analysis for the measurement of the electric power quality," *IEEE Trans. Instrum. Meas.,* vol. 44, no. 3, pp. 683-685, June 1995.

[84] D. D. Sabin, D. L. Brooks, and A. Sundaram, "Indices for assessing harmonic distortion from power quality measurements: definitions and benchmark data," *IEEE Trans. Power Del.,* vol. 14, no. 2, pp. 489-496, Apr. 1999.

[85] IEC Standard 61000-4-30, "Testing and measurement techniques—Power quality measurement methods," 2003.

[86] C.-I. Chen, Y.-C. Chen, Y.-R. Chang, and Y.-D. Lee, "An accurate solution procedure for calculation of voltage flicker components," *IEEE Trans. Ind. Elect.,* vol. 61, no. 5, pp. 2370-2377, May 2014.

[87] G. W. Chang and C.-I. Chen, "An accurate time-domain procedure for harmonics and interharmonics detection," *IEEE Trans. Power Del.,* vol. 25, no. 3, pp. 1787-1795, July 2010.

[88] G. Wiczynski, "Analysis of voltage fluctuations in power networks," *IEEE Trans. Instrum. Measur.,* vol. 57, no. 11, pp. 2655-2664, Nov. 2008.

[89] IEEE Standard 1159, "IEEE recommended practice for monitoring electric power quality," 2009.

[90] R. Naidoo and P. Pillay, "A new method of voltage sag and swell detection," *IEEE Trans. Power Del.,* vol. 22, no. 2, pp. 1056-1063, Apr. 2007.

[91] Y.-J. Shin, E. J. Powers, M. Grady, and A. Arapostathis, "Power quality indices for transient disturbances," *IEEE Trans. Power Del.,* vol. 21, no. 1, pp. 253-261, Jan 2006.

[92] R. G. Lyons, "Understanding digital signal processing," Prentice Hall, 2010.

[93] E. Jacobsen and R. Lyons, "The sliding DFT," *IEEE Signal Proc. Mag.,* vol. 20, no. 2, pp. 74-80, Mar. 2003.

[94] B. P. McGrath, D. G. Holmes, and J. J. H. Galloway, "Power converter line synchronization using a discrete Fourier transform (DFT) based on a variable sample rate," *IEEE Trans. Power Elect.,* vol. 20, no. 4, pp. 877-884, July, 2005.

[95] H. A. Darwish and M. Fikri, "Practical considerations for recursive DFT implementation in numerical relays," *IEEE Trans. Power Del.,* vol. 22, no. 1, pp. 42-49, Jan. 2007.

[96] A. A. Girgis and F. M. Ham, "A quantitative study of pitfalls in the FFT," *IEEE Trans. Aerosp. Elect. Sys.,* vol. AES-16, no. 4, pp. 434-439, July 1980.

[97] H. Wen, Z. Teng, Y. Wang, and X. Hu, "Spectral correction approach based on desirable sidelobe window for harmonic analysis of industrial power system," *IEEE Trans. Ind. Elect.,* vol. 60, no. 3, pp. 1001-1010, Mar. 2013.

[98] E. Lavopa, P. Zanchetta, M. Sumner, and F. Cupertino, "Real-time estimation of fundamental frequency and harmonics for active shunt power filters in aircraft electrical systems," *IEEE Trans. Ind. Elect.,* vol. 56, no. 8, pp. 2875-2884, Aug. 2009.

[99] F. Cupertino, E. Lavopa, P. Zanchetta, M. Sumner, and L. Salvatore, "Running DFT-based PLL algorithm for frequency, phase, and amplitude tracking in aircraft electrical systems," *IEEE Trans. Ind. Elect.,* vol. 58, no. 3, pp. 1027-1035, Mar. 2011.

[100] H. C. Lin, "Power harmonics and interharmonics measurement using recursive group-harmonic power minimizing algorithm," *IEEE Trans. Ind. Elect.,* vol. 59, no. 2, pp. 1184-1193 Feb. 2012.

[101] L. Hsiung-Cheng, "Fast tracking of time-varying power system frequency and harmonics using iterative-loop approaching algorithm," *IEEE Trans. Ind. Elect.,* vol. 54, no. 2, pp. 974-983, Apr. 2007.

[102] A. J. Roscoe, G. M. Burt, and J. R. McDonald, "Frequency and fundamental signal measurement algorithms for distributed control and protection applications," *IET Gen. Trans. Dist.,* vol. 3, no. 5, pp. 485-495, 2009.

[103] P. K. Dash, D. P. Swain, A. C. Liew, and S. Rahman, "An adaptive linear combiner for on-line tracking of power system harmonics," *IEEE Trans. Power Sys.,* vol. 11, no. 4, pp. 1730-1735, Nov. 1996.

[104] A. Bhattacharya and C. Chakraborty, "A shunt active power filter with enhanced performance using ANN-based predictive and adaptive controllers," *IEEE Trans. Ind. Elect.,* vol. 58, no. 2, pp. 421-428, Feb. 2011.

[105] M. I. Mareia, E. F. El-Saadany, and M. M. A. Salama, "Experimental evaluation of envelope tracking techniques for voltage disturbances," *Elsevier Electric Power Sys. Res.,* vol. 80, pp. 339-344, 2010.

[106] B. Singh and J. Solanki, "An implementation of an adaptive control algorithm for a three-phase shunt active filter," *IEEE Trans. Ind. Elect.,* vol. 56, no. 8, pp. 2811-2820, Aug. 2009.

[107] G. W. Chang, C.-I. Chen, and Q.-W. Liang, "A two-stage ADALINE for harmonics and interharmonics measurement," *IEEE Trans. Ind. Elect.,* vol. 56, no. 6, pp. 2220-2228, June 2009.

[108] C.-I. Chen, "A phasor estimator for synchronization between power grid and distributed generation system," *IEEE Trans. Ind. Elect.,* vol. 60, no. 8, pp. 3248-3255, Aug. 2013.

[109] C.-I. Chen and Y.-C. Chen, "Comparative study of harmonic and interharmonic estimation methods for stationary and time-varying signals," *IEEE Trans. Ind. Elect.,* vol. 61, no. 1, pp. 397-404, Jan. 2014.

[110] M. I. Marei, E. F. El-Saadany, and M. M. A. Salama, "A processing unit for symmetrical components and harmonics estimation based on a new adaptive linear combiner structure," *IEEE Trans. Power Del.,* vol. 19, no. 3, pp. 1245-1252, July 2004.

[111] L. HongXing and L. Bingzhang, "Adaptive control based on genetic algorithm and fuzzy tuning for unknown systems with time-delay," in *Proc. of IEEE 7th World Congress Intel. Cont. Auto.*, 2008, pp. 8650-8655.

[112] V. V. Terzija, N. B. Djuric, and B. D. Kovacevic, "Voltage phasor and local system frequency estimation using Newton type algorithm," *IEEE Trans. Power Del.,* vol. 9, no. 3, pp. 1368-1374, July 1994.

[113] V. V. Terzija and D. Markovic, "Symmetrical components estimation through nonrecursive Newton-type numerical algorithm," *IEEE Trans. Power Del.,* vol. 18, no. 2, pp. 359-363, Apr. 2003.

[114] V. V. Terzija, "Adaptive underfrequency load shedding based on the magnitude of the disturbance estimation," *IEEE Trans. Power Sys.,* vol. 21, no. 3, pp. 1260-1266, Aug. 2006.

[115] V. V. Terzija and H. J. Koglin, "Adaptive underfrequency load shedding integrated with a frequency estimation numerical algorithm," *IEE Proc.-Gen. Transm. Dist.,* vol. 149, no. 6, pp. 713-718, 2002.

[116] V. Terzija and V. Stanojevic, "Power quality indicators estimation using robust Newton-type algorithm," *IEE Proc. Gen, Transm. Dist.,* vol. 151, no. 4, pp. 477-485, 2004.

[117] V. V. Terzija, V. Stanojevic, M. Popov, and L. Van der Sluis, "Digital metering of power components according to IEEE standard 1459-2000 using the Newton-type algorithm," *IEEE Trans. Instrum. Measur.,* vol. 56, no. 6, pp. 2717-2724, Dec. 2007.

[118] V. V. Terzija and M. Akke, "Synchronous and asynchronous generators frequency and harmonics behavior after a sudden load rejection," *IEEE Trans. Power Systems,* vol. 18, no. 2, pp. 730-736, May 2003.

[119] I. Sadinezhad and V. G. Agelidis, "Slow sampling online optimization approach to estimate power system frequency," *IEEE Trans. Smart Grid,* vol. 2, no. 2, pp. 265-277, June 2011.

[120] V. V. Terzija, "Improved recursive Newton-type algorithm for frequency and spectra estimation in power systems," *IEEE Trans. Instrum. Measur.,* vol. 52, no. 5, pp. 1654-1659, Oct. 2003.

[121] V. V. Terzija, "Improved recursive Newton-type algorithm for power system relaying and measurement," *IEE Proc.-Gen. Transm. Dist.,* vol. 145, no. 1, pp. 15-20, 1998.

[122] V. V. Terzija and V. Stanojevic, "Two-stage improved recursive Newton-type algorithm for power-quality indices estimation," *IEEE Trans. Power Del.,* vol. 22, no. 3, pp. 1351-1359, July 2007.

[123] R. Chudamani, K. Vasudevan, and C. S. Ramalingam, "Real-time estimation of power system frequency using nonlinear least squares," *IEEE Trans. Power Del.,* vol. 24, no. 3, pp. 1021-1028, July 2009.

[124] M. Bettayeb and U. Qidwai, "A hybrid least squares-GA-based algorithm for harmonic estimation," *IEEE Trans. Power Del.,* vol. 18, no. 2, pp. 377-382, Apr. 2003.

[125] S. Mishra, "A hybrid least square-fuzzy bacterial foraging strategy for harmonic estimation," *IEEE Trans. Evolutionary Comp.,* vol. 9, no. 1, pp. 61-73, Feb. 2005.

[126] P. Jafarian and M. Sanaye-Pasand, "Weighted least error squares based variable window phasor estimator for distance relaying application," *IET Gen., Transm. & Dist.,* vol. 5, no. 3, pp. 298-306, 2011.

[127] M. D. Kusljevic, J. J. Tomic, and L. D. Jovanovic, "Frequency estimation of three-phase power system using weighted-least-square algorithm and adaptive FIR filtering," *IEEE Trans. Instrum. Measur.,* vol. 59, no. 2, pp. 322-329, Feb. 2010.

[128] I. Sadinezhad and V. G. Agelidis, "Real-time power system phasors and harmonics estimation using a new decoupled recursive-least-squares technique for DSP implementation," *IEEE Trans. Ind. Elect.,* vol. 60, no. 6, pp. 2295-2308, June 2013.

[129] L. A. L. De Almeida and A. C. d. C. Lima, "Covariance management based RLS algorithm for phasor estimation in severely noisy systems," *IEEE Trans. Power Del.,* vol. 13, no. 4, pp. 1067-1072, Oct. 1998.

[130] I. Kamwa and R. Grondin, "Fast adaptive schemes for tracking voltage phasor and local frequency in power transmission and distribution systems," *IEEE Trans. Power Del.,* vol. 7, no. 2, pp. 789-795, Apr. 1992.

[131] M. S. Sachdev and M. Nagpal, "A recursive least error squares algorithm for power system relaying and measurement applications," *IEEE Trans. Power Del.,* vol. 6, no. 3, pp. 1008-1015, July 1991.

[132] A. S. AlFuhaid and M. A. El-Sayed, "A recursive least-squares digital distance relaying algorithm," *IEEE Trans. Power Del.,* vol. 14, no. 4, pp. 1257-1262, Oct. 1999.

[133] R. E. Kalman, "A new approach to linear filtering and prediction problems," *Trans. of the ASME—Journ. Basic Engg.,* pp. 35-45, Mar. 1960.

[134] A. A. Girgis, "A new Kalman filtering based digital distance relay," *IEEE Trans. Power Appar. Sys.,* vol. PAS-101, no. 9, pp. 3471-3480, Sept. 1982.

[135] A. A. Girgis, W. B. Chang, and E. B. Makram, "A digital recursive measurement scheme for online tracking of power system harmonics," *IEEE Trans. Power Del.,* vol. 6, no. 3, pp. 1153-1160, July 1991.

[136] J. A. R. Macias and A. G. Exposito, "Self-tuning of Kalman filters for harmonic computation," *IEEE Trans. Power Del.,* vol. 21, no. 1, pp. 501-503, Jan. 2006.

[137] K. Kennedy, G. Lightbody, and R. Yacamini, "Power system harmonic analysis using the Kalman filter," in *Proc. of IEEE Power Engg. Soc. Gen. Meet.*, 2003, pp. 752-757.

[138] C. I. Chen, G. W. Chang, R. C. Hong, and H. M. Li, "Extended real model of Kalman filter for time-varying harmonics estimation," *IEEE Trans. Power Del.,* vol. 25, no. 1, pp. 17-26, Jan. 2010.

[139] P. K. Dash, R. K. Jena, G. Panda, and A. Routray, "An extended complex Kalman filter for frequency measurement of distorted signals," *IEEE Trans. Instrum. Measur.,* vol. 49, no. 4, pp. 746-753, Aug. 2000.

[140] P. K. Dash, A. K. Pradhan, and G. Panda, "Frequency estimation of distorted power system signals using extended complex Kalman filter," *IEEE Trans. Power Del.,* vol. 14, no. 3, pp. 761-766, July 1999.

[141] A. Routray, A. K. Pradhan, and K. P. Rao, "A novel Kalman filter for frequency estimation of distorted signals in power systems," *IEEE Trans. Instrum. Meas.,* vol. 51, no. 3, pp. 469-479, June 2002.

[142] C.-H. Huang, C.-H. Lee, K.-J. Shih, and Y.-J. Wang, "Frequency estimation of distorted power system signals using a robust algorithm," *IEEE Trans. Power Del.,* vol. 23, no. 1, pp. 41-51, Jan. 2008.

[143] C.-H. Huang, C.-H. Lee, K.-J. Shih, and Y.-J. Wang, "A robust technique for frequency estimation of distorted signals in power systems," *IEEE Trans. Instrum. Meas.,* vol. 59, no. 8, pp. 2026-2036, Aug. 2010.

[144] B. F. La Scala and R. R. Bitmead, "Design of an extended Kalman filter frequency tracker," *IEEE Trans. Signal Proc.,* vol. 44, no. 3, pp. 739-742, Mar. 1996.

[145] S. Bittanti and S. M. Savaresi, "On the parameterization and design of an extended Kalman filter frequency tracker," *IEEE Trans. Autom. Cont.,* vol. 45, no. 9, pp. 1718-1724, Sept. 2000.

[146] G. Benmouyal, "Frequency-domain characterization of Kalman filters as applied to power system protection," *IEEE Trans. Power Del.,* vol. 7, no. 3, pp. 1129-1138, July 1992.

[147] P. K. Ray and B. Subudhi, "Ensemble-Kalman-filter-based power system harmonic estimation," *IEEE Trans. Instrum. Measur.,* vol. 61, no. 12, pp. 3216-3224, Dec. 2012.

[148] O. Chaari, P. Bastard, and M. Meunier, "Prony's method: an efficient tool for the analysis of earth fault currents in Petersen-coil-protected networks," *IEEE Trans. Power Del.,* vol. 10, no. 3, pp. 1234-1241, July 1995.

[149] J. Zygarlicki, M. Zygarlicka, J. Mroczka, and K. J. Latawiec, "A reduced Prony's method in power-quality analysis-parameters selection," *IEEE Trans. Power Del.,* vol. 25, no. 2, pp. 979-986, Apr. 2010.

[150] C.-I. Chen and G. W. Chang, "An efficient Prony-based solution procedure for tracking of power system voltage variations," *IEEE Trans. Ind. Elect.,* vol. 60, no. 7, pp. 2681-2688, July 2013.

[151] E. A. Feilat, "Detection of voltage envelope using Prony analysis-Hilbert transform method," *IEEE Trans. Power Del.,* vol. 21, no. 4, pp. 2091-2093, Oct. 2006.

[152] F. F. Costa and A. J. M. Cardoso, "Harmonic and interharmonic identification based on improved Prony's method," in *Proc. of 32nd Ann. Conf. IEEE Ind. Elect.*, 2006, pp. 1047-1052.

[153] A. Andreotti, A. Bracale, P. Caramia, and G. Carpinelli, "Adaptive Prony method for the calculation of power-quality indices in the presence of nonstationary disturbance waveforms," *IEEE Trans. Power Del.,* vol. 24, no. 2, pp. 874-883, Apr. 2009.

[154] L. Hong, L. Zhong, H. Wolfgang, Z. Bo, and C. Guanrong, "Analyzing chaotic spectra of DC-DC converters using the Prony method," *IEEE Trans. Cir. Sys. II: Express Briefs,* vol. 54, no. 1, pp. 61-65, Jan. 2007.

[155] C.-I. Chen, "Design of measurement system based on signal reconstruction for analysis and protection of distributed generations," *IEEE Trans. Ind. Elect.,* vol. 60, no. 4, pp. 1652-1658, Apr. 2013.

[156] R. Kumaresan and D. W. Tufts, "Estimating the parameters of exponentially damped sinusoids and pole-zero modeling in noise," *IEEE Trans. Acous. Spe. Signal Proc.,* vol. 30, no. 6, pp. 833-840, Dec. 1982.

[157] Z. Leonowicz, T. Lobos, and J. Rezmer, "Advanced spectrum estimation methods for signal analysis in power electronics," *IEEE Trans. Ind. Elect.,* vol. 50, no. 3, pp. 514-519, June 2003.

[158] R. Kumaresan, "On the zeros of the linear prediction-error filter for deterministic signals," *IEEE Trans. Acous. Spe. Signal Proc.,* vol. 31, no. 1, pp. 217-220, Feb. 1983.

[159] N. Kamel, P. Sankaran, and B. Venkatesh, "Fault-current predetermination using time- limited CT secondary side measurements by the covariance-Prony method," *IEE Proc.-Gen. Transm. Distrib.,* vol. 151, no. 6, pp. 735-739, Nov. 2004.

[160] M. S. Mazzola, N. H. Younan, R. Soundararajan, and S. E. Saddow, "Application of the singular valve decomposition-Prony method for analyzing deep-level transient spectroscopy capacitance transients," *Review of Scien. Instrum.,* vol. 69, no. 6, pp. 2459-2463, June 1998.

[161] S. Lotfifard, J. Faiz, and M. Kezunovic, "Detection of symmetrical faults by distance relays during power swings," *IEEE Trans. Power Del.,* vol. 25, no. 1, pp. 81-87, Jan. 2010.

[162] F. F. Costa, D. A. Fernandes, L. A. L. De Almeida, and S. R. Naidu, "Prony's method versus FFT for analyzing power converters signals," in *Proc. of Europ. Conf. Power Elect. App.*, 2005.

[163] N. Soon-Ryul, K. Seung-Hwa, J. Liu-Ming, K. Sang-Hee, and M. Sang-Won, "A novel method based on Prony analysis for fundamental frequency estimation in power systems," in *Proc. of IEEE TENCON Spring Conf.*, 2013, pp. 327-331.

[164] P. K. Dash, D. P. Swain, A. Routray, and A. C. Liew, "An adaptive neural network approach for the estimation of power system frequency," *Elsevier Elect. Power Sys. Res.,* vol. 41, no. 3, pp. 203-210, 1997.

[165] L. L. Lai, W. L. Chan, C. T. Tse, and A. T. P. So, "Real-time frequency and harmonic evaluation using artificial neural networks," *IEEE Trans. Power Del.,* vol. 14, no. 1, pp. 52-59, Jan. 1999.

[166] M. Valtierra-Rodriguez, R. de Jesus Romero-Troncoso, R. A. Osornio-Rios, and A. Garcia-Perez, "Detection and classification of single and combined power quality disturbances using neural networks," *IEEE Trans. Ind. Elect.,* vol. 61, no. 5, pp. 2473-2482, May 2014.

[167] S. K. Jain and S. N. Singh, "Low-order dominant harmonic estimation using adaptive wavelet neural network," *IEEE Trans. Ind. Elect.,* vol. 61, no. 1, pp. 428-435, Jan. 2014.

[168] S. Osowski, "Neural network for estimation of harmonic components in a power system," *IEE Proc. Gen., Transm. Dist.,* vol. 139, no. 2, pp. 129-135, Mar. 1992.

[169] G. W. Chang, C.-I. Chen, and Y.-F. Teng, "Radial-basis-function-based neural network for harmonic detection," *IEEE Trans. Ind. Elect.,* vol. 57, no. 6, pp. 2171-2179, Jne 2010.

[170] S. Golestan, M. Monfared, F. D. Freijedo, and J. M. Guerrero, "Advantages and Challenges of a Type-3 PLL," *IEEE Trans. Power Elect.,* vol. 28, no. 11, pp. 4985-4997, Nov. 2013.

[171] S. Golestan, M. Monfared, F. D. Freijedo, and J. M. Guerrero, "Dynamics assessment of advanced single-phase PLL structures," *IEEE Trans. Ind. Elect.,* vol. 60, no. 6, pp. 2167-2177, June 2013.

[172] Q. Zhang, X.-D. Sun, Y.-R. Zhong, M. Matsui, and B.-Y. Ren, "Analysis and design of a digital phase-locked loop for single-phase grid-connected power conversion systems," *IEEE Trans. Ind. Elect.,* vol. 58, no. 8, pp. 3581-3592, Aug. 2011.

[173] S. Golestan, M. Ramezani, and J. M. Guerrero, "An analysis of the PLLs with secondary control path," *IEEE Trans. Ind. Elect.,* vol. 61, no. 9, pp. 4824-4828, Sept. 2014.

[174] S. Golestan and J. M. Guerrero, "Conventional synchronous reference frame phase-locked loop is an adaptive complex filter," *IEEE Trans. Ind. Elect.,* 2014.

[175] S. Golestan, M. Monfared, F. D. Freijedo, and J. M. Guerrero, "Performance improvement of a prefiltered synchronous-reference-frame PLL by using a PID-type loop filter," *IEEE Trans. Ind. Elect.,* vol. 61, no. 7, pp. 3469-3479, July 2014.

[176] M. Karimi-Ghartemani, "Linear and pseudolinear enhanced phased-locked loop (epll) structures," *IEEE Trans. Ind. Elect.,* vol. 61, no. 3, pp. 1464-1474, Mar. 2014.

[177] M. Karimi-Ghartemani and M. R. Iravani, "A nonlinear adaptive filter for online signal analysis in power systems: applications," *IEEE Trans. Power Del.,* vol. 17, no. 2, pp. 617-622, Apr. 2002.

[178] M. Karimi-Ghartemani and M. R. Iravani, "Robust and frequency-adaptive measurement of peak value," *IEEE Trans. Power Del.,* vol. 19, no. 2, pp. 481-489, Apr. 2004.

[179] M. Karimi-Ghartemani, S. A. Khajehoddin, P. K. Jain, A. Bakhshai, and M. Mojiri, "Addressing DC component in PLL and notch filter algorithms," *IEEE Trans. Power Elect.,* vol. 27, no. 1, pp. 78-86, Jan. 2012.

[180] M. Karimi-Ghartemani, H. Karimi, and M. R. Iravani, "A magnitude/phase-locked loop system based on estimation of frequency and in-phase/quadrature-phase amplitudes," *IEEE Trans. Ind. Elect.,* vol. 51, no. 2, pp. 511-517, Apr. 2004.

[181] K.-J. Lee, J.-P. Lee, D. Shin, D.-W. Yoo, and H.-J. Kim, "A novel grid synchronization PLL method based on adaptive low-pass notch filter for grid-connected PCS," *IEEE Trans. Ind. Elect.,* vol. 61, no. 1, pp. 292-301, Jan. 2014.

[182] M. Ciobotaru, V. G. Agelidis, R. Teodorescu, and F. Blaabjerg, "Accurate and less-disturbing active antiislanding method based on PLL for grid-connected converters," *IEEE Trans. Power Elect.,* vol. 25, no. 6, pp. 1576-1584, June 2010.

[183] M. Ciobotaru, R. Teodorescu, and F. Blaabjerg, "A new single-phase PLL structure based on second order generalized integrator," in *Proc. 37th IEEE Power Elect. Spec. Conf. (PESC)*, 2006, pp. 1-6.

[184] M. Ciobotaru, R. Teodorescu, and V. G. Agelidis, "Offset rejection for PLL based synchronization in grid-connected converters," *Proc. 23rd Ann. IEEE App. Power Elect. Conf. Expo. (APEC),* pp. 1611-1617, 2008.

[185] A. Nicastri and A. Nagliero, "Comparison and evaluation of the PLL techniques for the design of the grid-connected inverter systems," in *Proc. IEEE Int. Symp. Ind Elect.*, 2010, pp. 3865-3870.

[186] Y. F. Wang and Y. W. Li, "A grid fundamental and harmonic component detection method for single-phase systems," *IEEE Trans. Power Elect.,* vol. 28, no. 5, pp. 2204-2213, May 2013.

[187] S. M. Silva, B. M. Lopes, B. J. C. Filho, R. P. Campana, and W. C. Bosventura, "Performance evaluation of PLL algorithms for single-phase grid-connected systems," *Proc. IEEE 39th Ann. Meet. Ind. App. Conf.,* pp. 2259-2263, 3-7 Oct. 2004 2004.

[188] M. Karimi-Ghartemani, S. A. Khajehoddin, P. K. Jain, and A. Bakhshai, "Derivation and design of in-loop filters in phase-locked loop systems," *IEEE Trans. Instrum. Meas.,* vol. 61, no. 4, pp. 930-940, Apr. 2012.

[189] S. Golestan, M. Monfared, F. D. Freijedo, and J. M. Guerrero, "Design and tuning of a modified power-based PLL for single-phase grid-connected power conditioning systems," *IEEE Trans. Power Elect.,* vol. 27, no. 8, pp. 3639-3650, Aug. 2012.

[190] L. Feola, R. Langella, and A. Testa, "On the effects of unbalances, harmonics and interharmonics on PLL systems," *IEEE Trans. Instrum. Measur.,* vol. 62, no. 9, pp. 2399-2409, Sept. 2013.

[191] J. R. de Carvalho, C. A. Duque, M. V. Ribeiro, A. S. Cerqueira, T. L. Baldwin, and P. F. Ribeiro, "A PLL-based multirate structure for time-varying power systems

harmonic/interharmonic estimation," *IEEE Trans. Power Del.,* vol. 24, no. 4, pp. 1789-1800, Oct. 2009.

[192] M. K. Ghartemani, S. A. Khajehoddin, P. K. Jain, and A. Bakhshai, "Problems of startup and phase jumps in PLL systems," *IEEE Trans. Power Elect.,* vol. 27, no. 4, pp. 1830-1838, Apr. 2012.

[193] P. Rodriguez, A. Luna, M. Ciobotaru, R. Teodorescu, and F. Blaabjerg, "Advanced grid synchronization system for power converters under unbalanced and distorted operating conditions," in *Proc. 32nd Ann. Conf. IEEE Ind. Elect. (IECON)*, 2006, pp. 5173-5178.

[194] P. Rodriguez, A. Luna, I. Candela, R. Teodorescu, and F. Blaabjerg, "Grid synchronization of power converters using multiple second order generalized integrators," in *Proc. of 34th Ann. Conf. IEEE Ind. Elect. (IECON)*, 2008, pp. 755-760.

[195] F. J. Rodriguez, E. Bueno, M. Aredes, L. G. B. Rolim, F. A. S. Neves, and M. C. Cavalcanti, "Discrete-time implementation of second order generalized integrators for grid converters," in *Proc. of 34th IEEE Ann. Conf. Ind. Elect. (IECON)*, 2008, pp. 176-181.

[196] B. Burger and A. Engler, "Fast signal conditioning in the single phase systems," in *Proc. of European Conf. Power Elect. App.*, Graz, Austria, 2001.

[197] P. Rodriguez, A. Luna, I. Candela, R. Mujal, R. Teodorescu, and F. Blaabjerg, "Multiresonant frequency-locked loop for grid synchronization of power converters under distorted grid conditions," *IEEE Trans. Ind. Elect.,* vol. 58, no. 1, pp. 127-138, Jan. 2011.

[198] P. Rodriguez, A. Luna, R. S. Munoz-Aguilar, I. Etxeberria-Otadui, R. Teodorescu, and F. Blaabjerg, "A stationary reference frame grid synchronization system for three-phase grid-connected power converters under adverse grid conditions," *IEEE Trans. Power Elect.,* vol. 27, no. 1, pp. 99-112, Jan. 2012.

[199] S. Vazquez, J. A. Sanchez, M. R. Reyes, J. I. Leon, and J. M. Carrasco, "Adaptive vectorial filter for grid synchronization of power converters under unbalanced and/or distorted grid conditions," *IEEE Trans. Ind. Elect.,* vol. 61, no. 3, pp. 1355-1367, Mar. 2014.

[200] J. Matas, M. Castilla, J. Miret, L. Garcia de Vicuna, and R. Guzman, "An adaptive prefiltering method to improve the speed/accuracy tradeoff of voltage sequence

detection methods under adverse grid conditions," *IEEE Trans. Ind. Elect.,* vol. 61, no. 5, pp. 2139-2151, May 2014.

[201] P. Rodriguez, A. Luna, I. Etxeberria, J. R. Hermoso, and R. Teodorescu, "Multiple second order generalized integrators for harmonic synchronization of power converters," in *proc. of IEEE Energy Conv. Congr. Expo. (ECCE)*, 2009, pp. 2239-2246.

[202] A. Cardenas, C. Guzman, and K. Agbossou, "Frequency Locked Loop for grid-connected VSI synchronization and power analysis," in *Proc. of IEEE Int. Symp. Ind. Elect.*, 2012, pp. 1386-1392.

[203] P. M. Djuric, M. M. Begovic, and M. Doroslovacki, "Instantaneous phase tracking in power networks by demodulation," *IEEE Trans. Instrum. Measur.,* vol. 41, no. 6, pp. 963-967, Dec. 1992.

[204] M. Akke, "Frequency estimation by demodulation of two complex signals," *IEEE Trans. Power Del.,* vol. 12, no. 1, pp. 157-163, Jan. 1997.

[205] R. Zivanovic, "An adaptive differentiation filter for tracking instantaneous frequency in power systems," *IEEE Trans. Power Del.,* vol. 22, no. 2, pp. 765-771, Apr. 2007.

[206] A. Elrayyah, A. Safayet, Y. Sozer, I. Husain, and M. Elbuluk, "Efficient harmonic and phase estimator for single phase grid-connected renewable energy systems," *IEEE Trans. Ind. Appl.,* vol. 50, no. 1, pp. 620-630, Jan./Feb. 2013.

[207] L. Angrisani, R. Schiano Lo Moriello, M. D'Arco, and C. A. Greenhall, "A digital signal processing instrument for real-time phase noise measurement," *IEEE Trans. Instrum. Measur.,* vol. 57, no. 10, pp. 2098-2107, 2008.

[208] L. Angrisani, M. D'Apuzzo, and M. D'Arco, "A digital signal-processing approach for phase noise measurement," *IEEE Trans. Instrum. Measur.,* vol. 50, no. 4, pp. 930-935, Aug. 2001.

[209] L. Angrisani, A. Baccigalupi, and M. D'Arco, "Evaluating phase noise power spectrum with variable frequency resolution," *IEEE Trans. Instrum. Measur.,* vol. 53, no. 3, pp. 685-691, June 2004.

[210] C. A. G. Marques, M. V. Ribeiro, C. A. Duque, P. F. Ribeiro, and E. A. B. Da Silva, "A controlled filtering method for estimating harmonics of off-nominal frequencies," *IEEE Trans. Smart Grid,* vol. 3, no. 1, pp. 38-49, Mar. 2012.

[211] C. A. G. Marques, M. V. Ribeiro, and E. A. B. da Silva, "Enhanced demodulation-based technique for estimating the parameters of fundamental component in power systems," *IET Gen. Transm. Dist.,* vol. 5, no. 9, pp. 979-988, 2011.

[212] M. D'Apuzzo and M. D'Arco, "A time-domain approach for the analysis of nonstationary signals in power systems," *IEEE Trans. Instrum. Measurem.,* vol. 57, no. 9, pp. 1969-1977, Sept. 2008.

[213] M. M. Begovic, P. M. Djuric, S. Dunlap, and A. G. Phadke, "Frequency tracking in power networks in the presence of harmonics," *IEEE Trans. Power Del.,* vol. 8, no. 2, pp. 480-486, Apr. 1993.

[214] J. F. Kaiser, "On a simple algorithm to calculate the 'energy' of a signal," *Proc. Int. Conf. Acoustics, Speech, and Sig. Proc.,* pp. 381-384, 3-6 Apr 1990 1990.

[215] J. F. Kaiser, "Some useful properties of Teager's energy operators," in *IEEE Int. Conf. Acous. Spe. Signal Proc.*, 1993, pp. 149-152.

[216] T. K. Abdel-Galil, E. F. El-Saadany, and M. M. A. Salama, "Online tracking of voltage flicker utilizing energy operator and Hilbert transform," *IEEE Trans. Power Del.,* vol. 19, no. 2, pp. 861-867, Apr. 2004.

[217] I. Kamwa, A. K. Pradhan, and G. Joos, "Robust detection and analysis of power system oscillations using the Teager-Kaiser energy operator," *IEEE Trans. Power Sys.,* vol. 26, no. 1, pp. 323-333, Feb. 2011.

[218] A. Subasi, A. S. Yilmaz, and K. Tufan, "Detection of generated and measured transient power quality events using Teager energy operator," *Elsevier Energy Conv. and Manag.,* vol. 52, pp. 1959-1967, 2011.

[219] M. A. Eldery, E. F. El-Saadany, and M. M. A. Salama, "An on-line measurement of symmetrical components utilizing the energy operator," in *Proc. of IEEE Power Engg. Soc. Gen. Meet.*, 2006, pp. 1-5.

[220] M. A. Eldery, E. F. El-Saadany, and M. M. A. Salama, "A novel energy operator algorithm for voltage envelope tracking," *IEEE Trans. Power Sys.,* vol. 20, no. 1, pp. 510-512, Feb. 2005.

[221] M. A. Eldery, E. F. El-Saadany, and M. M. A. Salama, "A simple energy operator computational method for voltage flicker assessment," *IEEE Trans. Power Del.,* vol. 21, no. 3, pp. 1743-1750, July 2006.

[222] E. Robles, J. Pou, S. Ceballos, J. Zaragoza, J. L. Martin, and P. Ibanez, "Frequency-adaptive stationary-reference-frame grid voltage sequence detector for distributed

generation systems," *IEEE Trans. Ind. Elect.,* vol. 58, no. 9, pp. 4275-4287, Sept. 2011.

[223] D. W. P. Thomas and M. S. Woolfson, "Evaluation of frequency tracking methods," *IEEE Trans. Power Del.,* vol. 16, no. 3, pp. 367-371, July 2001.

[224] M. B. Duric and Z. R. Durisic, "Frequency measurement in power networks in the presence of harmonics using fourier and zero crossing technique," in *Proc. of IEEE Power Tech*, 2005, pp. 1-6.

[225] L. Asnin, V. Backmutsky, and M. Gankin, "Comparative characteristics of main methods for dynamic estimation of frequency and magnitude parameters in power systems," in *Proc. of 22nd Convention of IEEE Elect. Electro. Engr.*, 2002, pp. 35-38.

[226] S. Valiviita, "Zero-crossing detection of distorted line voltages using 1-b measurements," *IEEE Trans. Ind. Elect.,* vol. 46, no. 5, pp. 917-922, Oct. 1999.

[227] C. T. Nguyen and K. Srinivasan, "A new technique for rapid tracking of frequency deviations based on level crossings," *IEEE Trans. Power Appar. Systems,* vol. PAS-103, no. 8, pp. 2230-2236, Aug. 1984.

[228] S. Valiviita, "Neural network for zero-crossing detection of distorted line voltages in weak AC-systems," in *Proc. of IEEE Instrum. Measur. Tech. Conf.*, 1998, pp. 280-285.

[229] S. Das, S. Prasid, G. Bandyopadhyay, and A. K. Chattopadhyay, "Wavelet transform application for zero-crossing detection of distorted line voltages in weak AC-systems," in *Proc. of IEEE first India Ann. Conf.*, 2004, pp. 464-467.

[230] V. Friedman, "A zero crossing algorithm for the estimation of the frequency of a single sinusoid in white noise," *IEEE Trans. Signal Proc.,* vol. 42, no. 6, pp. 1565-1569, June 1994.

[231] O. Vainio and S. J. Ovaska, "Digital filtering for robust 50/60 Hz zero-crossing detectors," *IEEE Trans. Instrum. Measur.,* vol. 45, no. 2, pp. 426-430, Apr. 1996.

[232] O. Vainio and S. J. Ovaska, "Noise reduction in zero crossing detection by predictive digital filtering," *IEEE Trans. Ind. Elect.,* vol. 42, no. 1, pp. 58-62, Feb. 1995.

[233] O. Vainio and S. J. Ovaska, "Multistage adaptive filters for in-phase processing of line-frequency signals," *IEEE Trans. Ind. Elect.,* vol. 44, no. 2, pp. 258-264, Apr. 1997.

[234] O. Vainio, S. J. Ovaska, and M. Polla, "Adaptive filtering using multiplicative general parameters for zero-crossing detection," *IEEE Trans. Ind. Elect.,* vol. 50, no. 6, pp. 1340-1342, Dec. 2003.

[235] H.-E. Liao, "Two discrete oscillator based adaptive notch filters (OSC ANFs) for noisy sinusoids," *IEEE Trans. Signal Proc.,* vol. 53, no. 2, pp. 528-538, Feb. 2005.

[236] A. Lopez, J.-C. Montano, M. Castilla, J. Gutierrez, M. D. Borras, and J. C. Bravo, "Power system frequency measurement under nonstationary situations," *IEEE Trans. Power Del.,* vol. 23, no. 2, pp. 562-567, Apr. 2008.

[237] M. D. Kusljevic, "A simple recursive algorithm for frequency estimation," *IEEE Trans. Instrum. Measur.,* vol. 53, no. 2, pp. 335-340, Apr. 2004.

[238] M. D. Kusljevic, "Adaptive resonator-based method for power system harmonic analysis," *IET Sci. Meas. Tech.,* vol. 2, no. 3, pp. 177-185, 2008.

[239] A. Abdollahi and F. Matinfar, "Frequency estimation: A least-squares new approach," *IEEE Trans. Power Del.,* vol. 26, no. 2, pp. 790-798, Apr. 2011.

[240] M. D. Kusljevic, "A simple recursive algorithm for simultaneous magnitude and frequency estimation," *IEEE Trans. Instrum. Measur.,* vol. 57, no. 6, pp. 1207-1214, June 2008.

[241] F. Wang and M. H. J. Bollen, "Frequency-response characteristics and error estimation in RMS measurement," *IEEE Trans. Power Del.,* vol. 19, no. 4, pp. 1569-1578, Oct. 2004.

[242] M. Albu and G. T. Heydt, "On the use of RMS values in power quality assessment," *IEEE Trans. Power Del.,* vol. 18, no. 4, pp. 1586-1587, Oct. 2003.

[243] X. X. Yang and M. Kratz, "Power system flicker analysis by RMS voltage values and numeric flicker meter emulation," *IEEE Trans. Power Del.,* vol. 24, no. 3, pp. 1310-1318, July 2009.

[244] M. Mojiri, M. Karimi-Ghartemani, and A. Bakhshai, "Estimation of power system frequency using an adaptive notch filter," *IEEE Trans. Instrum. Meas.,* vol. 56, no. 6, pp. 2470-2477, Dec. 2007.

[245] M. Mojiri, M. Karimi-Ghartemani, and A. Bakhshai, "Time-domain signal analysis using adaptive notch filter," *IEEE Trans. Signal Proc.,* vol. 55, no. 1, pp. 85-93, Jan. 2007.

[246] G. Fedele, C. Picardi, and D. Sgro, "A power electrical signal tracking strategy based on the modulating functions method," *IEEE Trans. Ind. Elect.,* vol. 56, no. 10, pp. 4079-4087, Oct. 2009.

[247] G. Fedele and L. Coluccio, "A recursive scheme for frequency estimation using modulating functions method," *Elsevier App. Math. and Computations,* vol. 216, pp. 1393-1400, 2010.

[248] H. A. Preisig and D. W. T. Rippin, "Theory and application of the modulating function method-I. Review and theory of the method and theory of the spline-type modulating functions," *Elsevier Journ. Comp. & Chem. Engg.,* vol. 17, no. 1, pp. 1-16, 1993.

[249] E. Clarke, *Circuit Analysis of A.C. Power Systems,* New York: Wiley, 1943.

[250] M. Ciobotaru, "Reliable grid condition detection and control of single-phase distributed power generation systems," *PhD Thesis, Aalborg University,* 2009.

[251] J. A. Rosendo Macias and A. G. Exposito, "Efficient moving-window DFT algorithms," *IEEE Trans. Cir. Sys. II: Ana. Dig. Signal Proc.,* vol. 45, no. 2, pp. 256-260, Feb. 1998.

[252] Y. F. Wang and Y. W. Li, "Three-phase cascaded delayed signal cancellation PLL for fast selective harmonic detection," *IEEE Trans. Ind. Elect.,* vol. 60, no. 4, pp. 1452-1463, Apr. 2013.

[253] IEC Standard 61000-4-13, "Testing and measurement techniques-Harmonics and interharmonics including mains signaling at AC power port, low frequency immunity test," 2002.

[254] IEC Standard 61000-4-7, "Testing and measurement techniques-General guide on harmonics and interharmonics measurements and instrumentation, for power supply systems and equipment connected thereto," 2002.

[255] European Standard EN-50160, "Voltage characteristics of electricity supplied by public distribution systems," 1999.

[256] S. Kay, "A fast and accurate single frequency estimator," *IEEE Trans. Acoust. Speech and Sig. Proc.,* vol. 37, no. 12, pp. 1987-1990, 1989.

[257] G. Andria, A. Dell'Aquila, and L. Salvatore, "Analysis of distorted unbalanced waveforms in inverter drives," *IEEE Trans. Power Elect.,* vol. 4, no. 2, pp. 298-310, Apr. 1989.

[258] A. G. Yepes, F. D. Freijedo, J. Doval-Gandoy, O. Lopez, J. Malvar, and P. Fernandez-Comesana, "Effects of discretization methods on the performance of resonant controllers," *IEEE Trans. Power Elect.,* vol. 25, no. 7, pp. 1692-1712, July 2010.

[259] G. Fedele and A. Ferrise, "Non adaptive second-order generalized integrator for identification of a biased sinusoidal signal," *IEEE Trans. Auto. Cont.,* vol. 57, no. 7, pp. 1838-1842, July 2012.

[260] H. E. P. de Souza, M. C. Cavalcanti, F. Bradaschia, E. J. Bueno, and M. Rizo, "A generalized delayed signal cancellation method for detecting fundamental-frequency positive-sequence three-phase signals," *IEEE Trans. Power Del.,* vol. 25, no. 3, no. 3, pp. 1816-1825, July 2010.

[261] Y. F. Wang and Y. W. Li, "Grid synchronization PLL based on cascaded delayed signal cancellation," *IEEE Trans. Power Elect.,* vol. 26, no. 7, pp. 1987-1997, July 2011.

[262] S. R. Shaw and C. R. Laughman, "A Kalman-filter spectral envelope preprocessor," *IEEE Trans. Instrum. Meas.,* vol. 56, no. 5, pp. 2010-2017, Oct. 2007.